Structure and Asymmetry in Simulations of Supernova Explosions

by

Carola I. Ellinger

A Dissertation Presented in Partial Fulfillment
of the Requirements for the Degree
Doctor of Philosophy

Approved September 2011 by the
Graduate Supervisory Committee:

Patrick Young, Chair
Steven Desch
Francis Timmes
Evan Scannapieco
Cecilia Lunardini

ARIZONA STATE UNIVERSITY

December 2011

ABSTRACT

There are many lines of evidence for anisotropy at all scales in the explosions of core collapse supernovae, e.g. visual inspection of the images of resolved supernova remnants, polarization measurements, velocity profiles, "natal kicks" of neutron stars, or spectroscopic observations of different regions of remnants. Theoretical stability considerations and detailed numerical simulations have shown that Rayleigh-Taylor (RT) instabilities arise in the star after the explosion, which leads to the early fragmentation of parts of the ejecta. The clumps thus created are of interest to a variety of topics, one of them being the formation environment of the solar system. There is a high probability that the solar system formed in the vicinity of a massive star that, shortly after its formation, exploded as a core collapse supernova. As argued in this thesis as well as other works, a core collapse supernova generally is a good candidate for chemically enriching the forming solar system with material. As forming proto–planetary systems in general have a high probability of being contaminated with supernova material, a method was developed for detecting tracer elements indicative supernova contamination in proto–planetary systems. The degree of the anisotropy of the supernova explosion can have dramatic effects on the mode of delivery of that material to the solar system, or proto–planetary systems in general. Thus it is of particular interest to be able to predict the structure of the supernova ejecta. Numerical simulations of the explosions of core collapse supernovae were done in 3 dimensions in order to study the formation of structure. It is found that RT instabilities result in clumps in the He- and C+O rich regions in the exploding star that are overdense by 1-2 orders of magnitude. These clumps are potential candidates for enriching the solar system with material. In the course of the further evolution of the supernova remnant, these RT clumps are likely to evolve into ejecta knots of the type observed in the Cassiopeia A supernova remnant.

ACKNOWLEDGEMENTS

This work was supported by NSF grant #0807567 and The NASA Astrobiology Institute. This work also made use of and benefitted from the computing resources at the ASU Advanced Computing Center (A2C2).

TABLE OF CONTENTS

LIST OF TABLES

LIST OF FIGURES

Chapter 1

INTRODUCTION

Morphological, kinematic, and compositional structures are ubiquitous in observations of supernovae (SNe) and young supernova remnants (SNRs). These structures span scales from unipolar asymmetries across the whole remnant to the astronomical unit (AU) scale like high density knots being shredded in the reverse shock of Cassiopeia A (Cas A). The dense knots in SNRs are of particular interest from a nucleosynthetic and astrobiological point of view as vehicles for enrichment of star and planet-forming material in high mass star formation regions, as well as for interpreting observations of remnants. Spectroscopic observations in a multitude of young SNRs have established that they are SN material, and they have been observed in young SNRs of various ages. They are prime candidates for probing the turbulent flow of matter in core-collapse (CC) SN explosion from both theoretical and observational aspects.

Multiple physical processes drive their formation. Although it has long been known (Epstein 1979, Falk & Arnett 1973, Chevalier 1976) that the flow of matter in a SN explosion should be unstable to turbulence, it was not initially included in computer models of supernova simulations. Inherently a multi-dimensional problem, 1D simulations do not capture the behavior. Direct observational evidence of high velocity nickel and low velocity hydrogen in the explosion of SN 1987A spurred a tremendous amount of numerical modeling of that supernova in 1, 2, and 3 dimensions. Generally, what was learned from those was that fragmentation of the ejecta early on is necessary to explain the observed light curves and the early detection of X-rays and gamma-rays from the remnant. Arnett et al. (1989) point out a number of sites/events in an exploding star that can lead to deviation from spherical behavior, and point out the formation of RT fingers by shock passage as

the most important one. However, in most cases RT instabilities are not able to mix out sufficient Ni to explain the high velocities observed in 1987A for those isotopes, as these instabilities were typically found to arise well outside of the Ni-rich layers of the supernova. "Pre-mixing" some Ni-rich material out to radii where it could become entrained in the RT instabilities would remedy this problem (Herant and Benz 1992), however no definite mechanism has been found for this "pre-mixing", although it is assumed to be related to the explosion mechanism. During the revival of the explosion shock, convection is taking place between the proto-neutron star and the stalled shock wave. It has been shown that it results in large-scale convection with only a small number of convective cells, and further leads to incomplete turnover, i.e. the rising material continues to move outwards once it has been launched in the convection. Although these instabilities/convection have not been found to result directly in knots, the perturbations can act as seeds for later instabilities, can impose large scale, low mode asymmetries (bipolar, etc. explosions), and can possibly mix metals (above O) out to larger radii.

RT instabilities arise commonly in situations where a less dense fluid is accelerated into a denser fluid (e.g. when a less dense fluid is supporting a denser fluid against gravity). This is an unstable situation, and any small fluctuation in thermodynamic quantities grow and render the system unstable. Bubbles of the less dense fluid rise into the heavy fluid, while columns or spikes of the denser fluid penetrate into the lighter one. Shear flows at the interface between the two fluids are subject to Kelvin-Helmholtz (KH) instabilities. Eventually the flow becomes highly non-linear, and the result is the famous RT fingers, i.e. columns of material ending in a mushroom- shaped top.

A related phenomenon is the Richtmyer-Meshkov (RM) instability, which results in very similar looking features. The main difference is that RM instabilities

result from the interface between two fluids being impulsively accelerated, typically by a strong shock, instead of a lighter fluid being accelerated into a heavier one. Both scenarios, a shock accelerated into an interface between heavy to light and light to heavy fluids are unstable in the RM sense. Commonly, vorticity resulting from non-parallel density and pressure gradients as a result of the shock -interface interaction is cited as causing the RM instability. Again, shear flows between the rising and falling fluids result in the characteristic KH-mushrooming. These two instabilities (RT and RM) seem to be used somewhat interchangeably to describe turbulence in SN explosions, as there is no defining or clear-cut difference in appearance between them. Indeed, Richtmyer and Meshkov studied RT instabilities in the strong-shock limit; so there is no actual, fundamental difference between them.

In an exploding star RT or RM unstable regions can be set up by the outward propagating blast wave as Arnett et al. (1989) have pointed out. Density varies in a pre-SN star roughly as r^{-3}, however the profile can be more or less steep at different locations. If the profile is flatter than r^{-3}, the outgoing shock decelerates, and material starts piling up behind it. The deceleration of the shock reverses the pressure gradient behind it, i.e. the pressure gradient becomes opposite in direction to the density and gravitational gradients. If the reversed pressure gradient becomes large enough, the region becomes RT unstable. In other words, the piling up of material right behind the decelerating shock increases the density there, while the material a little further in is still moving at the original speed and non-compressed density, so in effect this lighter material is accelerated into the denser piled-up material. Herant & Woosley (1994) and Woosley & Weaver (1995) report this process. This same piling up of material creates a reverse shock that travels back through the already shocked material to the center. This reverse shock is the main driver for the inverted density and pressure gradients.

As the formation of structure and clumps shapes the ejecta of SNe, it determines how this material is returned to and interacts with the surrounding ISM. Dense clumps are mixed with the ISM differently than uniform (lower density) gas. The particular form in which SN ejecta is returned to the ISM also plays an important role in the formation history of our solar system. There is convincing evidence that the solar system was contaminated with material from a nearby SN explosion at its birth (e.g. Wadhwa et al. 2007), and it has been shown that this contamination occurred via small dust grains of SN material (Ouellette et al. 2007); gaseous material has been found to not be able to contribute material to a forming solar system if a disk had already formed. Dust grains can form from SN ejecta that can cool sufficiently before becoming too tenuous from the expansion. This situation is most likely achieved in over–dense regions, such as the ejecta knots observed in Cas A, or like the RT or RM instability fingers seen in multi-D SN simulations.

Having reliable theoretical predictions for the ejecta structure in SN explosions can thus contribute a big step towards the understanding of the formation events in our solar system and the early remnant stage of SNRs. Much can be learned already from detailed spectroscopic observations of young supernova remnants, however some key features need to be obtained from theoretical considerations. Of importance are a specific class of unstable isotopes (further described in chapter 2), which are very unlikely to be directly measured in observations. If abundant and stable elements that are uniquely co-produced could be identified, these could however be used as proxies or tracers in observations (cf. chapter 3). Although multi-D calculations of SN explosions have been carried out, most are terminated shortly after shock breakout, and to date only one (Herant and Benz 1992) follow the explosion to 90d after core bounce. None have published detailed isotopic yields. The main focus of those calculations was the hydrodynamic evo-

lution, and nucleosynthesis was not followed with an extensive nuclear reaction network.

Thus, the goal of this thesis is to investigate the formation of clumps and structure in supernova explosions with accurate determination of the composition and thermodynamic evolution, and discuss the results in the context of a SN enrichment scenario of the forming solar system. This thesis is divided into four main chapters, each constituting a project or paper. In chapter 2 I will discuss the specific isotopes and present arguments for the feasibility of the SN injection scenario as their origin. The work in this chapter was done as a project with Dr. Steven Desch, and presented in fulfillment of the comprehensive examination requirement. As many protoplanetary systems are observed near massive stars that will likely explode as SNe before the protoplanetary systems migrate from that region, it stands to reason that other protoplanetary system are subjected to the same fate as our solar system was at birth. In that case, chapter 3 investigates the probability of detecting evidence for such a SN contamination in other protoplanetary systems. The work in this chapter was done in collaboration with Dr. Patrick Young and appeared as Young et al. (2009) in the *Astrophysical Journal*. Chapter 4 deals with a very specific aspect of the SN injection scenario, namely the co-injection of the three stable oxygen isotopes (^{16}O, ^{17}O, and ^{18}O). As naturally a whole slew of different elements, not just a selected few, would be injected, there has been some debate if the SN injection scenario is consistent with all isotopes found in the solar system. This work was published in the *Astrophysical Journal* as Ellinger et al. (2010), and was done in collaboration with Dr. Patrick Young and Dr. Steven Desch. Finally, chapter 5 presents 3D simulations of a 15 $M_{\odot}$ progenitor exploded with different asymmetries, and the structure that is observed to form. The work in this chapter was done with Dr. Patrick Young, Dr. Chris Fryer, and Dr. Gabe Rockefeller,

and will be submitted for publication to the *Astrophysica Journal*. Chapter 6 offers some concluding thoughts.

Chapter 2

SHORT-LIVED RADIONUCLIDES IN THE EARLY SOLAR SYSTEM

Short-lived radionuclides (SLRs) are radioactive isotopes that decay with mean lives of around $0.15 - 23$ million years (Myr). Their presence at the formation of the Solar System has been firmly established (e.g. Wadhwa et al. 2007), however, there is still some debate about the details of their soure(s). The most extensively studied SLR is ^{26}Al MacPherson et al. (1995), which has a mean life of 1.02 Myr, others that have been detected and which are considered in this study are listed in table D.1 with their half lives and abundances (errors have been omitted for ease of reading; see also Appendix B for more detailed descriptions).

The mean lives of the SLRs are so short compared to the age of the Solar System (4.5672 ± 0.0006 Gyr, Amelin et al. (2002)), that any SLRs that existed at the beginning of the Solar System are extinct today. Yet their presence (and in some cases, their abundances) can still be inferred from anomalous abundance patterns of their decay products. The Solar System formed out of material that was almost exclusively in a gas phase (Nuth et al. 2006) and then cooled and condensed into solids (e.g. Russell et al. 2006; Messenger et al. 2006). The first solids were sub-micrometer sized minerals, which then aggregated into bigger grains (and then into asteroids, meteorite parent bodies, comets, planetesimals and eventually into planets (e.g. Russell et al. 2006). The oldest known solids are the grains known as Calcium-Aluminum-rich inclusions (CAIs), whose age has been determined through Pb-Pb dating (using the decay of both ^{235}U to ^{207}Pb and ^{238}U to ^{206}Pb simultaneously, see e.g. Podosek and Cassen 1994) and is taken to define the age of the Solar System. CAIs also contain the most refractory minerals known, which is why they are presumed to be the first to condense from the solar nebula.

Once a grain or mineral condenses from the solar nebula, it is (for this purpose) essentially a closed system. Its composition is said to be locked-in, meaning it does not acquire material from or lose material to the outside world. It is thus effectively taking a sample of the forming Solar System at a particular time. Any unstable isotope that is found in it must have been in the material from which the grain condensed. Let X be an unstable isotope that decays into stable isotope Y with a mean life of τ_X. Then the abundance of Y in that grain can be written as:

$$Y(t) = Y_0 + X_0 \cdot (1 - e^{-t/\tau_X}) = Y_0 + X(t), \tag{2.1}$$

where Y_0 and X_0 are the initial abundances of the unstable and stable isotope. This equation assumes that there are no other decay channels into isotope Y, which is an appropriate assumption for the SLRs. The quantities that are usually available for measurement are $Y(t)$ and $X(t)$, and one seeks to determine either one or all of Y_0, X_0, and t. The difficulty with the SLRs is that t (i.e. the time at which their composition is measured) is much larger than their mean lives, thus for any one single grain it is impossible to determine how much of Y and X were initially in it. Fortunately, a single CAI contains multiple grains of different mineralogy, which all formed at roughly the same time and place (since they are all incorporated into the same CAI). Equation 2.1 is valid separately for each grain, thus one can establish a system of equations to determine Y_0, X_0, and the time differences Δt_i between the formation of individual minerals. Note that the absolute ages of the grains or CAIs cannot be determined with SLRs; long–lived radionuclides (e.g. Pb) need to be used for this.

With the exception of ^{10}Be, all of the SLRs are produced in various stellar nucleosynthetic events like thermonuclear (type Ia) and core-collapse (type Ib, Ic, II; 'CC') SNe, asymptotic giant branch stars, and novae. Beryllium-10 is destroyed during nucleosynthesis; its main production site is in spallation reactions between

energetic particles and intermediate mass atoms like C, N or O (Reeves, Fowler, & Hoyle 1970). Since it is destroyed in nuclear reactions the abundance of ^{10}Be in the Early Solar System was expected to be lower that actually measured. The high abundance of ^{10}Be was initially understood to require a period of intense irradiation processes in the Early Solar System (McKeegan, Chaussidon, & Robert 2000). However, a more recent analysis by Desch (2004) showed that the trapping of galactic cosmic rays is the likely source of the ^{10}Be in the Early Solar System. The origin of ^{10}Be is therefore considered as separate from the others, and exclude it from this analysis. In the remainder of this chapter I will consider the origin of the other 8 SLRs.

2.1 Possible Origins for the SLRs

As there are multiple (astrophysical) production sites there are naturally multiple possible models that can be conceived to explain the presence of the SLRs, that need not be mutually exclusive. The simplest model - inheritance from the parent molecular cloud - has been ruled out on the basis of the short half lives as compared to galactic chemical evolution time scales. As stars enrich the ISM with 'new' material when they die, isotopes of long enough (i.e. on the order of or greater than the average time between stellar enrichment events) half lives can attain a 'steady state abundance' level in the ISM. However, it has been shown that Galactic Chemical evolution models are inable to reproduce the measured abundance of all SLRs (Meyer & Clayton 2000, Nittler & Dauphas 2006), save for a specific case of a SN enrichment event that occurred close in time and space to the forming solar system. It has also been suggested that the SLRs could have been produced locally during the formation (Shu et al. 1997, Lee et al. 1998, Gounelle et al. 2001), however, there are large discrepancies between thus predicted and actually measured abundances. Especially the abundance of ^{60}Fe is problematic as it is only produced in

neutron-rich environments, which can only be achieved during fast/explosive stellar nucleosynthesis (Lee et al. 1998). Thus I will only focus on the SN enrichment scenario occurring close to the forming solar system, to assess its feasibility.

Type II (CC) SNe have been shown to produce virtually all elements in the universe (e.g. Woosley & Weaver 1995, (e.g. Rauscher et al. 2002a), Chieffi & Limongi 2006, Thielemann et al. 1996), thus only one source would be needed for the SLRs. Furthermore, only a core-collapse SN explosion is likely to occur near a forming planetary system. Up to 90% of the stars in the galaxy are born in the vicinity of other stars, but most of those star clusters disperse with timescales of $\sim 10^6$ yrs (Lada et al. 1984). Massive stars (> 15 $M_{\odot}$) end their lives before they disperse from their birthplace, and thus can contaminate a nearby forming Solar System with their SN ejecta (Hester et al. 2004). The life times of low mass star is 2-3 orders of magnitude longer than the lifetime of an open star cluster, and thus has dispersed from the cluster long before it enters its AGB-phase and could contaminate the nascent solar system. This situation is readily observed in HII regions, like the Orion nebula where sun-like stars with protoplanetary disks form in the vicinity of the central massive stars (Hester & Desch 2005).

This scenario has been explored to greater or lesser extent by different groups. The first to consider the injection of SN ejecta were Cameron and Truran (1977), who proposed that a SN shock wave could actually trigger the collapse of a denser chunk of ISM material into a Solar System. It was then further explored by Wasserburg et al. (1998). A different scenario considers the injection of SLRs into an already formed protoplanetary disk, i.e. after the Solar System started forming (e.g. Meyer et al. 2005, Sahijpal & Soni 2006, Loonie et al. 2006, Miki et al. 2007, Harper et al. 1996, Arnett et al.). A more detailed description of the previously published research can be found in Appendix C.

The general approach to this model is to define certain parameters to characterize it. First off, a nearby forming solar system or proto-solar nebula will only intercept a small fraction of the ejecta from a SN. Then a time delay of around one Myr is necessary during which the injected SLRs mix with the solar system before solids form and decay freely. The injected fraction is taken only from a portion of the SN, such that only material outside a certain radius or boundary (often mistakenly called mass cut, based on the 'mass cut' that is used in SN calculations to designate the radius where the explosion is initiated) of the progenitor star is considered. It is assumed that this material can find its way into the forming Solar System somehow, perhaps through Rayleigh-Taylor fingers (e.g. Foster & Boss 1997) or in the form of dust (Ouellette et al. 2007). The material inside of this boundary is assumed to fall back onto the remnant. The injected fraction of the ejecta contains the SLRs in abundances that are determined by the injection fraction, time delay, and progenitor star. Through optimizing these parameters, the abundances of ^{26}Al, ^{36}Cl, ^{60}Fe, ^{41}Ca, and in some cases, ^{108}Pd, and ^{129}I has been shown to be reproducible to within factors of ~ 2.

While this approach so far has given satisfactory results, one major issue is that each of the SLRs in question are produced in different, spatially distinct, burning regions (or zones) in the star (e.g. Woosley & Weaver 1995, Meyer & Clayton 2000, Thielemann et al. 1996 Rauscher et al. 2002a). Therefore, using just one boundary may be an over-simplification of the problem. The goal of this analysis was to show that by relaxing slightly the assumption of uniformly mixed ejecta (by adopting three boundaries) a much better fit to the meteoritic data can be obtained. The innermost part of the star (the Fe-core) forms the proto-neutron star or black hole, thus this material is excluded from the yields in calculated SN ejecta.

This leaves three shells (two boundaries) from which material can be injected into the Solar System.

2.2 The Injection Model

For the injection model I assume an Orion-like setting, i.e. a nascent Solar System in the immediate vicinity of a massive star. This is quite similar to the setting that other groups have (mostly implicitly) assumed. The massive star goes SN before any solids have started condensing in the Solar System, but after the proto-sun and accretion- or protoplanetary disk have already formed. Part of the SN ejecta will be intercepted by the solar system, which has been shown to be able to survive such a blast wave (Ouellette et al. 2007). With the assumption of an already formed proto-planetary disk I implicitly also assume that the disk, will receive the majority of the material from the ejecta, and that the Sun's composition remains essentially unchanged. I take the mass of the proto-planetary disk to be 0.01 $M_{\odot}$ with a composition as given by Lodders (2003).

The standard procedure so far has been to explicitly or implicitly anchor the distance or dilution factor, the time delay, and the boundary each on individual SLRs (usually ^{26}Al and ^{41}Ca) and from there infer the abundances of the other SLRs under consideration. I would like to go a slightly different route, and similarly to Looney et al. (2006) find the best fitting parameter simultaneously. The purpose of that approach is to make our results more robust. The parameters I set out to optimize are as follows.

It is assumed that the abundances of the SLRs can be explained with a certain fraction or dilution factor, f, of the entire ejecta of one core-collapse SN. Whereas most other groups interpret the dilution factor to be due to geometric dilution, this assumption is not made here, and thus no corresponding distances will be given. Observations (e.g Reed et al. 1995, Hughes et al. 2000) of SNe show that

their ejecta is neither uniform nor homogeneous, and details of clumping and structure formation in SN explosions will be explored in chapter 5. The dilution factor was one of the main parameters that varied logarithmically between 5.3×10^{-7} and 8.2×10^{-5}.

Three boundaries will be used to divide up the SN into three main shells. The innermost boundary, s_0, was defined by the beginning of the data of the ejecta yields, which excluded the Fe-core. Thus it was fixed. The location s_1 and s_2 of the other two boundaries were adjustable and were taken as parameters. In addition to the dilution factor, I assume that each of the three shells have their own weighting factor, w_i, that accounts for different portions of each shell being injected. I opted to keep the weighting factor w_2 of the outermost shell fixed to 1.0 (i.e. all of this shell modulo f was injected). My preliminary optimization runs almost exclusively yielded $w_2 \simeq 1$, therefore I deemed it unnecessary to make it adjustable. The other two weighting factors (w_0 and w_1) and two boundaries (s_1 and s_2) are taken as parameters to be optimized simultaneously. Lastly, I assume a time delay, Δt, between the SN explosion and the incorporation of the ejecta (SLRs) into solids. This time delay was also one of the main parameters that was varied between 0.4 Myr and 1.3 Myr.

To summarize, I assumed six variable parameters that characterized our model. These parameters are dilution factor, time delay, location of two boundaries, and two weighting factors. Furthermore, I will consider a range of progenitor stars to the SN, so the mass of the progenitor becomes a seventh variable parameter. These parameters will be optimized to match the constraints on the system, which are the abundances of the eight SLRs. These are listed in table D.1. Appendix B gives a brief description of them and the references for their abundance measurements. The optimization was done with a user-written IDL program. There is one

more constraint than there are parameters, thus the optimization of parameters can give insights into the feasibility of the SN injection model. It might not give a convincingly unique fit, given the uncertainties in SN nucleosynthesis calculations and in the meteoritic data, however it can tell whether SN material is a valid source of the SLRs or not.

2.2.1 Methodology

The optimization program is written in IDL and uses the built in, non-linear optimization routine CONSTRAINED_MIN. It requires a user-supplied function with the parameters to be optimized as variables. CONSTRAINED_MIN uses first partial derivatives of the optimizing functions and is based on a implenentation of the GRG algorithm from Winward Technologies. I minimized the reduced–χ^2 function

$$\chi^2 = \frac{1}{N-m} \sum_i \sum_j \left(\frac{\log_{10}(w_j \cdot A_i) - \log_{10}(A_{i,obs})}{\sigma_i} \right)^2 . \qquad (2.2)$$

N is the number of varied parameters, m is the number of constraints, A_i is the calculated abundance of isotope i, w_j is the weighting factor for shell j, $A_{i,obs}$ is the observed abundance of isotope i (see table D.1), and σ_i is the assumed uncertainty in the measurement of the abundance of isotope i. The logarithmic uncertainty for ^{26}Al was assumed to be 0.1, that for ^{36}Cl was assumed to be 1.0, and everything else was assumed to be 0.3. I chose those errors so that in the optimization routine ^{26}Al, which is known with the highest certainty, will be the main driver of the optimization. Note that the total number of constraints is 8 (the measured abundances of the 8 SLRs) and the total number of varied parameters is 7. This means that the system is slightly over-constrained and therefore the solutions that I get should be non-trivial solutions.

Constrained-min's output consisted of a report file detailing the results and a variable (inform) containing the termination status. The variable contains a number between -3 and 9, this number represents the degree, of sorts, to which the mini-

mization was successful. A value of zero and one means that a minimum point has almost certainly been found, and increasing larger values indicate an increasingly smaller likelihood that a minimum point has been found. Essentially values of 2 or larger mean that various conditions have failed before a certain minimum point could be found (see IDL documentation for more details). Negative values indicate that a fatal error of some kind has occurred. Most of the inform values that I got were either a 0, 1, or 7. I rejected all results that did not have an inform value of 0 or 1.

For the composition of the SN ejecta I used the yields calculated by Rauscher et al. (2002a). Rauscher et al. (2002a) computed models, using the KEPLER package, of the chemical evolution of solar metallicity stars of different masses from the beginning of core hydrogen burning to and including the explosion as a type II SN (2002). In their computations they divided each star into 1000 spherical shells, called zones, that were concentric with the center of the star. These zones were adaptively placed and were adjusted in each computational step for nucleosythetic reaction rates and weak interaction rates, and used new opacity tables Rauscher et al. (2002a). Rauscher et al. (2002a) used in their calculations the most up-to-date data and accounted for neutrino losses and mass loss due to stellar wind (Rauscher et al. 2002a). They calculated the abundances of up to 2200 stable and unstable isotopes starting at ^{1}H and accounted for the decay of any isotope through the evolution of the star. The results of the computations were saved to files.

These files for the results of the computations are machine-readable ASCII files that can be found on their website (www.nucleosynthesis.org). Each file consists of a table of the mass fraction of each isotope for each ejected zone. Rauscher et al. (2002a) employ a very concise naming convention to distinguish between the different types of stars. The filenames are in the form of e.g. s25a41d; the 's' means

that the progenitor star started with a solar composition, the first number (in this example '25') designates the mass of the progenitor star in solar masses (in this case it would be a 25 $M_{\odot}$ star), the next three characters (in this example 'a41') designate the set of nuclear reaction rates used to evolve the star to the point of core collapse, and the last character (in this example 'd') designates either the explosion energy or the amount of ^{56}Ni ejected. In most cases, an explosion energy of 1.2×10^{51} ergs or/ and 0.10 solar masses of ^{56}Ni was used (this is designated by the letters 'A', 'c', 'd', 'g', and 'n'). For some of the stars a lot of different rate sets were used; unless otherwise noted I used the stars with the rate set 'a28'. For the 21 $M_{\odot}$, there was only one data file. For further details see Rauscher et al.'s website. There are also two different file extensions for the SN yield files, .expl-comp which contains the mass fractions of each calculated isotope, and .expl-yield which contains the mass fraction of each calculated isotope plus the contributions of all its radioactive progenitor isotopes. For our calculations I used the .expl-yield files.

Initially I attempted to combine the zones into burning layers using the method that Meyer et al. employed in their paper (1995). Meyer et al. graphed the ^{16}O and ^{28}Si mass fraction vs. interior mass as an indicator for density gradients. A change in composition is accompanied by a large density gradient, and signifies a change in the burning process. They thus distinguished between 8 major burning zones. Each layer was named by the two or three most abundant elements (Meyer et al. 1995). For some of the progenitor stars considered by Rauscher et al. (2002a) this turned out to be non-trivial, as some burning zones might mix or merge with neighboring zones at the end of the stars life (Rauscher et al. 2002a). During the process of optimization, these eight shells where then attempted to be merged into only 3-5 shells. The boundaries between shells were adjusted to find the boundaries that yielded the lowest χ^2 value.

However, as it turned out, the boundaries that would produce the best fit did not always coincide exactly with the actual boundary between two burning zones. It seems that a mix of adjacent burning zones, where perhaps the exact location of the boundaries, in a sense, indicate the degree of mixing, or a mixing fraction is preferred. So instead of constraining the boundaries to burning zones, a different approach was used.

The best matching boundaries were found iteratively during the optimization process. The program was given two boundaries to start, both at the beginning of the data, 0.2 $M_\odot$ apart. The weighting factors were optimized by finding the lowest χ^2 and the boundaries separately incremented by 0.2 $M_\odot$ to find all possible combinations of boundaries for a given dilution factor and time delay. After the best fitting boundaries were found the dilution factor and decaytime were incremented. I thus generated a grid of χ^2 values for time delays between 0.4-1.3 Myr and dilution factors between $5 \times 10^{-7} - 1 \times 10^{-4}$ for each progenitor. These were graphed as contours as a function of delay time and distance, one for each progenitor star (see fig. D.1).

2.3 Results

2.3.1 With ^{26}Al

Figure D.1 shows the results for each progenitor of the optimization routine as contour plots. Shown are the contours of χ^2 as a function of time delay and dilution factor. Nearly all considered progenitors achieved a minimum in χ^2 within the assumed ranges of time and dilution factor. Thus, SNe can be concluded to provide a valid source for the SLRs in the Solar System, at least within the assumptions made here. As other authors have shown before (see Appendix C), it is entirely possible that the SLRs in the Solar System have a SN origin. However, it is probably more difficult to derive a unique solution from the achieved best fits, since all of the

progenitors provide acceptable solutions. Table D.2 lists the optimized parameters for each progenitor with the corresponding χ^2 value. The 21 $M_\odot$ progenitor is the only case that shows a contour at $\chi^2 = 0.5$, and is also the case for which the lowest overall χ^2 value was reached. Table D.3 shows that the abundances of all SLRs are reproduced to within $10-15\%$). The worst case is the 30 $M_\odot$ progenitor; the first prominent contour occurs for $\chi^2 = 3.0$.

The 20 $M_\odot$ seems to be a special case. It shows notably different contours than all the other progenitors, and was probably not optimized within the given range of time delays and dilution factors. While this issue was not further investigated, it was noted that Rauscher et al. (2002a) describe a transition of burning processes between their $19-21$ $M_\odot$ models. They mention that in this mass range the C-burning process transitions from convective to radiative burning. This affects the structure and nuclear fusion rates which would affect the specific amount of each isotope produced (and destroyed) in the star.

The optimized time delay and dilution factor for each progenitor are also summarized in figure D.3. The 'error-bars' indicate the extend of the contour that is twice the smallest χ^2 value achieved for each progenitor. This contour is drawn as a dashed line for each progenitor in figure D.1. The overall optimized time delay seems to be ~ 1 Myr, and is quite consistent between all the progenitors. The overall optimized dilution factor is slightly less straight forward. There is a notable dependence on progenitor mass, which is expected. The mass of the ejecta is in general proportional to the progenitor mass in this mass range. Therefore, a larger progenitor will eject more mass, and thus require a smaller dilution factor. Overall, the optimized dilution factor seems to be between $\sim (7-10) \times 10^{-6}$.

Table D.2 also shows common trends in the other parameters. The innermost boundary, s_0, is determined by the start of the data files. The next boundary,

s_1, often sits just a little further out. It seems to be somewhat correlated with the Si abundance, and is close to or just outside the peak Si abundance. Si is produced by the fusion of two ^{16}O atoms (and emission of an alpha particle), so the extend of O-burning seems to influence the location of s_1. This boundary is also always outside of the peak in ^{53}Mn abundance and in five out of the eight progenitor models inside the inner peak in ^{60}Fe abundance. In the other three cases it coincides with the center of the (inner) ^{60}Fe abundance peak.

The outer boundary, s_2, often coincides (or almost coincides) with the boundary between the O/C and the He/C shells. The zones inside of this boundary look like they could be the site of hydrostatic and/or explosive C and Ne burning. C/Ne burning produces lots of free neutrons and protons, which are necessary to produce all of the SLRs. Notable in this region is the relatively high abundance (as compared to the rest of the ejecta) of r-process SLRs (^{107}Pd, ^{129}I, and ^{182}Hf). This boundary also lies just outside (or sometimes at) the outer peak of the ^{60}Fe abundance (which coincides with the peak in ^{182}Hf abundance). This suggests that at that mass coordinate most of the free protons and neutrons are absorbed, and do not produce many more SLRs (and other isotopes). Thus the extend of the C and Ne burning zones could influence the location of s_2.

The weighting factors also show common trends. The weighting factor w_0 (for the shell between s_0 and s_1) is generally between $0.1 - 0.5\%$. I suspect that the main reason for that is ^{53}Mn, which becomes quite abundant in this shell. In all progenitors, the abundance of ^{53}Mn peaks at $\sim 5 \times 10^{-3}$. Injecting more than just a small amount would add too much of that isotope to the Early Solar System inventory. Since the produced abundance of ^{53}Mn is fairly independent of progenitor mass, it makes sense that the optimized w_0 converged to about the same value for each progenitor. The weighting factor w_1 (for the shell between s_1 and s_2 is gener-

ally much less than one, but varies over more than an order of magnitude ($1-60\%$). No clear pattern in the variations is evident yet.

2.3.2 With ^{135}Cs

Due to recent suggestions that the origin of ^{26}Al is possibly decoupled from source of the other SLRs (Bizzarro et al. 2007), I also performed the optimization procedure with ^{26}Al replaced by ^{135}Cs. All other parameters were left the same. The results are shown in figure D.2 as contour plots. These figures show roughly the same general behavior as in the standard cases. For the interpretation of the contours it is important to note that the assumed error for ^{135}Cs was larger than that for ^{26}Al (0.5 as opposed to 0.1). A quick look at the reduced χ^2 equation (eq. 2.2) will show that, even for the same goodness of fit, the runs with ^{135}Cs will yield a smaller χ^2 value. Consequently, since the χ^2 values for both sets of runs are approximately the same, the set of ^{135}Cs -runs are interpreted to provide slightly worse matches than the ^{26}Al -runs. The conclusion that I draw from this is that it is possible, but I deem it less likely that ^{26}Al is decoupled from the rest of the SLRs. Again, the feasibility of the SN injection scenario is not voided, but a unique fit can not be derived from this set either.

2.4 Discussion

Several assumptions were made without much justification, that may or may not over–simplify the problem. One assumption that was made implicitly was that SN ejecta is mixed to some degree. We assumed three shells, each with a different weighting factor, thereby assuming that different amounts of material from different parts of the SN become incorporated. If SN ejecta expands uniformly, retaining its onion-skin layering, the weighting factors would be expected to be similar in value for the different shells. Consequently, if the weighting factors differ substantially between shells, the most straight forward interpretation is that the ejecta was mixed,

and a chunk of SN material of the relative composition indicated by the weighting factors and shell boundaries hit the solar system. This interpretation is motivated both by the structure of SNR observations, and the likelihood that only dust grains can be injected into a proto–planetary disk.

Although all preliminary optimization runs were supportive of the decision to fix w_2 to a value of 1.0, this could nevertheless have influenced the pattern of values for the other two weighting factors. This automatically enforces 100% injection of the SLRs in the H-envelope and parts of the He-rich shell. The main SLR that is produced in this region of the star is ^{26}Al during its hydrostatic lifetime. If the envelope was ejected by the star before the SN explosion (as is the case in Wolf-Rayet stars), this material (specifically the SLRs contained in it) would be lost from the SN injection scenario. Furthermore, dust condensation in metal-poor environments like an H-envelope is difficult. Therefore, the $w_0 = 1.0$ condition may not be valid for all scenarios.

While it might be a stretch to consider the weighting factors proof that and how the SN material was mixed, it is at least noteworthy that the values of the weighting factors are quite in line with the expected mixing in SN ejecta. As different numerical modeling of 1987A-like progenitors have shown, and as I will discuss in more detail in chapter 5, often only little of the metals (i.e. $\bar{A} >^{16}$ O) is entrained in the unstable flow that clumps the material (i.e. interpreted to resemble the $w_0 \sim 0.1\%$ injection of the zones rich in Si+Fe group elements), the dominant elements are those of the hydrostatic O/C and He zones (i.e. resembling the $w_1 \sim 10\%$ injection). It promotes, rather than contradicts, the idea that a clump of SN material is responsible for the SLRs, and not a uniform influx of SN gas.

A crucial assumption that was made was that the SLRs that are produced in the SN can somehow find their way into the nascent solar system, but the full

picture of the delivery has yet to be worked out in detail (although the theoretical framework exists). In a recent set of papers, Ouellette et al. have determined that dust particles of 0.1μm or larger size are necessary (2010; 2007). Assuming that the stellar material blown off in a SN explosion expands uniformly (i.e. in a homologous shell, so that its density is given by $M_{ejected}/(4/3\pi[r^3_{outer} - r^3_{inner}])$), they found, in 2D hydrodynamic calculations, that its density is much too tenuous to become mixed into a protoplanetary disk. Instead, a bow shock develops and diverts the flow of gas around the proto–planetary disk. Ouellette et al. also included test particles representing dust grains in their calculations of different size, and found that particles larger than 0.1μm have enough momentum to decouple from the gas flow, and subsequently propagate into the proto–planetary disk, where they evaporate (thus are stopped). In the context of the SN enrichment scenario, this evaporation does not matter (or perhaps is even beneficial), as the SLRs are only required to have been in the Solar System, distributed approximately uniformly, by the time that the first solids started condensing. It is not necessary for the SN dust grains to remain intact, as they would re-condense when solids start forming in the proto–planetary disk.

In this sense, the differing weighting factors can be interpreted as chemical fractionation that occurred during the condensation process. In other words, only a small amount of Fe-group metals, and only part of the O-rich material, condensed into dust, while the remaining (majority?) of SN material remained in the gas phase. Whether this is rooted in the physical processes resulting in dust condensation is beyond the scope of this thesis. However, it should be remarked that even in this context, the best-fitting weighting factors do not contradict mixing in SN ejecta, since the most straight-forward explanation would still be that dust condensed from a chunk of those relative amounts.

Recent developments in the cosmo-chemistry community have cast doubts on the one-time presence of some SLRs, in a sense undermining some of the arguments for a SN injection scenario. Essentially, due to low-number statistics and incorrectly applied data analysis techniques, the abundance of ^{60}Fe in primitive meteorites is roughly an order of magnitude lower than previously reported in the literature; in some cases this turns results into null-results (Telus et al. 2011; Ogliore et al. 2011). There are still positive detections of this isotope in meteorites, but at a lower level than previously thought. ^{41}Ca may suffer, to a slightly lesser degree, from the same problems. This does not automatically void the SN enrichment hypothesis, but at the very least makes it more problematic. Furthermore, recent measurements of ^{36}Cl have determined its abundance at much higher levels also than previously reported, and have almost unambiguously shown it to be of late-stage, local irradiation processes in the solar nebula (Jacobsen et al. 2011). SN production of this isotope was at least an order of magnitude lower than the (old) meteoritic abundance, so it would not contradict with the irradiation origin. But it now poses a different constraint on the SN enrichment scenario.

The fact that injection into the protoplanetary disk of the forming solar system is likely mediated by dust grains only places some constraints on the SN ejecta by making the implicit assumption that dust forms in SN ejecta. The topic of dust formation in SN ejecta is very hotly debated, and I only want to make a few general remarks here as they pertain to this topic. SN material is very hot and and ionized immediately upon ejection from the explosion and expands rapidly; dust, in contrast, condenses from gas that is cool ($<\sim$ 2000K) and dense. SN ejecta initially cools only via adiabatic expansion, as the gas is still ionized, and opaque to radiation. Electronic transitions, which are efficient ways for hot, optically thin gases to cool, do not occur until electrons have started recombining with the bare

nuclei in the SN gas (a process that in and of itself will also cool the gas and decreases its opacity) and the gas has become optically thin enough for some radiation to start escaping. Thus, initially the SN gas is too hot to condense dust, but once it is cool enough its density is possibly too low, so that there seems to be just a narrow transition region where conditions are just right for dust formation. Most direct measurements of the amount of dust in SNe indicate that only on the order of $10^{-3} - 10^{-5}$ $M_{\odot}$ of dust forms, while the presence of dust in the early universe seems to require SNe to be much more efficient at producing dust. There are some unknowns that go into determining the amount of dust from observation that are typically taken as parameters to be fitted within a limited parameter space. The temperature of the dust, for example, determines at what wavelengths it can be detected, thus the choice of telescope plays a role. Different species of dust grains have different characteristic emission lines, thus the composition of the dust determines its emission profile. For example, very recent observations of SN1987A with Herschel, which found 0.4-0.7 $M_{\odot}$ of dust, suggest that some components of the condensed dust may have been missed in previous observations (Matsuura et al. 2011). Dust condensation calculations in SN ejecta– like gas also show that dust does condense, though in wildly varying amounts depending on the composition of dust that is assumed to condense. Again, there are some unknowns that are assumed as parameters, for example chemical composition of the regions undergoing condensation, the temperature and density history, and the detailed conditions are likely not equilibrium conditions as is often assumed.

One uncertainty having a great influence on answering this question is the structure of the gas expelled in the SN explosion. The relative abundances of the chemical elements in localized regions determine the type and amount of dust that can condense there. Turbulence can influence the existence and size of overdense

clumps and thus affect injection of SN material into proto–planetary disks. As already outlined in the introduction, there is copious evidence, both theoretical and observational, that SNe explode turbulently, i.e. some degree of clumping is already present by the time of shock breakout. Turbulence implies mixing of material, but then the question is how much (and the answer to this will surely depend, possibly to a substantial degree, on the type of the SN progenitor). SN 1987A seems to require some overturn of material (i.e. Fe- rich ejecta mixed out into the H-envelope), and Cas A also shows evidence for incomplete overturn (viz. Fe-rich ejecta that seems to have moved past the Si-rich ejecta), however, the particular location of the reverse shock combined with just the onset of overturn (the ”pistons” in DeLaney et al. 2010) seem enough to explain observations. From these two SNe (and others as well), it seems that SN explosions do not result in a uniformly mixed gas, nor do they fully retain the nicely layered ”onion-skin” structure from their MS lifetimes. Rather, the answer is some complicated ”in-between”.

Chapter 3

FINDING TRACERS FOR SUPERNOVA PRODUCED ^{26}Al

3.1 Introduction

While the subject of the origin of SLRs in the solar system in particular is still contentious, supernovae must be a significant contributor to the population of ^{26}Al enriched systems in the Galaxy. Knowing the abundances of SLRs in extrasolar stellar systems could, in principle, tell us much about the nature of their planetary systems and help target the search for habitable planets. Of course, the very nature of SLRs means that they are long gone from virtually all observable stellar systems, and even if present their trace abundances would be difficult to measure and to distinguish from stable isotopes of the same element. It is desirable to identify easily observable species that are uniquely co-produced with SLRs.

In this chapter I will concentrate on proxies for supernova-produced ^{26}Al . This isotope is created by three processes: proton capture on ^{25}Mg during H burning in very massive stars and ^{25}Mg (p,γ)^{26}Al and ^{23}Na (α,n)^{26}Al during carbon and neon burning. During the C and Ne burning stages the dominant reaction is determined by the ratio of ^{23}Na /^{25}Mg . The proton capture has a higher rate by a factor of approximately one hundred, but must contend with a free proton number much less than that of free α particles (rates from Cyburt et al. 2010). These processes produce a large ^{26}Al /^{27}Al ratio. The production from H burning is likely to be lost in winds by the most massive stars. For SNe with WC and WO progenitors all ^{26}Al will be removed before the supernova. As is shown, ^{26}Al enrichment from H burning in stars does not come with production of any high abundance species that can be used as tracers. The more promising pathways for proxy studies would appear to be carbon and neon burning. In Sec 3.2 I will discuss the calculations used in the study, including progenitors, supernova explosion calculations, and nu-

cleosynthesis post-processing. In Sec 3.3 I will discuss whether it is appropriate to use the cospatial abundances or full-star averages as diagnostics. In Sec 3.4 I will discuss which observable species are produced cospatially with ^{26}Al . Some of these species are produced in a broader region than ^{26}Al , so I will examine multiple species which can be used to resolve degeneracies. Possibilities for detection are summarized in Sec 3.5.

3.2 Calculations

These calculations explore four different progenitor models each for a range of explosion scenarios. We use a large set of thermally driven 1D explosions with varying delays for a star of initial mass 23 $M_\odot$ and a more restricted range of explosions for a 16 $M_\odot$ and 23 $M_\odot$ with the hydrogen envelope stripped in a case B binary scenario and a 40 $M_\odot$ that ends its life as a type WC/O after extensive mass loss. We also examine a 3D explosion of the 23 $M_\odot$ binary progenitor. This set of models is certainly not a complete representation of the diversity of supernovae. However, it provides a cross section of very different progenitors and explosions. Any trends that are identifiable in this entire ensemble of models can be considered robust across the majority of supernovae.

3.2.1 Progenitors

Four progenitor models were produced as initial conditions for 3D explosion calculations: two single stars, 40 $M_\odot$ and 23 $M_\odot$, and two stars where the hydrogen envelope was removed during a red giant phase to mimic a common envelop evolution, 23 $M_\odot$ and 16 $M_\odot$. All use solar composition.

The models were produced with the TYCHO stellar evolution code (Young and Arnett 2005). The model is non-rotating and includes hydrodynamic mixing processes (Young and Arnett 2005; Young et al. 2005). The inclusion of these processes, which approximate the integrated effect of dynamic stability criteria for

convection, entrainment at convective boundaries, and wave-driven mixing, results in significantly larger extents of regions processed by nuclear burning stages. Mass loss uses the prescriptions of Kudritzki et al. (1989) for OB mass loss and Bloecker (1995) for red supergiant mass loss, and Lamers and Nugis (2002) for WR phases. The physics involved are explored in Young and Arnett (2005); Young et al. (2005); Meakin and Arnett (2007b); Arnett et al. (2009)). A 177 element network terminating at ^{74}Ge is used throughout the evolution. The network uses the NON-SMOKER rates from Rauscher and Thielemann (2001), weak rates from Langanke and Martínez-Pinedo (2000), and screening from Graboske et al. (1973). Neutrino cooling from plasma processes and the Urca process is included.

All four models were produced with the TYCHO stellar evolution code (Young and Arnett 2005). In the absence of information on the composition of Cas A's progenitor, the Grevesse and Sauval (1998) solar abundances were used to ease later comparison with earlier calculations. The models do not include rotation and include hydrodynamic mixing processes (Young and Arnett 2005; Young et al. 2005). Rotation is a smaller effect than the hydrodynamic mixing in terms of core sizes, and therefore masses of material at various stages of nuclear processing, at core collapse (Young et al. 2005; Meakin and Arnett 2007b, a; Arnett et al. 2009). The magnitude of the effect of rotation becomes comparable to that of wave driven mixing only for massive stars rotating near breakup. The possibility remains that there is a strong interaction between rotation and internal waves, but the theoretical framework to evaluate this does not yet exist. In terms of internal structure, rotation was considered to be a perturbation on the existing hydrodynamic mixing smaller than the other uncertainties in the study. The main area in which rotation may have an important effect on this study is in enhancing the mass loss. Since mass loss is uncertain to begin with, below the possible impact of increased mass

loss on our results is discussed. Angular momentum is also important to some supernova mechanisms, such as the jet driven model, but such a mechanism was not used here. Explosion asymmetries which may be induced by rotation are examined in a parametrized way. Mass loss uses the prescriptions of Kudritzki et al. (1989) for OB mass loss, Bloecker (1995) for red giant/supergiant mass loss

The 40 $M_\odot$ star develops an instability during the late main sequence which should lead to a Luminous Blue Variable (LBV) phase, so we remove 1 $M_\odot$ from the envelope as a conservative estimate for the mass lost in eruptions. This model develops a core of He plus triple α products with a maximum extent of 19 $M_\odot$ and a very thin (< 0.1 $M_\odot$ envelope of CNO burning products. Since N is rapidly destroyed at triple α temperatures, the N rich material disappears quickly as the thin CNO layer is removed by mass loss. The core is subsequently eroded by mass loss as a WC and then WO star. The final mass at collapse is 7.8 $M_\odot$.

The single 23 $M_\odot$ star evolves normally as a red supergiant. The final mass is 14.4 $M_\odot$, with a 5 $M_\odot$ H-rich envelope. The main uncertainty in this progenitor is the extent of red supergiant mass loss. Mass loss predictions for cool stars are based on empirical relations, not physical theories. Our rates are similar to those observed, but a factor of two change could be admissible. This star has a core of material with $\bar{A} \geq 16$ of $\sim$6.5 $M_\odot$, with an additional 3 $M_\odot$ of material partially processed by triple α burning. The internal structure differs substantially from the 23 $M_\odot$ progenitor with a "binary event".

The 23 $M_\odot$ star with artificial binary evolution has its hydrogen envelope removed when the star is at the base of the first ascent red giant branch. At this point the radius exceeds 200 $R_\odot$, which is larger than the separation of many massive star binaries. The convective envelope has not reached the hydrogen burning shell, so the He core size and abundance profile of CNO products within the core are

not modified. It was not attempted to change the structure of the star aside from removing the envelope. Mass loss removes any residual H, and the star evolves as a WNL and WN until core collapse. The final mass is 6.4 $M_{\odot}$, with a nitrogen-rich He envelope.

The 16 $M_{\odot}$ binary reaches a final mass of 5 $M_{\odot}$. At collapse there is a residual envelope of $\sim$ 0.01 $M_{\odot}$ with 30% hydrogen. A further 0.5 $M_{\odot}$ of material is completely H depleted but N enriched. A significant fraction of this material does not have CNO equilibrium abundances because of mixing of C/O rich material out from the He shell convective zone.

3.2.2 1D Explosions

To model collapse and explosion, a 1-dimensional Lagrangian code developed by Herant et al. (1994) was used. This code includes 3-flavor neutrino transport using a flux-limited diffusion calculation and a coupled set of equations of state to model the wide range of densities in the collapse phase (see Herant et al. 1994; Fryer et al. 1999, for details). It includes a 14-element nuclear network (Benz et al. 1989) to follow the energy generation. This code was used to follow the collapse of the star through bounce. To get a range of explosion energies, it was opted to remove the neutron star and drive an explosion by injecting energy just above the neutron star surface (in the innermost 15 zones, roughly 0.035 $M_{\odot}$). The duration and magnitude of energy injection of these artificial explosions were altered to produce the different explosion energies. During energy injection, the proto-neutron star is modeled as a hard surface. The neutrino flux from the proto-neutron star was not included, but the energy injected by this neutrino flux is minimal compared to the artificial energy injection. Shortly after the end of the energy injection, the hard neutron star surface was turned into an absorbing boundary layer, mimicking the accretion of infalling matter due to neutrino cooling onto the proto-neutron star.

In this manner, the explosion can be modeled out to late times, even if there is considerable fallback.

The problem of the arbitrary nature of 1D explosions is onerous and far beyond the scope of this paper. Young and Fryer (2007) and Young et al. (2005) discuss the explosion calculations used here in detail, the choice of parameters, and their uncertainties. A comparison of the technique used here, and other techniques used in the literature, with the currently studied explosion mechanisms is discussed in Fryer et al. (2008). For further details, see this paper.

3.2.3 3D Explosions

The 3-dimensional simulations use the output of the 1-dimensional explosion (23 $M_\odot$ star, 23m-run5) when the shock has reached 10^9 cm. The structure of this explosion was then mapped into the 3D Smooth Particle Hydrodynamics code SNSPH (Fryer et al. 2006) by placing shells of particles whose properties are determined by the 1-dimensional structure. The number of particles is determined by the mass and density of that shell (see Hungerford et al. 2005a; Fryer et al. 2006, for details). Mapping of 1-dimensional explosions into multi-dimensional calculations to study mixing has a long history; for example, Fryxell et al. (1991) (see Fryer et al. (2007a) for a review). The initial perturbations caused by a cartesian grid or smooth particle hydrodynamics setup provide seeds for convection that are on par with what is expected from convection prior to stellar collapse (again see Fryer et al. (2007a) for a review). But the mixing is primarily driven by the asymmetric explosion.

Both observational and theoretical evidence indicate that asymmetry is strong and ubiquitous in supernovae (i.e. Fryer et al. 2007b; Fryer and Young 2007; Hungerford et al. 2005a). To simulate an asymmetric explosion, the velocities were modified within each shell based on its angular position. The velocities of particles within 30° of the z-axis were increased by a factor of 6 and the remaining parti-

cles were decreased by a factor of 1.2, roughly conserving the explosion energy. These will be referred to as high velocity structures (HVS). No angular dependence was introduced in the thermal energy. At these early times in the explosion, much of the explosion energy remains in thermal energy, so the total asymmetry in the explosion is not as extreme as the velocity modifications suggest. For a detailed discussion on choosing asymmetry parameters for 3D explosions see Hungerford et al. (2005a, b); Fryer and Warren (2004). Figure D.4 shows the velocities vectors 40s after the launch of the explosion. The large velocity asymmetry results in roughly a factor of two spatial asymmetry between the axes. In this calculation, the explosion was modeled using 1 million smooth particle hydrodynamics particles.

3.2.4 Nucleosynthesis Post-processing

The network in the explosion code terminates at ^{56}Ni and cannot follow neutron excess so to accurately calculate the yields from these models a post-process step was used. Nucleosynthesis post-processing was performed with the Burn code (Young and Fryer 2007), using a 524 element network terminating at ^{99}Tc. The network uses the current REACLIB rates described in Rauscher and Thielemann (2001), weak rates from Langanke and Martínez-Pinedo (2000), and screening from Graboske et al. (1973). Reverse rates are calculated from detailed balance and allow a smooth transition to a nuclear statistical equilibrium (NSE) solver at $T > 10^{10}$K. For this work Burn chooses an appropriate timestep based on the rate of change of abundances and performs a log-linear interpolation in the thermodynamic trajectory of each zone in the explosion calculation. The code also has available modes for analytic adiabatic trajectories, arbitrary density trajectories coupled with the equation of state solver in TYCHO (Young and Arnett 2005), Big Bang conditions, and hydrostatic (stellar) burning. Neutrino cooling from plasma

processes and the Urca process is calculated. The initial abundances are those of the 177 nuclei in the initial stellar model, and the network machinery is identical to that in TYCHO.

3.3 Clump Geometry and Injection

Given that the production of ^{26}Al and its proxies is limited to localized regions of the star/explosion, any potential signal one might look for in a young supernova remnant or an individual protoplanetary disk impacted by supernova ejecta will be wiped out if an average abundance for the whole star is calculated. Fortunately, the average ejecta composition is probably not the appropriate quantity to add to the disk. While the solar system was not considered in particular, it does give some clues as to injection scenarios. It has become clear that injection of the SLRs important to heating (i.e. ^{60}Fe and ^{26}Al) occurred early enough to be incorporated into Ca-Al inclusions (CAIs) that formed $4.567.2 \pm 0.6$ Ma. Within a million years planetesimals began accreting and differentiating, and within a few million years undifferentiated chondrite parent bodies accreted, signaling that the SLRs were by then mostly extinct (Wadhwa et al. 2007). This suggests a brief injection event rather than a slow accumulation.

This brief infusion of material and the nature of supernova ejecta both encourage the decision to consider the injection of material into a disk as an overdense clump of ejecta. In this analysis of potential proxies the case of a dense knot of ejecta encountering a protoplanetary disk was thus considered. Both the likelihood of such a knot encountering a disk and the amount of material that will be incorporated was important to consider.

First it was estimated how much material can enter the disk. Ouellette et al. (2007) consider the interaction of a uniformly expanding supernova (homogenous material without clumps) with a disk at distances from 0.1 to 0.9 pc. This gives an

average density of material in the ejecta of order 10^2 g cm^{-3}. They find that the reverse shock caused by the initial ejecta/disk interaction develops into a bow shock that deflects most of the supernova material around the disk, with only of order of order of a percent of material penetrating the shock and reaching the disk (also Hester et al. 2004). This provides a lower limit to the amount of material entering a disk. An ejecta knot with the typical characteristics of those in the Cassiopeia A SNR would have a mostly or completely unmixed composition, and could deliver pure ^{26}Al -rich material to a disk. Dense optical and infrared knots have densities at least three orders of magnitude greater. Such a knot may have a large enough momentum to overcome the bow shock ram pressure without being deflected beyond the disk. The knot may be shredded in the shock, but the material could still pass through the low velocity post-shock region to be incorporated into the disk. A dense knot is also the most likely part of the ejecta to undergo dust condensation. Ouellette et al. (2010) explore dust injection into a disk and find that for particle with a diameter $> 0.01\mu$ m the injection efficiencies approach 100%. An unmixed knot provides the best opportunity of injecting material into the disk and the best-case scenario for detecting ^{26}Al proxies. One can thus expect from a minimum of 1% and likely more to 100% of the material in a knot to penetrate the disk. The hydrodynamics of an interaction between a knot and the disk bow shock are beyond the scope of this paper, so the likelihood of encountering one or more such knots and the bulk compositional effects were considered here.

The range of conditions in knots of course varies. X-ray emitting structures have fairly low densities and large sizes (10-100 cm^3, 1000AU (Gerardy and Fesen 2001; Hwang and Laming 2003; Patnaude and Fesen 2007)) while optical knots with rapid cooling are dense and compact ($10^3 - 10^5$ cm^3 and 100 AU with substructure down to the resolution limit of current observations). The masses of

observable knots appear to cluster around 10^{-5} $M_\odot$. One can reasonably expect up to $M_\odot$ of ejecta from a supernova. The metal-rich material will be a smaller mass but can still represent six to eight $M_\odot$ of C/O and heavier material in a maximal solar-metallicity case. We will use 10 $M_\odot$ of metal-rich ejecta as a conservative estimate. If all of this material goes into knots, one can expect of order 10^6 knots of a size 1000AU or smaller, thus with a maximum cross section of $\sim 10^{33}$ cm^2 for a spherical blob. The surface area of a sphere 0.3 pc in radius, a reasonable distance for a hypothetical pre-solar supernova is $\sim 10^{37}$ cm^2. A planetary disk with a radius of 100 AU will have a covering factor on this sphere of 10^{-6}. This disk is thus likely to encounter the mass equivalent of one ejecta knot from the explosion. If most of the mass of the ejecta is in high-density knots this represents a contribution from ~ 100 such structures. These are not much above the ambient density, so it is likely that they will be shunted aside by the bow shock. If all of the ejecta exists in dense clumps the disk is likely to encounter one or fewer from a single supernova. In any case, even for the generous assumptions used here, a planetary disk is likely to encounter only a small number of knots that contribute significantly to its mass. The estimates henceforth present the optimum scenario for detection, where the proto-planetary disk encounters a single ejecta knot from an ^{26}Al -rich region. The numbers in the following sections for amounts of proxies present in a disk assume that 100% of the knot material is incorporated into the disk. This is of course an upper limit. This limit can be approached if the aerogel scenario of Ouellette et al. (2010) is correct. There is sufficient oxygen present to bind all of the ^{26}Al into corundum or silicate dust. The injection efficiency will decrease if 1) dust particles are small, 2) dust formation is inefficient, and 3) high density gas still cannot penetrate a bow shock.

3.4 Results

3.4.1 Cospatial production of ^{26}Al and Elements in 1D explosions

The co-production of ^{26}Al was examined with elements that are, in principle, easily observable in stars and/or the ISM. A substantial amount of ^{26}Al can be made in the high temperature H-burning shell of a massive star. This is the least relevant production region for our purposes (proxies for supernova production) since most stars that produce large amounts of the isotope also lose their H envelope to winds before they explode. Winds from WR stars could contribute to enrichment of stellar systems, and the 20-25 $M_{\odot}$ range has the potential to produce ^{26}Al in high concentrations that remains until the explosion, but unfortunately this does not lend itself to proxy studies. No high abundance elements save helium are produced in significant amounts in this region. For heavier elements CNO rearrangement by CNO cycle burning occurs, but not uniquely to the ^{26}Al rich region. Isotopic information could be diagnostic, but is difficult to come by, so we will concentrate of ^{26}Al produced by high temperature processes. Though this H-burning material may be the largest contributor to the Galactic 1.8 MeV background, it is probably less represented in direct injection of ejecta into disks because the cooling of the ejecta is less efficient than in metal-rich material (see Section 3.3).

^{26}Al is quickly destroyed at high (oxygen burning) temperatures and does not survive O shell burning. Thus for proxies one was practically limited to abundances and abundance ratios of elements with Z=6-16. The abundant elements in this range are the α elements plus Na. The peak ^{26}Al abundances coincide with temperatures slightly above 2×10^9 and 1.5×10^9 K. The higher temperature is close to the onset of explosive C and Ne burning. The latter does not correspond to a major explosive burning stage. This material has undergone C burning in the progenitor star at temperature around 8×10^8K. The production of ^{26}Al in the hy-

drostatic phase is only moderate, but the abundance rises significantly when heated to $\sim 1.5 \times 10^9$K by the shock. This heating creates a significant free particle abundance, enhancing production of species by p, n, and α captures. This region was referred to as "sub-explosive C burning" for brevity.

First let one consider Na and Mg, which one might expect to be produced co-spatially with elemental Al. These species are produced primarily through α captures (and subsequent decays) during C and Ne burning. Figure **??** shows the Na abundance in the ejecta for each progenitor as a function of mass coordinate. The explosion shown is that with the smallest compact remnant. The peak temperatures reached by a given mass coordinate do vary with explosion energy. The primary effect of this is to move the mass coordinate of the peak slightly outward, but the coproduction is not changed. The primary effect of the change in explosion energy is that lower energy explosions have large amounts of material fall back onto the compact remnant. This material does not escape into the ISM, so the explosion was examined with the smallest compact remnant to evaluate the largest range of conditions possible in the ejecta. (Note that there is no mixing possible in these 1D explosions and no artificial mixing is imposed, so the mass coordinate reflects the original stratification of the star.) Though these species trace fairly well the Al production overall, they are also produced in regions which do not efficiently create the specific isotope we are interested in. For enrichment by a knot of material elevated Mg and Na alone are poor proxies for ^{26}Al , as they can be abundant in material that is poor in the desired isotope.

Mg abundances (Figure D.9) are somewhat elevated in regions where ^{26}Al is produced relative to the average Mg abundance in the total region of the star in which Mg is produced, but Na can be either depressed or elevated. The degree of elevation of Mg can range from less than a factor of two to almost an order of

magnitude. What about Na and Mg abundance ratios? The different production channels (Ne and C burning) can result in similar enhancements of ^{26}Al for regions with O abundances that differ by factors of a few. Due to the highly variable degree of enhancement of NA and Mg, and their production in regions of the star much more extensive than the ^{26}Al region, the Mg/Na and Mg or Na/O ratios are unreliable indicators of the presence of ^{26}Al without knowledge of the characteristics of the source supernova.

The next set of elemental comparisons are to Si, the next higher mass α element (Figure D.11). These abundances turn out to be highly diagnostic because of the production channel. Complete Ne burning raises the Si abundance from $\log(X) \sim -3$ to ~ -1.5, primarily in ^{28}Si . This is the typical abundance in the high ^{26}Al regions. Temperatures are not high enough to produce significant amounts of S, so S/Si drops by a factor of about 10. The typical S/Si ratio in material that has not undergone O burning or later stages is about 0.5. Oxygen burning produces S efficiently at low entropies (^{16}O(^{16}O,γ)^{32}S) and at high T transitioning to QSE, where S is thermodynamically favored over Si. As a result there is only a narrow range of mass in the star where S/Si drops much below 0.5. This coincides with the peak mass fraction of ^{26}Al , though relatively high production of the isotope occurs in a somewhat broader region.

Very high ratios of Si or S to O ($> 10^{-1}$) in the ejecta knots argue strongly against the presence of ^{26}Al because the material has been processed sufficiently to destroy it. Si mass fractions of between 10^{-1} and 10^{-2} are typical of the high T ^{26}Al production. Even more diagnostic is the S/Si ratio (Figure D.12). In every case for both Ne burning and C burning where X(^{26}Al) $> 10^{-5}$, S/Si drops to < 0.05 from a value close to 0.5 in all of the other regions outside the Si shell. Interior to this the S/Si rises rapidly as QSE conditions favor higher S equilibrium

abundances. In the sub-explosive C burning low S/Si reflects processing durning hydrostatic burning with accompanying production of ^{26}Al during the explosion.

One additional correlation exists that is potentially important to astrobiology. P is present in all biological systems on earth. Though it now appears that the elemental rations of C:N:P do vary across different species, P often plays a role as a limiting chemical agent in many systems (Redfield 1958; Elser 2003; Sterner and Elser 2002). The injection of P from supernova ejecta along with ^{26}Al could therefore impact the suitability of a system for life considerably more than similar enhancements of other elements. The abundance of P in the ejecta tracks ^{26}Al well (Figure D.10) for Ne burning. P and ^{26}Al are correlated for sub-explosive C burning as well, but the P enhancement is not as large.

3.4.2 ^{26}Al in a 3D explosion

The 3D case shows two principal concentrations of ^{26}Al production (Figure D.13). The 3D explosion is spherically symmetric with two high velocity structures. These are produced by imposing increased velocity on ejecta as described in § 3.2.3. We will refer to these henceforth as high velocity structures (HVS). The highest concentrations are in a bubble near the terminal end of the HVS. The second region is a smaller bubble in the HVS, in particular a ring where the high velocity material emerges into a lower density region and begins to spread laterally. Henceforth these two regions will be referred to as the bubble and ring, respectively.

A similar pattern of behavior was found in the 3D explosion to the 1D results. In this particular case, little of the material is explosively processed. In the spherically symmetric region of the 3D explosion no material is processed at high enough temperatures to produce ^{26}Al . The HVS have a large region that consists of material that underwent carbon burning in the progenitor star at temperatures of $\sim 8 \times 10^8$K and reached peak shock temperatures of between 1 and 2×10^9K. The

latter is too low for extensive explosive C burning. This is the ^{26}Al bubble. The ring consists of material that undergoes Ne burning in the progenitor ($1 - 1.5 \times 10^9$K) and explosive Ne and/or C burning ($2.2 - 2.8 \times 10^9$K). The Ne burning ring has a steep temperature gradient and is very narrow. As in the 1D explosions, S/Si is very low and P production is high.

Though similar in many respects, the 3D explosion, with its more complicated thermodynamic history, is a reminder that 1D results do not tell the whole story of ^{26}Al production. When starting from an initial composition similar to the bubble (a C and O rich mantle), the yield of ^{26}Al is increased by burning at higher temperatures and higher densities. In a 1D explosion this ^{26}Al is then rapidly destroyed by succeeding reactions as burning continues. However, if density drops more rapidly after the initial shock heating and compression there is a succeeding freezeout phase instead. In this case the high production can be achieved without subsequent destruction. These conditions pertain to the rapidly expanding HVS. This is the reason for the higher ^{26}Al production in the sub-explosive C burning bubble than the explosive ring, the opposite of the pattern found in the 1D results. This freezeout process resulting from the rapid expansion of the HVS produces one additional effect which may be useful in terms of proxies. Large amounts of ^{18}F are produced under the same high T conditions that create ^{26}Al . If this excess flourine is not destroyed by subsequent burning it preferentially decays by $^{18}\mathrm{F}(\gamma, \alpha)^{14}\mathrm{N}$ at temperatures above T$\sim 1 \times 10^9$K. Thus we have a population of mixed knots with high levels of both N and O, Si, and S. These are potentially analogous to the Mixed Emission Knots (MEKs) identified by Fesen (2001) in Cassiopeia A.

In this particular simulation, the overall explosion is not energetic enough to eject a great deal of material that is explosively processed. Most of the spherically symmetric ejecta comes from the C/O rich He-burning ash and the Ne/O-rich C

burning ash. Most of the material that reaches explosive C burning temperatures or higher is contained in the HVS. The HVS are colimated by the density of the stellar material through which they pass, and develop a wide opening angle once they reach low density regions. As a result, there is an exclusion zone around the equator of the explosion that receives little ^{26}Al enrichment.

3.5 Discussion

So far the production of ^{26}Al in supernova explosions has been discussed. The important question to be addressed now is whether one can actually detect the characteristic enhancement or ratios of nucleosynthetic products discussed above that can reliably indicate the presence of ^{26}Al in supernova ejecta or its historic presence in a planetary system. There are three potential avenues for detection: direct detection of the isotope in question, detection of some anomalous abundance or abundance ratio of other species in the photosphere of a star that is characteristic of material enriched in ^{26}Al , or detection of an abundance or abundance ratio in gas phase material from a disk or supernova that is characteristic of ^{26}Al -rich material. Each of these will be in turn.

Direct detection of ^{26}Al is possible through gamma-ray observations of the radioactive decay of the nucleus to ^{26}Mg . The 1.809 MeV decay line has been observed as a galactic background (Diehl et al. 2008). This data confirms that ^{26}Al is present in the galaxy in amounts commensurate with production by massive stars with an additional contribution from AGB stars and novae. Unfortunately, the sensitivity limits and in particular resolution of current MeV instruments do not allow us to associate the emission with particular material on the small scales and low abundances of individual stellar systems or structure in supernova remnants. In addition, if one wish to find stellar systems that were enriched during their formation,

the short half life of ^{26}Al means that will be long decayed in any completely formed system.

The second area of interest is the detection in a planetary system. Since direct detection is not a possibility due to instrumental limitations in protoplanetary disks and the finite lifetime of the isotope in mature stellar systems one must consider potential proxies. This means examining gas-phase abundances in disks or photospheric abundances of the primary star. In both of these cases one is dealing with the abundances of elements, not individual isotopes since isotopic information is not in general available. Detectability in an external planetary system was considered, assuming the injection and complete mixing of a 10^{-5} $M_{\odot}$ knot into a nebula of 0.013 $M_{\odot}$ (equivalent to the minimum mass solar nebula) with a composition from Grevesse et al. (2007). Knots with the same composition as a zone with the highest mass fraction of ^{26}Al was considered. A knot with a mass fraction Si of $10^{-1.5}$ will increase the Si abundance of the nebula by 2.5%. The oxygen fraction will increase by $\sim$ 10-20%. P tends to be produced at a level near $10^{-2.5}$, which will increase P by $\sim$ 30%. In the most N enriched conditions (which do not prevail in all of the ^{26}Al -rich regions) N may also be enriched by a few tens of percent. A few percent is more typical. This is a best-case scenario. A more massive disk will result in more dilution of injected material and smaller changes in the gas-phase abundances. Photospheric abundances are complicated by the evolution of the star itself. Low mass stars will be depleted in the species considered here due to gravitational settling of heavy nuclei. The stellar composition may also not reflect the disk composition if the injection occurs after the assembly of the star is mostly complete. Both of these processes will result in a smaller change in the stellar photospheric composition than that of the bulk disk.

Due to these factors the prospect for identification of ^{26}Al enrichment in solar-type systems through proxies is marginal. A high ratio of O/Si can indicate enrichment by the O-rich mantle of the star, but does not guarantee enrichment in ^{26}Al because its production is restricted to narrow regions of the oxygen rich part of the star. Mg and Na suffer from the same difficulty. The S/Si ratio is the best diagnostic in absolute terms, but the total amount of Si injected is small. Detecting a 2-3% decrease in the S/Si ratio of an extrasolar planetary system or host star requires the assumption that the S/Si ratio of the ISM is extremely uniform over the Galaxy. In fact, this ratio may well vary over the scale of a star cluster. P is closely correlated with the spatial distribution of ^{26}Al . Injection of an ^{26}Al rich region also increases its abundance significantly compared to a solar-like composition. P is sufficiently low in abundance that high signal to noise stellar spectra would be required for detection.

Detection of ^{26}Al -rich material in core-collapse supernova remnants is a much more favorable situation. In this case we are also considering elemental abundances of proxies due to the relatively high sensitivity limits and resolution issues for direct gamma-ray detection of ^{26}Al decay. In this case however, knots of ^{26}Al material are not mixed with a much more massive proto-planetary disk. The characteristically low S/Si ($\sim$ 0.05) is undiluted by mixing with ISM material in young remnants, so one should be able to predict which ejecta knots have high ^{26}Al in well-resolved cases like Cas A. This of course applies to O-rich knots, and material which has undergone O burning also has low S/Si. The primary difficulty in this endeavor is the lack of Si lines in the optical. Current studies of abundance ratios in the X-ray, where S and Si lines coexist, with XMM-Newton (Willingale et al. 2002) do not have the spatial resolution necessary to analyze individual knots. The Chandra Msec observation of Cas A should approach the spatial resolution

necessary when a complete analysis becomes available. It is unclear whether even high-resolution x-ray observations will bring to light such compositional variations. Overdensities of x-ray emitting material are much smaller than the optical knots, so separating out individual regions of differing composition may be an insurmountable problem.

High ionization lines of Si and strong S lines are observable in the near-IR, but the emission modeling necessary to derive abundance ratios from this information has not been carried out. With this additional modeling, however, optical-IR becomes our preferred method of discovery. O-rich knots with high Mg or Na or moderately enhanced Si are good candidates for a combined optical/IR survey. The high Mg and Na indicate processing at a range of temperatures that include the conditions favorable to ^{26}Al production. The S/Si ratio of these knots would then provide a strong test of whether they would contain ^{26}Al at high abundance. The Mixed Emission Knots in Cas A may also be excellent candidates. These knots are unique due to the simultaneous presence of significant emission from N and from O and S. The burning stages in a star that produce O and S destroy N very efficiently. It has therefore been assumed that these knots are most likely material from different locations in the progenitor star that are superimposed on line of sight or somehow mixed during the explosion. As it was seed above, it is possible for the explosive processes that produce ^{26}Al in O-rich regions to produce N enhancements as well. If these clumps are produced by a nucleosynthetic process rather than hydrodynamic mixing of discrete clumps from different locations in the progenitor, they are most likely produced in the same conditions favorable to ^{26}Al production.

Though less directly useful to the star and planet formation and astrobiology communities, characterization of the distribution of ^{26}Al in clumpy, asymmetric

supernova ejecta will give us a much stronger grasp of the physical processes and likelihood of injection of short-lived radioactive material into star-forming disks.

Chapter 4

COLLATERAL EFFECTS ON SOLAR NEBULA OXYGEN ISOTOPES DUE TO INJECTION OF ^{26}AL BY A NEARBY SUPERNOVA

4.1 Introduction

Although only the injection scenario was considered in chapter 2 while the inheritance and irradiation models were presumed as ruled out, the abundances of the SLRs alone have not yet enabled a definite discrimination between these possibilities. But Gounelle and Meibom (2007, hereafter GM07) have proposed that the oxygen isotopic ratios of early solar system materials may be used to rule out certain hypotheses. Specifically, they argue that if ^{26}Al and ^{41}Ca were injected by a nearby supernova into the Sun's protoplanetary disk, sufficient to produce the observed meteoritic ratio $^{26}\mathrm{Al}/^{27}\mathrm{Al} \approx 5 \times 10^{-5}$ (MacPherson et al. 1995), then the oxygen isotopic ratio of the solar nebula would be considerably altered: solar nebula materials formed before the injection would have oxygen isotopic ratios significantly different from later-formed materials. GM07 calculated the shifts in oxygen isotopic ratios accompanying injection of supernova ^{26}Al into the Sun's protoplanetary disk, using the isotopic yields in bulk supernova ejecta calculated by Rauscher et al. (2002b). A robust prediction of the GM07 models is that $^{17}\mathrm{O}/^{16}\mathrm{O}$ of pre-injection materials should be significantly higher, by several percent, than post-injection materials. Examples of pre-injection materials may exist in meteorites, or especially in the solar wind sample returned by the Genesis mission (Burnett et al. 2003). Since preliminary results from Genesis suggest the Sun is not isotopically heavy in oxygen (McKeegan et al. 2009), and because no such ^{17}O–rich (or ^{16}O–poor) components have been discovered in meteorites, GM07 rule out a supernova origin for the ^{26}Al and ^{41}Ca in meteorites.

The purpose of this chapter is to reproduce and refine the method pioneered by GM07, and to test the conclusion that ^{26}Al cannot have a supernova origin. GM07 originally considered only bulk ejecta of spherically symmetric supernova explosions. I begin the analysis with this case, but make necessary refinements to the method, and use current nucleosynthesis models to predict the isotopic yields. I then expand on the analysis of GM07, calculating the isotopic yields by allowing the disk to intercept ejecta from different parts of the supernova explosion rather than a uniformly mixed total yield, and by examining anisotropic explosions. I also simultaneously consider the injection of ^{41}Ca into the disk.

The chapter is organized as follows. In §2, I outline the method used to calculate shifts in oxygen isotopic composition due to supernova injection of ^{26}Al and ^{41}Ca, including updates to the method of GM07. In §3 I describe the results of nucleosynthesis simulations we have carried out, to determine the isotopic yields in supernova ejecta under various explosion scenarios. I determine the inputs needed to compute the shifts in solar nebula oxygen isotopic composition. These shifts in oxygen isotope before and after injection are presented in §4, and in §5 I draw conclusions.

4.2 Method

4.2.1 Calculation of Isotopic Shifts

The method of GM07 is fairly straightforward. They assume that meteoritic components that sample the solar nebula's starting composition, before the acquisition of ^{26}Al, can be identified and measured. Likewise, they assume samples after the acquisition of ^{26}Al can be identified and measured. Any difference in the oxygen isotopic content between samples of those two groups would then constitute a shift in oxygen isotopes brought about by the injection of supernova material. The predicted shift in oxygen isotopes due to injection of supernova material into

the proto-planetary disk can then be compared to the actual difference in oxygen isotopes before and after. In practice, because the vast majority of meteoritic components sample the solar nebula after injection, GM07 assumed a "final" value for the solar nebula oxygen isotopes, and used the isotopic yields in supernova ejecta to predict the initial composition. Testing the supernova injection hypothesis thus amounts to finding meteoritic inclusions with this initial oxygen isotopic composition. Such inclusions should have evidence for no live ^{26}Al at the time of their formation, and should be among the oldest meteoritic inclusions.

The earliest-formed solids in the solar system are widely accepted to be the calcium-rich, aluminum-rich inclusions (CAIs), both because they contain minerals that are the first solids expected to condense in a cooling solar nebula (Grossman 1972), and because their Pb-Pb ages are the oldest measured, at 4568.6 Myr (Bouvier and Wadhwa 2009). It is worth noting that because many of the minerals in CAIs are condensates, their isotopic composition should reflect that of the solar nebula gas. The vast majority of CAIs have inferred initial ratios $^{26}\mathrm{Al}/^{27}\mathrm{Al} \approx 5 \times 10^{-5}$ or appear to have been isotopically reset at a later date (MacPherson et al. 1995). Only in a handful of CAIs known as "FUN" CAIs (fractionation with unknown nuclear effects) has it been possible to set firm upper limits on the initial $^{26}\mathrm{Al}/^{27}\mathrm{Al}$ ratio and show these CAIs did not contain live ^{26}Al when they formed (Fahey et al. 1987; MacPherson et al. 1995). Thus, CAIs overall reflect the composition of the solar nebula at an early time, and FUN CAIs possibly record the oxygen isotopic abundance before the solar nebula acquired ^{26}Al.

To make more precise statements, it is necessary to quantify the oxygen isotopic composition of the nebula and various components. The molar fraction of oxygen in gas and rock can vary, so the relevant quantities are the ratios of the stable oxygen isotopes, $^{17}\mathrm{O}/^{16}\mathrm{O}$ and $^{18}\mathrm{O}/^{16}\mathrm{O}$. In the field of cosmochemistry, these

ratios are commonly expressed as deviations from a standard, in this case Standard Mean Ocean Water (SMOW), which has $^{17}\mathrm{O}/^{16}\mathrm{O} = 3.8288 \times 10^{-4}$ and $^{18}\mathrm{O}/^{16}\mathrm{O} = 2.0052 \times 10^{-3}$ (Oneal 1986). The fractional deviations of the isotopic ratios from these standard values are $\delta^{17}\mathrm{O}$ and $\delta^{18}\mathrm{O}$, and are measured in parts per thousand, or "permil" ($^{0}/_{00}$). [That is, $\delta^{17}\mathrm{O} = 1000 \times \left((^{17}\mathrm{O}/^{16}\mathrm{O})/(^{17}\mathrm{O}/^{16}\mathrm{O})_{\,\mathrm{SMOW}} - 1 \right)$.] It is also standard to report the quantity $\delta^{17}\mathrm{O} \approx \delta^{17}\mathrm{O} - 0.52\,\delta^{18}\mathrm{O}$, because this quantity is conserved during almost all chemical fractionation processes. [More precisely, $\Delta^{17}\mathrm{O} \equiv \ln(1+\delta^{17}\mathrm{O}) - 0.5247 \ln(1+\delta^{18}\mathrm{O})$ (Miller 2002).]

It is clear that the final oxygen isotopic composition of the nebula, (δ^{17}O,δ^{18}O)', will depend on its starting composition $(\delta^{17}\mathrm{O}, \delta^{18}\mathrm{O})_0$, the composition of the supernova material, $(\delta^{17}\mathrm{O}, \delta^{18}\mathrm{O})_{\,\mathrm{SN}}$, and the mass of supernova material injected (relative to the mass of the disk). It is straightforward to show that

$$\delta^{17}\mathrm{O}' - \delta^{17}\mathrm{O}_0 = \frac{x}{1+x} \left(\delta^{17}\mathrm{O}_{\,\mathrm{SN}} - \delta^{17}\mathrm{O}_0 \right), \tag{4.1}$$

where $\delta^{17}\mathrm{O}_{\,\mathrm{SN}}$ is the isotopic ratio of the supernova material injected into the disk, and $x \equiv M(^{16}\mathrm{O})_{\,\mathrm{SN}}/M(^{16}\mathrm{O})_{\,\mathrm{disk}}$ measures the mass of injected oxygen relative to the oxygen present in the disk (with a similar formula applying to $\delta^{18}\mathrm{O}'$). In terms of the masses involved,

$$x = \frac{M(^{16}\mathrm{O})_{\,\mathrm{SN}}}{M(^{26}\mathrm{Al})_{\,\mathrm{SN}}} \times \frac{M(^{26}\mathrm{Al})_{\,\mathrm{SN}}}{M(^{26}\mathrm{Al})_{\,\mathrm{disk}}} \times \frac{M(^{26}\mathrm{Al})_{\,\mathrm{disk}}}{M(^{27}\mathrm{Al}\,)_{\,\mathrm{disk}}} \times \frac{M(^{27}\mathrm{Al}\,)_{\,\mathrm{disk}}}{M(^{16}\mathrm{O})_{\,\mathrm{disk}}}. \tag{4.2}$$

Most of these terms are defineable. First, $M(^{26}\mathrm{Al})_{\,\mathrm{SN}}/M(^{26}\mathrm{Al})_{\,\mathrm{disk}} \equiv \exp(+\Delta t/\tau)$, where Δt is the time delay between supernova injection and isotopic closure of the meteoritic materials, and $\tau = 1.03$ Myr is the mean lifetime of ^{26}Al. By definition, $M(^{26}\mathrm{Al})_{\,\mathrm{disk}}/M(^{27}\mathrm{Al}\,)_{\,\mathrm{disk}} \equiv (26/27) \times (5 \times 10^{-5})$, because sufficient ^{26}Al must be injected to yield the meteoritic ratio. Finally, the isotopic abundances in the solar nebula are known (the ratio $^{27}\mathrm{Al}\,/^{16}\mathrm{O}$ is taken from Lodders (2003)), so we derive

$$x = \frac{4.846 \times 10^{-7}}{[M(^{26}\mathrm{Al})/M(^{16}\mathrm{O})]_{\mathrm{SN}}} \exp(+\Delta t/\tau). \tag{4.3}$$

Note that x is independent of the mass of the disk, but it increases with Δt, since larger values of Δt imply that more supernova material had to be injected to yield the same $^{26}\mathrm{Al}/^{27}\mathrm{Al}$ ratio, thereby implying larger isotopic shifts in oxygen associated with this injection.

Besides the time delay Δt, the major inputs needed to infer $(\delta^{17}\mathrm{O}, \delta^{18}\mathrm{O})_0$ are the isotopic composition $(\delta^{17}\mathrm{O}, \delta^{18}\mathrm{O})_{\mathrm{SN}}$ and ratio of ^{16}Oto ^{26}Al in the supernova ejecta, and the oxygen isotopic composition of the post-injection solar nebula. GM07 used bulk abundances of supernova ejecta calculated by Rauscher et al. (2002b) for the first set of quantities. They also assumed that the oxygen isotopic ratios of the post-injection solar nebula matched the SMOW values of the present-day Earth: $(\delta^{17}\mathrm{O}', \delta^{18}\mathrm{O}') = (0\ {}^{0}/_{00}, 0\ {}^{0}/_{00})$. This assumption is the main reason why they concluded that the pre-injection solar nebula had to be ^{17}O-rich, as it is now demonstrated. Rearranging equation 4.1 yields

$$\delta^{17}\mathrm{O}_0 = \delta^{17}\mathrm{O}' + x\left(\delta^{17}\mathrm{O}' - \delta^{17}\mathrm{O}_{\mathrm{SN}}\right). \tag{4.4}$$

Supernova ejecta tend to be ^{16}O-rich; in the extreme limit, $\delta^{17}\mathrm{O}_{\mathrm{SN}} \approx -1000\ {}^{0}/_{00}$. If $\delta^{17}\mathrm{O}' \approx 0\ {}^{0}/_{00}$ also, then $\delta^{17}\mathrm{O}_0 \approx +(1000x)\ {}^{0}/_{00}$. That is, $\delta^{17}\mathrm{O}_0$ is inferred to have been positive and potentially quite large if $x > 10^{-2}$. The isotopic yields of the supernova ejecta computed by Rauscher et al. (2002b) were consistent with such large values of x and $\delta^{17}\mathrm{O}_{\mathrm{SN}} < 0$, leading GM07 to conclude that generally $\delta^{17}\mathrm{O}_0 > 0\ {}^{0}/_{00}$. Indeed, for progenitor masses 15 - 25 $\mathrm{M}_{\odot}$, GM07 inferred $\delta^{17}\mathrm{O}_0 \approx +35$ to $+220\ {}^{0}/_{00}$. Since there are no early-formed meteoritic components with $\delta^{17}\mathrm{O}$ this high, and because the oxygen isotopic composition of the Sun appears to be consistent with $\delta^{17}\mathrm{O} \approx -60\ {}^{0}/_{00}$ (McKeegan et al. 2009), GM07 ruled out supernova injection of ^{26}Al and ^{41}Ca. This conclusion depends on a few

key assumptions that we update below. I consider the starting composition of the solar nebula, and take into account the non-homogeneity of supernova ejecta.

4.2.2 Solar Nebula Oxygen Isotopic Composition

Oxygen isotopic ratios potentially can test or rule out the supernova injection hypothesis, but several caveats must be applied to the method of GM07. The first and most important correction involves the oxygen isotopic composition of the solar nebula immediately before and after the injection of supernova material. GM07 assumed the post-injection composition was equal to SMOW; however, SMOW is widely understood not to reflect the oxygen isotopic ratios of the solar nebula immediately after injection. On a three-isotope diagram of δ^{17}O versus δ^{18}O, the oxygen isotopes of planetary and meteoritic materials are arrayed along a mixing line called the Carbonaceous Chondrite Anhydrous Mineral (CCAM) line discovered by Clayton et al. (1973). After correcting for isotopic fractionation by thermal and chemical processes, Young and Russell (1998) inferred a mixing line with slope 1.0 in the three-isotope diagram, and so I will refer to this mixing line as the "slope-1" line. Today the oxygen isotopic composition of the Earth (SMOW) is widely recognized to reflect a mixture of an isotopically lighter rocky component (to which CAIs belong), and an isotopically heavy reservoir (e.g. Clayton 2003; Young and Russell 1998). It is very likely that this component is isotopically heavy water, with $\delta^{17}\mathrm{O}, \delta^{18}\mathrm{O} > +30\ {}^{0}/_{00}$ (Clayton and Mayeda 1984; Lyons and Young 2005; Lyons et al. 2009). The existence of isotopically heavy water is supported by the discovery (in the primitive carbonaceous chondrite Acfer 094) of a poorly characterized product of aqueous alteration, with $\delta^{17}\mathrm{O} \approx \delta^{18}\mathrm{O} \approx +180\ {}^{0}/_{00}$ (Sakamoto et al. 2007). Quite possibly this heavy water is the result of a mass-dependent photodissociation of CO in the outer solar nebula by an external ultraviolet source (Lyons and Young 2005; Lyons et al. 2009). The photodissociation can be isotopically se-

lective because the different isotopologues of CO molecules can self-shield; $C^{17}O$ and $C^{18}O$ are optically thin and dissociate more completely, releasing ^{17}O and ^{18}O atoms that react with H_2 to form isotopically heavy water, while the abundant molecule $C^{16}O$ is more optically thick and does not as completely dissociate. The light CO molecule is eventually lost with the nebular gas. Whatever the source of the isotopically heavy component, SMOW only represents a late stage in nebular evolution, and does not represent the state of the nebula immediately after injection of supernova material.

Applying the same reasoning, it is likely that the starting composition of the solar nebula was lower (more ^{16}O-enriched) on the slope-1 line than most CAIs. The majority of CAIs tend to cluster near $(\delta^{17}O, \delta^{18}O) \approx (-41\ ^0/_{00}, -40\ ^0/_{00})$, i.e., $\delta^{17}O \approx -20.2\ ^0/_{00}$ (see Clayton 2003, and references therein); but many of the most primitive and unaltered CAIs cluster near $(\delta^{17}O, ^{18}O) \approx (-50\ ^0/_{00}, -50\ ^0/_{00})$, or $\Delta^{17}O \approx -24\ ^0/_{00}$ (Scott and Krot 2001). Likewise, Makide et al. (2009a) report $\Delta^{17}O = -23.3 \pm 1.9\ ^0/_{00}$ for "mineralogically pristine" CAIs. CAIs also contain grains of hibonite, spinel, and corundum, which are among the first minerals expected to condense from a cooling gas of solar composition (Ebel and Grossman 2000), and which are presumably even more primitive than CAIs themselves. Scott and Krot (2001) report that hibonite grains are also found to cluster near $(\delta^{17}O, \delta^{18}O) \approx (-50\ ^0/_{00}, -50\ ^0/_{00})$, or $\delta^{17}O = -24\ ^0/_{00}$, while Makide et al. (2009b) observed 4 hibonite grains from Allende and Semarkona to have oxygen isotopes in the range $\delta^{17}O = -32$ to $-17\ ^0/_{00}$. They also found that spinel grains from the CV chondrite Allende had $\delta^{17}O = -25 \pm 5\ ^0/_{00}$, and that corundum grains from the CM chondrite Semarkona clustered strongly in the range $\delta^{17}O = -24 \pm 2\ ^0/_{00}$. Krot et al. (2010) likewise report $\delta^{17}O = -24 \pm 2\ ^0/_{00}$ for primitive CAIs and amoeboid olivine aggregates, which are also believed to have con-

densed from solar nebula gas. From these results one infers that $(\delta^{17}O', \delta^{18}O') \approx (-50\ ^0/_{00}, -50\ ^0/_{00})$ in the solar nebula immediately after the injection of supernova material.

Meteoritic and other samples also constrain the initial (pre-injection) oxygen isotopic composition of the solar nebula, and find it to be very similar. As described above, very firm and low upper limits to initial $^{26}Al/^{27}Al$ exist for FUN CAIs that mark them as having formed before the injection of ^{26}Al and ^{41}Ca (Sahijpal and Goswami 1998). Krot et al. (2008) have identified a fractionation line associated with the FUN CAIs with $\delta^{17}O = -24.1\ ^0/_{00}$ that passes through $(\delta^{17}O, \delta^{18}O) \approx (-51\ ^0/_{00}, -52\ ^0/_{00})$. Presumably the original isotopic composition of the nebula matched that of the Sun, which might therefore be measured by Genesis mission (Burnett et al. 2003). Preliminary measurements can be interpreted as clustering on a fractionation line with $\delta^{17}O \approx= -26.5 \pm 5.6\ ^0/_{00}$ (McKeegan et al. 2009), which would intersect the slope-1 line at $(\delta^{17}O, \delta^{18}O) \approx (-56\ ^0/_{00}, -57\ ^0/_{00})$, and other analyses suggest $\delta^{17}O \approx -33 \pm 8\ ^0/_{00}$ [2σ errors] (McKeegan et al. 2010).

From these results it seems likely that the original solar nebula oxygen isotopic composition was near the Genesis preliminary result of $(\delta^{17}O, \delta^{18}O) \approx (-54\ ^0/_{00}, -53\ ^0/_{00})$, or possibly much lower along the slope-1 line. Subsequent reaction of rock with a ^{16}O-depleted reservoir then moved material along the slope-1 line to $(\delta^{17}O, \delta^{18}O) \approx (-41\ ^0/_{00}, -40\ ^0/_{00})$, where most CAIs are found (Clayton 2003, and references therein). FUN CAIs appear to represent an intermediate stage in this process, only partially evolved along the slope-1 line. To fix values, it is simply assumed that the solar system protoplanetary disk isotopic ratios started as $(\delta^{17}O, \delta^{18}O) = (-60\ ^0/_{00}, -60\ ^0/_{00})$.

The above discussion changes the criterion by which one can reject the supernova injection hypothesis. Because GM07 assumed an initial solar nebula com-

position near SMOW, they concluded that pre-injection samples necessarily would have had $\delta^{17}O > 0$, and the lack of such samples in meteorites ruled out the hypothesis. But I assert that the supernova injection hypothesis can be ruled out only if injection of supernova material necessarily shift the oxygen isotopic composition of the solar nebula from a composition near $(\delta^{17}O, \delta^{18}O) \approx (-60\ {}^{0}/_{00}, -60\ {}^{0}/_{00})$ to one far off the slope-1 line, or one on the slope-1 line but with $\delta^{17}O > -50\ {}^{0}/_{00}$. In this way, the GM07 method of using oxygen isotopic constraints might still allow a test of the supernova injection hypothesis.

4.2.3 Magnitude of Isotopic Shift

There are at least three scenarios wherein the shift in oxygen isotopes following injection of supernova material can be consistent with the above constraints. From equation 4.1, it is seen that even if the supernova ejecta and the protoplanetary disk differ in oxygen isotopic composition by hundreds of permil, the shift in oxygen isotopes may be small (< 1 permil) if the injected mass is small, so that $x < 10^{-2}$. More precisely, if ^{26}Al and the other SLRs are injected by a supernova into the solar nebula disk, then the magnitude of the shift in oxygen isotopes will depend on the fraction of ejecta oxygen that accompanies Al. In this first scenario, O and Al may be significantly fractionated during delivery of the ejecta to the solar nebula. For example, Ouellette et al. (2007) find that effectively only material condensed from the supernova ejecta into large ($> 1\,\mu$ m radius) grains can be injected directly into a protoplanetary disk. In the extreme event that the only grains that entered the protoplanetary disk were corundum ($Al_2\ O_3$) grains, the isotopic shifts in oxygen would be negligible ($< 0.001\ {}^{0}/_{00}$). Or, if only 10% of the oxygen in the ejecta condensed into grains, and 90% remained in gas that was excluded from the disk, then the isotopic shifts in oxygen isotope (for a given amount of injected ^{26}Al) would be 10 times smaller than predicted by GM07. It is therefore not possible to determine

the shifts in oxygen isotopes following injection into a disk without quantifying the degree to which O and Al are fractionated between gas and solids. In what follows, the limit of no fractionation assumed, as such a calculation is beyond the scope of the present investigation; but dust condensation in supernova ejecta is considered to be a very important effect, one that potentially could significantly reduce the predicted isotopic shifts.

In the second scenario, the shifts in oxygen isotopes could also remain small if the injected material was simply higher than expected in ^{26}Al (or lower in O), so that again $x < 10^{-2}$. The calculations of GM07 relied on the bulk abundances calculated by Rauscher et al. (2002b). That is, GM07 assumed that the injected material uniformly sampled the entirety of the supernova ejecta. Such a uniform sampling is unlikely, as supernovae often do explode in a clumpy fashion and asymmetrically. It has long been understood that asymmetries or hydrodynamic instabilities may disrupt the stratification of the progenitor star, but they do not result in large scale compositional mixing (e.g. Joggerst et al. 2008; Hungerford et al. 2005b; Fryxell et al. 1991). The X-ray elemental maps of the Cassiopeia A supernova remnant (Hwang et al. 2004) dramatically demonstrate that massive stars are likely to explode as thousands of clumps of material, each sampling different burning zones within the progenitor. Ouellette et al. (2010) have argued that this may be a near-universal feature of core-collapse supernovae; at the very least, observations do not rule out this possibility. So it is more than possible that the solar nebula received materials from only limited regions within the ejecta in which the ^{26}Al/^{16}O ratio could have varied considerably from the average value for the ejecta. The non-uniformity of the ^{26}Al/^{16}O ratio may be magnified if the star explodes asymmetrically, allowing explosive nucleosynthesis to proceed differently even in parcels of gas in the same burning zone.

Finally, in the third scenario by which isotopic shifts may conform to measurements, x need not be small, and the isotopic shifts may approach $10\ ^0/_{00}$ in magnitude, so long as the injection moved the composition up the slope-1 line by $\approx 10\ ^0/_{00}$ (i.e., the change in δ^{17}O equalled the change in δ^{18}O, both being $< 10\ ^0/_{00}$), or down the slope-1 line by a comparable or even larger amount. A shift from an initial composition $(\delta^{17}\mathrm{O}, \delta^{18}\mathrm{O})_0 \approx (-60\ ^0/_{00}, -60\ ^0/_{00})$, consistent with Genesis measurements of the Sun's composition, to $(\delta^{17}\mathrm{O}, \delta^{18}\mathrm{O})' \approx (-50\ ^0/_{00}, -50\ ^0/_{00})$, consistent with primitive meteoritic components, would not conflict with the data. Alternatively, a shift from an initial composition $(\delta^{17}\mathrm{O}, \delta^{18}\mathrm{O})_0 \approx (-60\ ^0/_{00}, -60\ ^0/_{00})$, to $(\delta^{17}\mathrm{O}, \delta^{18}\mathrm{O})' \approx (-70\ ^0/_{00}, -70\ ^0/_{00})$, or even $(\delta^{17}\mathrm{O}, \delta^{18}\mathrm{O})' \approx (-80\ ^0/_{00}, -80\ ^0/_{00})$, followed by mixing with the ^{16}O-poor reservoir that moves solar nebula solids up the slope-1 line, would also conform to the data.

In the next section I compute the isotopic yields in core-collapse supernovae of various progenitor masses, both in spherically symmetric explosions (as considered by Rauscher et al. 2002b) and asymmetric explosions. These calculations allow me to predict the oxygen isotopic composition $(\delta^{17}\mathrm{O}, \delta^{18}\mathrm{O})_{\mathrm{SN}}$ and the ratio x of the supernova material at various locations within the explosion, to assess the range of possible isotopic shifts under the second and third scenarios. A supernova injection scenario would be ruled out, unless either the injection of material results in small overall shifts (i.e. the injected material contains a high ^{26}Al abundance relative to oxygen, or vice versa, a low oxygen abundance relative to Al), or the oxygen isotopes are shifted along the 'slope-1 line', in which case shifts of up to $\sim$10 permil in either direction are allowed.

4.3 Isotope Production within Supernovae

4.3.1 Numerical Methods

The yields of oxygen isotopes, ^{41}Ca, and ^{26}Al were calculated in several core-collapse supernova scenarios, listed in Table D.4. These calculations explore four different progenitor models, with a range of explosion scenarios for each, and are the same as used in chapter 3. A large set of thermally driven 1D explosions was used with varying kinetic energies and delays, for a star of initial mass 23 $M_\odot$ and a more restricted range of explosions for a 16 $M_\odot$, and 23 $M_\odot$, with the hydrogen envelope stripped in a case B binary scenario, and a single 40 $M_\odot$ progenitor that ends its life as a type WC/O after extensive mass loss. I also examine a 3D explosion of the 23 $M_\odot$ binary progenitor. Details of the simulations can be found in Young et al. (2009). The set of progenitor models we selected by no means samples the entire diversity of supernovae, but it represents a variety of cases across a large range of progenitor masses and explosion parameters. It is sufficiently diverse to make generalizations for behaviors that appear across all models.

The initial intent of the 3D simulation was to create a fully 3-dimensional calculation of an explosion with a moderate bipolar asymmetry (Young et al. 2006). The interesting behavior of ^{26}Al in the explosion then prompted us to consider the composition of this material in relation to an isotopic enrichment scenario of the solar system. Both observational and theoretical evidence indicate that asymmetry is strong and ubiquitous in supernovae (e.g. Fryer et al. 2007b; Young and Fryer 2007; Hungerford et al. 2005a; Lopez et al. 2009b). In the situation of supernova injection the asymmetric model's primary utility lies not in modeling a specific event, but rather sampling a wide range of thermodynamic histories for material capable of producing ^{26}Al. Injected material is likely to sample only a small region of the supernova, meaning we can treat each SPH particle as an isolated trajectory

whose further evolution is not dependent upon the progenitor star or or global parameters of the explosion. Any explosion that produces a similar thermodynamic trajectory will end up with similar yields. I can thus probe a large variety of explosion condition not accessible to 1D calculations without a prohibitive investment of computational time. Therefore this asymmetric simulation can be considered sufficiently generic to justify its usage for this investigation.

The asymmetric explosion was created with a geometric aspect ratio and final kinetic energy axis ratio designed to be roughly consistent with the degree of asymmetry implied by supernova polarization measurements. To simulate an asymmetric explosion, the velocities are modified within each shell by increasing those of particles within 30° of the z-axis by a factor of 6; I will refer to these parts of the supernova as high velocity structures (HVSs). The velocities of the remaining particles were decreased by a factor of 1.2, roughly conserving the explosion energy. This results in a 2:1 morphology between the semimajor to semiminor axes ratio by the end of the simulation. No angular dependence in the thermal energy was introduced. At these early times in the explosion, much of the explosion energy remains in thermal energy, so the total asymmetry in the explosion is not as extreme as the velocity modifications suggest. For a detailed discussion on choosing asymmetry parameters for 3D explosions see Hungerford et al. (2003), Hungerford et al. (2005b), Fryer and Warren (2004).

As noted above, although only one 3D model is considered, the results I get from that model are representative of a range of nucleosynthetic conditions that may occur in multiple explosion/progenitor scenarios. Each parcel of gas follows its own density and temperature evolution, which is determined by the local velocity of the parcel of gas. It is the local conditions of the gas that matter; it is unaware of the global evolution. An example of the trajectories from the Ring and Bubble regions

are shown in Figure D.14. The Figure shows the temperature, density, and radiation entropy evolution for representative ^{26}Al-rich particles in the explosion. The lines are labeled with ^{26}Al, ^{18}F, and ^{18}O abundances at the emd of the simulation (before complete radioactive decay of ^{18}F). Three classes of trajectories can be seen: high temperature and high entropy, high temperature and low entropy, and low temperature, high entropy. Predictably, the high temperature, low entropy trajectories tend to have low ^{18}F (and therefore ^{18}O) abundances due to the photodisintegration of ^{18}F into $^{14}\mathrm{N} + \alpha$. High temperature, high entropy trajectories have a higher reverse rate for that reaction, preserving slightly more ^{18}F. The low temperature particles have the highest ^{18}F abundance at the end of burning.

The asymmetric explosion samples trajectories with a large span of velocity evolutions reasonable for plausible asymmetries. As we demonstrate with the 1D models and in Young et al. (2009), the sites of production for ^{26}Al are similar across a wide range of stellar masses, so as long as we sample the particle trajectories well in a single asymmetric explosion, the results are robust to very large changes in progenitor mass and explosion asymmetry. This assumption is valid, since we are looking for regions in the explosion that produce plausible abundances, not a bulk yield.

The network in the explosion code terminates at ^{56}Ni and cannot follow neutron excess, so to accurately calculate the yields from these models we turn to a post-process step. Nucleosynthesis post-processing was performed with the Burn code (Young and Fryer 2007), using a 524 element network terminating at ^{99}Tc. The initial abundances in each SPH particle are the 177 nuclei in the initial stellar model. The network machinery is identical to that in TYCHO (for details of the simulations see Young et al. 2009).

4.3.2 Production of ^{26}Al in 1D and 3D explosions

There are three primary sites for production of ^{26}Al in a massive star and its accompanying supernova. It can be produced by hydrogen burning at high temperatures in the shell-burning regions of massive stars or evolved AGB stars. But neither of these production sites is important to the supernova injection scenario, as discussed in Young et al. (2009). In the 1D simulations, the two dominant production sites are two peaks in ^{26}Al abundances that coincide with peak temperatures in the explosion of 2.2×10^9 K and 1.5×10^9 K, in material that has undergone hydrostatic C burning in the progenitor. The higher of the two temperatures is sufficient for explosive C and Ne burning, the lower of the temperatures is near explosive C burning. The production of ^{26}Al in both regions is due to a significant increase in the flux of free p, n, and α-particles. At higher temperatures, characteristic of O burning, ^{26}Al is quickly destroyed.

Within the 3D calculations, ^{26}Al is produced in two main regions (see Figure D.15), similar to the 1D results. The first is a ring-like structure and an associated small bubble where the two HVSs emerge into a lower density region, and which we denote the "Ring". Material in the Ring has undergone explosive Ne and C burning during the explosion at temperatures slightly above 2×10^9 K, and corresponds to the explosive C and Ne region in the 1D simulations identified above. The second region, further out at the terminal end of the HVSs, is denoted the "Bubble" (see Figure D.15). Within the Bubble, material has undergone hydrostatic C burning and then experienced peak shock temperatures $\sim 1.5 \times 10^9$ K during the explosion, and corresponds to the second of the ^{26}Al peaks in the 1D simulations identified above (which I will refer to as sub-explosive C burning region). While the production sites of ^{26}Al in the simulation in 3D occur in zones of about the same temperatures as in the 1D cases, the peak in ^{26}Al abundance in those regions are

reversed from the corresponding regions in 1D (i.e. the peak that is higher in ^{26}Al in 1D is lower in ^{26}Al in 3D, and vice versa). An important aspect of the Bubble is that due to the rapid expansion of the HVSs, its density drops rapidly, quenching some of the nuclear reactions. The decrease in density in the 1D simulations occurred at a slower rate, conversely more of the ^{26}Al was able to be processed into other species. This freezeout of nuclear reactions (suppressing subsequent destruction of ^{26}Al) in the 3D simulation is the reason for the higher production of ^{26}Al in the Bubble, as compared to the Ring.

In 3D, the ^{41}Ca production occurs in only one main production site, in a region adjacent to and partly overlapping the Ring in the 3D simulation (see Figure D.16), and in both the explosive C/Ne and sub-explosive C burning regions in the 1D calculations. The production of ^{41}Ca requires a high ^{40}Ca abundance as the seed nucleus, and the main production channel is p- and n-capture onto ^{40}Ca. The slower drop in density and temperature in the 1D calculations tended to favor a low level production of ^{41}Ca, which is why its abundance is slightly higher as compared to the 3D calculation. In the 3D calculation, ^{41}Ca is produced in the Ring, but the faster expansion of the material there due to the velocity asymmetry shuts off the reactions faster than in the 1D models, and the final ^{41}Ca abundance is lower than in 1D. In the bubble region, the lower temperature and rapid density falloff preclude any significant ^{41}Ca production.

Within the zones where ^{26}Al is produced, the M(^{26}Al)/M(^{16}O) ratios can differ significantly from the bulk abundances. For the 1D models, these ratios can vary by a factor of ~ 1 up to a factor of ~ 100 between the explosive C/Ne burning region and the sub-explosive C burning region, with a typical variation of a factor of $\sim 2-3$. For example, in model 23e-1.5 the M(^{26}Al)/M(^{16}O) ratio varies from $(6.7-8.4)\times 10^{-6}$, and for model 16m-run2 varies from 1.6×10^{-7} to 1.7×10^{-5}.

These are to be compared to the abundances in the bulk of the ejecta, which are M(^{26}Al)/M(^{16}O) $\approx 6.7 \times 10^{-6}$ for model 23e-1.5, $\approx 1.7 \times 10^{-6}$ for model 16m-run2, and varies between 4.0×10^{-7} to 1.9×10^{-4} across all 1D explosions. In the 3D model, the ratios are M(^{26}Al)/M(^{16}O) $\approx 1 - 4 \times 10^{-4}$ in the SPH particles in the Bubble, $\approx 1 - 4 \times 10^{-5}$ in the SPH particles in the Ring, and 2.88×10^{-5} for the bulk supernova abundances. Thus one notes that injection of material from the Bubble brings in an order of magnitude less oxygen (essentially all ^{16}O) per ^{26}Al atom than injection of material from the supernova overall or from the Ring.

4.3.3 Production of O isotopes in ^{26}Al-producing regions

The abundances and isotopic compositions of oxygen within a localized region of the supernova can vary significantly from the bulk values, as their production is sensitive to the density, temperature, and composition, and to their variations with time in that region. In the 1D explosions, density falls off roughly as a power law (Arnett 1996). Because this maintains a high density in the region where ^{26}Al forms by explosive C and Ne burning, ^{18}O is effectively synthesized into heavier species. ^{17}O is also synthesized into heavier species but is also created by neutron captures onto ^{16}O. The net effect is that both ^{17}O and ^{18}O are reduced relative to ^{16}O, and the ^{18}O/^{17}O ratio is reduced. In the 23e-1.5 model, their mass fractions in the ^{26}Al rich zones never exceed $\sim 10^{-5}$, and the isotopic composition in nearly all our 1D cases approaches $(-1000\ {}^{0}/_{00}, -1000\ {}^{0}/_{00})$, effectively pure ^{16}O.

The details of oxygen isotopic abundances in the ^{26}Al rich zones of the 3D explosion differ. The more rapid expansion of the material in the 3D calculation limits the processing of ^{17}O and other isotopes into heavier species, so the yield of those is higher than in the 1D calculations. As one of the main burning products of explosive Ne burning, ^{16}O is quite abundant in the Ring. However, some of the free p and n produced during explosive burning capture onto ^{16}O, producing ^{17}O,

so the Ring (as Figure D.15 shows) is quite enriched in ^{17}O relative to the rest of the explosion. In the Bubble, ^{16}O is not produced explosively, and is mostly left over from the progenitor. The increased flux of free particles also burns some of the ^{16}O there to ^{17}O and ^{18}O. The freezeout from the expansion limits the processing of these isotopes into heavier species, so the 3D explosion is richer in these isotopes than the 1D simulation.

Part of the reason for the large variation in ^{18}O isotopic yields is that most of it is produced by decay of ^{18}F($t_{1/2} = 110$ minutes), which was co-produced with ^{17}O and ^{18}O. Thus it depends sensitively on how much ^{18}F is present once nuclear burning shuts off, which in turn depends sensitively on the trajectories taken by the gas. At low temperatures the classical decay reaction $^{18}\mathrm{F} \rightarrow {}^{18}\mathrm{O} + e^{+}$ completely dominates, but at high temperatures (above $\sim 10^9$ K), and low proton density, another decay channel opens up for ^{18}F, and it can decay also via $^{18}\mathrm{F} \rightarrow {}^{14}\mathrm{N} + \alpha$ (Görres et al. 2000). The branching ratio of these two reactions is very sensitive to temperature at around 1×10^9 K, with higher temperatures overwhelmingly favoring the decay to $^{14}\mathrm{N} + \alpha$.

The amount of ^{18}F remaining at the end of burning is highly dependent on the time taken to drop below that temperature, and the density evolution, as high entropies favor the destruction over the synthesis. Because of the power law drop off, the density in the 1D calculations stayed higher for a longer period of time, as compared to the 3D calculation, thus isotopes had a longer time window in which they could be processed to higher species. The density of the 3D calculation dropped faster due to the increased velocities of particles to create the asymmetry, so the nuclear burning shut off earlier, and more isotopes like ^{17}O, ^{18}O, or ^{18}F survived the nucleosynthesis of the explosion. This results in a substantial variation in the ^{18}F abundance between the 1D and the 3D calculation, and that same effect (i.e.

how quickly the density drops) is also responsible for the variation in abundance of particles in the Ring and the Bubble by the end of the 3D simulation.

In the 1D simulations the full decay of all ^{18}F after the explosion was calculated in the reaction network. The 3D simulation was terminated earlier in its evolution before complete decay of the ^{18}F. As the temperature at that point in the explosion was well below 10^9 K, we assumed that any ^{18}F still present would decay into ^{18}O, as this is the only significant channel at these lower temperatures.

4.4 Solar system oxygen isotopic shifts accompanying ^{26}Al delivery

4.4.1 Spherically Symmetric Supernova Explosions

It is now possible to calculate the shifts in oxygen isotopic abundances before and after the injection of supernova material, using equation 4.1. As described in §2, the initial composition of the solar nebula was probably close to $(\delta^{17}\mathrm{O}, \delta^{18}\mathrm{O})_0 \approx (-60\ ^0/_{00}, -60\ ^0/_{00})$, and this is adopted as the starting value. Based on the numerical simulations of §3, I have calculated the ratios x and the isotopic abundances $(\delta^{17}\mathrm{O}, \delta^{18}\mathrm{O})_{\mathrm{SN}}$ within the ejecta overall, and within the regions where ^{26}Al is produced.

I begin with the case of the 1D explosions. The regions where ^{26}Al is produced are those we identified as the C/Ne explosive burning region, and the sub-explosive C burning region. For these purposes, these regions were defined based on the ^{26}Al content. The exact amount of ^{26}Al produced varied among the simulations, but the (radial) abundance distribution of ^{26}Al in each simulation showed two distinct peaks that were at least one order of magnitude higher than the average ^{26}Al mass fraction. Thus the ^{26}Al-rich regions in the 1D simulations were defined to be at least one order of magnitude higher in mass fraction than the average distribution. The final isotopic composition of the solar nebula following injection of supernova material has been calculated first assuming the material had the average (bulk) com-

position of the ejecta for comparison with Gounelle and Meibom (2007), and then that of one of these ^{26}Al-rich regions. The results are presented in Tables D.5- D.7 and in Figure D.17. These results for injection of bulk ejecta from 1D explosions conforms closely to the findings of GM07 using the 1D models of Rauscher et al. (2002b). The ejecta are generally very ^{16}O-rich, with δ^{17}O and δ^{18}O that are large and negative.

GM07 likewise found, using the 1D models of Rauscher et al. (2002b), that the ejecta are depleted in ^{17}O, and in most cases ^{18}O as well. (Their 15 $M_\odot$ case is enriched in ^{18}O, in contrast to our 16 $M_\odot$ case). Similarly to our 23 $M_\odot$ models, both the 21 $M_\odot$ and the 25 $M_\odot$ model of Rauscher et al. (2002b) are very depleted in ^{17}O and ^{18}O, and the composition of those ejecta approach $-1000\ ^0/_{00}$ for both δ^{17}O and δ^{18}O, although the Rauscher et al. (2002b) models tend to be slightly richer in ^{17}O and ^{18}O than ours. The similarity between the Rauscher et al. (2002b) bulk abundances and those calculated for this work are unsurprising. Post-He burning stages rapidly destroy ^{17}O and ^{18}O, resulting in the oxygen in interior zones being nearly pure ^{16}O. A 20-25 $M_\odot$ model has a very large oxygen mantle. The slightly higher fraction of heavy isotopes in the Rauscher et al. (2002b) arise in a somewhat larger He shell that results from a less accurate treatment of mixing in their earlier stellar models.

These differences reflect the variability inherent in calculations of nucleosynthesis in massive stars, especially where small shifts in stable isotopes are concerned. I also find, as did GM07, that the isotopic shifts associated with injection from ejecta from 1D supernova explosions tend to be large (tens of permil), but not in all cases. In the 23m runs, ^{26}Al is produced more abundantly, and the ^{26}Al/^{16}Oratios yield $x < 10^{-2}$ in these explosions. In the 23m cases, the ejecta are particularly ^{16}O-rich, but relatively less oxygen needs to be injected per ^{26}Al because

more ^{26}Al is produced. (It should be remembered that 23m is a binary case, where a significant fraction of the ^{17}O and ^{18}O have been removed by mass loss from the He shell, and production of ^{26}Al has been enhanced by higher peak shock temperatures relative to the 23 $M_\odot$ single star models.) The isotopic shifts associated with injection from 23m 1D explosions are typically $< 3\ ^0/_{00}$.

For all the cases the shifts in both δ^{17}O and δ^{18}O are negative and similar in magnitude; that is, the injection of material from this supernova moves the composition down the slope-1 line. Later nebula evolution would produce materials that move back up this line. The most favorable case is the 23m supernova. The magnitude and direction of the isotopic shifts associated with the 23m case are such that current measurements of solar nebula materials do not rule out this possibility, even for bulk abundances. As it is argued below, however, bulk abundances are not the best representation of the abundances of injected material.

Tables D.5, D.6, and D.7 and Figure D.17 also show the isotopic shifts associated with injection from only ^{26}Al-rich regions within the supernova. Even when considering injection of ^{26}Al-rich regions only, the conclusions are not much changed: the isotopic shifts in oxygen generally are many tens of permil, and make the solar nebula more ^{16}O-rich. The sub-explosive C burning region of the 16m model is the only case that does not move the nebular composition along the slope 1 line. In general the sub-explosive C burning in the higher mass models provide the best results, as they produce the highest ratio of ^{26}Al to oxygen.

Tables D.5, D.6, and D.7 also give the yields of ^{41}Ca produced in each of the 1D explosion scenarios. The post-injection ^{41} Ca/^{40} Ca ratio is generally more than sufficient to match the meteoritic ratio, and a time delay is implied before isotopic closure, so that ^{41}Ca can decay. For the ejecta from the 23 $M_\odot$ progenitors, the implied time delay (for ^{41}Ca to decay to a level ^{41} Ca/^{40} Ca $= 1.4 \times 10^{-8}$) for

the 23m cases is ~ 0.7 Myr for all three regions considered (i.e. bulk, explosive C/Ne burning, and sub-explosive C burning). The implied time delay for injection from the 23e cases is ~ 1.3 Myr for all three regions, and from the 23e-0.7 cases is 1.4 Myr (for the sub-explosive C burning region) – 1.7 Myr (for the other two regions). The time delays for the other progenitor cases are all within those ranges. The range of these time delays are very similar to the range of 1.0 – 1.8 Myr calculated by Gounelle and Meibom (2007). The effect of this time delay is to cause ^{26}Al to decay, too, before isotopic closure, and to increase the isotopic shifts in oxygen. The shifts are increased by factors of 2 (for the 23m) at the low end to 5.2 (for the 23e-0.7 cases) at the high end. If isotopic closure is to be achieved in a few $\times(10^5 - 10^6)$ yr (MacPherson et al. 1995; Kita et al. 2005), then injection from the 23e and 23e-0.7 would seem to introduce too much ^{41}Ca to match constraints. Injection from the more energetic 23m progenitor cases are consistent with a small shift in oxygen isotopes downward along the slope-1 line, as well as the final ^{41} Ca/^{40} Ca ratio of the solar nebula.

4.4.2 Asymmetric Supernova Explosions

In Table D.8 and Figure D.17 the yields of ^{26}Al, ^{41}Ca, and oxygen isotopes in various regions of the ejecta in the simulation of the 3D explosion are presented. I calculate the isotopic shifts if the injection uniformly samples all of the ejecta (bulk), if it samples the Ring material, and if it samples the Bubble material. By design, membership in the Bubble and Ring material is defined by high ^{26}Al content. These ^{26}Al-rich regions do not have well-defined edges, instead fading out monotonically in ^{26}Al-abundance as one moves out into the surrounding ejecta (see Figure D.15). In order to not impose an arbitrary geometry on these regions we determined membership by ^{26}Al amount per SNSPH particle. I used two different lower limits or thresholds for inclusion – 1.5×10^{-13} M$_\odot$ of ^{26}Al per particle for

a maximum extent of the ^{26}Al rich region, and 1.5×10^{-11} $M_{\odot}$ per particle for a minimum extent of the ^{26}Al-rich region ("high ^{26}Al" case). The most ^{26}Al-rich SPH particles in the Ring and Bubble had 1.5×10^{-10} $M_{\odot}$ and 4.8×10^{-10} $M_{\odot}$ of ^{26}Al, respectively. Each threshold picked out all SPH particles in the respective regions that it identified.

Overall, the ejecta of the 3D simulation are much richer in ^{17}O and ^{18}O than the 1D simulations, but also contain two regions (the Ring and the Bubble) in which the ^{26}Al production is increased over the 1D calculations. As we have previously discussed, the production of ^{18}O is significantly altered from the 1D results. The added yield from the decay of ^{18}F to ^{18}O makes the ejecta significantly richer in this isotope, and results in large (tens of permil) to very large (hundreds of permil) and positive shifts in δ^{18}O for material from both the Ring and Bubble, and the bulk. This is in stark contrast to the ^{18}O poor ejecta produced in the 1D simulations, and emphasizes the sensitive dependence on the prevailing thermodynamic conditions of ^{18}O production. The production of ^{17}O is much less sensitive to the thermodynamic conditions. In the 3D simulation we also see an increase over the 1D cases in the production of ^{17}O in the ^{26}Al rich regions and the bulk; however the change is not as drastic as in ^{18}O. This again differs from the 1D calculations, and the more ^{17}O-rich ejecta result in positive shifts in δ^{17}O, on the order of -1 to $+15$ $^{0}/_{00}$ for the Bubble and bulk, and close to $+100$ $^{0}/_{00}$ for the Ring.

Table D.8 also shows the ^{41} Ca/^{40} Ca ratio following injection of material from the 3D supernova into the solar nebula. If injection comes from the Bubble region only, the amount of ^{41}Ca injected is too low to conform to meteoritic ratios, and injection from the Bubble can be ruled out on these grounds. Injection of material from the Ring or bulk regions, in contrast, imply reasonable time delays $\approx 0.66 - 0.90$ Myr. This implies an increase in oxygen isotopic shifts of < 2.5 over

what is presented in Table D.8. These time delays are just below the ones Gounelle and Meibom (2007) calculate, which again is explained by the faster density- drop off in the 3D calculation producing slightly less ^{41}Ca than in 1D.

When an explosion samples a variety of thermodynamic trajectories through asymmetry, including those that result in freeze-out conditions due to rapid expansion, the overriding conclusion to be derived is that a very large range in oxygen isotopic shifts is allowed. It would seem extremely unlikely that conditions in an asymmetric explosion would conspire to yield a small isotopic shift consistent with the meteoritic constraints, though more "normal" trajectories that do not experience this freeze-out process are still candidate production sites, as seen in 1D.

4.5 Discussion

As Nichols et al. (1999) strongly advocated, injection of supernova ejecta can produce measurable "collateral damage" to stable isotope systems in protoplanetary disks. GM07 in particular point to the role of oxygen isotopes in constraining this process. The point of that paper was that the injection of ^{26}Al (and ^{41}Ca) from a single nearby supernova necessarily would have brought in significant levels of oxygen isotopically distinct from the pre-injection solar nebula. The solar nebula after injection, they argued, would differ in its oxygen isotopes by several tens of permil from the pre-injection values, which they robustly predicted would be more ^{17}O-rich than the solar nebula. They cited the Genesis measurements of solar wind oxygen as those most likely to sample the pre-injection solar nebula. Since preliminary results from Genesis (McKeegan et al. 2009, 2010) are revealing the Sun to be ^{16}O-rich, GM07 would rule out injection of ^{26}Al and ^{41}Ca from a single supernova.

In this chapter, I attempted to reproduce the calculations of GM07, to apply their method of using oxygen isotopes to test the supernvoa injection hypothesis. I made necessary corrections to their method, mostly in regard to the presumed

oxygen isotopic composition of the (post-injection) solar nebula. GM07 assumed this was identical to SMOW, meaning the pre-injection solar nebula had to be more ^{17}O-rich than almost any known inclusions. Considerable evidence was presented that the post-injection composition was in fact much more ^{16}O-rich than that, closer to $(-60\ {}^{0}/_{00}, -60\ {}^{0}/_{00})$. Stellar nucleosynthesis calculations were carried out to calculate the isotopic yields of ^{26}Al, ^{41}Ca and oxygen isotopes in a variety of supernova explosion scenarios, including the 1D (spherically symmetric) cases as well as 3D (asymmetric) explosions. Because ^{26}Al and ^{41}Ca are observed to be correlated (Sahijpal and Goswami 1998), we also simultaneously considered injection of ^{41}Ca into the solar nebula. I then computed the shifts in oxygen isotopes and the final ^{41} Ca/^{40} Ca ratio in the solar nebula following injection of sufficient supernova material to produce the meteoritic ratio ^{26}Al/^{27}Al $= 5 \times 10^{-5}$.

The 1D simulations largely confirm the results of GM07, that isotopic shifts are likely to be tens of permil and to make the solar nebula more ^{16}O-rich than before the injection. It was found that injection of material from either the bulk or the explosive C/Ne burning and sub-explosive C burning regions of supernovae moved the composition of the solar nebula down the slope 1 line. The 23 $M_{\odot}$ progenitors led to isotopic shifts in oxygen which moved the composition of the solar nebula down the slope-1 line, with the less energetic explosions producing larger shifts and time delays. The 23m progenitors, which were the most energetic of the 23 $M_{\odot}$ cases and especially effective in producing ^{26}Al, generated shifts that amounted to only $< 6\ {}^{0}/_{00}$, including a time delay of 0.7 Myr for ^{41}Ca to decay to its meteoritic value. This scenario, at least, is consistent with all the applied meteoritic constraints. If less than 100% of the oxygen penetrated the solar nebula material due to, for example, dust condensation, all but one of the 1D cases are consistent with the evidence from the early solar system.

It was note that this conclusion differs from what GM07 infer for injection of bulk ejecta from 21 $M_\odot$ and 25 $M_\odot$ progenitors. GM07 likewise found isotopic shifts downward along the slope-1 line, but with a magnitude of 40 to 50 permil. It is worth noting that had GM07 assumed the same starting composition for the solar nebula, $(-60\ {}^0/_{00}, -60\ {}^0/_{00})$, as in this analysis, then they would have found the solar nebula oxygen isotopic composition to be $(-82\ {}^0/_{00}, -82\ {}^0/_{00})$ after injection of supernova material from an 25 $M_\odot$ progenitor, and $(-81\ {}^0/_{00}, -74\ {}^0/_{00})$ after injection of supernova material from an 21 $M_\odot$ progenitor. Although these shifts are moderately large, they are down the slope-1 line. As was established in §4.2.3, this would not have been incompatible with the meteoritic constraints, as some very ^{16}O-rich meteoritic samples in this range are known, including CAIs in Isheyevo, at $\approx (-68\ {}^0/_{00}, -66\ {}^0/_{00})$ (Gounelle et al. 2009), and a ferromagnesian cryptocrystalline chondrule in the CH chondrite Acfer 214, at $\approx (-75\ {}^0/_{00}, -75\ {}^0/_{00})$ (Kobayashi et al. 2003). Subsequently the mass-independent fractionation process would have shifted the nebula upward along the slope-1 line, erasing this isotopic shift and eventually producing the composition $(\delta^{17}O, \delta^{18}O) \approx (-40\ {}^0/_{00}, -40\ {}^0/_{00})$ common to most CAIs (e.g. Itoh et al. 2004). I conclude that the supernova injection hypothesis cannot be rejected based on 1D models.

This investigation of other parameters suggest that it is even more difficult to be conclusive about supernova injection. A small number of progenitor masses undergoing spherically symmetric collapse were considered; in a few cases other parameters were varied, such as varying the explosion energy, or allowing for loss of a hydrogen envelope in a binary scenario, or allowing an asymmetrical explosion. In most of these cases the isotopic shifts in oxygen were large. Among the cases considered here, the final $\delta^{17}O$ values in the solar nebula varied from $-379\ {}^0/_{00}$ to $+15\ {}^0/_{00}$, and the final $\delta^{18}O$ values varied from $-379\ {}^0/_{00}$ to $+18000\ {}^0/_{00}$. As

GM07 found, most of the cases where meteoritic abundances of ^{26}Al are injected lead to large ($> 10\ ^{0}/_{00}$) shifts in oxygen isotopes. I also considered the yields in a 3D anisotropic explosion of a 23 $M_{\odot}$ progenitor, in the bulk ejecta and two ^{26}Al-rich zones analogous to those in the 1D explosions. I found that a wide range of outcomes is possible, with oxygen isotopic shifts as large as hundreds of permil, or as low as $< 3\ ^{0}/_{00}$. The fact that ^{18}Fcan decay to ^{14} N instead of ^{18}Oat high temperatures makes the yield of ^{18}Oespecially sensitive to the thermodynamic trajectory of the ejecta, which partially accounts for the spread in the ^{18}O yields. On the one hand, the wide range of possible outcomes makes it nearly impossible to state conclusively that all supernova injection scenarios can be ruled out. On the other hand, the wide range of possible outcomes seems to imply a degree of fine tuning so that the oxygen isotopic shifts in the solar nebula were not large, especially for the 3D case.

I conclude that the hypothesis, that the ^{26}Al in the solar nebula was due to supernova material injected into the Sun's protoplanetary disk, can still be made compatible with meteoritic constraints, under two scenarios. The first is that the injected supernova material came from either the bulk ejecta, or from a region in a supernova that experienced thermodynamic conditions like the subexplosive C burning zone. The latter is more physically likely. With a 0.7 Myr time delay, the injection would have moved the solar nebula oxygen isotopic composition from $(\delta^{17}\mathrm{O}, \delta^{18}\mathrm{O}) \approx (-60\ ^{0}/_{00}, -60\ ^{0}/_{00})$ to a more ^{16}O-rich value along the slope one line. All but one of our explosions produce movement along the slope 1 line. I calculated shifts as small as $\approx (-63\ ^{0}/_{00}, -63\ ^{0}/_{00})$, which would have produced an accompanying meteoritic ratio $^{41}\mathrm{Ca}/^{40}\mathrm{Ca} = 1.4 \times 10^{-8}$. Subsequent mixing of rocky material with a ^{16}O-depleted reservoir would have then moved the composition of meteoritic inclusions up the slope-1 line to values $(\delta^{17}\mathrm{O}, \delta^{18}\mathrm{O}) \approx$

$(-50\ {}^{0}/_{00}, -50\ {}^{0}/_{00})$, consistent with primitive CAIs, and further up the slope-1 line with time.

The second scenario is one in which only dust grains are injected in to the protoplanetary disk, and very little of the supernova oxygen condenses into dust grains. If only the most refractory grains such as corundum were injected, then potentially $x \ll 10^{-5}$, and the isotopic shifts would be negligible ($\ll 1\ {}^{0}/_{00}$), for nearly all the cases considered here. It is worth noting that Ca is equally refractory to Al and is likely to condense from supernova ejecta under the same conditions that Al condenses, so the meteoritic abundance of ^{41}Ca could still be matched following injection of ^{26}Al. Ouellette et al. (2007) have calculated that only 1% of gas-phase ejecta are injected into a disk. If almost all of the Ca and Al in the ejecta are locked up in large grains (radii $> 0.1\,\mu$ m) that are efficiently injected (Ouellette et al. 2010), but less than a few percent of the oxygen is, then potentially all of the isotopic shifts in oxygen calculated here should be reduced by a factor of about 100. Essentially all of the 1D cases considered here would then conform with the meteoritic constraints, and even some of the 3D cases as well.

To summarize, as GM07 state, oxygen isotopes can be a powerful constraint on supernova injection models. These calculations of oxygen isotopic shifts following injection from the bulk ejecta of 1D supernovae broadly match the results of GM07. Had GM07 assumed the same starting composition of the solar nebula as this analysis, and considered a smaller time delay between injection and isotopic closure, they would have found isotopic shifts for 20 - 25 $M_{\odot}$ progenitors that would not be inconsistent with meteoritic constraints. The calculations presented here of the same case predict shifts that are similar, although smaller in magnitude, and which are also consistent with meteoritic constraints. The existence of an example that is consistent with the oxygen isotopic composition and the ^{41} Ca/^{40} Ca

ratio of the solar nebula means that the supernova injection hypothesis cannot be ruled out. Because the nucleosynthesis of oxygen differs in asymmetric explosions, a much wider range of oxygen isotopes is possible in 3D explosions. Because of the contingent nature of the injection it becomes difficult to make any statement about the possibility that the solar nebula acquired ^{26}Al from such an asymmetric explosion. Finally, all oxygen isotopic shifts are reduced if only large grains are injected into the protoplanetary disk, and only a small fraction of oxygen condenses into large grains. Quantifying the fractionation of Al and O during injection into a protoplanetary disk is the focus of ongoing work by this research group. If only a few percent of the total oxygen is injected, then nearly all the 1D explosions considered here could be consistent with the meteoritic constraints on oxygen isotopes and ^{41}Ca abundances. I therefore conclude it is premature to rule out the supernova injection hypothesis based on oxygen isotopes.

Chapter 5

STRUCTURE FORMATION IN EXPLOSIONS OF A 15 $M_\odot$ PROGENITOR

5.1 Introduction

Morphological, kinematic, and compositional structures are ubiquitous in the observations of supernovae (SNe) and supernova remnants (SNRs). These structures span scales from unipolar asymmetries across the whole remnant to sub-AU (astronomical unit) sized high density knots being shredded in the reverse shock of the Cassiopeia A (Cas A) SNR. The dense knots in SNRs are of particular interest from a nucleosynthetic and astrobiological point of view as vehicles for the chemical enrichment of star and planet-forming material in high mass star formation regions, as well as for interpreting observations of remnants. They carry nearly undiluted material from the metal-rich mantle of the former star and thus are good candidates for studying hydrodynamics and mixing processes during the explosion with both numerical and observational tools.

Multiple physical processes drive structure formation. Although it had long been known that instabilities would grow in the shock launched in a supernova explosion (Chevalier 1976), most explosion studies focused on 1-dimensional models (primarily due to the high computational requirements of multi-dimensional simulations). But SN 1987A demonstrated the wide variety of observables affected by these instabilities: broad line widths in the infrared and gamma-ray lines of several elements (Erickson et al. 1988; Witteborn et al. 1989), low velocity hydrogen features in the spectrum 221 days after the explosion (Hoeflich 1988), and indirect evidence from light curve models (Woosley 1988; Shigeyama et al. 1988; Arnett et al. 1989). All these observables suggested deep mixing had occurred in the explosion (see Fryer et al. 2007a, for a review).

While turbulence occurs during many stages of the collapse and explosion process of a massive star, the particular focus of this paper are the instabilities caused by the interaction of the SN shock wave with steep gradients in the profile of the exploding star. Arnett et al. (1989) reviewed a number of sites/events in an exploding star that can lead to deviations from spherical behavior, and point out that the formation of Rayleigh-Taylor (RT) fingers by shock passage as the most important. RT instabilities arise commonly in situations where a less dense fluid is accelerated into a denser fluid (e.g. when a less dense fluid is supporting a denser fluid against gravity), or more generally, where a fluid of higher entropy is accelerated into one with lower entropy. In the limit of impulsive acceleration this is referred to as a Richtmyer-Meshkov (RM) instability. Bubbles of the higher entropy fluid rise into the less entropic fluid, while columns or spikes of that penetrate into the higher entropy fluid. Shear flows at the interface between the two fluids are subject to Kelvin-Helmholtz (KH) instabilities. In the case of RM instabilities, both scenarios, a shock accelerated into an interface going from heavy to light and light to heavy fluids are unstable in the RM sense. The RM instability results in very similar looking features as the RT instability. It is likely that both instabilities are occurring during the explosion, and distinguishing between them may be somewhat subjective. For ease of reading I will refer to the whole class of instabilities henceforth as RT instabilities unless the distinction makes an important difference in the interpretation.

In computer simulation of the shock propagation through the star, multiple sites have been found to become unstable and result in the growth of RT instabilities. Nearly all simulations to date (Fryxell et al. 1991; Müller et al. 1991; Herant and Benz 1992, 1991; Hachisu et al. 1991, 1992; Nagataki et al. 1998; Kifonidis et al. 2003, 2006; Hungerford et al. 2003, 2005a; Joggerst et al. 2009, 2010b; Hammer

et al. 2010) find that strong instabilities grow. The RT instabilities most often arise at the He/metals interface for different progenitor models, which typically resulted in the mixing down of H and He, and the mixing out of at least C and O, and often higher- A elements like ^{24}Mg, Si, and the Fe-group, though not always in sufficient quantities to explain observations on SN1987A. A higher degree of non-linearity in the RT instabilities can be achieved with an asymmetric shock front (Hachisu et al. 1992). Fryxell et al. (1991) showed that, except for very coarse grids, the mode of the instability (i.e. the average spacing between RT fingers) is independent of resolution. Hachisu et al. (1992) and Herant and Benz (1991) also showed that the amplitude of artificial seed perturbations (which are imposed to a) counter the damping of the highest modes due numerical and/or artificial viscosity, and b) to mimic fluctuations which are likely present in physical stars) does not influence the RT instabilities significantly, as long as there is a perturbation.

Often more than one region becomes unstable in simulations, and the different instabilities then in many cases interact and merge. Extending their study to higher resolution, Müller et al. (1991) discovered that the RT fingers first form at the H/He interface, but is then overrun by RT forming at the He/metals interface. Using a slightly different approach, Herant and Benz (1991, 1992) modeled 1987A with a particle-based numerical scheme, and obtained similar results. Depending on the progenitor used, multiple sites became RT unstable, which in some case merged to just one instability. Müller et al. (1989) also emphasized the importance of using an accurate stellar density profile, since the polytropic profile in their earlier calculations showed no evidence for unstable regions. Herant and Benz (1992) in a sense expanded on this conclusion by demonstrating the different RT morphologies achieved with different progenitor star profiles.

These early results (e.g. Müller et al. 1991; Herant and Benz 1992; Hachisu et al. 1992), though, suggested that such mixing as the shock moves through the star was insufficient to explain the mixing in SN 1987A. To enhance this transport, scientists revived research studying initial perturbations from convection in stellar progenitors(Bazan and Arnett 1998; Kane et al. 2000) and in the explosion by studying aspherical effects in the core-collapse engine(Herant et al. 1992, 1994). In the core-collapse engine, these studies showed that turbulence above the proto-neutron star is important in producing an explosion. Although there are disagreements as to the nature of the instabilities (standing accretion shock vs. Rayleigh Taylor, etc.) this convection-enhanced engine is the current favored model in core collapse(Herant et al. 1994; Burrows et al. 1995; Mezzacappa et al. 1998; Fryer and Warren 2002; Blondin et al. 2003; Buras et al. 2003; Blondin and Mezzacappa 2006; Burrows et al. 2006; Fryer and Young 2007). This convective engine can produce highly asymmetric explosions. Such asymmetries will drive mixing as the shock moves out of the star.

Hungerford et al. (2003, 2005a) studied the effect of these explosion asymmetries on the mixing using 3-dimensional models. Their results showed that artificially imparted explosion asymmetries can dominate the mixing, producing broad line profiles like those in SN 1987A (where symmetric runs of the same explosion energy could not). This work found that ^{56}Ni was mixed well into the hydrogen layer for the most asymmetric explosions and argued that the asymmetries could explain both the rapid rise in gamma-ray radiation as well as the redshift of the gamma-ray emission.

Realizing the importance of perturbations set up by the shock revival mechanism, multi-dimensional explosion calculations are now being used for shock propagation calculations. Kifonidis et al. (2003) followed the explosion mechanism and

the propagation of the blast wave simultaneously in 2D. RT instabilities, during the early convection that revived the shock, resulted in a slightly aspherical distribution of ^{56}Ni. This distribution imprinted long-wavelength perturbations on the Si/O layer, and out of which RT instabilities grew as that interface became unstable. RT instabilities were also observed at the He/CO interface. They also found that the deeper RT instability at the Si/O interface resulted in the mixing out of some Ni. Hammer et al. (2010) use a 3D explosion calculation from Scheck (2007) to follow the shock propagation through a 15.5$M_{\odot}$ blue supergiant star in 2D and 3D under differing initial conditions. This is one of the first calculations to follow both the launch of the shock and the ensuing explosion in 3D. Some slight deformation from sphericity by the supernova engine seeds the later growing RT instabilities in their simulations (no artificial seed perturbations were implemented), with the sites of the largest deformation resulting in the largest RT plumes. RT fingers again formed at the He/CO interface, and also at the Si/O interface, and fragmented into clumps.

Joggerst et al. (2009) presented simulations for a small number of progenitors - 2 masses and 2 metallicities - in 2D, and Joggerst et al. (2010b) extend that study to 3D, though in the interest of saving computational resources all explosion models were initiated in 1D. Prominent RT instabilities develop again at the He/O interface, though instabilities at the Si/O are possibly suppressed due to the explosion mechanism used. The more massive progenitor in each case showed a wider region of instabilities, and Joggerst et al. (2009) state that in the solar metallicity, 25$M_{\odot}$ case, RT instabilities extended down past the O shell and into the Si/S layer, resulting in increased mixing out of Fe-group material. They, again, find that the profile of the specific progenitor has a large influence on the extent and morphology of the RT region.

The formation of RT and RM instabilities by shock interaction with interfaces thus is a robust feature in supernova explosion simulations. Some variance in the details and location of the RT and RM instabilities exists between different calculations, mostly due to the uncertainty in post-main sequence stellar structure and due to different explosion algorithms used. Previous calculations were generally more focused on the emergence of and mixing that these instabilities produce, as they were often compared to SN1987A. However, in order to be able to make meaningful comparisons to older remnants like Cas A, where the evolution is dominated by the interaction of the ejecta with surrounding stellar winds and/or ISM, it is necessary to extend these calculations to a much longer time after shock breakout. Among other things, this can shed more light on the further evolution of the clumps created by RT instabilities, and help firmly establish their relationship to features like the dense ejecta knots in Cas A.

It is my aim to follow structures from their formation all the way to the young remnant phase, e.g. similar in age to Cas A. Identifying the location and timing of structure formation and modification, and comparing them to observations of young SNR will elucidate the proximate deposition of nucleosynthesis products in the interstellar medium of star and planet formation regions and the history of SNRs. In this paper I present the first step in this endeavor, 3 dimensional simulations of a 15 $M_{\odot}$ SN explosion evolved out to the homologous expansion phase. This will establish the methodology for simulations out to later times with circumstellar medium interactions and comparison of different progenitors and explosion asymmetries. I also propose a method of characterizing the sizes of overdense clumps that can be compared directly with observations. In section 5.2 I describe these simulations and the parameters that I explored. I offer an analysis useful for observational comparison for determining typical clump sizes in section 5.4. A dis-

cussion of the results is presented in section 5.3, and some concluding remarks are presented in section 5.5

5.2 Simulations

5.2.1 Progenitor and Collapse Calculations

The progenitor used is a 15 $M_\odot$ progenitor of solar metallicity. It was evolved up to the onset of core collapse with the stellar evolution code TYCHO (Young and Arnett 2005). Some major abundances are shown in figure D.19. The model is non-rotating and includes hydrodynamic mixing processes (Young and Arnett 2005; Young et al. 2005; Arnett et al. 2009). The inclusion of these processes, which approximate the integrated effect of dynamic stability criteria for convection, entrainment at convective boundaries, and wave-driven mixing, results in significantly larger extents of regions processed by nuclear burning stages. Mass loss uses updated versions of the prescriptions of Kudritzki et al. (1989) for OB mass loss and Bloecker (1995) for red supergiant mass loss, and Lamers and Nugis (2002) for WR phases. A 177 element network terminating at ^{74}Ge is used throughout the evolution. The network uses the most current Reaclib rates (Rauscher and Thielemann 2001), weak rates from Langanke and Martínez-Pinedo (2000), and screening from Graboske et al. (1973). Neutrino cooling from plasma processes and the Urca process is included.

To model collapse and explosion, I use a 1-dimensional Lagrangian code to follow the collapse through core bounce. This code includes 3-flavor neutrino transport using a flux-limited diffusion calculation and a coupled set of equations of state to model the wide range of densities in the collapse phase. (see Herant et al. 1994; Fryer 1999, for details), It includes a 14-element nuclear network (Benz et al. 1989) to follow the energy generation. Following the beginning of the explosion in 1D saves computation time and is sufficient for this problem, as I were mainly

interested in the formation of structure during the passage of the shock. The explosion was followed until the revival of the shock, and then mapped into 3D to follow the rest of the explosion and further evolution in 3 dimensions. The mapping took place when the supernova shock wave has moved out of the Fe-core and propagated into the Si-S rich shell. The radial density profile at the time of mapping into 3D is shown in figure D.18.

5.2.2 Computational Method

I used the 3-dimensional Lagrangian hydrodynamics code SNSPH (Fryer et al. 2006) to model the explosion of the progenitor. SNSPH is a particle-based algorithm and is based on the version of SPH developed by Benz (1984, 1988, 1989). The code is designed for fast traversal on parallel systems and for many architectures. The sizes (scale lengths) of the SPH particles is variable, and the time stepping is adaptive. The radiation transport was modeled with a 2D, explicit flux-limited diffusion scheme (Herant et al. 1994) adapted to 3 dimensions.

There is an intrinsic scatter in density and pressure in SPH methods, due to the variability of and dependence on the smoothing length. In these simulations, this scatter has a 1σ error of $\sim 5-10\%$ in the lowest resolution simulations. It is likely that convection in burning shells before/during stellar collapse produces density perturbations at a $\sim$ 10% in any case (Arnett and Meakin 2011), so this artificial scatter is likely comparable with the true initial conditions (Fryer et al. 2006).

Some small perturbation in the thermodynamic variables is necessary for fluid instabilities to arise. Calculations in non-particle based schemes use an artificial perturbation in velocity and/or density and/or pressure to seed instabilities; the amplitude of these perturbations is up to 10% (e.g. Fryxell et al. 1991; Müller et al. 1991). In the calculations of the Müller, Arnett, and Fryxell group, different ampli-

tudes in the perturbations has resulted in different growth rates of the instabilities, but not in different modes or morphologies.

5.2.3 Burning and Cooling

SNSPH was augmented with a nuclear reaction network code running parallel to the SPH calculation and a radiative cooling routine for optically thin plasmas of arbitrary composition. Abundance tracking for those routines was achieved by adding abundance information of 20 isotopes (those used in the network) to the SPH particles. These abundances were followed in the code along with each particle, but chemical diffusion was neglected. The only physical effect that influenced the chemical composition of an SPH particle was through nuclear burning/ radioactive decay calculated by the network.

The nuclear burning code consists of 20-isotope library comprised of mostly alpha-chain reactions to track energy generation, and is capable of burning in normal and nuclear statistical equilibrium (NSE) conditions during the explosion, and following radioactive decay only for evolution after the explosion. The isotopes used in the network, and tracked in SNSPH, are shown in table D.9. The reaction rates for this network are taken from REACLIB Rauscher and Thielemann (2001). The network runs in parallel to the hydrodynamics calculations, and features its own time step subcycling algorithm in order to not slow down the hydrodynamics. The network libraries and algorithm are the same as those used in TYCHO. Changes in energy and composition are fed back into the SPH calculation at each (SPH) time step.

The number of isotopes in the network can be scaled arbitrarily. I chose to scale the network to 20 isotopes to get a workable balance between network accuracy and computational feasibility. Due to the small number of isotopes considered in the network, it does not accurately calculate the yields of individual isotopes.

However, I have found this code to be able to accurately model the energy production during explosive burning to within 20%. Accurate yields will be calculated for these runs with a much larger version of this network code for a future paper.

The network in the explosion code terminates at ^{56}Ni and neutron excess is directed to ^{56}Fe. To accurately calculate the yields from these models I turn to a post-process step. Nucleosynthesis post-processing was performed with the Burn code (Young and Fryer 2007), using a 524 element network terminating at ^{99}Tc. The Burn solver is computationally identical to that in TYCHO and SNSPH. The network uses the current REACLIB rates described in Rauscher and Thielemann (2001), weak rates from Langanke and Martínez-Pinedo (2000), and screening from Graboske et al. (1973). Reverse rates are calculated from detailed balance and allow a smooth transition to a nuclear statistical equilibrium (NSE) solver at $T > 10^{10}$K. For this work Burn chooses an appropriate timestep based on the rate of change of abundances and performs a log-linear interpolation in the thermodynamic trajectory of each zone in the explosion calculation. Neutrino cooling from plasma processes and the Urca process is calculated. The initial abundances are those of the 177 nuclei in the initial stellar model.

All runs, except for one, presented in this paper were run with the network in place. One version of the canonical run was computed before the network was added, and serves as a baseline to compare the effects of the network, in particular the decay of Ni in the post-explosion phase.

The radiative cooling routine is based on the cooling tables from the CHIANTI atomic database for optically thin astrophysical plasmas, and assumes collisional ionization equilibrium. The cooling tables include a very large fraction of all possible electronic transitions for each element from H to Zn. They give rates for gases of arbitrary composition, and are weighted by the chemical abundance and

ionization state of each considered element in each SPH particle. As this routine is only for optically thin plasmas, it was turned off during the explosion. Furthermore, a simple prescription for calculating optical depth based on Thompson and free-free scattering was used and compared to SPH particle size to determine optical thickness (and thus, whether radiative cooling should be used or not).

5.2.4 Simulation Runs

A brief summary of all simulations done for this paper is presented in table D.10. The canonical run (1M_burn) is a spherically symmetric explosion modeled with 1 million SPH particles. It was assumed that at the point in time of the 3D-mapping most of the fallback had already occurred, and the neutron star was cut out. Any gravitational influence of the neutron star on the further evolution of the explosion was therefore neglected. This assumption was tested and partially verified in two runs with a central gravity source with absorbing boundary was included to simulate a compact central object (CCO). Run 1M_burn_CCO used a gravity source of initial mass 1.5 $M_\odot$ and radius 4×10^{-4} $R_\odot$, run 1M_burn_CCO2 used an initial mass of 1.35 $M_\odot$ and radius of 1×10^{-4} $R_\odot$. Mass and linear and angular momentum accreted on the central object was tracked. Although the presence of the CCO did affect the kinematics in the layers below the O/C shell (further described in section 5.3), it had only a secondary effect on the fluid instabilities of interest in this paper. Both runs exhibited very similar behavior, although it was naturally more pronounced in run 1M_burn_CCO with the larger central gravity source. While this would be an unacceptable simplification for the evolution of the whole remnant, the approximation has minimal impact for the study of structure growth due to RT instabilities at the He/OC interface. Since the smaller gravity source in run 1M_burn_CCO2 is near the compact object mass derived from the 1D explosion to that point, I will limit further discussion mostly to that run. I conducted further runs

to uniformly compare the effect of asymmetries without inclusion of the central gravity source, since the run time was about 10 times longer with a central mass than the typical run time for the 1M runs. The radius of the progenitor at the time of collapse was ~ 430 $R_{\odot}$, which was the same in all simulations.

I were also interested in studying the effect of an asymmetric blast wave on the formation of RT instabilities. Both observational and theoretical evidence indicate that asymmetry is strong and ubiquitous in supernovae (e.g. Fryer et al. 2007b; Young and Fryer 2007; Hungerford et al. 2005a; Lopez et al. 2009b). Spectropolarimetric analysis of core-collapse SNRs indicate that large scale asymmetry is a common and standard feature in SN which originates deep in the explosion process and is associated with bipolar outflows ("jets"; see e.g. Wang and Wheeler 2008). Departures from axisymmetry are also common (Wang and Wheeler 2008). Decomposition of Chandra images of supernova remnants into moments has shown that bipolar explosions can explain the observed distribution of elements Lopez et al. (2009b, a). Anisotropic explosions of CC SNe have also often been blamed for the high space velocities of neutron stars and pulsars (Fryer et al. 1998; Herant 1995; Scheck et al. 2004). It has been proposed that an asymmetry along one direction of the explosion imparts a substantial momentum on the neutron star as it forms (e.g. Nordhaus et al. 2010). Calculations of X-ray and γ-ray line profiles in uni–polar and bi–polar SN simulations are consistent with observations of SN1987A and CasA (Hungerford et al. 2003, 2005a). Furthermore, the likely explosion mechanism(s) produce (and seem to require) low mode asymmetries in the center of the star (e.g. Herant et al. 1994), but typically result in slightly higher modes than uni- or bi-polar explosions.

Inclusion of a central gravity source did result in a slight, global distortion from sphericity of material inside of the shock, but not the shock itself. In order to

test different strengths of axisymmetric asymmetries (and since the CCO was excluded from most runs), I did several runs with imposed uni– or bi–polar explosion asymmetries. It should be noted that the imposing of asymmetry in these runs is not meant as a substitute for accurate treatment of the explosion mechanism, but merely an attempt at quantifying structure formation in parameterized asymmetric explosions.

The asymmetries were implemented by modifying the velocities of particles in and inside of the shock according to the prescription in Hungerford et al. (2003), viz.:

$$v_{radial} = (\alpha + \beta |z|/r) v_{radial}^{sym} \tag{5.1}$$

for the jet scenarios, where the values for α and β were taken from table 1 in that paper. The 1M_jet4* cases resulted in an initial velocity aspect ratio of 2:1 between the highest and the lowest velocities, the 1M_jet2 cases resulted in an initial aspect ratio of 3:2. I thus repeated the Hungerford et al. (2003) "jet2" and "jet4" scenarios, implemented at the beginning of each simulation. Although these initial aspect ratios resulted in a strong initial bipolar asymmetry, most of the energy was probably thermalized, and produced only very mildly aspherical supernovae. I therefore repeated the 1M_jet4 calculation once the shock reached the edge of the O-rich layer in a "late" asymmetry case (1M_jet4L) and another case for when the shock had propagated well into the C rich layer (1M_jet4LL), in order to achieve more pronounced (and likely exaggerated) final asymmetries in the remnant.

I repeated the canonical run with 10 million (10M; run 10M_burn) and 50 million (50M; run 50M_burn) particles to gauge the dependence of the properties of the instabilities on the resolution of the simulations. I also computed a single-lobe scenario for each of the two jet asymmetries. As all runs, minus one, were per-

formed with the reaction network switched on, the radioactive decay from ^{56}Ni was tracked as well.

The simulations in this paper explode the stars into vacuum; there is no surrounding material (e.g. CSM, ISM) as there would be in reality. Typical densities of stellar winds (and other material in the space between stars) are at least several orders of magnitude smaller than the surface density of stars, and thus do not influence the initial expansion of the explosions. However, as the stellar material continues to expand, it will sweep up the surrounding interstellar material in its wake, and interactions between the ejecta with the swept-up material will become non- negligible when the mass of the swept-up material approaches that of the ejecta. Assuming a generic ISM density of 1 H atom per cm^3, and taking the mass of the swept up material to equal that of the ejecta (9.4 $M_\odot$), this will occur after the SN has expanded to a radius of $\simeq$ 4pc or about 1.8×10^8 $R_\odot$. If the ISM density is an order of magnitude higher, this distance will be less (by a factor of 2.15). Similarly, the presence of a RSG wind (since the progenitor lost ~ 4 $M_\odot$ in a post-main sequence wind) will reduce that distance again. At 0.5 yrs, when most of the simulations were terminated, the remnants had expanded to an average radius of 3.3×10^6 $R_\odot$, thus I are assuming that the expansion of these runs would not have been significantly affected by inclusion of a surrounding medium. However, for accurate comparisons to actual remnants at later times than I probe here, this needs to be accounted for. Further evolution of these remnants with these effects included is planned for a later publication.

5.3 Formation of Structure and Instabilities

5.3.1 Rayleigh-Taylor and Richtmeyer-Meshkov instabilities

I find that prominent instabilities develop in each simulation at the He/OC interface. At the start of the 3D simulations, the shock starts out sub-sonically ($\mathscr{M} \leq 0.5$) in

the Si/S–rich layer, still showing aspects of an accretion shock. It quickly turns into an explosion shock and becomes slightly supersonic ($\mathscr{M} \sim 2$) as it is moving out of the Si/S rich layer. The SN shock wave continually decelerates as it is moving through the O-rich layer of the star, though it remains supersonic, and picks up speed again once it enters the C-rich layer. The deceleration in the O-rich layer is caused by the increase in ρr^3 there, which is actually non-constant in that layer. The initial deceleration of the shock upon entering the O-rich shell results in some mixing across the Si/O boundary, however that region is unstable only for a brief period of time. A small reverse shock is reflected at the O/C boundary that travels inwards. Once the shock reaches the He-rich layer its speed increases again due to the decrease in ρr^3 . Some mixing is observed across the OC/He boundary as the shock traverses it, however, RT instabilities do not form until the shock enters the H-envelope.

By the time it arrives at the He/H interface the shock has reached a (maximum) peak speed of 19,500 km s^{-1} (which is several tens of times the local sound speed). As the blast wave enters the H-envelope it is again rapidly decelerated. The shock sweeps up the H-rich material, which results in a piling up of matter and a reverse shock. The reverse shock created by the collision of the blast wave with the H-envelope travels inwards in mass and decelerates the outward moving material behind the SN shock, which thus results in the observed piling-up of matter between it and the blast wave. This pile-up of material occurs at the He/OC interface, and forms a thin, dense He-rich shell behind the shock. This dense shell first becomes apparent at 24 min after the start of the simulation, and shows very small amplitude, high-mode deviations from sphericity (cf. figure D.21, first panel. The evolution of the run is shown at 50 min, as the modes in density variation are more clearly visible). The scatter in density is $\sim 13\%$ of the average value in this region,

and the scatter in velocity is $\sim 10\%$. Although at the higher end, this is in line with the artificially imposed perturbations in density and/or velocity found in previous simulations published in the literature to seed convection. RT instabilities arise because the material just outside of the dense shell experiences a net acceleration towards this dense shell due to the reverse shock passing by, eventually resulting in columns or spikes of dense material growing outwards (in the radial sense), and bubbles of material sinking inwards (not readily visible). After about 2.5 hrs a web-like pattern, delineating the walls between slightly unevenly spaced cells of "spikes" (i.e. growing into the higher entropy fluid) and "bubbles" (i.e. growing into the lower entropy fluid) of material (see fig. D.21) have formed, and some of the vertex points of these cells are starting to form into RT spikes. A 3D density plot of this is shown in figure D.21 in the second panel.

The instability grows at the interface between the He and the C+O shell (i.e. the interface seen at $\log(r) \sim -0.4$ in Figure D.19). This interface coincides with a quite sharply decreasing $\rho \mathrm{r}^3$, which is hit by a strong shock that has reached a Mach number of ($\mathscr{M} \sim 8$) there, which has the potential of becoming unstable to RM instabilities. Some mixing of He, C, and O, seems to be occurring in this region behind the shock (and before the reverse shock is launched). However, deviations from sphericity are not noticed until a dense shell of material has started piling up (as described above), by which time the shock has already passed this region and the reverse shock has just traversed it. RT instabilities arise when a fluid of higher entropy is accelerated into a fluid of lower entropy (i.e. when the pressure in the less dense fluid is higher than in the denser fluid). This results in continuous deceleration of the less dense fluid. RM instabilities arise when a supersonic shock is accelerated into a (stationary) interface between two fluids, where this interface can be caused by a change in density, entropy, composition, or equation of state. This

is an instantaneous deceleration of material. RM instabilities may also be regarded as the impulsive limit of RT instabilities. As real world situations touch aspects of both, their classification may be difficult (and perhaps somewhat subjective). Different instabilities in these simulations exhibit characteristics of both, and vary in character according to whether they arise during the SN shock passage or in the dense shell behind the shock. The instability that grows at the He/CO interface seems to be in the RT-sense. It is quite possible, though, that a RM instability did arise briefly at this interface, "pre-perturbing" this region, and thus seeding the RT instability from the deceleration of the SN shock wave. This could potentially explain why only one instability was observed to grow, although multiple sites seem to become briefly unstable (or had the potential to), most likely in the RM- sense, as shock–acceleration of an interface followed by mass pile-up from shock deceleration was a situation unique to the He/OC interface. In this case a region of higher entropy is established behind the reverse shock, which results in the high density spikes growing radially outward. As the dominant mechanism for forming the instability appears to have been the RT setup, I will refer to that instability as RT instability in the following.

The RT instabilities significantly grow until about 43.8 hrs, and their velocity is indistinguishable from the homologous expansion or the rest of the material by $\sim$ 9.5d, at which time the star has expanded to about 30 times its size at the time of the explosion. A brief progression of this is shown in figure D.21, showing snapshots at 50 min, 2.6 hrs, and 26 hrs of the symmetric 1M run. After that, since the explosions were only simulated expanding into vacuum, the RT fingers do not change but just expand homologously with the rest of the ejecta.

The dominant elements in the RT fingers are ^{16}O, ^{12}C, and ^{4}He. H does not appear to be significantly mixed into the plumes (beyond what was already present

in the region that became unstable), however it is mixed down into the interior below the RT region in pockets.

All nuclear burning is done at 1300 sec, i.e. at about the same time when the first signs of RT instabilities become apparent, at which time the peak temperature falls below 1×10^7 K. The only difference that can be seen between runs with and without burning is that the chemical composition of the RT fingers is shifted some towards O.

The RT instabilities in these simulations freeze out shortly after becoming non-linear. The spikes grow essentially radially outward, only a few are observed to bend significantly, and interaction between two plumes remains a rare occasion (if this happens at all). The degree of bending seems to increase slightly as I go higher in resolution and in the 1M_burn_CCO run, however, in none of these simulations does the flow become turbulent.

5.3.2 Symmetric Initial Conditions

Figures D.23 to D.39 show abundance maps of the isotopes ^{1}H, ^{4}He, ^{12}C, ^{16}O, ^{44}Ti, and ^{56}Ni or ^{56}Fe for all these runs and the corresponding densities. In all plots, the chemical abundance of an element or isotope is given as mass fraction, and the density is given in code units (1×10^{-6} $M_\odot$ ${R_\odot}^{-3} \approx 6 \times 10^{-6}$ g cm^{-3}). The yields for the canonical run are given in table D.11.

Figure D.22 shows a comparison of density plots for the different resolutions tested. All plots are at approximately the same time in the evolution, i.e. at $\sim$ 22 hrs after the explosion. As mentioned above, at this point the RT instabilities are still growing, however, this is the furthest that I currently have evolved the 50M_burn run. As expected, the 50M_burn resolves the RT filaments and clumps much better than the 1M runs. The spikes in the 1M runs appear more stubby, while in the 50M_burn run one can distinguish the mushroom shaped cap from the "stem"

or filament. There is overall a higher number of RT spikes present, indicating that a higher mode was set up. Furthermore, there are many more 'wisps' or filaments between the RT fingers, suggesting that the largest KH instabilities are becoming resolved. The mushroom caps, or "RT clumps", on the other hand, appear at only a slightly smaller diameter as those in the canonical run. The size of the RT clumps is not strongly dependent on resolution. Furthermore, the base where the RT fingers grow out of is wider (radially speaking) in the 50M_burn run due to the 'resolution increased' KH mixing, and the fingers reach a little further out into the H-envelope. As the RT fingers are still in the growing phase, it is possible that some fingers might reach close to the edge of the H-envelope if the run is evolved further.

Interestingly, the RT fingers of the 10M_burn run appear morphologically quite similar to the ones in the 1M run, but appear to be closer in number to the 50M_burn run. Furthermore, the extent of the RT region (i.e. from the base to the tip of the fingers) is the most narrow of all three runs, although it is slightly further evolved than the 50M_burn run. This deviation from the expected trend can probably be understood in terms of the average number of neighboring particles per particle (average neighbors, for short). Both the 1M and the 50M_burn runs were set up with 50 average neighbors, however, the 10M_burn run was set up with 60 average neighbors. Increasing the average number of neighbors increases the number of interpolation points per SPH particle, and correspondingly also the scale length of the SPH particles, i.e. smoothes out the thermodynamic quantities more. Thus, the gradients between the RT fingers and the surrounding gas are less steep, and the RT fingers grow more slowly. However, as the length of the RT fingers appear similar in size, a higher number of neighbors (or an increased number of particles) means more particles per RT finger, which seems to increase the mode of the RT fingers (i.e. shorten the wavelength scale between spikes). The number of

the RT fingers in run 50M_burn is about twice that of the canonical run, while the number in run 10M_burn is about three times that of the canonical run.

For a better visualization of this, the canonical run was repeated with a set-up of 38 and 70 average neighbors each, shown in figures D.30, D.31, and D.32. As previously observed, the run with the higher average number of neighbors shows less extended RT spikes, although it is further along in its evolution, however, the number of RT spikes (i.e. the RT mode) does not seem to have been noticeably influenced. It also seems to be the case that in the 1M_burn_38nbrs run, the RT fingers are of differing lengths, whereas in the 1M_burn_70nbrs run, all RT fingers appear to be nearly the same length. This suggests/shows that the scale height of the SPH particle (influenced by the number of neighbors) plays a role to what degree non-linear growth of the RT fingers (e.g. through KH instabilities) is resolved/suppressed. The effect, if any, of changing the number of neighbors on the distribution of elements seems to be minor, as Junk et al. (2010) also state. The only slight difference that can be detected is that the oxygen appears to be drawn a little further into the RT in the 1M_burn_70nbrs run. (Furthermore, there appears to be the beginning of a high-mode, low amplitude instability between the O and the Si layers, but nothing seems to evolve out of that in any of the other, later runs).

The distribution of the (plotted) abundances also appears to not be affected by the chosen resolution. There does appear to be a more significant 'gap' between the bottom edge of the RT region and the Ti-rich region in the 50M_burn than the canonical run, however the plotted 50M_burn run is about 4hrs behind the canonical run plots in evolution, which could possibly explain that difference. Also apparent in the 10M_burn abundance plots at about 45 deg. is a pocket of H (i.e. envelope material) that is 'punching' a hole through the bottom edge of the RT region. As observed in the 1M_burn_38nbrs and 1M_burn_70nbrs runs, the O seems

to reach further into the RT fingers in the 10M_burn (higher number of neighbors) and 50M_burn (overall more particles per RT finger) than the canonical run.

In most runs the forming neutron star was cut out to save computation time, under the assumption that the explosion had progressed far enough that the added dynamics from the forming compact remnant would not be significant. The validity of this assumption was tested with two runs (1M_burn_CCO and 1M_burn_CCO2) where a central gravity source with absorbing boundary was placed to mimic the gravity from a central compact object. Run 1M_burn_CCO used an initial central gravity source of 1.5 $M_{\odot}$, run 1M_burn_CCO2 used 1.35 $M_{\odot}$. Although both runs were started out with spherically symmetric initial conditions (aside from SPH-typical inter-particle deviations), a few large convective plumes develop almost immediately after the start of the simulation. They arise from the pressure gradient set up by the additional gravitational acceleration to be in the opposite direction of the entropy gradient. Some material in the falling plumes is accreted onto the central object and imparts some momentum onto it. The plumes slowly grow in extend and slosh around somewhat, and eventually the flow pattern "freezes out" and leaves the central region asymmetric. The plumes always remain a distance behind the shock, thus the shock wave remains spherical, and sets up RT instabilities at the He/OC interface by the same conditions as described above. A somewhat slower growth rate is noted, which is expected from the added gravitational force from the central gravity source. The flow pattern of the convective plumes does eventually reach the RT instabilities, but only once the RT are already well established. Thus the main effect they have on the RT instabilities is to distort the region as a whole slightly from sphericity, which in turn causes some of the fingers to bend slightly more. I conclude that the influence of this convection on the RT fingers is secondary, but note that it is, unsurprisingly, critical to the evolution of the whole remnant.

Besides a very noticeable partial overturn and a few "frozen out" convective plumes distorting the central parts, there are several minor differences that were noted. The shock speed is decreased slightly, and reaches a peak speed of $\sim 16,700$ km s^{-1} before entering the H-rich layer. The CCO2 run accretes 0.14 M$_{\odot}$ onto the central object, which has a space velocity of 5.3 km s^{-1} at 25 hrs after the explosion. Run CCO accretes 0.25 M$_{\odot}$ and has a space velocity of 21.6 km s^{-1}. Furthermore, most of the Ni/Fe-group elements synthesized in the explosion fell victim to fallback onto the CCO, thus the Ni-bubble effect is suppressed. In run 1M_burn_CCO2, using a less massive initial gravity source, only slightly more Ni survives. The nucleosynthesis is altered slightly by the convective plumes, Ti is increased while other α-chain products are slightly decreased, and more He (α's) seem to be present in the central part. Table D.11 compares the fully post-processed abundances of a few isotopes to the canonical run. Furthermore, the central convection partially mixes the region interior to the RT instabilities; in particular O and C are distributed throughout the central region. H and He are again observed to be mixed slightly past the RT instabilities in pockets; this effect is more pronounced where the the strongest outflows from the central convection occurred. Oxygen also is mixed further out by the RT filaments above those regions.

5.3.3 Imposed Asymmetries

Figures D.33 and D.34 show density and abundance plots of the two different jet scenarios implemented at the first time step of the computation. Shown are snapshots at ~ 0.5 yrs after the explosion, after which time a significant fraction of the ^{56}Ni produced in the explosion had decayed. An elongation along the symmetry axis (vertical axis) can be seen. Also visible is a bubble hollowing out the region inside of the RT fingers. This bubble (or accumulation of many small bubbles) coincides with regions of high Ni abundance (high Fe abundance in the plots from

Ni-decay). This is likely a bubble generated by energy deposition from decay of ^{56}Ni. Dense knots of high H, C, and O (though not He) abundance can be seen in this region also. The presence of H (and C) suggests that this is material that has been mixed down into the Ni-bubble. Although there are a few spots where the Ni/Fe is punching through the base of the RT fingers, it stays mostly confined to the central region.

The energy from the radioactive decay heats the surrounding gas, which subsequently tries to expand. Any regions low in Ni (e.g. H,C material mixed down) are compressed by the expanding Ni-gas into knots. Furthermore, the heated Ni-gas expands against the base of the RT fingers, compressing this into a dense, narrow shell. The highest densities at 0.5 yrs are seen in this compressed shell surrounding the Ni-gas, and in the knots in the Ni-bubble. The Ti abundance (without post-processing) seems to be very tightly correlated to the Ni/Fe abundance. Nuclear burning does not appear to have been influenced in either run by the asymmetry. In the simulations it was assumed that all decay energy is absorbed by the gas. Therefore, the effect of the Ni-decay should be treated as an upper limit.

Figure D.33 shows a slice through one of these runs at 1 yr after collapse in density and abundance maps for Fe and non-Fe elements. The density map clearly shows the effect of clumping caused by the "Ni-bubble", i.e. the fragmentation caused by the decay of ^{56}Ni to ^{56}Co and ^{56}Fe. This Ni-bubble can be seen in all other runs at $\sim$0.5 yrs that tracked the radioactive decay of ^{56}Ni. Comparison of the density map to the distribution of ^{56}Fe shows that the low-density "bubbles" coincide with high abundance of Fe, strongly suggesting that the "bubbles" were caused by the decay to ^{56}Fe. ^{56}Ni decays to ^{56}Co via beta decay on a time scale of $\sim$5 days; ^{56}Co decays to ^{56}Fe via beta decay on a time scale of 77 days. Both decays emit an energy of slightly over 2 Mev per decay each, which is, in these

simulations, absorbed near the place where it was emitted in the decay, and goes into heating the surrounding matter instead of escaping. All material is still assumed to be optically thick at all wavelengths. Regions with high abundance of Ni/Co will experience more heating, and subsequent expansion, which compresses regions of low Ni/Co abundance, creating an appearance of multiple bubbles interspersed with low-Fe clumps.

5.3.4 Stability Considerations

When doing numerical hydrodynamic simulations of astrophysical objects it is important to consider factors arising out of the numerical setup, rather than physical processes, that could lead to fluid instabilities. SPH codes use an artificial viscosity term in order to dampen unphysical oscillations in regions of strong compressive flows (i.e. shocks) and to prevent numerically undesirable penetration of particles. Viscosity has the effect in general of resisting instabilities in the flow of fluids. The viscosity of the gas in stars is generally much smaller than the artificial viscosity added to the code. In addition to the artificial viscosity, there is also numerical viscosity that arises from rounding errors and the discretization of the problem. While the artificial viscosity can be chosen so that it is zero in those parts of the gas where it is not needed, numerical viscosity can never be completely eliminated (however, judicious choices for initial conditions and simulation set-up generally keep it to a minimum).

In fluid instabilities the highest modes (i.e. those with the smallest associated length scale or wavelength) tend to grow the fastest. In the limit of zero viscosity (and surface tension) the smallest wavelength that can grow is limited by the resolution in the simulation. If the viscosity is non-zero, its effect is to dampen the growth of modes with the smallest wavelength, i.e those below a characteristic

length, which is given by

$$\lambda_{\max} = 4\pi(\nu^2 \mathrm{A}/g)^{1/3} \tag{5.2}$$

(see Chandrasekhar 1961), where ν is the kinematic viscosity, g is the local gravitational acceleration and A is the Atwood number, which was taken to be 0.9. In the runs with 1 million particles the size of $\lambda_{\max}$ given by the kinematic bulk velocity in the region where the RT instabilities first become visible is between 23 $R_\odot$ – 44 $R_\odot$. For comparison, the size (diameter) of the spacing between the weblike structure is about 5 $R_\odot$ – 10 $R_\odot$ at the point in time when it first becomes apparent. For the run with 50 million particles the wavelength of the mode(s) is about 2 $R_\odot$ – 5 $R_\odot$, while $\sim$12 $R_\odot < \lambda_{\max} <\sim$25 $R_\odot$, which is again larger than the wavelength of the mode.

Visual comparison of e.g. figure D.22 of the 50M_burn run to the 1M_burn run and 10M_burn run shows that the number of RT fingers increases slightly with resolution. The increase in resolution going to 10 million particles is a factor of $\sqrt[3]{10} = 2.15$ and going to 50 million particles gives an increase of $\sqrt[3]{50} = 3.68$. The number of RT fingers in the 10M run is about double that of the 1M run, in accordance with the increase factor in resolution, however, the number of RT fingers in the 50M run is approximately the same as in the 10M run. This suggests that the mode of the RT instability is marginally unresolved in the 1M runs and resolved in the 10M and and 50M runs, although the size of the clumps at the end of the fingers appears as approximately the same across each resolution (further discussed in section 5.4).

It would appear then that the mode of the RT instability is not being determined (primarily) by viscosity. It should be noted, though, that the determination of $\lambda_{\max}$ only considered the bulk/shear artificial viscosity (the 'α' term in the Monaghan viscosity description) not the von Neumann-Richtmyer term (the 'β' term),

whereas SPH includes both (plus numerical viscosity). Thus the total viscosity, artificial and otherwise, is likely higher which would increase $\lambda_{\max}$. Thus I would like to take this as an indication that the RT instabilities are approximately resolved, and not set by the viscosity term. However, KH instabilities are likely only beginning to be resolved in the 50M_burn run, and I consider this to be the main reason for the different morphologies of the RT instabilities across the different resolutions.

More importantly, though, is that equation 5.2 assumes constant entropy, which is not a good approximation for the region under consideration. A more appropriate analysis would be to consider the Brunt-Väisälä frequency, which in the limit of radiation pressure dominated gas is approximately:

$$\omega^2 \approx \frac{1}{S}\frac{\Delta v}{\Delta t}\frac{\Delta S}{\Delta r} \tag{5.3}$$

for decelerating plasmas. Here, S is the entropy, ΔS is the change in entropy over distance Δr, and $\Delta v/\Delta t$ is the deceleration of the gas. In regions where the net acceleration is opposite of the entropy gradient (i.e. where $\Delta S/\Delta r$ and $\Delta v/\Delta t$ have opposite signs), ω^2 is negative and the region is unstable. In the region where the RT instabilities are occurring the entropy sharply increases and the net acceleration of the material in the reverse shock is inward (i.e. a deceleration), thus this region is susceptible to instabilities. The logarithmic change in entropy $\Delta(\log S)/\Delta r$ is ≈ 0.4 and the deceleration is $\approx 3.3 \times 10^{-2}$ $\mathrm{R}_\odot/\mathrm{s}_{100}^2$, giving a time scale for the growth of $\sim 8.7\mathrm{s}_{100}$. This is about what is observed for the growth of RT instabilities in the simulations, further strengthening the conclusion that the RT mode is being established by physical driving rather than artificially high viscosity in the simulation.

Lastly, since self-gravity is included in SNSPH, it is worthwhile to formally rule out gravitational collapse as a main driving factor for the clumps. The Jeans length, $l_J = c_s/\sqrt{G\rho}$, i.e. the smallest length scale stable to gravitational collapse,

was found to be between 600 $R_\odot$ – 4000 $R_\odot$ in the region where the clumps are forming. Self-gravitating collapse is thus assumed to be negligible.

5.3.5 Comparison to Previous Works

A further test of the results presented in this paper is a comparison to similar studies published in the literature. Although most earlier simulations were conducted in 2D, it is still be worthwhile to include those in a comparison. In a comparison of growth rates in 2D and 3D simulations Kane et al. (2000) show that (keeping the simulation parameters similar) adding the third dimension only results in a faster growth rate (and thus larger size) of the RT fingers. The sites that become unstable (He/H and O/He interfaces) remain the same. The faster growth rate of (linear) instabilities in 3D is likely due to a lower effective drag force on the fingers in 3 dimensions (Hammer et al. 2010) , although Joggerst et al. (2009) remark that in their simulations the initially faster growth rate in 3D is 'counteracted' later in the simulations when the RT fingers become highly non-linear, so that the final size of the RT unstable regions is the same in 2D and 3D.

5.3.5.1 Formation of He/OC Instability

Like Arnett et al. (1989) I find that the instability is associated with the dense mass shell, however in a later paper the group clarifies that first the H/He interface becomes weakly RT unstable, but it is the RT instability forming a little later at this dense mass shell that becomes the dominant instability and merges with the first, giving the appearance of only one instability. In these calculations there is a spread of velocities behind the shock once it has pased the O/C interface. Correspondingly I note that Fryxell et al. (1991) map their simulations into 2D after the reverse shock is already on its way back inwards, and use seed perturbations in velocity behind the shock of 10% amplitude. Nagataki et al. (1998) use seed amplitudes as high as 30%. Proceeding in a very similar fashion (but using SPH), Herant and Benz (1992)

note that a velocity perturbation amplitude of 10% (5% peak-to-peak) or greater results in instabilities independent of the initial seed amplitude (i.e. is needed to get a sufficient growth rate of the RT instabilities). Kifonidis et al. (2003) note that the instability at the Si/O interface has imparted a strong perturbation onto the OC/He interface before that becomes unstable. This suggests that indeed such high velocity perturbations are needed for the growth of RT instabilities, but that they seem to naturally arise from the hydrodynamics from the interaction of the shockwave with the He/metals interface (and H-envelope). Contrasting this, though, are Joggerst et al. (2009) who use only a 2% seed perturbation to obtain sufficient RT instability growth. They are, presumably, using a significantly higher resolution than Fryxell et al. (1991) and Nagataki et al. (1998) (and Herant and Benz (1992)), thus less damping of the highest modes is present and possibly smaller seed amplitudes are required.

I find like Joggerst et al. (2009) that RT instabilities arise in regions where the SN shock decelerates, which in both these simulations and in theirs occurs at the H/He interface. However, while Joggerst et al. (2009) find the blast wave responsible for setting up the RT instabilities and the reverse shock for stabilizing the region again, I find that it is reverse shock which makes the region unstable (as an aside, Joggerst et al. (2010b) also find that the reverse shock causes the instabilities). Kifonidis et al. (2003) describe all three of their instabilities as arising from the shock deceleration at those interfaces resulting in reversed gradients from piling up of material into dense shells. The highest shock speed in their calculations ($\sim 20,000$ km s^{-1} when entering the He-layer) is very similar to those in this paper ($\sim$ 19700 km s^{-1} when entering the H-envelope), although they find that an increase in density (ρr^3) slows down the shock in the He- layer, while this is not observed in these calculations. This different density profile of the progenitor is

likely the reason for the difference in RT instabilities between these calculations and theirs.

Many previous calculations have found that instabilities develop in 2 or even 3 distinct regions, which often, but not always, merged into just one. (cf. Arnett et al. (1989); Fryxell et al. (1991); Müller et al. (1991, 1989); Kifonidis et al. (2003), and Hammer et al. (2010) (2D)) This difference from these single instability may in part be due to the different progenitor structures used, though the results in Hammer et al. (2010) suggest that the dimensionality of the calculations (2D vs 3D) may play a role too. As Herant and Benz (1991, 1992) and Müller et al. (1989) clearly illustrate, different progenitor structures (even if of the same main sequence mass) can result in very different explosion and post-explosion dynamics. An n=3 polytropic progenitor profile does not contain unstable regions while a power-law profile does (Müller et al. 1989). Moreover, the steepness of density and entropy contrasts at the edges of hydrostatic burning zones have a direct influence on the formation and strength of instabilities, as the stark difference between Arnett's and Woosley's progenitors in Herant and Benz (1992) illustrates. While these progenitor shows a steepening in density at the He/O interface as do those progenitors used in Herant and Benz (1992) (although it does not have the kinks as in Nomoto's progenitor), the transition across the He/H interface is less noticeable in these progenitor than Weaver's or Woosley's, and both of those show only one RT instability (at the He/metals interface) in Herant and Benz (1992).

Müller et al. (1991) note that (second to the progenitor structure at the time of collapse) the treatment of the equation of state and compressibility of the gas have pronounced effects on the degree to which the O/He interface becomes unstable and the strength/size of the RT plumes developing at that interface. From their stability analysis it seems that both steeper density and pressure gradients, and

less compact (i.e. smaller density) progenitors tend to a larger initial linear growth rate. I presume a larger initial growth rate to translate more pronounced instabilities even in the non-linear regime. A comparison of growth rates between compressible and incompressible gasses (and a test calculation with a different value for γ) lead the authors to conclude that the choice of equation of state can either somewhat suppress ($\gamma = 4/3$) or increase the linear growth rates, in particular at the He/O interface.

5.3.5.2 Si/O Instability

The results presented in this paper did not find any significant instability at the Si/O interface of the type as seen in Hammer et al. (2010); Kifonidis et al. (2003, 2006). It seems that although conditions for the onset of instability were met at various locations in the O-rich shell, conditions were not right for their sustained growth. Indeed, a slight, high mode distortion from sphericity between the O-rich and the Ni/Fe-rich material is noted in almost all abundance plots. In the 1M_burn_CCO and -CCO2 runs large convective plumes arise, although that seems to be caused mostly by the dynamics of the fallback. Kifonidis et al. (2006) also seem to observe late time convection above the proto-neutron star, originating from convection in the neutrino heated layer during shock revival. The effect there is to deform the shock with a 1:1.5 axis ratio, and cause a large scale asymmetry in the later evolution and distribution of RT instabilities. In these simulations, the shock wave moves well ahead of the convective plumes, which only slightly distort the shape of the ejecta once RT are already set up.

Although the 3D aspect of these calculations were started very shortly after shock revival, the bounce and the revival were followed in 1D, thus the only perturbations present at the beginning of the 3D calculations were those intrinsic to the particle representation. Figure D.20 shows that $\rho \mathrm{r}^3$ in the region $-2.5 <$

$\log(r) < -1.8$ (which contains the Si/O interface at $\log(r) \sim 2$) rises similarly as in the H-dominant region ($\log(r) > 1$), however, no significant instabilities grow from that interface. Possibly a strong shock (i.e. $\mathscr{M} \gg 1$) is required to cause instabilities (as RM instabilities), and a density inversion is required to sustain their growth (through a transition to RT instabilities). The shock is transitioning to supersonic speeds as it moves out of the Si/S layer, and thus may not be strong enough for RM instabilities (or possibly weak RM instabilities are instantaneously set up, but then die away nearly as soon as they are created). However, since a main difference is the treatment of the shock revival, I find it more likely that perturbations from the shock revival phase are necessary to seed growing instabilities at the Si/O interface.

Kifonidis et al. (2003), who were the first to find a RT instability at the Si/O interface, contrast their results with Arnett et al. (1989), Fryxell et al. (1991), and Müller et al. (1991) and also proposed that the differences are either due to the different (more accurate?) treatment of the explosion mechanism, insufficient resolution (although Joggerst et al. (2009) seem to rule out/find no evidence for this), different progenitor structures, or a combination thereof. It is noteworthy, though, that although Kifonidis et al. (2003) describe three regions as RT-unstable (Si/O, CO/He, and He/H interfaces), it is the instability at the CO/He boundary that is the most prominent. It is also notable that only Hammer et al. (2010) also find an instability at the Si/O interface, while the simulations presented in this paper show a brief instability but no sustained growth in all runs but the one with a central gravity source that mainly results in mixing, not density clumps. Both Hammer et al. (2010) and Kifonidis et al. (2003, 2006) follow almost the entire explosion with their own multi-dimensional codes, and the 3D calculations presented here commence at shortly after the successful shock revival was calculated in 1D. Kifonidis et al. start their 2D calculations from a 1D collapse model 20ms after collapse;

Hammer et al. (2010) use a model from Scheck et al. where the explosion was followed in 3D starting a few ms after bounce. Both papers have in common (and differ in this respect from other calculations) that multi-dimensional convection during the shock revival phase is included, and that a neutrino-heating mechanism, as opposed to a piston or a thermal bomb, was used or naturally arose to induce the explosion.

Related to that I note that Hammer et al. (2010), Joggerst et al. (2010b), Joggerst et al. (2009) and Kifonidis et al. (2003) find a significant amount of Si and Ni/Fe in the instabilities, while all other groups do not. these 1M_burn_CCO2 run seems to have a few pockets of high Si production (as well as C, perhaps from alpha-rich freeze-out from the plume-dynamics) that is then mixed out somewhat by the large central convection, while much of the Fe-group elements fell back onto the central object. Joggerst et al. (2009) and Joggerst et al. (2010b) do not start the multi-D aspect of their simulations until 20 – 100 s after bounce (depending on model), much later than Hammer et al. (2010), Kifonidis et al. (2003, 2006), and these simulations, giving further strength to the argument that seeds are needed for instabilities at the Si/O interface to grow into the non-linear regime. The non-linear evolution through KH instabilities seems to be more vigorous in Joggerst et al. (2009, 2010b), and possibly as a result more material from the Si- and Fe- group rich material is entrained in the unstable flow. Also of note is that the explosion models used by Joggerst et al. were initiated by a piston located at the base of the O shell, which is probably the main reason that no Si/O instabilities were observed in those calculations.

5.3.5.3 The ”Dense Mass Shell”/ He Wall

After the passage of the shock through a density transition, a dense mass shell or pile-up of material is seen in most previously published simulations as well as

those in this paper. In these and Müller et al. (1991)'s runs a dense He shell seems to coincide with the location of the RT instability, as the reverse shock imparts a net acceleration of higher entropy material into it, making this region unstable. Kifonidis et al. (2003), Joggerst et al. (2009), Joggerst et al. (2010b) and Hammer et al. (2010) find that a dense He shell forms from the deceleration of the shock at the He/H interface. Kifonidis et al. (2003) find a dense shell building up and leading to each of the instabilities they observe. However, in Kifonidis et al. (2003) and the 2D simulations of Hammer et al. (2010) the effect of it is preventing the plumes from entering into the H envelope. Since the RM plumes do move into the H envelope in Hammer et al. (2010) 's 3D simulations, this is possibly an effect of the dimensionality of the simulation related to the different growth rates in 2D vs. 3D. It could also be related to the different locations in the stars that become RT/RM unstable - if it becomes unstable it can not also form a "wall" around the plumes at some later time. In other words, the He-wall can only potentially prevent plumes inside of it from moving past it, not the ones growing from it.

5.3.5.4 The "Ni-bubble"

Herant and Benz (1992) follow their simulations out to 90d after the explosion and find that the decay energy of Ni has hollowed out the central parts in a Ni-bubble. I find a very similar effect occurring in nearly all these runs at 0.5 yrs after the explosion. I do not see discernible features of a Ni-bubble in run 1M_burn_CCO or -CCO2, since a majority of the Ni fell back onto the proto- neutron star. Like in Herant and Benz (1992), the Ni-bubble is not observed to significantly alter any aspects of the RT clumps.

5.3.5.5 RT vs RM Instability

There seems to be some variance in the literature as to the types and number of instabilities that form. Arnett et al. (1989), Fryxell et al. (1991), and Müller et al. (1991)

find that RT instabilities form at the H/He and the He/metals interfaces, Herant and Benz (1992) also find between 1-3 regions (depending on progenitor) develop RT instabilities, at minimum at the He/metals interface, presumably through a similar mechanism. As I elaborated above, I also find RT instabilities to be responsible for the instabilities that develop. Hachisu et al. (1991, 1992); Nagataki et al. (1998); Hungerford et al. (2003, 2005a) also classify the instabilities they observe as being of the RT kind. In contrast, Hammer et al. (2010) find RM instabilities in their simulations, while Kifonidis et al. (2003, 2006) find that both types of instabilities occur. Hammer et al. (2010) specify that while there are RMIs at both the CO/He and He/H interfaces in their 2D simulations, they only see the one at the (C+O)/He interface in their 3D simulation. The explanation they give for this is that in 3D the shock is nearly spherical at the He/H interface (as opposed to being quite aspherical at the CO/He interface) and thus not able to generate the amount of vorticity necessary to trigger RM instability before this interface is overrun by the plumes from the instability deeper in. Kifonidis et al. (2006) also state that it is the vorticity generated by the blast wave, deformed by instabilities further in from the explosion, interacting with the He/H boundary that results in RM instabilities there. Since an RM instability is an impulsive acceleration across an entropy boundary, the role of the vorticity is to generate a seed perturbation from which an instability can grow.

Kane et al. (2000) note that it is a combination of RM instabilities (from the blast wave) followed by RT instabilities (caused by the deceleration of the blast wave, i.e. the reverse shock) that causes the overall instabilities, although in their simulations both the He/H and the O/He interfaces become unstable. I seem to observe a similar phenomenon, as first some mixing across the OC/He interface is observed (presumed to be caused by RM instabilities), followed by RT instability growing once the reverse shock travels back through this region. Thus, perhaps,

there are multiple different classes of instabilities; prompt impulsively driven ones (RMIs) in the mantle, where the shock is moving supersonically, that are relatively unaffected by (artificial) seed perturbations; those near where the bounce shock stalled, that need a seed perturbation from the convection during the shock revival to grow; and those related to entropy inversions accompanying reverse shocks (RTIs).

5.3.5.6 Morphology of Instability

As the shock wave propagates through the star it compresses the CO and the He layer together some, so that when the RT instability sets in at the H/He boundary, most of the C and much O are there to become mixed into the RT filaments. Fryxell et al. (1991) find that O is mixed into the RT fingers and from there out into the H envelope, while H and He are mixed down towards the center. Herant and Benz (1992) also find that H is mixed down in H pockets, which are later compressed into clumps by the Ni-bubble effect. Other groups find similar results in that the main elements in the RT plumes are O,C, and He, although Fryxell et al. (1991) also find that Mg and higher elements seem to become entrained at the bottom of the RT flow, while Hammer et al. (2010), Joggerst et al. (2009, 2010b), and Kifonidis et al. (2003) also find Si and Ni -group elements to be mixed out by the RT/RM instabilities. In this respect these results are more similar to Arnett et al. (1989), Fryxell et al. (1991), and Müller et al. (1991) who find that no elements heavier than O become entrained in the RT fingers.

Kifonidis et al. (2003) find that the shock remains spherical, and that RT plumes grow from a circular region. Kifonidis et al. (2006) find that strong convection above the PNS during the shock revival distorts the shock significantly from sphericity, which then corresponds to a very non-spherical distribution of RM and RT plumes including plumes growing out of larger plumes. Hammer et al. (2010) find RT plumes growing mostly in the radial direction, with their extent influenced

by the convection above the proto-neutron star. KH instabilites occur, but do not distort the RT plumes quite much as in other grid-based calculations. It is perhaps noteworthy that the number of RT fingers Hammer et al. find seems comparable to these 1M calculations. Joggerst et al. (2010b) find vigorous KH mixing in both 2D and 3D that increases the non-linearity and interactions between RT plumes. Their 2D cases seem to resemble those of Müller et al. (1991).

The simulations presented in this paper seem to produce much less turbulent mixing than presented in other papers (e.g. Joggerst et al. 2010b, 2009; Hammer et al. 2010). In these simulations, only a few plumes are observed to bend significantly, and interaction between two plumes remains are isolated events. The degree of bending seems to increase slightly as I go higher in resolution, however, in none of these simulations does the flow become turbulent, as seen in Joggerst et al. (2010b), Joggerst et al. (2010a), or Kifonidis et al. (2003). No KH-rippling or roll-up is observed on the ”surface” or ”edge” of the RT filaments (save for the mushroom caps) that would facilitate mixing and enhance non- linear growth. KH instabilities seem to be better captured in grid-based codes, since these codes have a lower intrinsic (i.e. no artificial) viscosity, which is why there is less turbulence in these simulations.

Although all these simulations were conducted with grid-based codes, the simulations by Herant and Benz (1992) and ours indicate that there is no major change in going to a particle- based code. The major difference seems to be a decreased amount of KH instabilities along the edges of the RT or RM plumes, thus resulting in less chaotic/turbulent behavior in SPH simulations. This has been observed in the literature before, see e.g. Agertz et al. (2007) and references therein. Particularly in that paper it is pointed out that jumps in density effectively prevent the formation of KH instabilities in the standard SPH formalisms. In a sense, the

jump in resolution associated with this density jump (since resolution in SPH depends on density) results in a restoring force for this interface. Agertz et al. (2007) describe a gap in particle distribution that forms between the two fluids as a result of this. I do not see this pronounced gap in these simulations since the transition between regions of different density is continuous, not step-like as in their paper. Nevertheless, the absence of the extensive KH induced mixing in these calculations may be partly attributable to this phenomenon. Different solutions or improvements have been suggested to remedy this; e.g. Price (2008) propose the inclusion of an artificial thermal conductivity term to prevent the formation of a discontinuous pressure profile at contact discontinuities.

Kifonidis et al. (2003) achieve a resolution of 0.0006 km ($\Delta r/r \approx 10^{-4} - 10^{-5}$), for the smallest refinement level at approximately the time that RT fingers develop at the He/CO interface. They note that a resolution of at least $\Delta r/r = 10^{-6}$ is necessary to resolve all relevant RT instabilites. They find ≈ 10 large RT plumes in a half circle, which become very non-linear through KH roll-up. Kifonidis et al. (2006) achieves a slightly higher resolution, with a similar degree of non-linearity (KH-roll up). Hammer et al. (2010) use a radial resolution of $\Delta r/r = 10^{-2}$ and an angular resolution of $\sim 1^{\circ}$ in each angular coordinate (corresponding to 7.776×10^7 grid points), Joggerst et al. (2010b) use a resolution of 512^n, where $n = 2$ for 2D and $n = 3$ for 3D, (which would correspond to $\sim 1.34 \times 10^8$ interpolation points for their 3D simulation without refinement considered). Although it is hard to tell, Joggerst et al. (2010b, 2009) seem to find a comparable number of large RT plumes in 2D as Kifonidis et al. (2003). In 3D Joggerst et al. (2010b) observe a higher degree of KH induced mixing than in 2D, and it seems that they resolve higher RT modes in 3D than presented in this paper (although that appearance may also have been caused by KH instabilities breaking up the RT plumes into smaller pieces). Fryxell

et al. (1991) specifically study the dependence of the RT fingers on the resolution. It seems that a grid of 250^2 for a quadrant of the star is sufficient for resolving the RT instabilities. Hachisu et al. (1992) quote a similar resolution as necessary for saturating the mode of the RT instabilities. However, much higher resolutions are necessary for resolving shear flow instabilities along the RT edges. Indeed, the maximum resolution used by Fryxell et al. (1991) mostly resolves the mushrooms caps better, a resolution fthese times higher than that is necessary to get significant KH instabilities along the fingers (Fryxell et al. 1991).

This comparison suggests that the RT instabilities (not considering the effect of KH instabilities) is approximately resolved in current high resolution simulations. Consequently, the mode of the RT instability in these highest resolution run is likely resolved also, while those in the 1M runs are close to being resolved. However, this comparison also shows that a much higher resolution in simulations is necessary and important for resolving KH instabilities along the flow edges. KH instabilities are just beginning to be resolved in these 50M run.

Junk et al. (2010) compare the ability to resolve shear flow instabilities of different hydro codes (SPH: VINE and the Price 08 code, AMR: FLASH and PLUTO), and find that the artificial viscosity in SPH codes has the largest influence on the growth of KH instabilities. The commonly used values for artificial viscosity in SPH- codes significantly suppress KH instabilities; the suppression is increased if there is a density contrast between the shearing fluids. The suppression of KH instabilities can be significantly reduced for same-density shear flows by using the Balsara 95 modification to the artificial viscosity prescription. Furthermore, the figures in their paper indicate that the KH instabilities in grid based codes are much smaller than in SPH codes. Thus I conclude that the RT instabilities are sufficiently resolved in these simulations that SNSPH is an accurate tool for studying the devel-

opment of RT instabilities in SN explosions. For the detailed small scale evolution of the RT fingers and clumps grid based codes are better suited.

5.4 Structure Characteristics

5.4.1 Power Spectrum Analysis

The primary aim in this work is to characterize the size distribution of clumps in the years following a supernova. In an effort to quantitatively describe the clump sizes, and in order to tell differences between the different runs, I calculated the power spectrum of the clumps sizes in each simulation.

The Fourier transform of a periodic signal in time decomposes that signal into its frequency components. Similarly, the Fourier transform of a periodic signal in space decomposes that signal into its wavenumber components. Thus, by treating the spatial data for the clumps as a signal that has a period equal to the size of the simulation, I can calculate the power spectrum of the wavenumbers of which it is composed and determine the corresponding wavelengths. The power spectrum versus wavelength will then show local maxima at the characteristic length scales (wavelengths) of the system, allowing us to infer typical sizes of clumps. The challenge is, since this method will pick up both the clumps as well as the spaces in between, to separate out the length scales of interest to us. Using the cross sectional data slices for the simulations can facilitate this. A related approach (e.g. WTA analysis, see Lopez et al. 2009b) has demonstrated its utility for interpreting observational data.

The Fourier transforms were calculated in IDL (Interactive Data Language) with the built-in `FFT` function. Since the RT fingers created overdense regions with a steep density gradient at the clump boundaries that makes them well defined, a density threshold was used to select that region. Although this brings with it the risk that the eventual size scales of these fingers are dependent on the density

threshold chosen to select them, the density gradient is steep enough that I find this to introduce only small errors. Minor changes in the density threshold do not significantly affect the size of the chosen region. The density threshold was set high enough that most of the web-structure and filaments were avoided. However, for comparison I also analyzed one case with the filaments included (figure D.43).

The Fourier transforms were taken by compressing slices of data through the 3D simulations to 2-dimensional images of 4096×4096 pixels. The size of these image arrays was mainly determined by the largest 2D array that IDL would process. The 'sampling rate' of the pixels must be chosen such that the Nyquist critical frequency (f_{Ny}) resolves the small scales I am interested in. Furthermore, my interest is in the short wavelength, large wavenumber regime, which is notorious for containing the noise in the transform. Furthermore, I have to be wary of any aliasing which may occur. Although IDL calculates the Fourier coefficients up to $\pm f_{Ny}$, frequencies higher than that may still be folded into the frequencies below the Nyquist frequency. However, the power approaches zero at the largest wavelengths in all the fourier transformed data, therefore it is likely that strong aliasing is not an issue.

In an effort to reduce edge effects and aliasing in the Fourier transforms, the image was set to correspond to a physical size on a side equal to $8\times$ the radius of the simulation at the given time snapshot. Thus, the sampling frequency was determined by the distance between two array elements/pixels, $\Delta = 1px = 8 \times \mathrm{R0}/N$, where N is the size of the image array in each dimension (4096) and R0 is the radius of the simulation as given by SNSPH. Thus, the Nyquist critical frequency is $f_{Ny} = \frac{1}{2\Delta} = N/(16 \times \mathrm{R0}) = 2^8/\mathrm{R0}$. The smallest length scale that can be resolved then is $0.0004\times$R0. I am expecting the typical sizes of the clumps on the order of 1% of the radius of the remnant, therefore I deem that resolution as sufficient.

For a clearer representation of the clumps, I transformed slices of the 3D simulations into a 2D image. This way, it is possible to almost completely avoid clumps close to a given line-of-sight being artificially merged together into one bigger clump in the conversion to the 2D image. When filling out the array, care needed to be taken to account for the non-zero size of the SPH particles. It was noted that some clumps contained artificial small gaps or holes. I deemed the gaps as artificial since they arose from SPH particles that did not make the cut into a slice, but nevertheless had a density contribution to it. I opted against using a smoothing algorithm to smooth out those features, as that would have introduced too much artificial noise into the data (and thus the transforms). Finally, the density in the clumps was set to 1 for this purpose to minimize the noise on pixel-to-pixel scale, and the pixels not containing part of a clump were set to zero. Each dimension (x,y,z) was divided into 30 slices, and the central slices were used to compute the Fourier transforms. For the symmetric runs, slices in only one plane were used; for the asymmetric runs, slices parallel and perpendicular to the asymmetry were used.

The power spectrum was computed for each transform by computing the sum squared amplitude at each pixel, $P_{ij} = |\mathscr{F}_{ij}|^2$, where P_{ij} is the power and $\mathscr{F}_{ij}$ is the (complex) value of the Fourier transform in the pixel of row i, column j. Before the calculation of the power, the computed FFT coefficients were normalized to set the zero frequency component to 1. The 2D power spectrum plots were then summed azimuthally (i.e. were binned into concentric annuli centered on the center of the 2D FFT array, and the values of the power in each annulus was summed, and plotted versus its corresponding wavelength). This improves the signal to noise at small wavelengths and provides an estimate of size scales for the entire remnant.

Figures D.40– D.61 show the results of the Fourier transforms of the slices through the simulations. The upper left and right panels in each figure shows the 2D

image and the 2D power spectrum of the data versus wavenumber, both expanded around the origin to show detail. The second panel shows the summed power spectrum vs. wavelength over all length scales, and the third panel shows an expanded view of the power spectrum at small length scales. In each figure, the number of SPH particles considered in the Fourier analysis is indicated.

All plots show significant power at the short/shortest length scales, indicating the presence of small scale structure. In all simulations, the size scale for the shortest wavelengths indicated in all power spectrum plots is at $\sim 3\%$ to $\sim 16\%$ of the size (radius) of the remnant. While all runs show structure down to that smallest value, the higher end of that range tended to be populated by those runs that showed contribution from the filaments or stems to the clumps in the FFT plots. All FFT plots also show significant power at a length scale of $50-60\%$ of the respective remnant size, which corresponds to the diameter of the shell of clumps created by the fluid instabilities.

Figures D.40, D.41, and D.42 show the FFT results for the canonical 1M, the 10M, and the 50M runs. All show a trough at $\sim 1.8 \times 10^3$ $R_\odot$ and a broad, shallow peak for length scales greater than that, and a number of narrow, tall peaks for length scales smaller than that. The broad peak at the largest wavelengths correlates with the size of the whole RT structure complex in the remnants. While the broad peak is very similar in each, there are differences in the narrow peaks in each simulation. The expanded views (panels 3) in each figure show that the canonical 1M run has a somewhat well defined peak centered at roughly 110 $R_\odot$, while the 10M run shows a series of peaks (almost oscillations) with the first local maximum at $\sim$40 $R_\odot$, and 50M run also shows a peak between 0 $R_\odot$ – 200 $R_\odot$ that is roughly Poisson-shaped and has a local maximum at $\sim$40 $R_\odot$. It looks similar to the 1M run, but is much better defined and does not ”trail out” like the one in the 1M run. All three runs

show another peak/ double peak centered at a length scale of $\sim 1 \times 10^3$ $R_\odot$, which seems to correlate to the inner diameter of the RT clump structure.

The zoomed-in panel of the FFT decomposition of the canonical run shows the peak(s) at the smallest wavelengths in detail. The maximum at 110 $R_\odot$ mentioned above is associated with a somewhat well defined broader peak between 50 $R_\odot$ and 150 $R_\odot$, followed by another fairly well defined peak at slightly below 200 $R_\odot$. Comparison with the slice through the original data suggests that the first peak (between 50 $R_\odot$ – 200 $R_\odot$) mostly corresponds to the density clumps, whereas the peaks following it likely corresponds mostly to the space in between those clumps.

Applying this comparison to the 10M_burn run is more difficult, since the space between clumps is closer to the size of the clumps there. Thus, the series of peaks for wavelengths greater than $\sim$ 100 $R_\odot$ likely is dominated by the length scales between two clumps, however, the length scales smaller than that, especially the peak at 40 $R_\odot$, likely indicates size scales for the clumps themselves.

For the 50M_burn run a similar situation is encountered, although here it can be more convincingly argued that the first maximum at 40 $R_\odot$ corresponds to the dominant size scale of the clumps. However, it is also true that using just a density threshold for selecting the clumps is less accurate than in the lower resolution runs for two reasons. The density contrast between the clumps and the filaments is less pronounced, and the RT fingers are more non-linear in this run (e.g. more bending and interacting is observed, as well as RT filaments growing out of the mushroom top of others). Thus, choosing a threshold high enough that only clumps are apparent only selects part of the RT clumps (i.e. the mushrooms caps). Lowering the threshold also selects most of the RT filaments (mushroom stems).

When the filaments are added into the FFT analysis, two main differences can be seen at small length scales. The first is that with the filaments, the broad peak at 0-200 $R_\odot$ is much flatter, and has a narrow peak at $\sim$ 100 $R_\odot$ superposed on it. This peak seems to correlate with the typical spacing between the RT fingers. As the size of the clumps is very similar to the 10M_burn run, one would expect there to be a corresponding feature in the FFT decomposition, and indeed, small peaks at $\sim$ 40 $R_\odot$, $\sim$ 60 $R_\odot$, and $\sim$ 70 $R_\odot$ can be discerned (and actually, one finds in the data image that there are some clumps with approximately ellipsoidal cross sections, suggesting an oblate or prolate shape for some clumps). The second difference is that the peak between 450-650 $R_\odot$ is much higher, higher in fact than the one at 0-200 $R_\odot$. This peak, as well as the smaller one just inside of it (at $\sim$ 370 $R_\odot$) probably corresponds to the typical lengths of the filaments.

Comparing the FFT power spectra of the other runs to their respective data "images" in the same spirit, much of the same features are found. Comparing the Fourier transformed data of the 1M_no–burn run at each of three time snapshots shows that over time the maximum at small wavelengths that indicates the typical clump size becomes more apparent over time. This is because as the RT fingers grow, the density contrast between the mushroom caps constituting the RT clumps and the ambient gas increases. Thus, using a density threshold to select the overdense RT clumps is more accurate for the later times. While the RT fingers expand homologously and at the same rate with the rest of the remnant after a few days, they do not diffuse.

The power spectra of the run where the number of neighbors was varied also show very similar features. The peak at smallest wavelengths is composed of a series of peaks of very similar amplitude though; there is not any one peak that "sticks out" above the others (very similar to the FFT spectrum of the 10M_burn

run). This is more noticeable in the power spectrum for run 1M_burn_70nbrs, for which the data image shows clumps distributed in a narrow ring, resembling the fact that all RT fingers grew to approximately the same length. However, it is noted that the clump size in the data slices seems somewhat smaller than in the other 1 million particle runs; a corresponding feature can be seen in the respective power spectra as a small peak at $\sim 60\ R_\odot$. This value is similar to what is found for the 10M and 50M runs. All of these runs (1M_burn_38nbrs, 1M_burn_70nbrs, 10M_burn, 50M_burn) have a different initial conditions setup for particle distribution than the other 1M runs (all asymmetric 1M runs were based on 1M_burn). Any similarities I see in the small scale power spectrum are not artifacts of the problem setup.

The power spectra of the bipolar explosions, shown in figures D.50 – D.53) show some differences to the symmetric runs discussed above. The most obvious difference is a peak, constituting the global maximum in each plot, at $\sim 3 - 9 \times 10^5\ R_\odot$, which itself features 3 spikes. At short wavelengths, the distribution of the structure is also different from the symmetric runs. Each of the bipolar runs show a series of distinct peaks out to $\sim 7.5 \times 10^4\ R_\odot$, though the exact placement and shape of those peaks differ slightly among the bipolar runs. The three to four prominent peaks in the power spectra in that range likely mostly corresponds to the added spacings between the ring of clumps and those inside of it, and the ring of clumps and the RT clumps outside of it. The power at wavelengths shorter than that range is likely still determined by the typical sizes of the clumps (RT and otherwise). Overall, the main difference between the plots parallel and perpendicular to the polar axis is that those for the parallel case show a little less power at the shortest wavelengths. As the asymmetry is not very pronounced, it is probably reasonable that there is no major difference. It should be noted that in these simulations the Ni-bubble is clearly discernible in the data images, causing the different distributions

of 'power' at small length scales. The power in structures at these intermediate scales completely swamps any signal from the $\sim$100 $R_\odot$ individual clump scale in the symmetric simulations.

The two late "jet4" scenarios (run 1M_burn_jet4L and 1M_burn_jet4LL) in the following plots (figures D.54 – D.57) also show the 3-spiked peak at large wave lengths, but shifted inward to $0.1 - 1.5 \times 10^5$ $R_\odot$ as these simulations were followed to only 0.1 yrs after the explosion. The distribution at short length scales is again in several narrow distinct peaks, similar to the 'early' bipolar asymmetries discussed above. It should be noted that in the run 1M_burn_jet4LL the density contrast between the RT clumps and the ambient gas (including the filaments) was not very large, thus the density threshold necessary to select mostly complete clumps again selected most of the RT filaments as well. Thus the Fourier transformed data is dominated by those features (between $1.5 - 3.5 \times 10^4$ $R_\odot$), and most of the power that is present at smallest length scales is likely due to the small spaces between the RT features.

Finally, the single-lobe asymmetries show similarities to the bipolar scenarios. This is not too surprising, since, to first order, the main difference between those is the number of lobes in the asymmetry, and secondly, the dominant feature at this point in each of those simulations is the shell of clumps generated by the Ni-bubble.

5.5 Conclusion

It is well established that instabilities readily arise in supernova simulations, and grow to form distinct structures. Differences appear between groups, and between different simulations from a single group. The behavior is affected by the choice of progenitor model, how the explosion is handled, the presence of initial perturbations, resolution, and dimensionality. I perform simulations of ex-

plosions of a 15 $M_{\odot}$ progenitor to determine the behavior of this code when producing instability-related small scale structures (as opposed to global asymmetries) and comparing it to previous work. I also develop a power spectrum formalism for quantifying the size scales of structures in the explosion. Both of these topics are groundwork for extending these simulations to the supernova remnant phase, including adding new physics such as x-ray cooling. The final goal of this work is to identify the origin of structures observed in young supernova remnants and predict their properties over the evolution of the SNR.

Rayleigh-Taylor instabilities are effective at creating numerous clumps of predominantly He, C, and O in these simulations of supernova explosions. These clumps form at the terminal ends of RT spikes developing in the explosion, and are initially at least one order of magnitude denser than the SN ejecta they grow into. Their size scales range from $\sim 1\%$–$\sim 8\%$ of the size (diameter) of the remnant, which is about 1-2 orders of magnitude bigger than the x-ray ejecta knots found in Cas A. Their size relative to the remnant is around $\sim 0.1 - 0.01\%$. Therefore, the RT clumps probably are not the ejecta knots, but they may well be related, possibly evolving into them as the remnant ages and cooling fragments the clumps.

I have considered the feasibility of RT mode that is set up in each run in various aspects, and concluded that the mode of the instability is likely approximately resolved in the 50 million particle run, and just under-resolved in the 1 and 10 million particle runs. I found that the size of the RT clumps decreases when increasing the resolution to 10M, but stays approximately the same increasing the resolution further to 50M. I determined that the occurrence of the instability is due to physical processes, rather than numerical artifacts, and thus find SNSPH a useful and suitable tool for the study of formation and further evolution of small scale structure in the explosion of SNe. I am aware, however, of the limitations of stan-

dard SPH formulations to resolve KH instabilities, which become important in the non-linear growth phase of the RT plumes. Improvements to SPH codes in the form of additional correction terms have been published and verified in the literature (e.g. Balsara 1995; Price 2008), which I intend to implement and test as a next step in this endeavor.

Plumes form at the OC/He interface in these simulations, as most other groups have found also. I see RT fingers forming at only one interface, not two or three, although the evolution of the velocity profile suggests that other interfaces briefly enter an instability. As in Kifonidis et al. (2003), I see a dense shell of He-rich material piling up as the shock enters the H-envelope, however in these simulations this pile-up of material results in RT instabilities, and not in a "wall" confining the RT plumes inside of it.

In the absence of a surrounding medium that would eventually interact with the ejecta, the RT filaments and clumps are permanent features. these simulations show that the clumps detach from the ends of the filaments. At the point in its evolution when the ejecta gas has expanded into the optically thin regime, it can efficiently cool by radiation from electronic transitions. This cooling should contribute further to the condensation and fragmentation of the clumps into sub-clumps as the clumps depart from pressure equilibrium with the surrounding medium. Inclusion of a mass loss-generated circumstellar environment or ISM in the calculations is not expected to destroy the clumps, but it will have a significant effect on them. As the SN gas expands, it sweeps up surrounding material, eventually creating a dense shell with which it will interact at some point. A reverse shock that arises eventually from this interaction travels back through the ejecta, and will compress and heat the RT clumps. Rapid cooling should result in fragmentation and increased density in the clumps. and shocks probably shred them into smaller pieces. This

process can be seen acting on optical ejecta knots in Cas A in multiple epochs of *HST* observation.

Dense bullets are also observed in some scenarios in the regions interior to of the RT fingers. ^{56}Ni produced in the explosion is abundant in this central region, which, if it does not fall back onto the central compact object, it heats through its decay to Co and Fe. Thus, the Ni-rich region expands and compresses the regions without (much) Ni. O, He, and H, which has been mixed down into the Ni region, is compressed into dense clumps, which in all simulations in which they occur end up slightly exceeding the density in the RT clumps. No significant Ni-bubble was observed in the CCO runs since a majority of the Ni that was produced fell back onto the compact remnant.

Neither of these clumps appear to contain much Fe-group material. ^{44}Ti, closely following the distribution of ^{56}Ni, is in the part of the Ni-bubble that expands, and does not become mixed into the bullets/clumps in that region. Artificial asymmetries can mix some Fe- group elements closer to the RT fingers, but not significantly into the RT flow. Only in the most extreme imposed asymmetry (the 1M_jet4LL scenario) and fallback– induced convection (runs 1M_burn_CCO and -CCO2) are the RT fingers affected by the asymmetry. In the 1M_jet4LL scenario, RT fingers are significantly elongated along the polar axis, while they are nearly absent at the equator. In the two runs including the central compact object the central convection imparts a global, low mode asymmetry on the remnant after the RT fingers have formed, and mostly affects the central distribution of elements. In general, though, the formation of RT instabilities seems to be quite insensitive to the mode of any global asymmetry.

I find that these explosion simulations produce instability-related structures qualitatively similar to those found by other groups. These simulations are suitable

precursors to further calculation of SNR evolution with cooling and CSM interaction. I can create quantitative predictions of the distribution of sizes of over dense structures in the remnant which are suitable for with similar analyses of observations.

Chapter 6

CONCLUDING REMARKS

In Chapter 4 we established that either bulk SN material or material that was explosively processed in the C/Ne shell or sub-explosively processed in the C- layer is consistent with a SN enrichment scenario of the forming solar system. In the 15 $M_\odot$ star in Chapter 5 the inner 3.1 $M_\odot$ of the ejecta experience explosive burning conditions. The total ^{26}Al produced in the explosive nucleosynthesis is 1.23×10^{-6} $M_\odot$. Using an injection fraction of $f = 10^{-6} \times 9.0/3.1$ (the factor $9.0/3.1$ arises from injecting only the inner 3.1 $M_\odot$, and not all of the ejecta) and a time delay of $\Delta t = 1$ Myr (see Chapter 2) to calculate the amount injected gives $\sim 1.3 \times 10^{-11}$. This is approximately an order of magnitude less than needed for the above parameters of the injection scenario, however may still be approximately consistent, especially if the time delay is less (~ 0.1 Myr).

If it is supposed that, as advocated in, e.g., Ouellette et al. (2010), it is material from an overdense feature like an RT clump that is responsible for delivering SN material to and into the forming solar system, then the explosively processed material is not the appropriate part of the SN to consider. Chapter 5 showed that it is mainly the material from the hydrostatic He and C layers that is subject to RT instabilities. These layers are only minimally processed by explosive nucleosynthesis, if at all. It is interesting to note that the ^{26}Al produced hydrostatically during the star's lifetime reaches the highest abundance at the bottom of the H-layer (He-rich shell), while the abundances of ^{41}Ca, ^{53}Mn, and ^{60}Fe drop to zero there. Thus the RT instabilities seem to bring about mixing between these two regions, creating favorable conditions for injection of this material into a forming solar system. Studying the evolution of the RT clumps (e.g. dust condensation, SN reverse-shock interaction) would be a promising future endeavor.

The typical distance of a proto–planetary disk from a massive star/SN seems to be around $0.1 - 2.0$pc (e.g. Hester et al. 1996). Taking the average speed of SN ejecta to be 4000 Km/s (=4000 pc/Myr), it would take the ejecta about 25-500 yrs to reach such proto–planetary disks. Dust is observed to form in the ejecta in the first 2 years of a SN explosion (e.g. Kozasa et al. 1989; Moseley et al. 1989). Recent Herschel data of SN1987A suggests that copious amounts of dust can potentially be found in SNRs as young as ~ 24 yrs (Matsuura et al. 2011), i.e. in the parts of the ejecta not yet traversed by the reverse shock. Therefore, SN dust is likely present at the time the SN debris reaches a proto–planetary system. It is assumed that the ejecta are incident on a proto–planetary disk before interactions with swept-up material becomes important. As estimated in Section 5.2.4, interactions of the ejecta with the surrounding material will become important once it has reached a radius of order of a few parsec i.e. further away that typical distances of proto–planetary disks. The HII regions around massive stars usually do not contain enough mass to significantly interact with the SN ejecta (unless the massive star lost a significant part of its mass in a wind before the explosion). This suggests that the supernova enrichment of the early solar system took place via interaction with one of the RT clumps.

Although a definite link between ejecta knots (a la Cas A) and fluid instabilities arising during the explosion of SNe has not been established, a somewhat clear picture is slowly emerging. It has been well demonstrated in this and other works that large scale fluid instabilities do arise, and lead to clumping of large parts of the mantle in an exploding massive star. It is also well established that dense ejecta knots exist in young SNR, which seem to be quite long-lived features (as they are seen in Cas A, a SNR of age 340 yrs, e.g. Hammell and Fesen (2008); and Puppis

A, at an age of $\sim$ 4000 yrs, e.g. Katsuda et al. (2008)). Eventually, though, they are expected to diffuse into the local ISM.

It is probable that the RT clumps found to arise from the propagation of the SN shock wave do not directly correspond to the ejecta knots of the type seen in Cas A. The Cas A ejecta knots are at least 1-2 orders of magnitude smaller, are observed at or ahead of the main SN shock wave, and are overdense with respect to the ambient gas by 2-4 orders of magnitude (e.g. Fesen et al. 2011). The RT clumps of this study remain behind the blast wave, and are overdense by 1-2 orders of magnitude (somewhat resolution dependent) at $\sim$ 22 hrs, and slightly less than a factor of 10 at $\sim$ 30 yrs. Furthermore, there are a few small groupings of ejecta knots in Cas A that may be the result of the fragmentation of much larger knots (Fesen et al. 2011). It is likely that the RT clumps found in chapter 5 are altered by interactions with reverse shocks and ISM, but not initially/rapidly destroyed. These interactions are expected to further fragment the RT clumps, possibly creating Cas A- like ejecta knots (numerical models of, e.g., Wang and Chevalier (2002) suggest this). It is conceivable that this would lead to increased densities in the clumps (perhaps through shock compression and/or efficient cooling). Also noteworthy is that the passage of the reverse shock heats the material it traverses to ionizing temperatures (above $\sim 10^6$K), which should evaporate most to all of the dust present there. Low opacities should allow for efficient cooling, which could lead to re-condensation of dust. The general feeling on dust in slightly older SNRs like Cas A and older is that there is not much dust present (only a small fraction of a $M_\odot$). Emission of ejecta dust has been associated with the FMK's in Cas A, i.e. with regions in the ejecta already traversed by the reverse shock. While it is entirely possible that the majority of the dust in those remnants is still undetected (see, e.g. the discussion in Ouellette et al. (2010)), there is also the other option, namely that

only small quantities of dust are present at these times. If this is the case, a straightforward explanation might be that the dust has been destroyed by the passage of the reverse shock and subsequent extended heating, and only a small amount survived or re-condensed.

Much more further work is required to answer the questions posed above. Simulations of the remnant expansion of the runs presented in Chapter 5 to follow the interaction with a surrounding ISM are planned for the future to shed light on the further evolution of the RT clumps. Following the evolution of the simulations out to times equivalent to the physical ages of actual SNRs is planned to facilitate comparisons to young SNRs. Repeating these simulations with different progenitors will help in generalizing the properties of structure from RT instabilities to a broader range of SNe, as well as give the opportunity of comparing those to observations of SNe from different.

REFERENCES

Agertz, O., Moore, B., Stadel, J., Potter, D., Miniati, F., Read, J., Mayer, L., Gawryszczak, A., Kravtsov, A., Nordlund, Å., Pearce, F., Quilis, V., Rudd, D., Springel, V., Stone, J., Tasker, E., Teyssier, R., Wadsley, J., and Walder, R.: 2007, *MNRAS,* **380**, 963

Amelin, Y., Krot, A. N., Hutcheon, I. D., and Ulyanov, A. A.: 2002, *Science* **297**, 1678

Arnett, D.: 1996, *Supernovae and Nucleosynthesis*

Arnett, D., Fryxell, B., and Müller, E.: 1989, *ApJL,* **341**, L63

Arnett, D., Meakin, C., and Young, P. A.: 2009, *ApJ,* **690**, 1715

Arnett, W. D. and Meakin, C.: 2011, *ApJ,* **733**, 78

Balsara, D. S.: 1995, *Journal of Computational Physics* **121**, 357

Bazan, G. and Arnett, D.: 1998, *ApJ,* **496**, 316

Benz, W.: 1990, in J. R. Buchler (ed.), *Numerical Modelling of Nonlinear Stellar Pulsations Problems and Prospects*, pp 269–+

Benz, W., Thielemann, F.-K., and Hills, J. G.: 1989, *ApJ,* **342**, 986

Bloecker, T.: 1995, *A&A,* **297**, 727

Blondin, J. M. and Mezzacappa, A.: 2006, *ApJ,* **642**, 401

Blondin, J. M., Mezzacappa, A., and DeMarino, C.: 2003, *ApJ,* **584**, 971

Bouvier, A. and Wadhwa, M.: 2009, in *Lunar and Planetary Institute Science Conference Abstracts*, Vol. 40 of *Lunar and Planetary Inst. Technical Report*, pp 2184–+

Buras, R., Rampp, M., Janka, H.-T., and Kifonidis, K.: 2003, *Physical Review Letters* **90(24)**, 241101

Burnett, D. S., Barraclough, B. L., Bennett, R., Neugebauer, M., Oldham, L. P., Sasaki, C. N., Sevilla, D., Smith, N., Stansbery, E., Sweetnam, D., and Wiens, R. C.: 2003, *SSR,* **105**, 509

Burrows, A., Hayes, J., and Fryxell, B. A.: 1995, *ApJ,* **450**, 830

Burrows, A., Livne, E., Dessart, L., Ott, C. D., and Murphy, J.: 2006, *ApJ,* **640**, 878

Chandrasekhar, S.: 1961, *Hydrodynamic and hydromagnetic stability*

Clayton, R. N.: 2003, *Treatise on Geochemistry* **1**, 129

Clayton, R. N., Grossman, L., and Mayeda, T. K.: 1973, *Science* **182**, 485

Clayton, R. N. and Mayeda, T. K.: 1984, *Earth and Planetary Science Letters* **67**, 151

Cyburt, R. H., Amthor, A. M., Ferguson, R., Meisel, Z., Smith, K., Warren, S., Heger, A., Hoffman, R. D., Rauscher, T., Sakharuk, A., Schatz, H., Thielemann, F. K., and Wiescher, M.: 2010, *The Astrophysical Journal Supplement Series* **189(1)**, 240

DeLaney, T., Rudnick, L., Stage, M. D., Smith, J. D., Isensee, K., Rho, J., Allen, G. E., Gomez, H., Kozasa, T., Reach, W. T., Davis, J. E., and Houck, J. C.: 2010, *ApJ,* **725**, 2038

Diehl, R., Lang, M., Kretschmer, K., and Wang, W.: 2008, *New Astron. Rev.,* **52**, 440

Ebel, D. S. and Grossman, L.: 2000, *Geo. Co. A.,* **64**, 339

Ellinger, C. I., Young, P. A., and Desch, S. J.: 2010, *ApJ,* **725**, 1495

Elser, J. J.: 2003, *Ecology Letters* **10**, 1135

Erickson, E. F., Haas, M. R., Colgan, S. W. J., Lord, S. D., Burton, M. G., Wolf, J., Hollenbach, D. J., and Werner, M.: 1988, *ApJL,* **330**, L39

Fahey, A. J., Goswami, J. N., McKeegan, K. D., and Zinner, E.: 1987, *Geo. Co. A.,* **51**, 329

Fesen, R. A.: 2001, *ApJS,* **133**, 161

Fesen, R. A., Zastrow, J. A., Hammell, M. C., Shull, J. M., and Silvia, D. W.: 2011, *ArXiv e-prints*

Fryer, C., Benz, W., Herant, M., and Colgate, S. A.: 1999, *ApJ,* **516**, 892

Fryer, C., Burrows, A., and Benz, W.: 1998, *ApJ,* **496**, 333

Fryer, C., Young, P., Bennet, M. E., Diehl, S., Herwig, F., Hirschi, R., Hungerford, A., Pignatari, M., Magkotsios, G., Rockefeller, G., and Timmes, F. X.: 2008, in *Nuclei in the Cosmos (NIC X)*

Fryer, C. L.: 1999, *ApJ,* **522**, 413

Fryer, C. L., Hungerford, A. L., and Rockefeller, G.: 2007a, *International Journal of Modern Physics D* **16**, 941

Fryer, C. L., Mazzali, P. A., Prochaska, J., Cappellaro, E., Panaitescu, A., Berger, E., van Putten, M., van den Heuvel, E. P. J., Young, P., Hungerford, A., Rockefeller, G., Yoon, S.-C., Podsiadlowski, P., Nomoto, K., Chevalier, R., Schmidt, B., and Kulkarni, S.: 2007b, *PASP,* **119**, 1211

Fryer, C. L., Rockefeller, G., and Warren, M. S.: 2006, *ApJ,* **643**, 292

Fryer, C. L. and Warren, M. S.: 2002, *ApJL,* **574**, L65

Fryer, C. L. and Warren, M. S.: 2004, *ApJ,* **601**, 391

Fryer, C. L. and Young, P. A.: 2007, *ApJ,* **659**, 1438

Fryxell, B., Arnett, D., and Müller, E.: 1991, *ApJ,* **367**, 619

Gerardy, C. L. and Fesen, R. A.: 2001, *AJ,* **121**, 2781

Görres, J., Arlandini, C., Giesen, U., Heil, M., Käppeler, F., Leiste, H., Stech, E., and Wiescher, M.: 2000, *Physical Review Letters C,* **62(5)**, 055801

Gounelle, M., Krot, A. N., Nagashima, K., and Kearsley, A.: 2009, *ApJL,* **698**, L18

Gounelle, M. and Meibom, A.: 2007, *ApJL,* **664**, L123

Graboske, H. C., Dewitt, H. E., Grossman, A. S., and Cooper, M. S.: 1973, *ApJ,* **181**, 457

Grevesse, N., Asplund, M., and Sauval, A. J.: 2007, *SSR,* **130**, 105

Grevesse, N. and Sauval, A. J.: 1998, *SSR,* **85**, 161

Grossman, L.: 1972, *Geo. Co. A.,* **36**, 597

Hachisu, I., Matsuda, T., Nomoto, K., and Shigeyama, T.: 1991, *ApJL,* **368**, L27

Hachisu, I., Matsuda, T., Nomoto, K., and Shigeyama, T.: 1992, *ApJ,* **390**, 230

Hammell, M. C. and Fesen, R. A.: 2008, *ApJS,* **179**, 195

Hammer, N. J., Janka, H., and Müller, E.: 2010, *ApJ,* **714**, 1371

Herant, M.: 1995, *Phys. Rep.* **256**, 117

Herant, M. and Benz, W.: 1991, *ApJL,* **370**, L81

Herant, M. and Benz, W.: 1992, *ApJ,* **387**, 294

Herant, M., Benz, W., and Colgate, S.: 1992, *ApJ,* **395**, 642

Herant, M., Benz, W., Hix, W. R., Fryer, C. L., and Colgate, S. A.: 1994, *ApJ,* **435**, 339

Hester, J. J., Desch, S. J., Healy, K. R., and Leshin, L. A.: 2004, *Science* **304**, 1116

Hester, J. J., Scowen, P. A., Sankrit, R., Lauer, T. R., Ajhar, E. A., Baum, W. A., Code, A., Currie, D. G., Danielson, G. E., Ewald, S. P., Faber, S. M., Grillmair, C. J., Groth, E. J., Holtzman, J. A., Hunter, D. A., Kristian, J., Light, R. M., Lynds, C. R., Monet, D. G., O'Neil, Jr., E. J., Shaya, E. J., Seidelmann, K. P., and Westphal, J. A.: 1996, *AJ,* **111**, 2349

Hoeflich, P.: 1988, *Proceedings of the Astronomical Society of Australia* **7**, 434

Hungerford, A. L., Fryer, C. L., and Rockefeller, G.: 2005a, *ApJ,* **635**, 487

Hungerford, A. L., Fryer, C. L., Timmes, F. X., and McGhee, K.: 2005b, *Nuclear Physics A* **758**, 15

Hungerford, A. L., Fryer, C. L., and Warren, M. S.: 2003, *ApJ,* **594**, 390

Hwang, U. and Laming, J. M.: 2003, *ApJ,* **597**, 362

Hwang, U., Laming, J. M., Badenes, C., Berendse, F., Blondin, J., Cioffi, D., DeLaney, T., Dewey, D., Fesen, R., Flanagan, K. A., Fryer, C. L., Ghavamian, P., Hughes, J. P., Morse, J. A., Plucinsky, P. P., Petre, R., Pohl, M., Rudnick, L., Sankrit, R., Slane, P. O., Smith, R. K., Vink, J., and Warren, J. S.: 2004, *ApJL,* **615**, L117

Itoh, S., Kojima, H., and Yurimoto, H.: 2004, *Geo. Co. A.,* **68**, 183

Jacobsen, B., Matzel, J., Hutcheon, I. D., Krot, A. N., Yin, Q.-Z., Nagashima, K., Ramon, E. C., Weber, P. K., Ishii, H. A., and Ciesla, F. J.: 2011, *ApJL,* **731**, L28+

Joggerst, C. C., Almgren, A., Bell, J., Heger, A., Whalen, D., and Woosley, S. E.: 2010a, *ApJ,* **709**, 11

Joggerst, C. C., Almgren, A., and Woosley, S. E.: 2010b, *ApJ,* **723**, 353

Joggerst, C. C., Heger, A., and Woosley, S. E.: 2008, in B. W. O'Shea & A. Heger (ed.), *First Stars III*, Vol. 990 of *American Institute of Physics Conference Series*, pp 257–259

Joggerst, C. C., Woosley, S. E., and Heger, A.: 2009, *ApJ,* **693**, 1780

Junk, V., Walch, S., Heitsch, F., Burkert, A., Wetzstein, M., Schartmann, M., and Price, D.: 2010, *MNRAS,* **407**, 1933

Kane, J., Arnett, D., Remington, B. A., Glendinning, S. G., Bazán, G., Müller, E., Fryxell, B. A., and Teyssier, R.: 2000, *ApJ,* **528**, 989

Katsuda, S., Mori, K., Tsunemi, H., Park, S., Hwang, U., Burrows, D. N., Hughes, J. P., and Slane, P. O.: 2008, *ApJ,* **678**, 297

Kifonidis, K., Plewa, T., Janka, H., and Müller, E.: 2003, *A&A,* **408**, 621

Kifonidis, K., Plewa, T., Scheck, L., Janka, H.-T., and Müller, E.: 2006, *A&A,* **453**, 661

Kita, N. T., Huss, G. R., Tachibana, S., Amelin, Y., Nyquist, L. E., and Hutcheon, I. D.: 2005, in A. N. Krot, E. R. D. Scott, & B. Reipurth (ed.), *Chondrites and the Protoplanetary Disk*, Vol. 341 of *Astronomical Society of the Pacific Conference Series*, pp 558–+

Kobayashi, S., Imai, H., and Yurimoto, H.: 2003, in S. Mackwell & E. Stansbery (ed.), *Lunar and Planetary Institute Science Conference Abstracts*, Vol. 34 of *Lunar and Planetary Inst. Technical Report*, pp 1536–+

Kozasa, T., Hasegawa, H., and Nomoto, K.: 1989, *ApJ,* **344**, 325

Krot, A. N., Chaussidon, M., Yurimoto, H., Sakamoto, N., Nagashima, K., Hutcheon, I. D., and MacPherson, G. J.: 2008, *Geo. Co. A.,* **72**, 2534

Krot, A. N., Nagashima, K., Ciesla, F. J., Meyer, B. S., Hutcheon, I. D., Davis, A. M., Huss, G. R., and Scott, E. R. D.: 2010, *ApJ,* **713**, 1159

Kudritzki, R. P., Pauldrach, A., Puls, J., and Abbott, D. C.: 1989, *A&A,* **219**, 205

Lamers, H. J. G. L. M. and Nugis, T.: 2002, *A&A,* **395**, L1

Langanke, K. and Martínez-Pinedo, G.: 2000, *Nuclear Physics A* **673**, 481

Lodders, K.: 2003, *ApJ,* **591**, 1220

Lopez, L. A., Ramirez-Ruiz, E., Badenes, C., Huppenkothen, D., Jeltema, T. E., and Pooley, D. A.: 2009a, *ApJL,* **706**, L106

Lopez, L. A., Ramirez-Ruiz, E., Pooley, D. A., and Jeltema, T. E.: 2009b, *ApJ,* **691**, 875

Lyons, J. R., Bergin, E. A., Ciesla, F. J., Davis, A. M., Desch, S. J., Hashizume, K., and Lee, J.-E.: 2009, *Geo. Co. A.,* **73**, 4998

Lyons, J. R. and Young, E. D.: 2005, *Nature,* **435**, 317

MacPherson, G. J., Davis, A. M., and Zinner, E. K.: 1995, *Meteoritics* **30**, 365

Makide, K., Nagashima, K., Krot, A. N., and Huss, G. R.: 2009a, *ApJ,* **706**, 142

Makide, K., Nagashima, K., Krot, A. N., Huss, G. R., Hutcheon, I. D., and Bischoff, A.: 2009b, *Geo. Co. A.,* **73**, 5018

Matsuura, M., Dwek, E., Meixner, M., Otsuka, M., Babler, B., Barlow, M. J., Roman-Duval, J., Engelbracht, C., Sandstrom, K., Lakicevic, M., van Loon, J. T., Sonneborn, G., Clayton, G. C., Long, K. S., Lundqvist, P., Nozawa, T., Gordon, K. D., Hony, S., Panuzzo, P., Okumura, K., Misselt, K. A., Montiel, E., and Sauvage, M.: 2011, *ArXiv e-prints*

McKeegan, K. D., Kallio, A., Heber, V. S., Jarzebinski, G., Mao, P., Coath, C., Kunihiro, T., Wiens, R. C., Judith, A., and Burnett, D. S.: 2010, *AGU Fall Meeting Abstracts* pp B2316+

McKeegan, K. D., Kallio, A. P., Heber, V., Jarzebinski, G., Mao, P. H., Coath, C. D., Kunihiro, T., Wiens, R., Allton, J., and Burnett, D. S.: 2009, in *Lunar and Planetary Institute Science Conference Abstracts*, Vol. 40 of *Lunar and Planetary Inst. Technical Report*, pp 2494–+

Meakin, C. A. and Arnett, D.: 2007a, *ApJ,* **665**, 690

Meakin, C. A. and Arnett, D.: 2007b, *ApJ,* **667**, 448

Messenger, S., Sandford, S., and Brownlee, D.: 2006, *The Population of Starting Materials Available for Solar System Construction*, pp 187–208

Mezzacappa, A., Calder, A. C., Bruenn, S. W., Blondin, J. M., Guidry, M. W., Strayer, M. R., and Umar, A. S.: 1998, *ApJ,* **493**, 848

Miller, M. F.: 2002, *Geo. Co. A.,* **66**, 1881

Monaghan, J. J.: 2005, *Reports on Progress in Physics* **68**, 1703

Moseley, S. H., Dwek, E., Glaccum, W., Graham, J. R., and Loewenstein, R. F.: 1989, *Nature,* **340**, 697

Müller, E., Fryxell, B., and Arnett, D.: 1991, *A&A,* **251**, 505

Müller, E., Hillebrandt, W., Orio, M., Hoflich, P., Monchmeyer, R., and Fryxell, B. A.: 1989, *A&A,* **220**, 167

Nagataki, S., Shimizu, T. M., and Sato, K.: 1998, *ApJ,* **495**, 413

Nichols, Jr., R. H., Podosek, F. A., Meyer, B. S., and Jennings, C. L.: 1999, *Meteoritics and Planetary Science* **34**, 869

Nordhaus, J., Brandt, T. D., Burrows, A., Livne, E., and Ott, C. D.: 2010, *Physical Review: D,* **82(10)**, 103016

Nuth, III, J. A., Charnley, S. B., and Johnson, N. M.: 2006, *Chemical Processes in the Interstellar Medium: Source of the Gas and Dust in the Primitive Solar Nebula*, pp 147–167

Ogliore, R. C., Huss, G. R., and Nagashima, K.: 2011, in *Lunar and Planetary Institute Science Conference Abstracts*, Vol. 42 of *Lunar and Planetary Institute Science Conference Abstracts*, pp 1592–+

Oneal, J. R.: 1986, *Rev. Mineral* **16**, 561

Ouellette, N., Desch, S. J., and Hester, J. J.: 2007, *ApJ,* **662**, 1268

Ouellette, N., Desch, S. J., and Hester, J. J.: 2010, *ApJ,* **711**, 597

Patnaude, D. J. and Fesen, R. A.: 2007, *AJ,* **133**, 147

Podosek, F. A. and Cassen, P.: 1994, *Meteoritics* **29**, 6

Price, D. J.: 2008, *Journal of Computational Physics* **227**, 10040

Rauscher, T., Heger, A., Hoffman, R. D., and Woosley, S. E.: 2002a, *ApJ,* **576**, 323

Rauscher, T., Heger, A., Hoffman, R. D., and Woosley, S. E.: 2002b, *ApJ,* **576**, 323

Rauscher, T. and Thielemann, F.-K.: 2001, *Atomic Data and Nuclear Data Tables* **79**, 47

Redfield, A. C.: 1958, *American Scientist* **46**, 205

Russell, S. S., Hartmann, L., Cuzzi, J., Krot, A. N., Gounelle, M., and Weidenschilling, S.: 2006, *Timescales of the Solar Protoplanetary Disk*, pp 233–251

Sahijpal, S. and Goswami, J. N.: 1998, *ApJL,* **509**, L137

Sakamoto, N., Seto, Y., Itoh, S., Kuramoto, K., Fujino, K., Nagashima, K., Krot, A. N., and Yurimoto, H.: 2007, *Meteoritics and Planetary Science Supplement* **42**, 5149

Scheck, L., Plewa, T., Janka, H.-T., Kifonidis, K., and Müller, E.: 2004, *Physical Review Letters* **92(1)**, 011103

Scott, E. R. D. and Krot, A. N.: 2001, *Meteoritics and Planetary Science* **36**, 1307

Shigeyama, T., Nomoto, K., and Hashimoto, M.: 1988, *A&A,* **196**, 141

Sterner, R. W. and Elser, J. J.: 2002, *Ecological Stoichiometry: The biology of elements from molecules to the biosphere*, Princeton University Press

Telus, M., Huss, G. R., Nagashima, K., Ogliore, R. C., Tachibana, S., and Jilly, C. E.: 2011, in *Lunar and Planetary Institute Science Conference Abstracts*, Vol. 42 of *Lunar and Planetary Institute Science Conference Abstracts*, pp 2559–+

Wadhwa, M., Amelin, Y., Davis, A. M., Lugmair, G. W., Meyer, B., Gounelle, M., and Desch, S. J.: 2007, *Protostars and Planets V* pp 835–848

Wang, C.-Y. and Chevalier, R. A.: 2002, *ApJ,* **574**, 155

Wang, L. and Wheeler, J. C.: 2008, *ARA&A,* **46**, 433

Willingale, R., Bleeker, J. A. M., van der Heyden, K. J., Kaastra, J. S., and Vink, J.: 2002, *A&A,* **381**, 1039

Witteborn, F. C., Bregman, J. D., Wooden, D. H., Pinto, P. A., Rank, D. M., Woosley, S. E., and Cohen, M.: 1989, *ApJL,* **338**, L9

Woosley, S. E.: 1988, *ApJ,* **330**, 218

Young, E. D. and Russell, S. S.: 1998, *Science* **282**, 452

Young, P. A. and Arnett, D.: 2005, *ApJ,* **618**, 908

Young, P. A., Ellinger, C. I., Arnett, D., Fryer, C. L., and Rockefeller, G.: 2009, *ApJ,* **699**, 938

Young, P. A. and Fryer, C. L.: 2007, *ApJ,* **664**, 1033

Young, P. A., Fryer, C. L., Hungerford, A., Arnett, D., Rockefeller, G., Timmes, F. X., Voit, B., Meakin, C., and Eriksen, K. A.: 2006, *ApJ,* **640**, 891

Young, P. A., Meakin, C., Arnett, D., and Fryer, C. L.: 2005, *ApJL,* **629**, L101

APPENDIX A

NUMERICAL METHOD

A.1 A Synopsis of SNSPH

For a detailed description of SNSPH, see Fryer et al. (2006). In the following, only main points of interest for this work (and myself) are paraphrased from that paper, and from review papers on smoothed particle hydrodynamics (SPH). There are many reviews on the SPH algorithm, the ones extensively used in this work are Benz (1990), and Monaghan (2005).

SNSPH is a parallelized, 3 dimensional SPH algorithm modeled on the algorithm developed Benz. SPH is a Lagrangian scheme to model the Euler equations, and is a second order accurate integration scheme. In the SPH formalism, the equations for conservation of momentum is,

$$\frac{d\vec{v}_i}{dt} = -\sum_{j=1}^{N} m_j \left(\frac{P_i}{\rho_i^2} + \frac{P_j}{\rho_j^2} + \Pi_{ij} \right) \vec{\nabla}_i W(|\vec{r}_i - \vec{r}_j|, h) \tag{A.1}$$

and for conservation of energy is,

$$\frac{du_i}{dt} = \sum_{j=1}^{N} m_j \left(\frac{P_i}{\rho_i^2} + \frac{1}{2}\Pi_{ij} \right) \left(\vec{v}_i - \vec{v}_j\right) \vec{\nabla}_i W(|\vec{r}_i - \vec{r}_j|, h) \tag{A.2}$$

These equations are solved to advance the system in time. Time stepping is adaptive, and is determined by using the CFL criterion

$$\frac{v_x \cdot \Delta t}{\Delta x} + \frac{v_y \cdot \Delta t}{\Delta y} + \frac{v_z \cdot \Delta t}{\Delta z} \leq C, \tag{A.3}$$

where all symbols have their usual meaning, and C is the Courant number.

An artificial viscosity term including both bulk ($\Pi_l = \alpha \rho l c_s \vec{\nabla} \cdot \vec{v}$) and von Neumann-Richtmyer viscosity ($\Pi_q = \beta \rho l^2 (\vec{\nabla} \cdot \vec{v})^2$),

$$\Pi_{ij} = \begin{cases} \frac{-\alpha c_{ij} \mu_{ij} + \beta \mu_{ij}^2}{\rho_{ij}}, & \text{if} (\vec{v}_i - \vec{v}_j) \cdot (\vec{r}_i - \vec{r}_j) \leq 0; \\ 0 & \text{otherwise,} \end{cases} \tag{A.4}$$

has been included to model shocks, where c_{ij} and ρ_{ij} are the geometric means of the sound speed and density, respectively, between two particles i and j, and

$$\mu_{ij} = \frac{h\,(\vec{v}_i - \vec{v}_j)\cdot(\vec{r}_i - \vec{r}_j)}{|\vec{r}_i - \vec{r}_j|^2 + \varepsilon h^2} \tag{A.5}$$

ε is an estimate of the velocity divergence in the viscosity terms. This viscosity term is zero for receding particles to ensure that heat dissipation due to this viscosity only adds entropy to the system. The values for the coefficients used in this study were $\alpha = 1.0$ and $\beta = 2.0$.

Although this formulation of the artificial viscosity has been shown to work well in practice, it generates a large entropy in pure shear flows. Shear flows are expected to occur at growing RT plumes, although they are probably not pure shear flows. Nevertheless, the artificial viscosity could potentially dampen out any but the largest KH eddies that might try to form on the "surface" of RT plumes, thus less small scale mixing and turbulence is expected to occur. Although Benz 89 mention that Balsara et al 89 suggested an additional term multiplying equation A.5

$$\frac{f_i + f_j}{2} \tag{A.6}$$

$$f_i = \frac{|\langle\vec{\nabla}\cdot\vec{v}\rangle_i|}{|\langle\vec{\nabla}\cdot\vec{v}\rangle_i| + |\langle\vec{\nabla}\times\vec{v}\rangle_i| + 0.00001 c_i/h} \tag{A.7}$$

so that the artificial viscosity vanishes in pure shear flows; however this term was not implemented in SNSPH.

Self gravity is added in the form of an additional term,

$$-\vec{\nabla}\phi_i = -G\sum_{j=1}^{N} \frac{M(|\vec{r}_i - \vec{r}_j|)}{|\vec{r}_i - \vec{r}_j|^2}\frac{(\vec{r}_i - \vec{r}_j)}{|\vec{r}_i - \vec{r}_j|} \tag{A.8}$$

that is added to the momentum conservation. Since gravity is a long-range force, in principle the acceleration of a particle j is influenced by the gravitational interaction with all other particles in the simulation. Calculating the force due to gravity thus requires $O(N^2)$ operations, which is computationally infeasible for all but the smallest problems. SNSPH uses a multipole approximation to approximate

the gravitational force of a group of distant enough particles on particle j. A multipole acceptability criterion (MAC) is used to determine when this approximation is accurate enough:

$$r_c \geq \frac{b_{\max}}{2} + \sqrt{\frac{b_{\max}^2}{4} + \sqrt{\frac{3B^2}{\Delta_{\text{int.}}}}} \tag{A.9}$$

Here, $b_{\max}$ is the size of the cell, $B_2 = \sum_i m_i |\vec{r}_i - \vec{r}_{\text{cm}}|^2$ is the trace of the quadrupole tensor, and $\Delta_{\text{int.}}$ is the limit on the (absolute) error allowed. Thus, for particles inside r_c, pairwise summation is used, for all other particles the multipole approximation is used. This results in $O(N \log N)$ operation for the gravitational force calculation.

The particle formulism requires the use of a kernel function to describe the particles. In principle, any kernel can be used, as long as it is normalized to 1 and reduces to a delta function (point particle) in the limit of zero smoothing length. Different kernels have different behaviors that may be more advantageous for a given problem than others. The kernel implemented in SNSPH currently is a cubic spline kernel:

$$W(r,h) = \pi^{-1} h^{-3} \begin{cases} 1 - 1.5x^2 + 0.75x^3 & \text{if } 0 \leq x \leq 1, \\ 0.25(2-x)^3 & \text{if } 1 \leq x \leq 2, \\ 0 & \text{otherwise} \end{cases} \tag{A.10}$$

where $x = r/h$. This kernel has the advantage that it is identically zero outside of $2h$, thus the contribution of particles outside of this range is zero. The smoothing length, h, of the kernel is variable, and is calculated from

$$\frac{dh_i}{dt} = -\frac{1}{3}\left(\frac{h_i}{\rho_i}\right)\left(\frac{d\rho_i}{dt}\right) = \frac{1}{3} h (\vec{\nabla} \cdot \vec{v}) \tag{A.11}$$

Since the velocity divergence is already calculated for the artificial viscosity (eq. A.5), no additional computational steps are required.

With this kernel, a quantity A is then determined by interpolating ("smoothing") over the N_n neighboring particles,

$$A_S(r) = \sum_j A_j \left(\frac{m_j}{\rho_j} \right) W(\vec{r} - \vec{r}_j, h). \tag{A.12}$$

First, the rate of change of the flow variables are calculated, then those time derivatives (equations A.1, A.2, and A.12) are numerically integrated to advance to the next time step. The time integration is done with different methods, depending on the variable being updated. For internal energy, the second-order Adams-Bashford method is used:

$$u_{i+1} = u_i + \dot{u}_i \left(dt_i + \frac{dt_i^2}{2dt_{i-1}} \right) - \dot{u}_{i-1} \left(\frac{dt_i^2}{2dt_{i-1}} \right). \tag{A.13}$$

For the smoothing length, a second-order leapfrog method is used:

$$h_{i+1} = h_i + \dot{h}_i \left(\frac{dt_i + dt_{i-1}}{2} \right). \tag{A.14}$$

And position and velocity is integrated using the Press method:

$$\dot{x}_{i+1} = \frac{x_i - x_{i-1}}{dt_{i-1}} = \ddot{x}_i \left(dt_i + \frac{dt_{i-1}}{2} \right) \tag{A.15}$$

$$x_{i+1} = x_i + (x_i - x_{i-1}) \frac{dt_i}{dt_{i-1}} + \ddot{x}_i \left(\frac{dt_i (dt_i + dt_{i-1})}{2} \right). \tag{A.16}$$

For the first time step of a beginning or restarted calculation, it is assumed that $u_{i-1} = u_i$ and $x_{i-1} = x_i - \dot{x}_i dt$ to start the integration. Double precision is used to store current and previous position to minimize round-off error for particles that do not move much in one time step.

A.1.1 Energy transport

Radiation transport is done with a flux limited transport scheme that is modeled on the one developed by Herant et al. 94. For neutrino diffusion, their number, n_{nu}, is transported with

$$\frac{1}{c} \left(\frac{\partial n_\nu}{\partial t} \right) = \Lambda \nabla n_{nu}, \tag{A.17}$$

where c is the speed of light, and Λ is the flux limiter, which is taken as

$$\Lambda^{ij}_{\nu_l} = min\left(c, D^{ij}_{\nu_l}/r_{ij}\right). \tag{A.18}$$

$D^{ij}_{\nu_l}$ is the harmonic mean of the diffusion ocefficients for the species ν_l of particles i and j ($= 2DD^i_{\nu_l}D^j_{\nu_l}/(D^i_{\nu_l} + D^j_{\nu_l})$), and r_{ij} is the distance between particles i and j. In the SPH formulism, this leads to the following equation for the energy transport:

$$\frac{de^i_{\nu_j}}{dt} = \sum_j \Lambda^{ij}_{\nu_l}\left(\varepsilon^j_{nu_l} n^j_{nu_l} b^{j\to i}_{nu_l} - \xi^{i\to j}_{nu_l}\varepsilon^j_{nu_l} n^j_{nu_l} b^{i\to j}_{nu_l}\right)\nabla W_{ij}\frac{m_j}{\rho_j} \tag{A.19}$$

where n_{ν_l} and e_{ν_l} are the neutrino density and energy, ε_{ν_l} is the mean neutrino energy, and $\xi^{j\to i}$ is the redshift correction for the mean energy as seen by particle i, and $b^{i\to j}_{nu_l}$ are the fermion blocking factors for neutrinos.

Outside of a trapping radius, neutrinos are essentially in the free-streaming regime, and a light-bulb approximation is used. The free-streaming limit used in SNSPH is

$$\frac{dE_i}{dt} = L_\nu(1.0 - e^{\Delta\tau_i}), \tag{A.20}$$

with $\Delta\tau_i$ being the optical depth of a particle i. The trapping radius is evolved in time to ensure that the free-streaming limit applies.

Energy generation from nuclear reactions is calculated at each (SPH) time step via a call to a reaction network solver (provided by Patrick). The solver has its own time step sub-cycling algorithm so it does not appreciably decrease the time stepping in SNSPH. The calculated contribution from nuclear reactions is then added to equation A.2 before the integration.

A cooling term due to the escaping of energy emission from electronic transitions can be calculated, and also added to equation A.2 before the integration. The cooling term is calculated from tabulated cooling functions, from the CHIANTI database, for gases of pure composition each from H to Zn. The CHIANTI data tables are for astrophysical plasmas and assume collisional ionization equilibrium.

The contribution to cooling is calculated by weighting according to abundance of the element and by its ionization state. The ionization fraction of each element is calculated from interpolation of the Mazzotti et al. tables. Thus, the cooling term is calculated as follows:

$$\Lambda_{\text{cool}} = \left(\sum_i \sum_j \Lambda_{ij} f_{ij} \frac{n_j}{n} \right) \cdot n_{e^-} n_{ion} \tag{A.21}$$

where Λ_{ij} is the cooling function tabulated by C. Badenes (2009, private communication) per ionization state i for element j, f_{ij} is the fraction of element j that is in ionization state i as tabulated by Mazzotta et al. (ref??), n_j is the number density of element j, and n is the number density of the gas.

A.1.2 The tree

SNSPH uses a parallel hashed oct-tree algorithm to represent the spatial arrangements of particles in a simulation. Each particle is identified with a unique key that is indexed into a hash table; and the particles are sorted into Morton order. This ordering is such that particles that are close to each other in the sorted list are also close to each other in simulation space, thus the traversal of the tree (particle list) for determining gravitational forces between particles is reasonably fast. In a parallelization of the code, this ordering also results in generally good load balancing, as the list can be divided into chunks which are sent to the individual processors. The ordering ensures that the majority of interactions are for local particles, and the number of data requests for particles on other processors remains small.

APPENDIX B

THE SHORT-LIVED RADIONUCLIDES

Alumimun-26 has been of great interest, because it could principally be a major heat source for the melting and differentiation of large bodies in the Solar System. And it is also potentially very useful as a short-term chronometer. It has only one daughter isotope - ^{26}Mg - to which it decays through electron capture with a mean life of 1.02 Myr. Aluminum-26 excesses are generally found in refractory inclusions in carbonaceous chondrites, like Allende or Murchinson. While isotopic anomalies in ^{26}Mg in meteoritic material has been found before, the first definite evidence for the in situ decay ^{26}Al was found by Lee et al (1977) in the Allende meteorite. They determined the initial abundance in the Solar System of $^{26}\mathrm{Al}/^{27}\mathrm{Al}$ to be $(5.1 \pm 0.6) \times 10^{-5}$. Aluminum-26 has been studied in great detail since then (e.g. Stegmann & Begemann 1982, Jacobsen et al. 2007, Aléon, Goresy, & Zinner 2007, Guan et al. 2000, Russell et al. 1997), and the canonical ratio has been determined in over 1500 measurements (MacPherson, Davis, & Zinner 1995) to be $(5 \pm 5\%) \times 10^{-5}$. Aluminum-26 is produced in massive stars by proton capture on ^{25}Mg, which occurs in the H-burning shell (Meyer & Clayton 2000). It is also produced during explosive Ne burning (Meyer & Clayton 2000).

Chlorine-36 is a rather volatile isotope that has two decay modes. It decays with a half life of 0.3 Myr to either ^{36}Ar via beta-decay (98.1%) or ^{36}S via electron capture (1.90%), which are also volatile. Due to their volatility, they are not found in the refractory phases that other SLRs have been detected in. Nevertheless, Murty, Goswami, and Shukolyukov report tentative evidence for ^{36}Ar that can best be explained by in-situ decay of ^{36}Cl. They measured $^{36}\mathrm{Cl}/^{35}\mathrm{Cl} = (1.4 \pm 0.2) \times 10^{-6}$ in the Efremovka meteorite. Leshin, Guan, & Lin detect evidence for ^{36}Cl in CAIs in the Ningquiang carbonaceous chondrite (2004). They infer an initial abundance of $^{36}\mathrm{Cl}/^{35}\mathrm{Cl} \geq 3 \times 10^{-4}$, much higher than Murty et al.'s result. Their explanation for the difference is that since Argon induces large artifacts in the measuring process,

these abundances have been measured incorrectly. In massive stars ^{36}Cl is produced by the s-process during He burning, as well as in both hydrostatic and explosive O burning (Meyer & Clayton 2000).

New insights that have recently been gained suggest that ^{36}Cl was present much higher than previously measured, and that it is decoupled from the origin on ^{26}Al and other SLRs (Jacobsen et al. 2011, and references therein). Jacobsen et al. (2011) measure the abundance in wadalite from Allende CAIs at $\sim 1.8 \times 10^{-5}$, and conclude that ^{36}Cl was likely produced by late-stage solar energetic particle irradiation, and that its production was unrelated to that of the other SLRs.

Calcium-41 decays with a half life of 0.103 Myr to ^{41}K via electron capture. Excesses of ^{41}Ca are usually found in refractory inclusions. After reporting tentative evidence for in situ decay of ^{41}Ca in the Efremovka CAIs (Srinivasan et al. 1994), Srinivasan confirmed two years later the presence of that SLR in the Early Solar System. They determine a ratio of ^{41}Ca/^{40}Ca= $(1.41 \pm 0.14) \times 10^{-8}$ at the formation of the Efremovka CAIs (Srinivasan et al. 1996). Calcium-41 is produced in the same sites as ^{36}Cl, which is s-process during He-burning and O-burning (Meyer & Clayton 2000).

Manganese-53 has only one decay channel, which is electron capture to form ^{53}Cr. Its half life is 3.7 Myr. It is also found in refractory inclusions, specifically FUN inclusion. Excesses in ^{53}Cr possibly due to the decay of ^{53}Mn have been reported in some FUN inclusions (Papanastassiou 1986, Papanastassiou & Brigham 1989) and in pink spinels from Murchinson (Esat & Ireland 1989). The first definite evidence of ^{53}Cr due to the in-situ decay of ^{53}Mn was found by Birck & Allégre (1985). The isotopic ratio was determined by these authors to be ^{53}Mn/^{55}Mn= $(3.66 \pm 1.22) \times 10^{-5}$ (1985), and was later improved to $(4.4 \pm 1.0) \times 10^{-5}$ (Birck & Allégre 1988). In an extensive study of eucrites, angrites, chondrites, diogenites,

pallasites, and others, Lugmair & Shukolyukov measured the ^{53}Mn/^{55}Mn of those, and infer an abundance of ^{53}Mn/^{55}Mn$\sim$ $few \times 10^{-5}$ at the formation of the Solar System (1998). Manganese-53 is made in explosive Si-burning in massive stars (Meyer & Clayton 2000).

Iron-60 also has only one mode of decay, which is beta-decay to ^{60}Co with a half life of 1.5 Myr. Cobalt-60 decays to ^{60}Ni via beta-decay with a half life of $1925d$. Iron-60 is special in the sense that it is only produced during the nucleosynthesis of core-collapse supernovae. Thus, any excesses in ^{60}Ni that correlate with ^{56}Fe require a nearby supernova as the source. These correlated excesses have been detected by Birck & Lugmair in Allende inclusions, and a tentative upper limit of ^{60}Fe/^{56}Fe$\leq 1.6 \times 10^{-6}$ was determined (1988). Recently, Tachibana et al. determined the ^{60}Fe/^{56}Fe from unequilibrated ordinary chondrites to be between $(1.9 \pm 1.3) \times 10^{-7} - (5.6 \pm 2.5) \times 10^{-7}$ (Tachibana & Huss 2003, Tachibana et al. 2005). Iron-60 is made by C-burning and with the s-process (Meyer & Clayton 2000).

Very recent considerations, however, suggest that the abundance ratio of ^{60}Fe/^{56}Fe have been at times vastly overestimated (Ogliore et al. 2011; Telus et al. 2011). Essentially, low counts and incorrectly applied data reduction methods can result in a positive bias in the data, leading to larger abundance measurements. Using a more accurate technique, Telus et al. (2011) find that typical abundances for ^{60} are probably around one order of magnitude lower than previously reported in the literature, which in some cases would indicate a null- detection of the isotope. However, there are still some positive detections of the isotope, but at lower levels.

Palladium-107 has a half life of 6.5 Myr, and decays to ^{107}Ag through beta-decay. Evidence for in-situ decay of ^{107}Pd was found by Kelly & Wasserburg (1978) in the Santa Clara iron meteorite, and the abundance was found to be $^{107}Pd/^{110}Pd \geq$

2×10^{-5}. Chen & Wasserburg analyzed metal phases of the iron meteorites Cape York and Grant, and find abundance ratios for $^{107}Ag^*/^{108}$Pd (where the asterisk indicates silver due to the decay of ^{107}Pd) in the range from $1.5 \pm 0.2 \times 10^{-5}$ to $2.5 \pm 0.4 \times 10^{-5}$ (1983). Analysation of metal phases in the iron meteorite Gibeon gave an abundance ratio of $^{107}Ag^*/^{108}Pd = (2.4 \pm 0.05) \times 10^{-5}$ (Chen & Wasserburg 1990). Palladium-107 is made during continuous r- and s-process nucleosynthesis and in the innermost regions of the supernova (Meyer & Clayton 2000).

Iodine-129 decays through beta-decay to ^{129}Xe, and has a half life of 15.7 Myr. The daugher isotope xenon is a volatile element, and thus usually depleted in meteorites, thus excesses in xenon are usually prominent. Isochrons for ^{129}I/^{127}I have been determined in five LL chondrites by Bernatowitz et al (1988). The inferred initial abundance ratio at the time of formation of those chondrites for ^{129}I/^{127}I was in the range $(0.762 \pm 0.042) \times 10^{-4}$ to $(1.232 \pm 0.014) \times 10^{-4}$ (Bernatowitz et al. 1988). Before that, Lewis and Anders determined the abundance from magnetite and troilite samples from the primitive meteorites Murchison and Orgueil, and found ^{129}I/^{127}I= $(1.46 \pm 0.04) \times 10^{-4}$ at the formation of the Solar System (1975). Iodine-129 is predominantly made in the r-process, although there might be minor contributions from the s-process (Meyer & Clayton 2000).

Hafnium-182 decays to ^{182}Ta via beta-decay with a half life of 9 Myr, which in turn decays to ^{182}W via beta-decay with a half life of $114d$. Both hafnium and tungsten are refractory, and thus are expected in most meteorites. However, hafnium is lithophile whereas tungsten is siderophile, so these isotopes are useful in determining the time of metal-silicate segregation during the differentiation of asteroids. The initial abundance ratio of the solar system has been estimated to be $^{182}Hf/^{182}W = (2.4 \pm 0.1) \times 10^{-4}$ by Lee & Halliday (1996). Recently, Kleine et al. determined Hf-W isochrons in CAIs from Allende and measured an abundance

of $^{182}Hf/^{182}W = (1.07 \pm 0.1) \times 10^{-4}$ at the beginning of the Solar System (2005). In stars, hafnium-182 is predominantly made in the r-process. There might also be some contribution from the s-process during He- and C-burning (Meyer & Clayton 2000).

Cesium-135 has a half life of 2.3 Myr and decays to ^{135}Ba through beta-decay. Isotopic excesses of ^{135}Cs are difficult to measure, because its daughter isotope as well as the normalizing isotope ^{136}Ba also have contributions from the r-process. Analysis of CAIs in Allende, Beardsley, and Zag, nevertheless, show evidence of radiogenic ^{135}Cs, and Hidaka et al. (2003) propose an initial abundance of the Solar System at $^{135}\text{Cs}/^{133}\text{Cs} = (4.8 \pm 0.8) \times 10^{-4}$. ^{135}Cs is produced in massive stars by the r- and s-process.

APPENDIX C

BACKGROUND OF THE INJECTION MODEL

The paper by Cameron and Truran (1977) is the first that investigated a supernova origin for the SLRs. In the paper it was assumed that this supernova not only contributed the SLRs but also triggered the collapse of the presolar molecular cloud with a shockwave. As Cameron and Truran show in their paper, under certain conditions a supernova shockwave can trigger the collapse of a molecular cloud (the certain conditions being mostly the ratio of the densities inside the cloud and of the shockwave). The shockwave has to be slowed down, which is accomplished by the sweeping up of material on the way to the molecular cloud. They further propose that a substantial fraction of this diluted supernova shock material can enter into the molecular cloud via Rayleigh-Taylor instabilities. The only SLRs Cameron and Truran consider are ^{26}Al and ^{129}I, which, they state, are the only SLRs for which reliable nucleosynthesis data existed at that time. However, they also consider some longer-lived unstable and some stable isotopes, for which anomalous abundance patterns have been detected. For each they calculate a different dilution factor, and assume that there is a 1 Myr time delay until solid bodies form after the collapse. They find that the dilution factors span a range of two orders of magnitude, however, given the considerable uncertainties (e.g. in the nuclear reaction networks), they are still mutually consistent.

Wasserburg et al. (1998) picked up on the supernova trigger model almost two decades later when new and more reliable supernova nucleosynthesis data and more isotopic measurements from meteorites became available. They now are able to consider 5 of the SLRs, namely ^{26}Al, ^{36}Cl, ^{41}Ca, ^{53}Mn, and ^{60}Fe with the supernova yields from Woosley & Weaver (1995) 25 $M_{\odot}$ model. They assume a dilution factor that is determined with the canonical ^{26}Al/^{27}Al ratio, and furthermore, a time delay before the formation of solids, which is determined from the ^{41}Ca initial abundance. Using these two parameters they can reproduce the observed ^{36}Cl, and ^{60}Fe,

whereas the predicted ^{53}Mn is too high. They note that the production of ^{53}Mn depends sensitively on the position of the piston, and thus is rather uncertain.

A larger portion of the injection model have focused on just injection into either a solar nebula or a proto planetary disk, and have not required the triggering of the collapse of nebula. The first and most known group to consider this is the Meyer et al. group. They have computed their own supernova ejecta yields from their supernova models and use that to predict the abundances an injection with certain parameters would cause. They use the ejecta of their 25 $M_\odot$ progenitor, and try to reproduce the abundances of ^{26}Al, ^{36}Cl, ^{41}Ca, and ^{60}Fe with it. They assume injection into a 1 $M_\odot$ solar nebula. They use a fraction f ($\sim 2 \times 10^{-4}$ for their best case) of the ejecta calculated from the canonical ^{26}Al abundance and a seemingly arbitrarily picked time delay of 0.9 Myr. They employ a mass cut, which marks the boundary between the material of the supernova that is ejected and the material that is not. The location of it in the best-fitting case is the edge of the He-exhausted core (at 6.8 $M_\odot$ in their model), which the authors interpret to possibly indicate a WR star origin. They note that in order to not include any (significant) amount of ^{53}Mn the mass cut has to be outside of 2.8 $M_\odot$.

A rather extensive study of different stellar sources for the injection model has been conducted by Sahijpal and Soni (2006). In their paper they try to reproduce the abundances of ^{26}Al, ^{36}Cl, ^{41}Ca, ^{53}Mn, ^{60}Fe, ^{107}Pd, and ^{182}Hf with an AGB star, a supernova of various types, and a WR star. They find that the AGB star is an unlikely origin for the SLRs. In all their models they assume a 1 $M_\odot$ presolar cloud of radius r and distance D away, a free-decay time interval T ($30yr, 0.8$ Myr, 1.5 Myr) and a geometric dilution factor. A mass fraction η (~ 0.1) of the injected material will end up in the sun, and a net mass fraction $F = f\eta$ of the ejecta will homogenize with a mass fraction β ($= 1$ for entire cloud, $= 0.01$ for protoplanetary disk)

of the solar nebula. F is calculated from the canonical ^{26}Al abundance, the decay time from the ^{41}Ca abundance. They used the supernova models from Rauscher et al. (2002) and from Chieffi and Limongi (2004). They employed mass cuts at the O/Ne and O/C shells. They find that the Rauscher models produce smaller stable isotope anomalies, their preferred decay time is $T = 30yr$, and a mass cut at the O/Ne seems to work slightly better. The abundances of ^{41}Ca, ^{36}Cl, ^{182}Hf, ^{107}Pd can be satisfactorially reproduced, although ^{41}Ca requires a large decay time, and the inferred abundances of ^{60}Fe and ^{53}Mn are too high.

In that same year Looney et al. (2006) published a paper investigating just a type II supernova injecting material into either a solar nebula or a protoplanetary disk. They are also the first to explicitly mention that in order for this injection scenario to be physical, the Solar System has to have formed in a cluster similar to the Orion nebula and other HII regions. In their paper they are trying to reproduce ^{26}Al, ^{36}Cl, ^{41}Ca, ^{60}Fe, ^{107}Pd, ^{129}I, and ^{182}Hf using the supernova ejecta models of Woosley & Weaver (1995) and Rauscher et al (2002). They use a radioactivity distance ratio, which is essentially the ratio of the size of the Solar System to its distance from the supernova. The whole ejecta is diluted with a dilution factor that depends on the radioactivity distance and an injection efficiency, which is assumed to be 1 for a circumstellar disk, and 0.1 for a circumstellar envelope (or core). An adjustable time delay is used and optimized simultaneously with the radioactivity distance. A χ^2-fitting procedure is used to match the observed abundances by optimizing the radioactivity distance. They favor the 20 $M_\odot$ model of Rauscher et al. with a time delay of 1.8 Myr and radioactivity distance of just below 30. Note, they have excluded ^{53}Mn, of which too much will probably be injected with their optimized parameters.

The most recent model calculations have been done by Miki et al. (2007). They employ a "mixing-fallback" model to explain SLRs: a small fraction ($q \sim 10^{-2} - 10^{-3}$) of the 'inner' region is mixed with the 'outer' ejected region, the rest falls back onto the remnant. They want this mixing- fallback to occur within the C/O layer. They are using SN ejecta of Woosley & Weaver (1995), Rauscher et al. (2002), Chieffi and Limongi (2004), and Nomoto et al. (2006). They employ a time delay Δ of 0.7-1 Myr, a geometric dilution factor which includes an injection efficiency (α) to explain ^{26}Al, ^{41}Ca, ^{60}Fe, ^{53}Mn for two cases, injection into a 1 $M_\odot$ solar nebula of $0.1pc$ radius, distance between $2-5pc$ and injection efficiency of 0.1, and injection into a 0.01 $M_\odot$ disk of $100AU$ radius, distance of $0.3-0.8pc$ and injection efficiency of 1. They perform the same procedure for the non-mixing case and find that some mixing from inside is required to yield good results.

A bit older model was calculated by Harper (1996), a paper that does not seem to be cited too often. That paper predicts the SLR abundances as inferred from ISM abundance and stellar nucleosysthesis from supernovae. They use two different cases for the ISM abundance, closed-system decay, and three-phase ISM interdiffusion. For the stellar nucleosysthesis scenario (called late-spike mixing) they use (galactic) production ratios estimated r/s decomposition of the solar abundance distribution. Each case gets a free-decay interval, and is normalized to ^{129}I (so that is not overproduced). They find that the late-spike mixing scenario matches ^{107}Pd, ^{60}Fe, and ^{53}Mn very well, while ^{26}Al is two orders of magnitude too low and ^{182}Hf is an order of magnitude too high (^{135}Cs is a little higher that their given upper limit). The ISM scenarios do not match at all. They mention that the late-spike mixing scenario could also match the at that time newly found ^{41}Ca with a mixing time (free decay interval?) of up to 0.6 Myr. They note that supernova as the source of the "late spike" is much more likely, however, the ^{26}Al discrepancy needs to be

dealt with in order for this to be a serious model. AGB stars (they write) do not normally produce ^{53}Mn , and furthermore very special conditions are required for this case that are not observed.

APPENDIX D

TABLES AND FIGURES

Table D.1. Constraints

SLR	mean life	Abundance	relative to
^{26}Al	1.034 Myr	4.5×10^{-5}	^{27}Al
^{36}Cl	0.434 Myr	3×10^{-5}	^{35}Cl
^{41}Ca	0.149 Myr	1.4×10^{-8}	^{40}Ca
^{53}Mn	5.40 Myr	2×10^{-5}	^{55}Mn
^{60}Fe	2.16 Myr	1×10^{-6}	^{56}Fe
^{107}Pd	9.38 Myr	5×10^{-5}	^{108}Pd
^{129}I	22.7 Myr	1.4×10^{-4}	^{129}I
^{182}Hf	13.0 Myr	1.1×10^{-4}	^{180}Hf
^{135}Cs	33.2 Myr	4.8×10^{-4}	^{133}Cs

Table D.1: This table shows the initial abundances of the SLRs in the Early Solar System. Shown are the values that we used as constraints in our optimization procedure. The mean lives of the isotopes are taken from atom.kaeri.re.kr. References and a more detailed description for the abundances for each SLR can be found in Appendix B.

Table D.2. Optimized Parameters

Progenitor	χ^2	Decay time	Dilution factor	Boundaries s_0	s_1	s_2	Weighting factors w_0	w_1	w_2
15 $M_\odot$	1.450	1.0 Myr	1.3×10^{-5}	1.7	2.4	3.0	0.0015	0.014	1.0
19 $M_\odot$	1.272	1.0 Myr	7.3×10^{-6}	1.7	2.1	4.5	0.0023	0.069	1.0
20 $M_\odot$	1.112	1.2 Myr	9.2×10^{-6}	1.5	4.0	5.0	0.0018	0.25	1.0
21 $M_\odot$	0.343	0.9 Myr	4.6×10^{-6}	1.7	2.2	4.8	0.0032	0.10	1.0
25 $M_\odot$	0.760	1.0 Myr	7.3×10^{-6}	2.0	2.3	7.1	0.0	0.010	1.0
30 $M_\odot$	1.406	0.9 Myr	3.3×10^{-6}	1.7	2.1	10.1	0.0045	0.19	1.0
35 $M_\odot$	1.952	1.0 Myr	5.9×10^{-6}	1.7	2.1	11.7	0.0025	0.072	1.0
40 $M_\odot$	0.687	1.0 Myr	2.1×10^{-6}	2.0	3.6	5.4	0.038	0.58	1.0

Table D.2: This table lists the optimized parameters for each progenitor. For each progenitor, the lowest χ^2 value that was achieved is shown together with the corresponding parameters. The optimized decay time is given in Myr, the boundaries are given as mass coordinate in $M_\odot$ starting from the center outwards, and the weighting factors are given as a fraction of 1.

Table D.3. Reproduced abundances of SLRs for optimized cases.

	Abundances							
Progenitor	$^{26}Al/^{27}Al$	$^{36}Cl/^{35}Cl$	$^{41}Ca/^{40}Ca$	$^{53}Mn/^{55}Mn$	$^{60}Fe/^{56}Fe$	$^{107}Pd/^{108}Pd$	$^{129}I/^{127}I$	$^{182}Hf/^{180}Hf$
15 $M_\odot$	6.0×10^{-5}	1.4×10^{-6}	1.2×10^{-8}	2.0×10^{-5}	1.1×10^{-5}	5.8×10^{-5}	1.2×10^{-4}	4.0×10^{-5}
19 $M_\odot$	4.8×10^{-5}	1.8×10^{-6}	1.2×10^{-8}	2.0×10^{-5}	2.2×10^{-6}	3.6×10^{-5}	6.0×10^{-5}	7.4×10^{-5}
20 $M_\odot$	4.1×10^{-5}	2.4×10^{-5}	1.3×10^{-8}	2.0×10^{-5}	2.7×10^{-6}	4.3×10^{-5}	6.6×10^{-5}	5.6×10^{-5}
21 $M_\odot$	4.6×10^{-5}	3.3×10^{-6}	1.6×10^{-8}	2.0×10^{-5}	1.3×10^{-6}	4.9×10^{-5}	9.9×10^{-5}	1.1×10^{-4}
25 $M_\odot$	5.3×10^{-5}	2.0×10^{-6}	1.3×10^{-8}	2.3×10^{-5}	9.7×10^{-7}	4.2×10^{-5}	1.2×10^{-4}	5.7×10^{-5}
30 $M_\odot$	4.1×10^{-5}	3.3×10^{-6}	1.6×10^{-8}	2.0×10^{-5}	2.2×10^{-6}	6.4×10^{-5}	4.4×10^{-5}	1.6×10^{-4}
35 $M_\odot$	5.1×10^{-5}	2.1×10^{-6}	1.5×10^{-8}	2.0×10^{-5}	2.2×10^{-6}	5.5×10^{-5}	3.4×10^{-5}	1.8×10^{-4}
40 $M_\odot$	4.5×10^{-5}	3.6×10^{-6}	1.2×10^{-8}	2.1×10^{-5}	1.5×10^{-6}	9.0×10^{-5}	1.0×10^{-4}	7.1×10^{-5}

Table D.3: This table shows the reproduced abundances for the optimized parameters for each progenitor (listed in table D.2).

Table D.4. Explosion Simulations

Simulation	progenitor	Energy 10^{51} erg	M_{Rem} ($M_\odot$)	Delay ms
23e-0.8	23 $M_\odot$ single	0.8	5.7	20
23e-1.2	23 $M_\odot$ single	1.2	4.1	20
23e-1.5	23 $M_\odot$ single	1.5	3.2	20
23e-0.7-0.8	23 $M_\odot$ single	0.8	3.2	700
23e-0.7-1.5	23 $M_\odot$ single	1.5	2.3	700
16m-run1	16 $M_\odot$ binary	1.5	2.06	20
16m-run2	16 $M_\odot$ binary	0.8	2.43	20
16m-run4	16 $M_\odot$ binary	5.9	1.53	20
23m-run1	23 $M_\odot$ binary	1.9	3.57	20
23m-run2	23 $M_\odot$ binary	1.2	4.03	20
23m-run5	23 $M_\odot$ binary	6.6	1.73	20
40m-run1	40 $M_\odot$ single	10	1.75	20
40m-run5	40 $M_\odot$ single	1.8	4.51	20
40m-run9	40 $M_\odot$ single	2.4	6.02	20

Table D.4: Parameters for the different explosion simulations in 1D.

Table D.5. Oxygen isotopic shifts following injection from a 1D supernova:
Bulk

	16m-average	23m-average	40m-average	23e-average	23e-0.7-average
^{16}O	1.97 $M_\odot$	1.48 $M_\odot$	3.29 $M_\odot$	2.93 $M_\odot$	5.44 $M_\odot$
^{17}O	2.24×10^{-4} $M_\odot$	7.67×10^{-6} $M_\odot$	1.80×10^{-4} $M_\odot$	3.6×10^{-4} $M_\odot$	2.94×10^{-4} $M_\odot$
^{18}O	1.85×10^{-3} $M_\odot$	1.53×10^{-5} $M_\odot$	3.29×10^{-5} $M_\odot$	6.63×10^{-5} $M_\odot$	1.27×10^{-4} $M_\odot$
^{26}Al	1.91×10^{-4} $M_\odot$	1.52×10^{-5} $M_\odot$	2.17×10^{-5} $M_\odot$	2.15×10^{-5} $M_\odot$	
^{41}Ca	4.06×10^{-6} $M_\odot$	2.63×10^{-6} $M_\odot$	1.21×10^{-5} $M_\odot$	1.06×10^{-5} $M_\odot$	1.49×10^{-4} $M_\odot$
δ^{17}O	-719 $^0/_{00}$	-987 $^0/_{00}$	-899 $^0/_{00}$	-788 $^0/_{00}$	-854 $^0/_{00}$
δ^{18}O	-581 $^0/_{00}$	-996 $^0/_{00}$	-997 $^0/_{00}$	-993 $^0/_{00}$	-990 $^0/_{00}$
x	0.247	0.00375	0.105	0.0655	0.123
Final δ^{17}O	-191 $^0/_{00}$	-63.5 $^0/_{00}$	-139 $^0/_{00}$	-105 $^0/_{00}$	-147 $^0/_{00}$
Final δ^{18}O	-163 $^0/_{00}$	-63.5 $^0/_{00}$	-149 $^0/_{00}$	-117 $^0/_{00}$	-162 $^0/_{00}$
Final Δ^{17}O	-118 $^0/_{00}$	-31.1 $^0/_{00}$	-65.6 $^0/_{00}$	-45.1 $^0/_{00}$	-66.2 $^0/_{00}$
Δt	1.41 Myr	0.65 Myr	1.36 Myr	1.31 Myr	1.73 Myr

Table D.5: Our predicted shifts in O isotopes for the 1D simulations listed in table D.4, averaged over each progenitor mass.

Table D.6. Oxygen isotopic shifts following injection from a 1D supernova:
explosive C/Ne burning

	16m-average	23m-average	40m-average	23e-average	23e-0.7-average
^{16}O	5.19×10^{-1} M$_\odot$	5.14×10^{-1} M$_\odot$	4.83×10^{-1} M$_\odot$	1.35 M$_\odot$	1.86 M$_\odot$
^{17}O	1.47×10^{-7} M$_\odot$	2.89×10^{-7} M$_\odot$	2.76×10^{-8} M$_\odot$	8.79×10^{-7} M$_\odot$	4.96×10^{-6} M$_\odot$
^{18}O	4.41×10^{-7} M$_\odot$	4.02×10^{-6} M$_\odot$	1.70×10^{-8} M$_\odot$	1.64×10^{-8} M$_\odot$	3.21×10^{-8} M$_\odot$
^{26}Al	8.98×10^{-7} M$_\odot$	1.04×10^{-4} M$_\odot$	4.55×10^{-7} M$_\odot$	9.37×10^{-6} M$_\odot$	1.53×10^{-5} M$_\odot$
^{41}Ca	1.74×10^{-6} M$_\odot$	2.74×10^{-6} M$_\odot$	5.59×10^{-8} M$_\odot$	6.70×10^{-6} M$_\odot$	1.16×10^{-4} M$_\odot$
δ^{17}O	-999 $^0/_{00}$	-998 $^0/_{00}$	-999 $^0/_{00}$	-997 $^0/_{00}$	-994 $^0/_{00}$
δ^{18}O	-1000 $^0/_{00}$	-996 $^0/_{00}$	-1000 $^0/_{00}$	-1000 $^0/_{00}$	-1000 $^0/_{00}$
x	0.280	0.00241	0.514	0.0698	0.0587
Final δ^{17}O	-266 $^0/_{00}$	-62.3 $^0/_{00}$	-379 $^0/_{00}$	-121 $^0/_{00}$	-112 $^0/_{00}$
Final δ^{18}O	-266 $^0/_{00}$	-62.2 $^0/_{00}$	-379 $^0/_{00}$	-121 $^0/_{00}$	-112 $^0/_{00}$
Final Δ^{17}O	-147 $^0/_{00}$	-30.6 $^0/_{00}$	-227 $^0/_{00}$	-61.3 $^0/_{00}$	-56.1 $^0/_{00}$
Δt	1.51 Myr	0.77 Myr	1.03 Myr	1.34 Myr	1.75 Myr

Table D.6: Our predicted shifts in O isotopes for the 1D simulations listed in table D.4, averaged over each progenitor mass.

Table D.7. Oxygen isotopic shifts following injection from a 1D supernova:
sub-explosive C burning

	16m-average	23m-average	40m-average	23e-average	23e-0.7-average
^{16}O	1.78×10^{-1} M$_\odot$	3.85×10^{-1} M$_\odot$	2.47 M$_\odot$	1.84 M$_\odot$	1.91 M$_\odot$
^{17}O	1.81×10^{-4} M$_\odot$	1.03×10^{-6} M$_\odot$	1.88×10^{-7} M$_\odot$	4.18×10^{-5} M$_\odot$	4.86×10^{-5} M$_\odot$
^{18}O	3.12×10^{-4} M$_\odot$	7.32×10^{-6} M$_\odot$	6.51×10^{-8} M$_\odot$	8.31×10^{-5} M$_\odot$	9.14×10^{-5} M$_\odot$
^{26}Al	2.95×10^{-6} M$_\odot$	6.77×10^{-5} M$_\odot$	1.54×10^{-5} M$_\odot$	1.42×10^{-5} M$_\odot$	8.75×10^{-6} M$_\odot$
^{41}Ca	1.65×10^{-7} M$_\odot$	1.35×10^{-6} M$_\odot$	8.42×10^{-6} M$_\odot$	7.78×10^{-6} M$_\odot$	8.44×10^{-6} M$_\odot$
δ^{17}O	1503 $^0/_{00}$	-990 $^0/_{00}$	-1000 $^0/_{00}$	-944 $^0/_{00}$	-938 $^0/_{00}$
δ^{18}O	-221 $^0/_{00}$	-995 $^0/_{00}$	-1000 $^0/_{00}$	-980 $^0/_{00}$	-979 $^0/_{00}$
x	0.0292	0.00276	0.0775	0.0628	0.106
Final δ^{17}O	-15.7 $^0/_{00}$	-62.6 $^0/_{00}$	-128 $^0/_{00}$	-112 $^0/_{00}$	-144 $^0/_{00}$
Final δ^{18}O	-64.6 $^0/_{00}$	-62.6 $^0/_{00}$	-128 $^0/_{00}$	-114 $^0/_{00}$	-148 $^0/_{00}$
Final Δ^{17}O	$+19.2$ $^0/_{00}$	-30.7 $^0/_{00}$	-64.9 $^0/_{00}$	-55.3 $^0/_{00}$	-71.4 $^0/_{00}$
Δt	0.90 Myr	0.72 Myr	1.29 Myr	1.29 Myr	1.39 Myr

Table D.7: Our predicted shifts in O isotopes for the 1D simulations listed in table D.4, averaged over each progenitor mass.

Table D.8. ^{26}Al and O in the 3D explosion

	Bulk	Ring	Ring high Al26	Bubble	Bubble high Al26
^{26}Al ($M_\odot$)	1.474×10^{-6}	3.510×10^{-7}	2.420×10^{-7}	9.996×10^{-7}	9.585×10^{-7}
^{16}O ($M_\odot$)	0.511	2.888×10^{-2}	5.949×10^{-3}	7.025×10^{-3}	2.550×10^{-3}
^{17}O ($M_\odot$)	2.170×10^{-4}	3.400×10^{-5}	2.241×10^{-5}	1.021×10^{-5}	1.738×10^{-9}
^{18}O ($M_\odot$)	1.509×10^{-1}	3.553×10^{-3}	1.018×10^{-4}	7.314×10^{-3}	5.635×10^{-3}
^{41}Ca ($M_\odot$)	2.132×10^{-8}	2.039×10^{-8}	4.312×10^{-9}	1.827×10^{-11}	1.239×10^{-11}
δ^{17}O	$+43.9\ ^0/_{00}$	$+1894\ ^0/_{00}$	$+8258\ ^0/_{00}$	$+2573\ ^0/_{00}$	$-998.3\ ^0/_{00}$
δ^{18}O	$+129887\ ^0/_{00}$	$+53546\ ^0/_{00}$	$+6582\ ^0/_{00}$	$+460545\ ^0/_{00}$	$+978646\ ^0/_{00}$
x	0.16808	0.03987	0.01192	0.003406	0 .001289
Final δ^{17}O	$-45.1\ ^0/_{00}$	$+14.8\ ^0/_{00}$	$+37.9\ ^0/_{00}$	$-51.1\ ^0/_{00}$	$-61.2\ ^0/_{00}$
Final δ^{18}O	$+18638\ ^0/_{00}$	$+1995\ ^0/_{00}$	$+18.2\ ^0/_{00}$	$+1503\ ^0/_{00}$	$+1200\ ^0/_{00}$
Final Δ^{17}O	$-1608\ ^0/_{00}$	$-561\ ^0/_{00}$	$+27.8\ ^0/_{00}$	$-534\ ^0/_{00}$	$-477\ ^0/_{00}$
Δt	0.66 Myr	0.90 Myr	0.70 Myr	–	–

Table D.8: Our predicted shifts in O isotopes for the 3D simulation.

Table D.9. Isotopes

^{12}C	^{16}O	^{20}Ne	^{24}Mg	^{28}Si	^{31}P	^{32}S	^{36}Ar	^{40}Ca
^{44}Ca	^{44}Sc	^{44}Ti	^{48}Cr	^{52}Fe	^{56}Fe	^{56}Co	^{56}Ni	

Table D.9: Isotopes used in SNSPH and the network.

Table D.10. Runs

Run	Resolution	Asymmetry	implemented at	Network
Canonical / 1M_burn	1M	none		on
1M_burn_CCO2	1M	1.35 $M_\odot$ central gravity source	step 0	on
10M_burn	10M	none		on
50M_burn	50M	none		on
1M_no–burn	1M	none		off
1M_burn_38nbrs	1M	none		on
1M_burn_70nbrs	1M	none		on
1M_jet2	1M	bipolar	step 0	on
1M_jet4	1M	bipolar	step 0	on
1M_jet4L	1M	bipolar	step 200	on
1M_jet4LL	1M	bipolar	step 600	on
1M_single–jet2	1M	uni-polar	step 0	on
1M_single–jet4	1M	uni-polar	step 0	on

Table D.10: Parameters for the different computation runs considered in this chapter.

Table D.11. A table for the canonical yields

Element	1M_burn	1M_burn_CCO2
^{1}H	3.66 $M_\odot$	3.64 $M_\odot$
^{4}He	2.63 $M_\odot$	2.52 $M_\odot$
^{12}C	1.85×10^{-1} $M_\odot$	1.64×10^{-1} $M_\odot$
^{16}O	2.53 $M_\odot$	2.35 $M_\odot$
^{28}Si	6.60×10^{-2} $M_\odot$	2.70×10^{-2} $M_\odot$
^{32}S	4.11×10^{-2} $M_\odot$	1.77×10^{-2} $M_\odot$
^{44}Ti	3.00×10^{-4} $M_\odot$	4.21×10^{-4} $M_\odot$
^{56}Fe	6.50×10^{-3} $M_\odot$	5.74×10^{-3} $M_\odot$
^{56}Ni	1.07×10^{-1} $M_\odot$	6.40×10^{-2} $M_\odot$

Table D.11: Post processed yields for the canonical run and run 1M_burn_CCO2 shortly after nuclear burning had ceased.

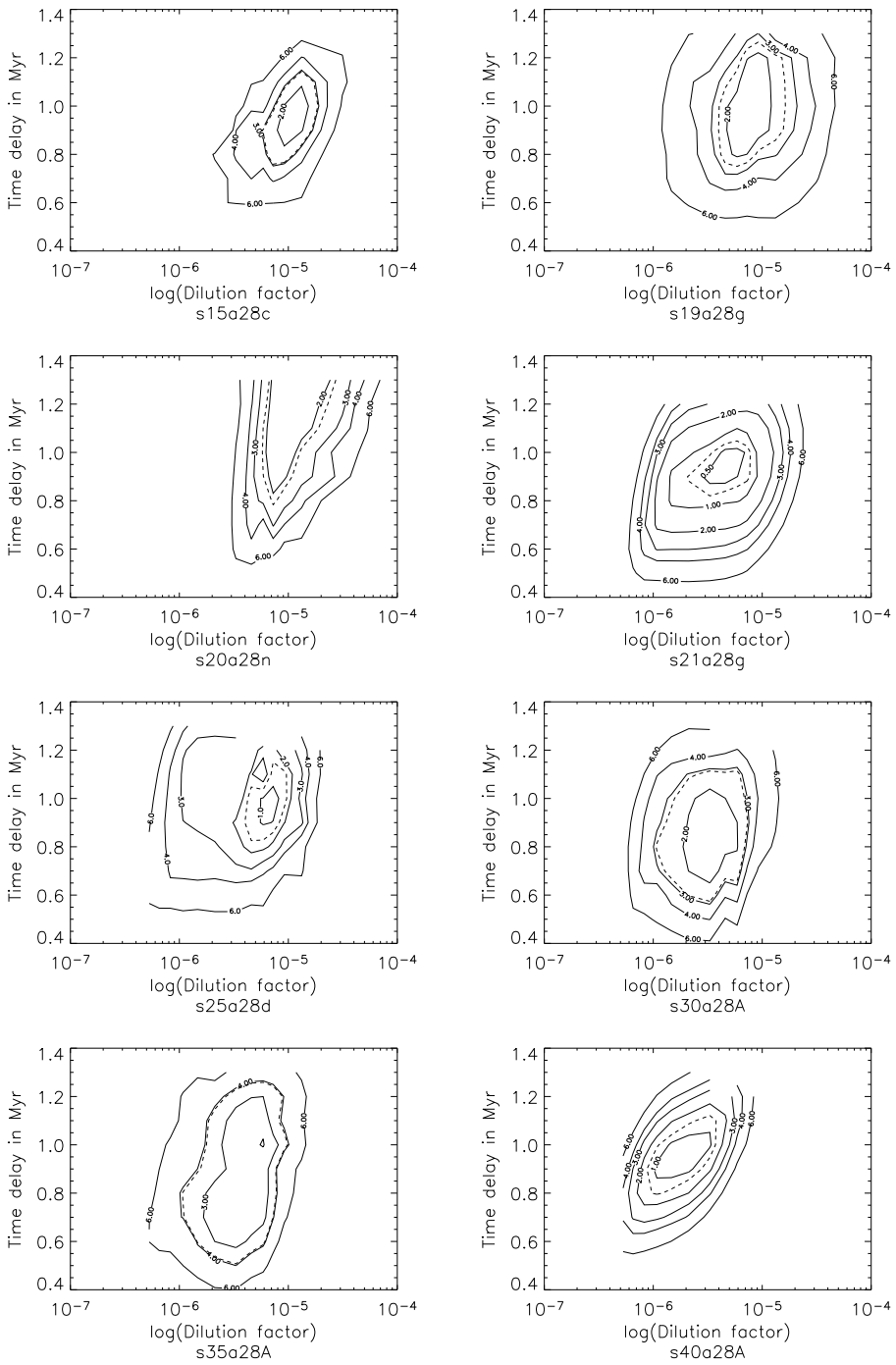

Figure D.1: Shown are the results of the optimization routine for each progenitor. The contours are labeled with the reduced χ^2 they represent (see eq. 2.2). The time delay (y-axis) is in Myr, the dilution factor is unitless and plotted on a logarithmic scale. The progenitor is noted in the subtitle of each graph (where essentially the two numbers following the first letter 's' indicates the mass of the progenitor). The dashed contour is at the χ^2 that is twice the smallest value achieved for each progenitor.

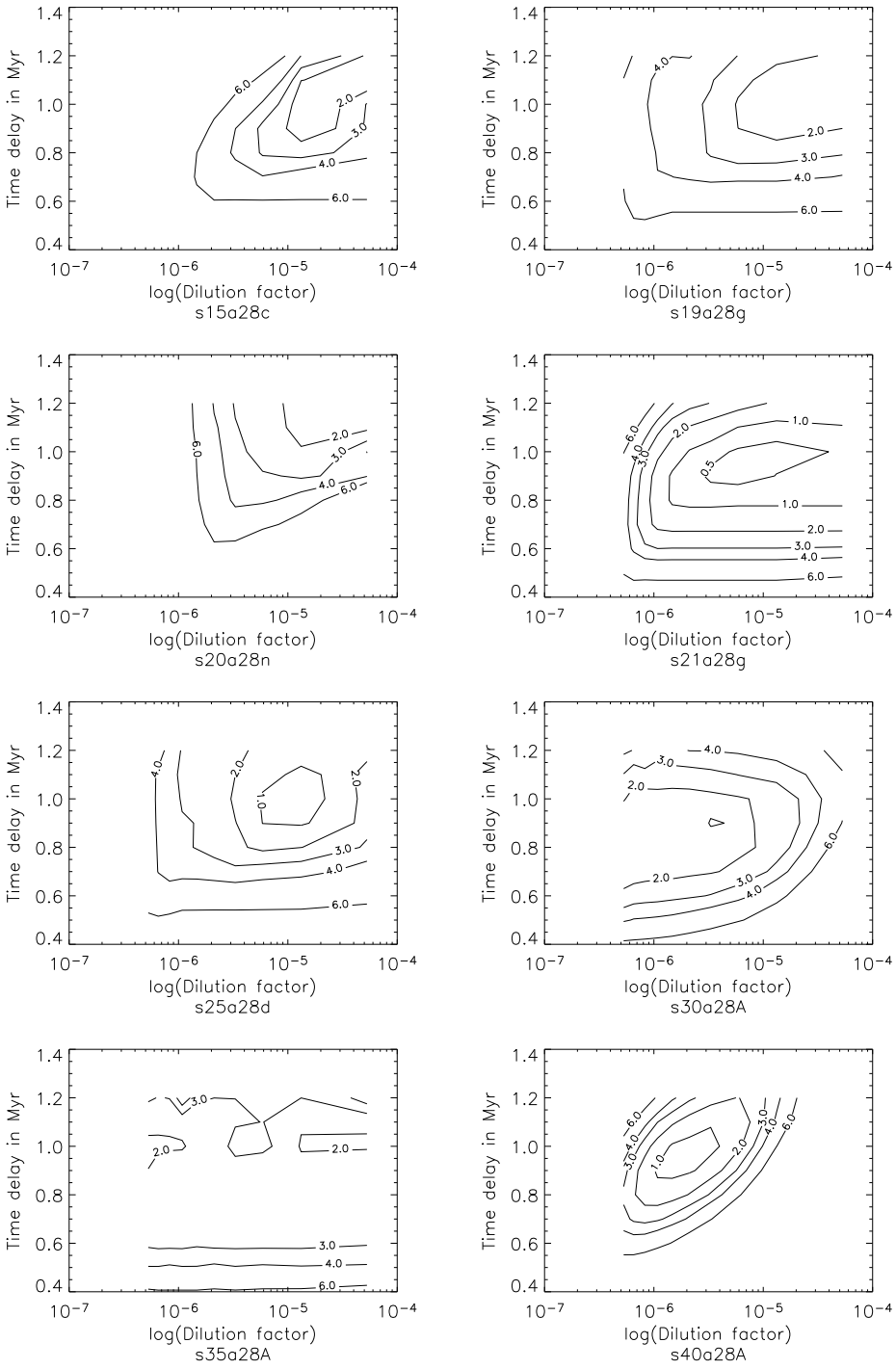

Figure D.2: Same as figure D.1, except that ^{26}Al was replaced by ^{135}Cs (with an error of 0.5) in the optimization routine. Note that, since the error for ^{135}Cs is higher than for ^{26}Al, the χ^2 value for the former will naturally be smaller for the same goodness of fit (see eq. 2.2). The 35 $M_\odot$ progenitor seems to not have been optimized in the given parameter space.

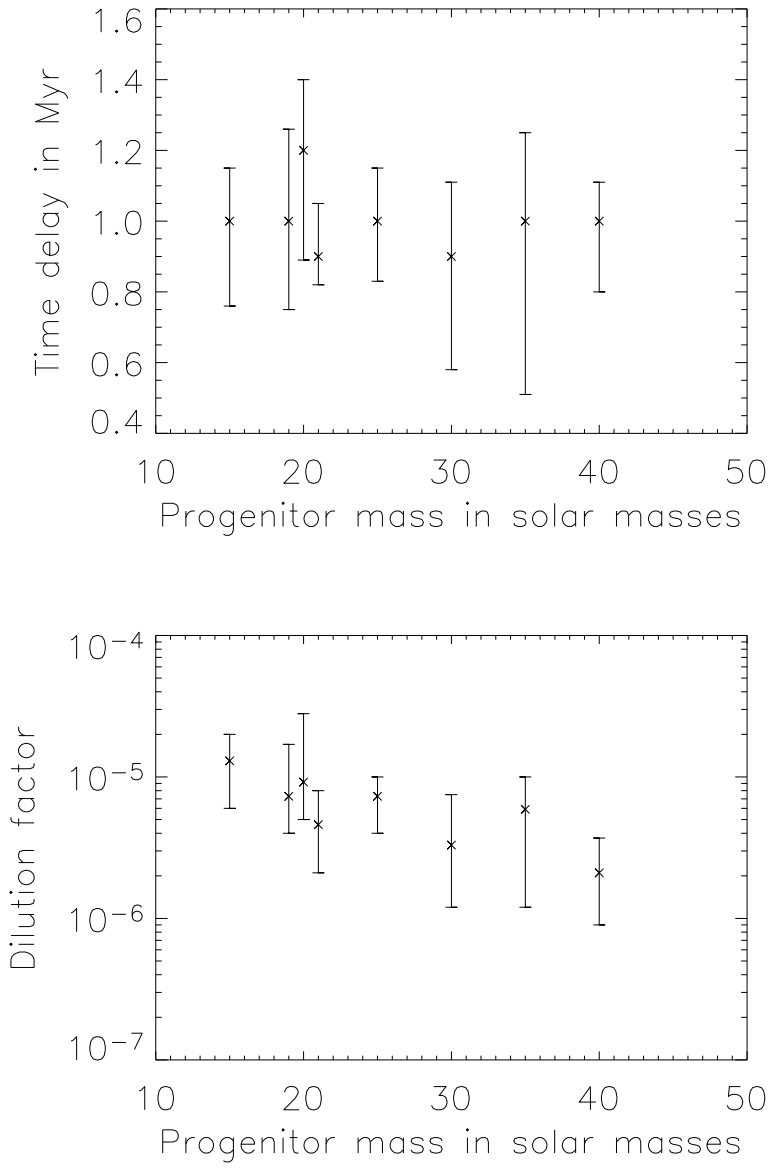

Figure D.3: Shown are the optimized time delays and dilution factors as a function of progenitor mass. The error bars mark the ranges of the contour that is twice the value of the lowest χ^2 achieved for each progenitor. The upper bound in each graph for the 20 $M_\odot$ progenitor are estimates since the parameter space was not explored further than that.

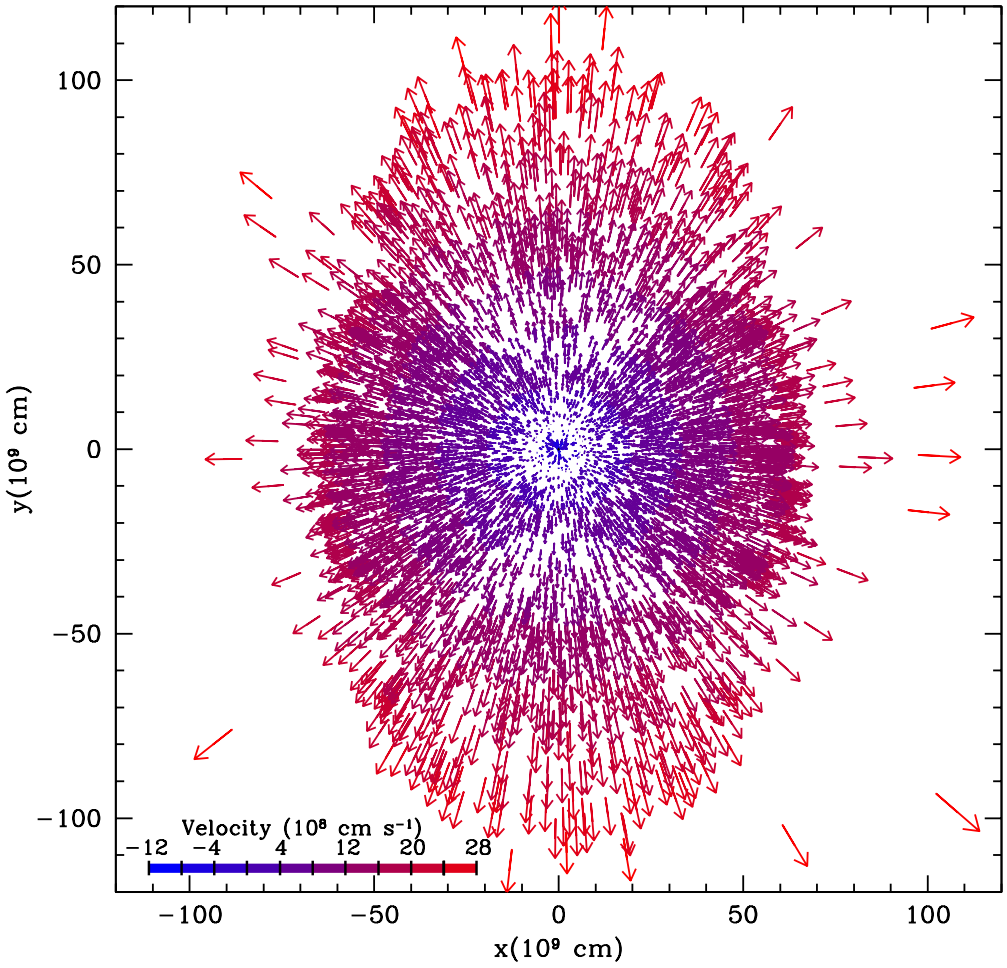

Figure D.4: Plot of particles in a wedge of the x-z plane ($|y|/r$ <0.006) of our 3-dimensional simulation 40 s after the start of our calculation. The vectors denote velocity direction and magnitude. The particles are color-coded by radial velocity. By this time, our large initial asymmetry has spherized to roughly factor of 2 asymmetry (this persists through much of the rest of the simulation).

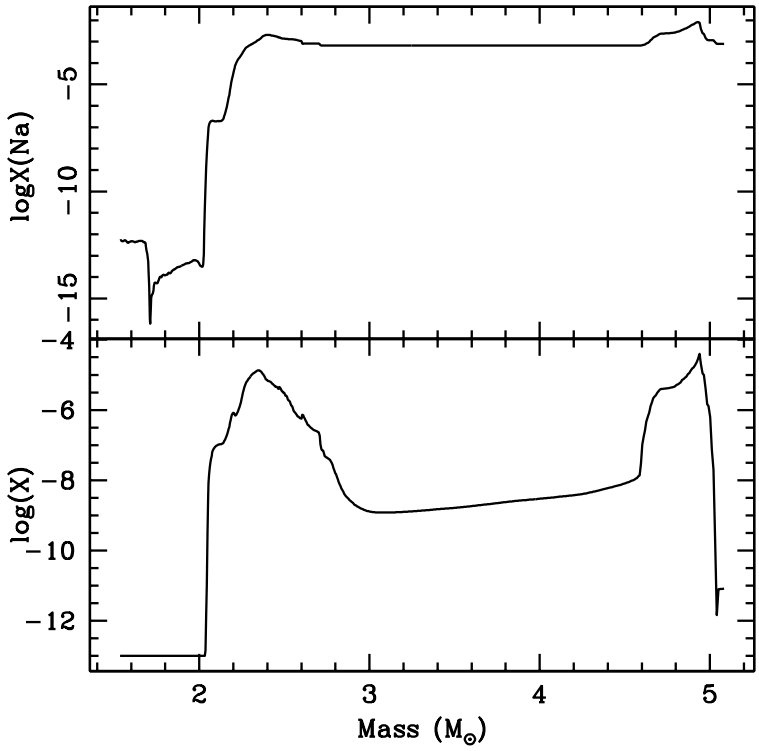

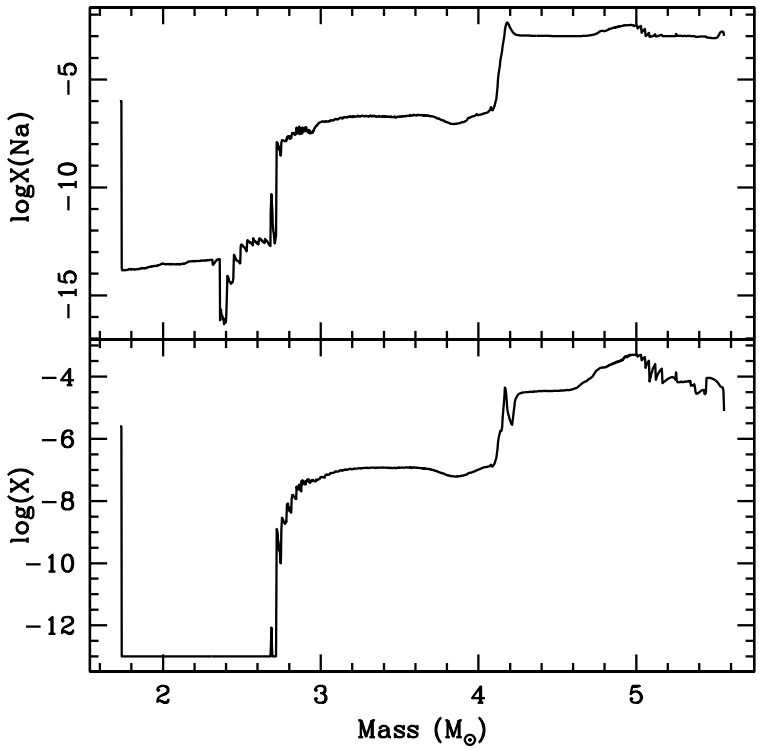

Figure D.5: See figure D.7 for caption.

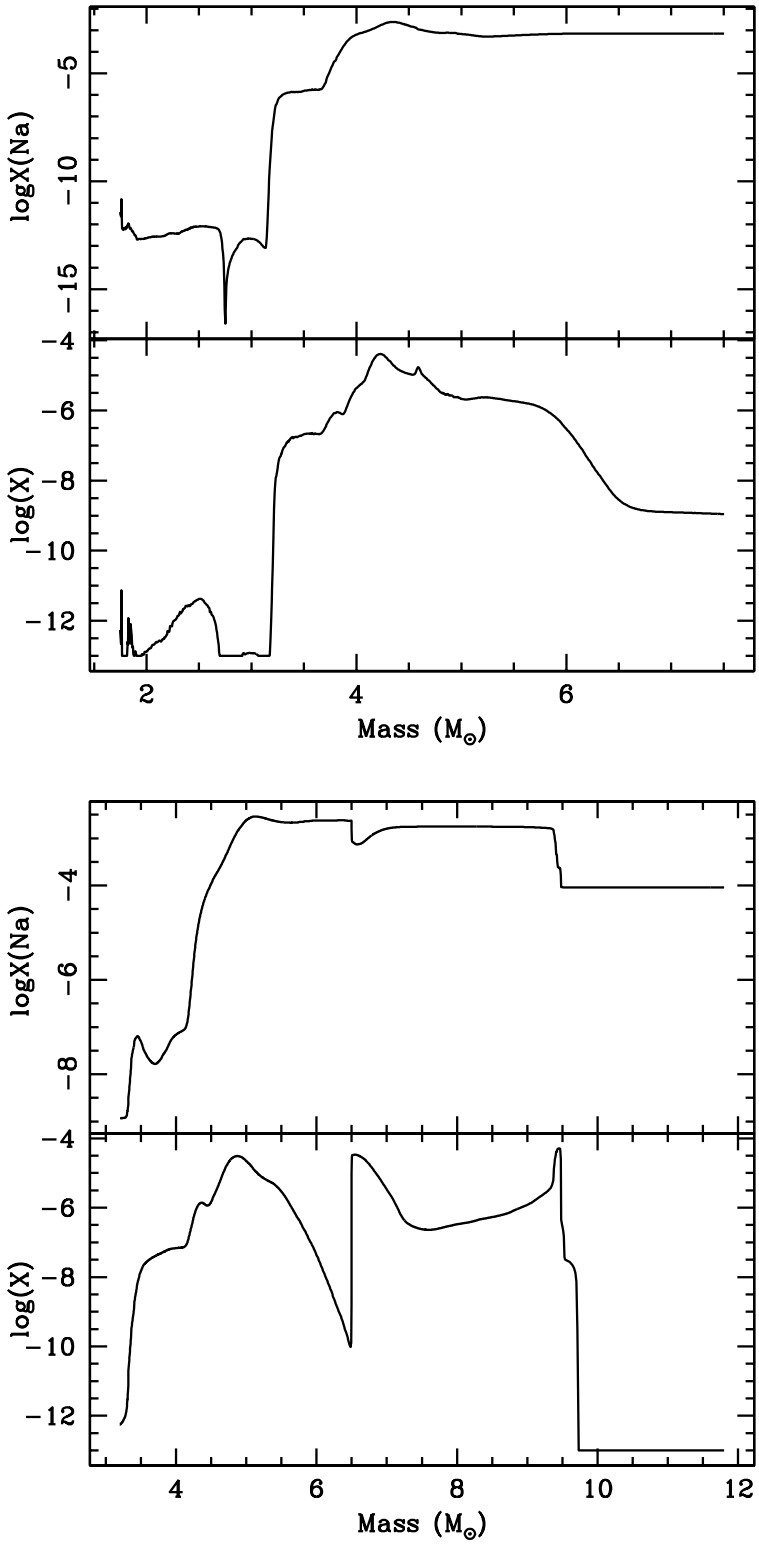

Figure D.6: See figure D.7 for caption.

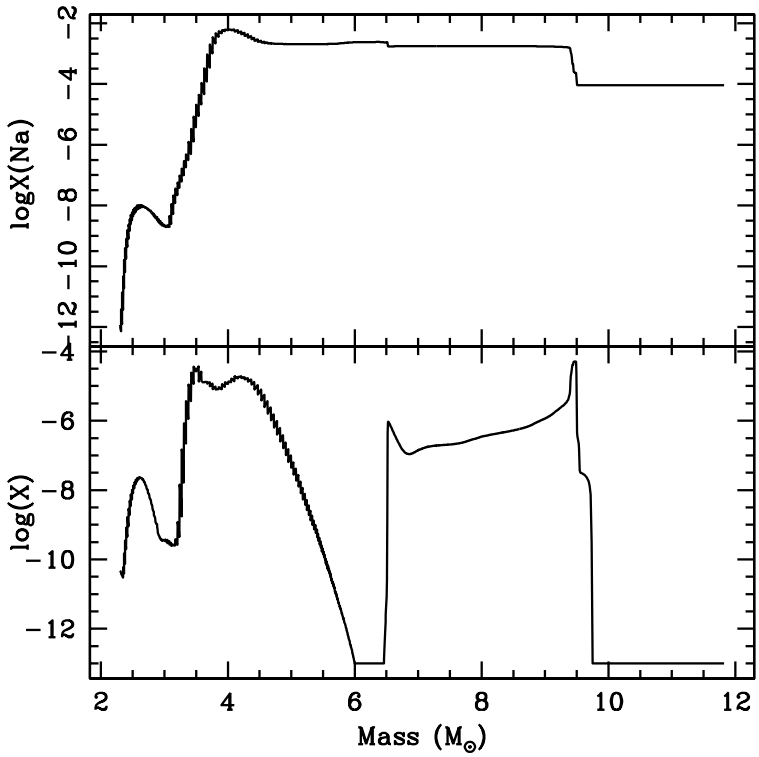

Figure D.7: Na (top) and ^{26}Al (bottom) for models 16m-run4, 23m-run5, 40m-run1, 23e-1.5, and d0.7s1.5. The abundances of both species drop considerably in the deepest layers. These regions have undergone oxygen burning during the star's lifetime or the explosion and produce no ^{26}Al . There are up to three peaks where X(^{26}Al)$> 10^{-}5$. These correspond to high temperature hydrostatic hydrogen burning and explosive burning at ~ 1.5 and $> 2.2 \times 10^{9}$ K. Models 16m, 23e, and 23 have a small hydrogen shell with enhanced ^{26}Al . The explosive C/Ne and sub-explosive C burning are close together and do not produce distinct peaks in 16m and 40m models.

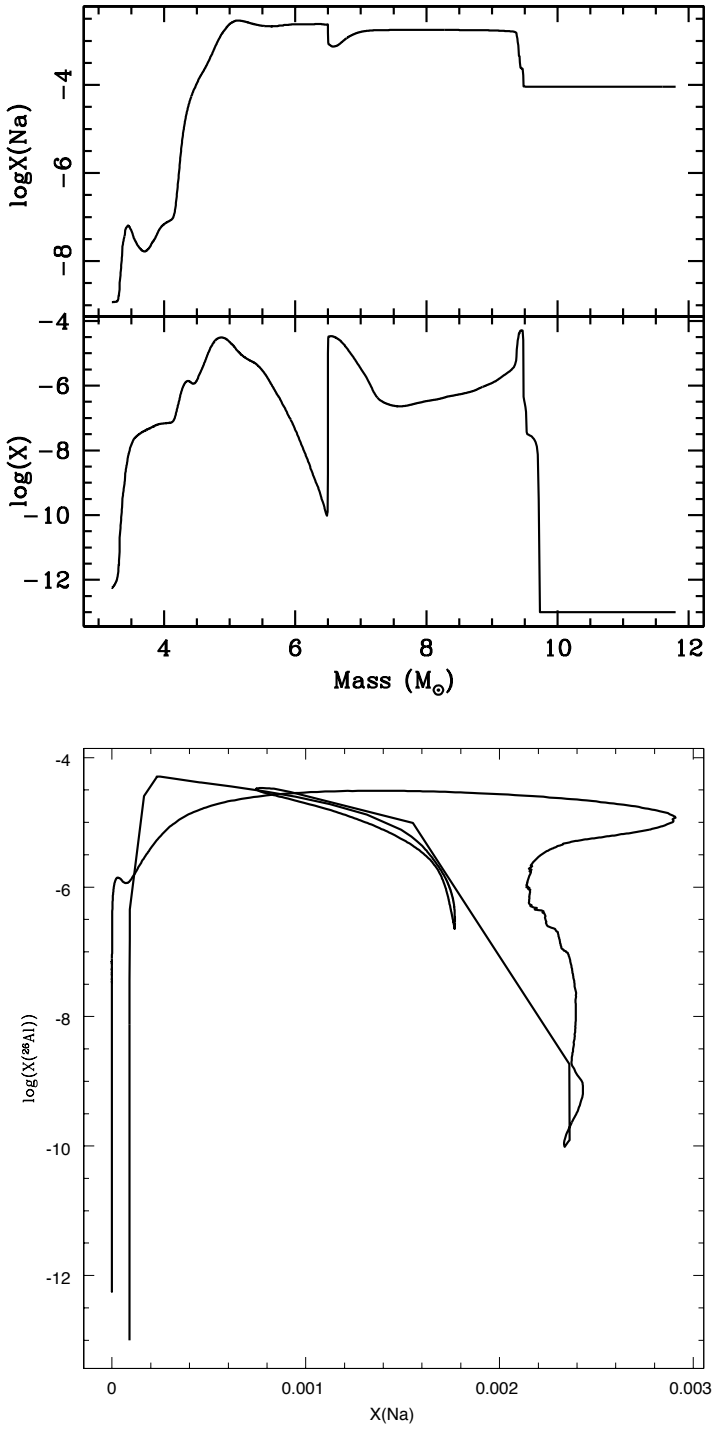

Figure D.8: Na and ^{26}Al (left) versus mass coordinate for the 23e-1.5 model (see Figure 2). ^{26}Al mass fraction versus Na mass fraction for the same model. There is a large range of Na abundance at high ^{26}Al mass fractions, and a large range of ^{26}Al values in regions enhanced in Na. The first peak corresponds to the H shell. This large range makes Na alone unsuitable for proxy studies.

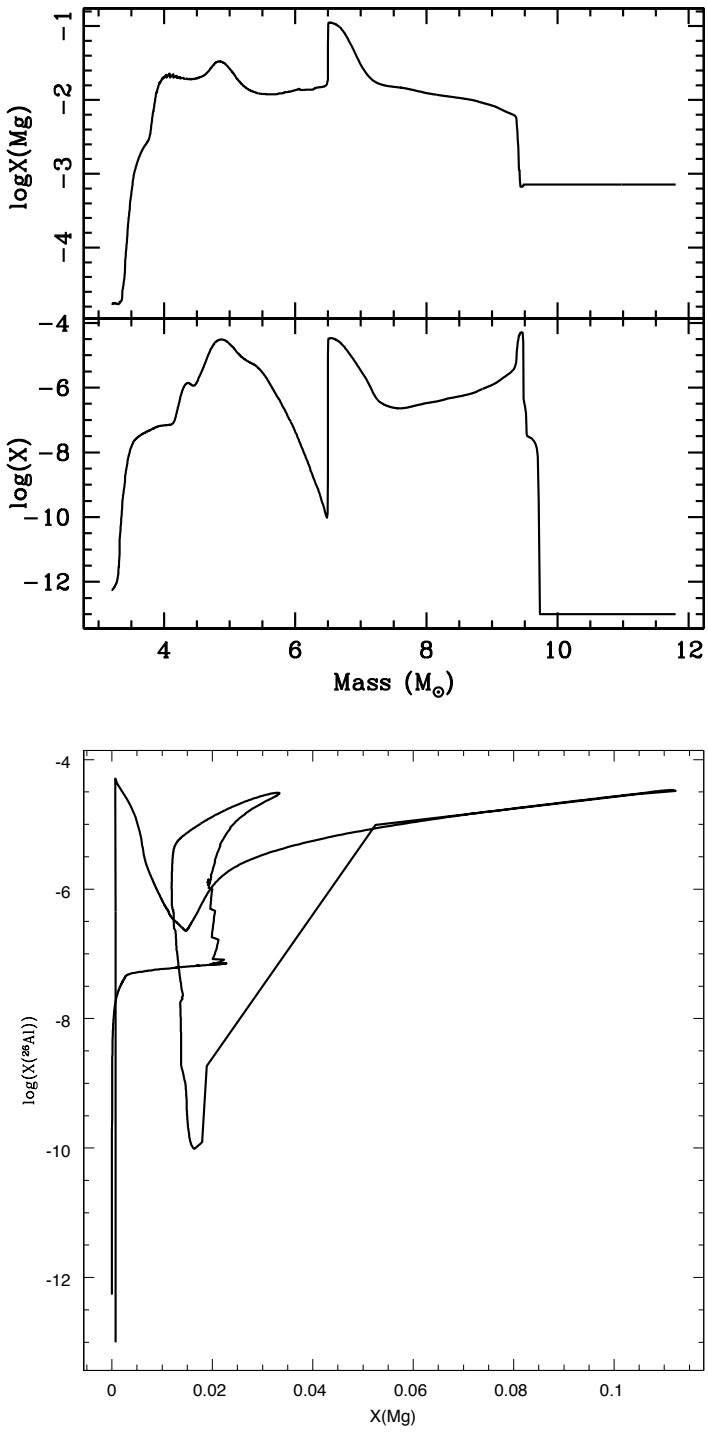

Figure D.9: Mg and ^{26}Al (left) versus mass coordinate for the 23e-1.5 model (see Figure 2). ^{26}Al mass fraction versus Mg mass fraction for the same model. There is a large range of Mg abundance at high ^{26}Al mass fractions. Very high enhancement of Mg only occurs for large ^{26}Al values, but this is not the case for all models. High Mg fractions are a good not conclusive indicator of high ^{26}Al abundances.

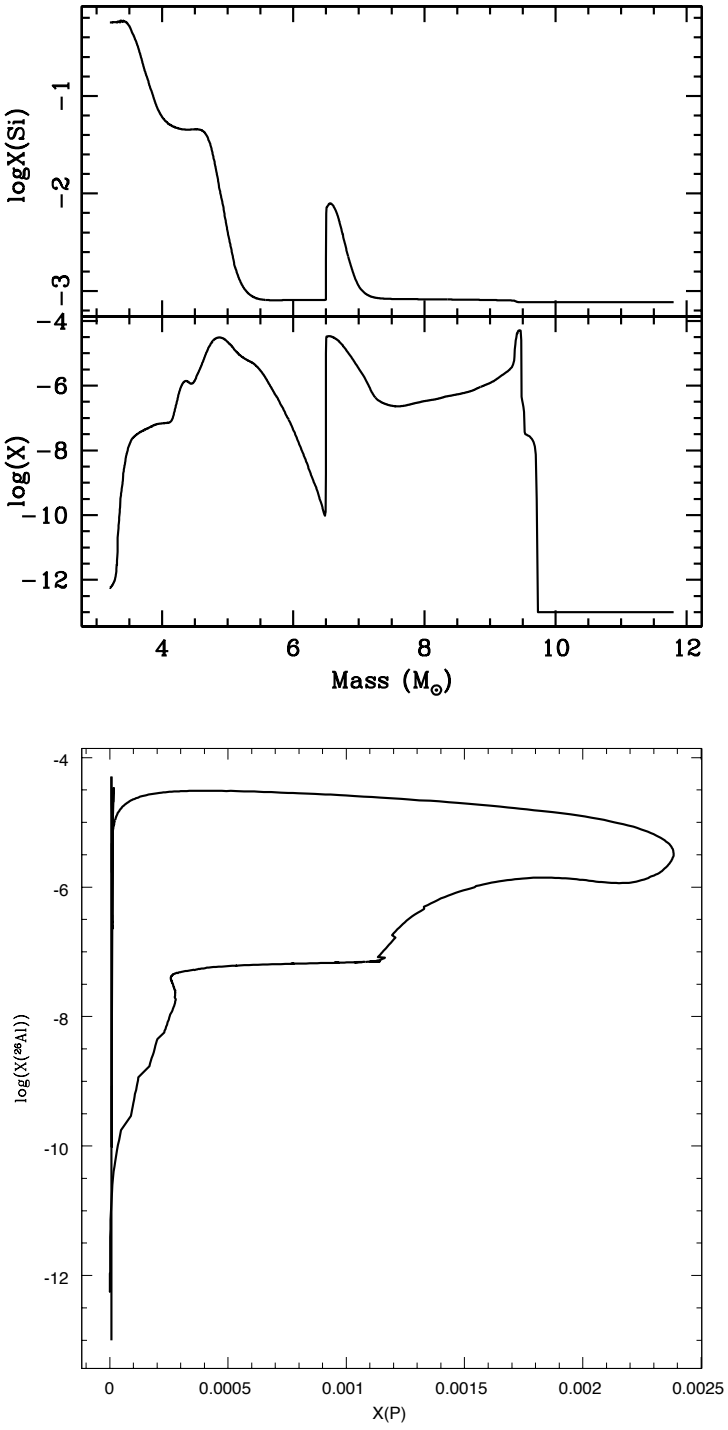

Figure D.10: P and ^{26}Al (left) for the 23e-1.5 model (see Figure 2). ^{26}Al mass fraction versus P mass fraction for the same model. The largest P enhancements occur for moderate to high ^{26}Al enhancements in all models. While P is of limited utility in proxy studies, indicators of ^{26}Al can also serve as P proxies, which would be of interest to astrobiology.

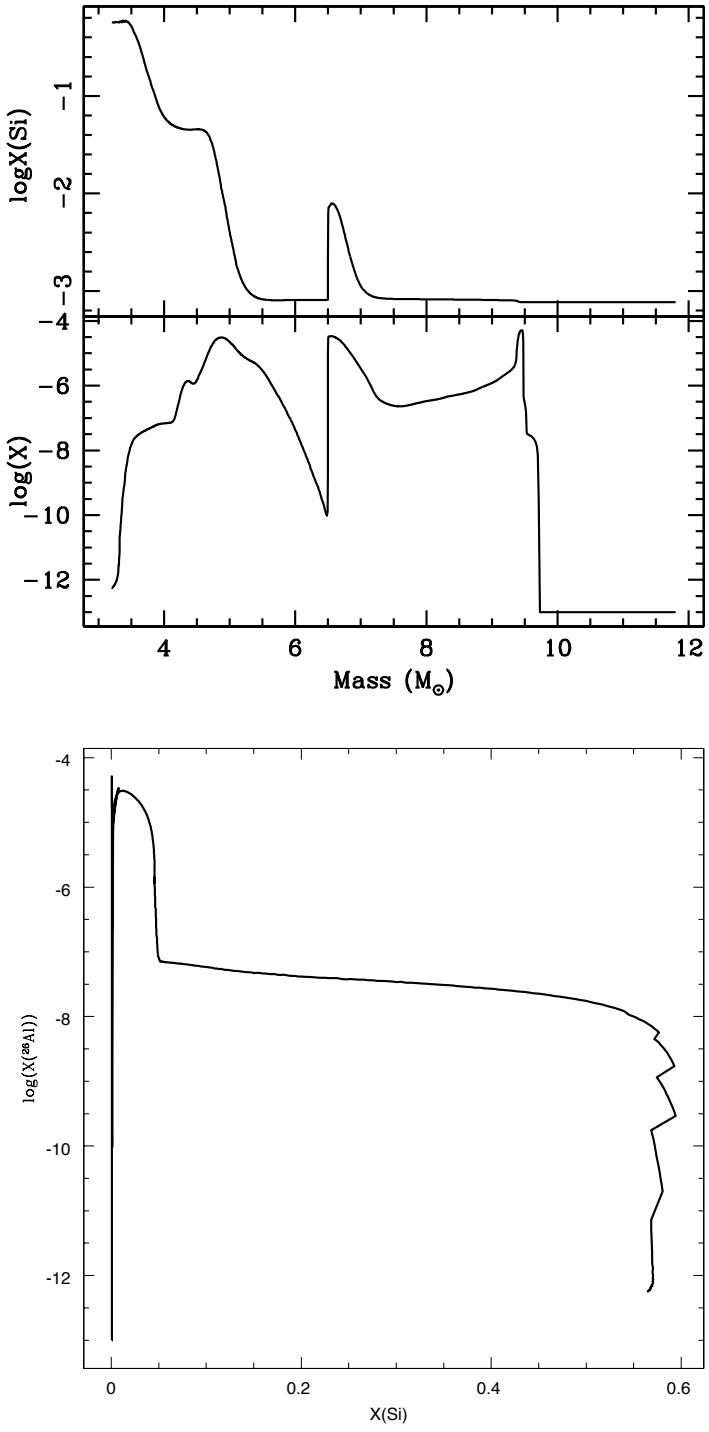

Figure D.11: Si and ^{26}Al (left) for the 23e-1.5 model (see Figure 2). ^{26}Al mass fraction versus Si for the same model. Si is modestly enhanced to a few percent for high ^{26}Al mass fractions. The peak at approximately solar Si abundance is from the H shell.

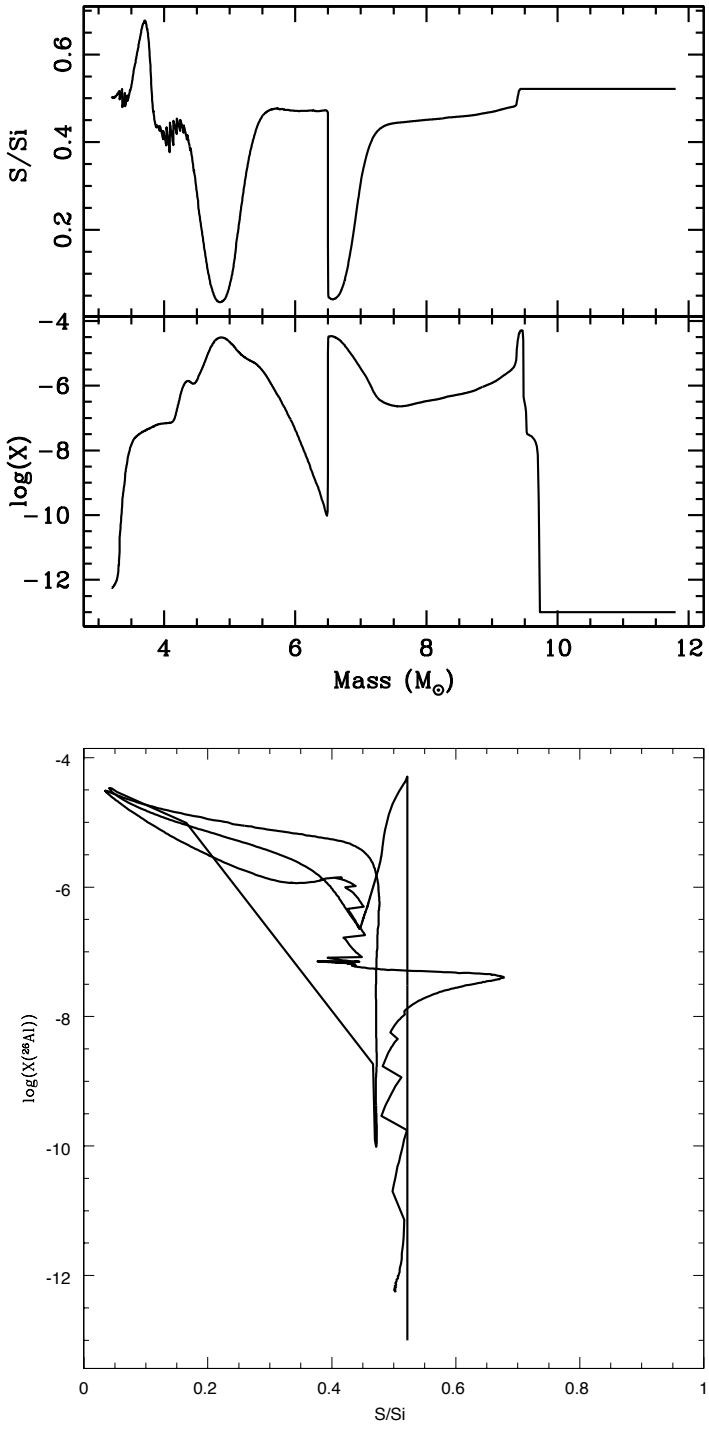

Figure D.12: S/Si and ^{26}Al (left) for the 23e-1.5 model (see Figure 2). ^{26}Al mass fraction versus S/Si for the same model. The S/Si ratio drops to low values only in the region os high ^{26}Al abundance. As for other species, the peak in ^{26}Al at solar values of S/Si corresponds to the H burning shell. Low S/Si should be uniquely diagnostic for material enhanced in ^{26}Al by explosive burning.

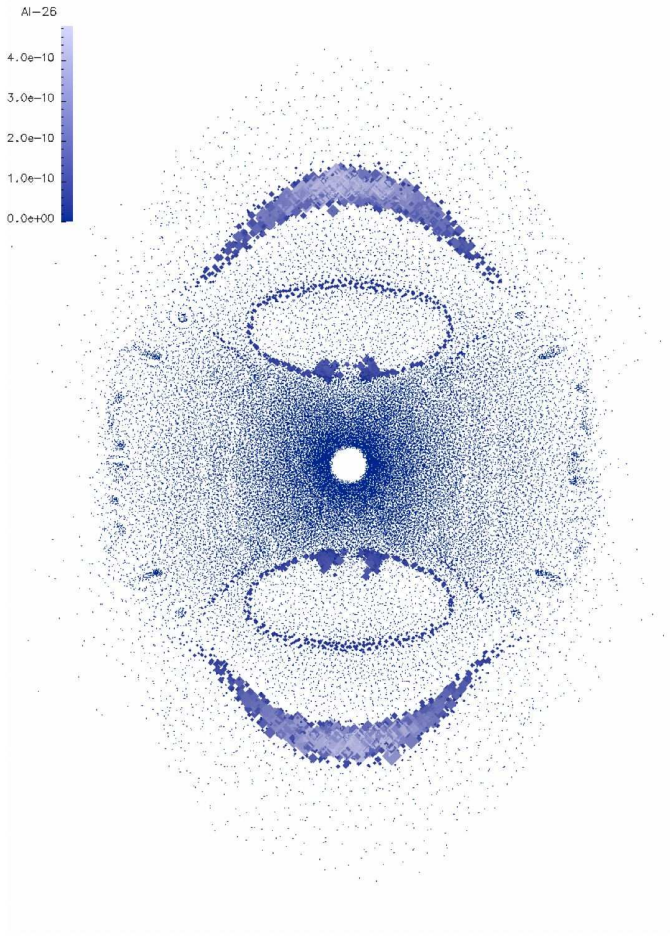

Figure D.13: ^{26}Al mass per particle for a 10^9cm thick slice through the x-z plane. The outer bubble of high ^{26}Al abundance has reached C burning temperatures. The inner ring and bubble reach Ne burning conditions.

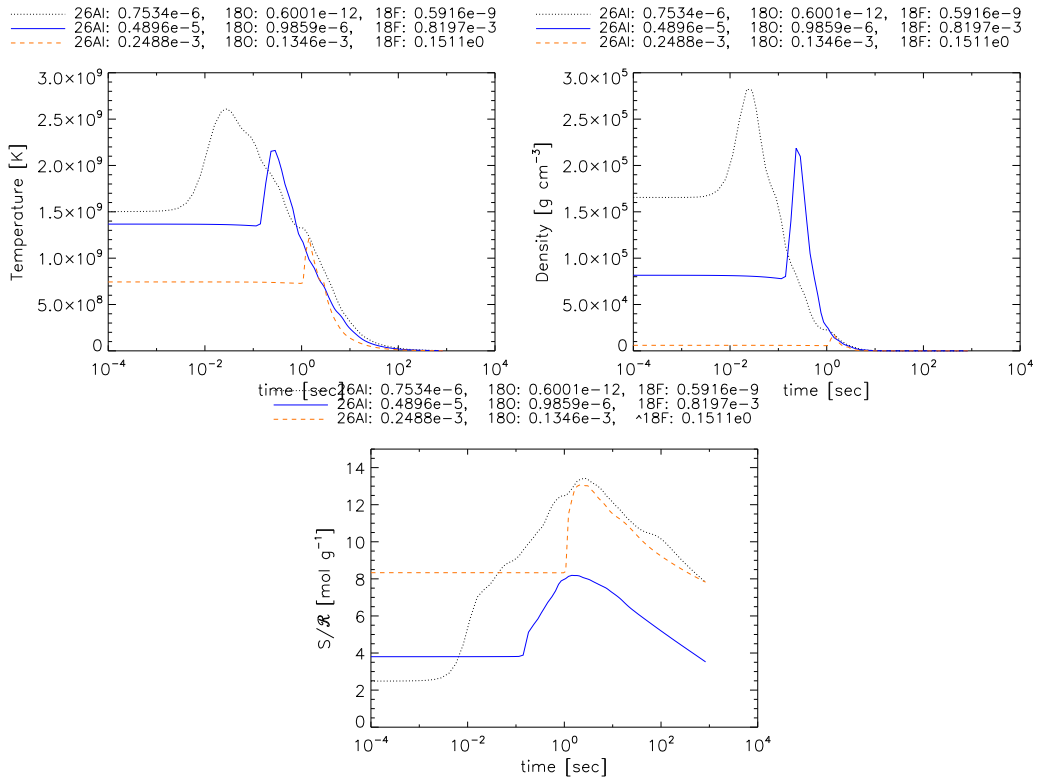

Figure D.14: Shown is the time evolution of temperature, density, and entropy for representative examples of particles from the Ring and Bubble region of the 3D calculation. Each line is labelled with the abundance of ^{26}Al, ^{18}O, and ^{18}F (above each graph) in mass fraction per particle at the end of the simulation.

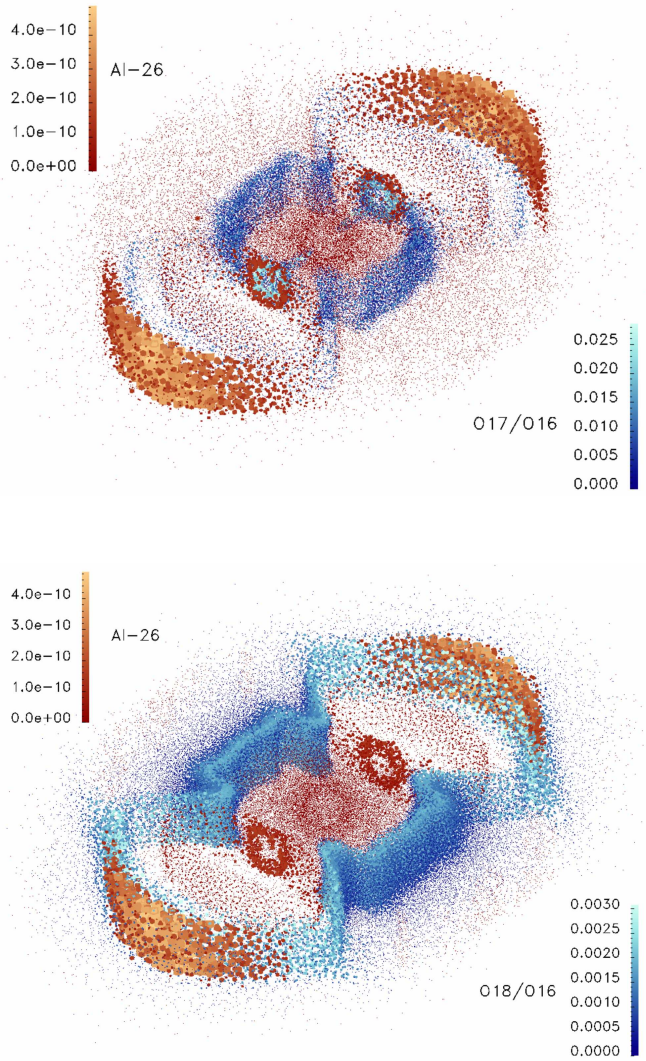

Figure D.15: Shown is a 2.0×10^{11} cm thick slice in the x-z plane of the 3D simulation. ^{26}Al abundances are in red-tones (amount per particle in $M_{\odot}$) and number ratio of ^{17}O/^{16}O (top panel) or ^{18}O/^{16}O (bottom panel) per particle in blue-tones. The sizes of the data points are arbitrarily chosen, but scale with their values. A color gradient was also used to visualize the different abundances per particle. The ligher colors/bigger data points correspond to higher abundances. Apparent is a Ring on either side of the center along the axis of symmetry, and further out from them the Bubbles, where the highest ^{26}Al abundance is found.

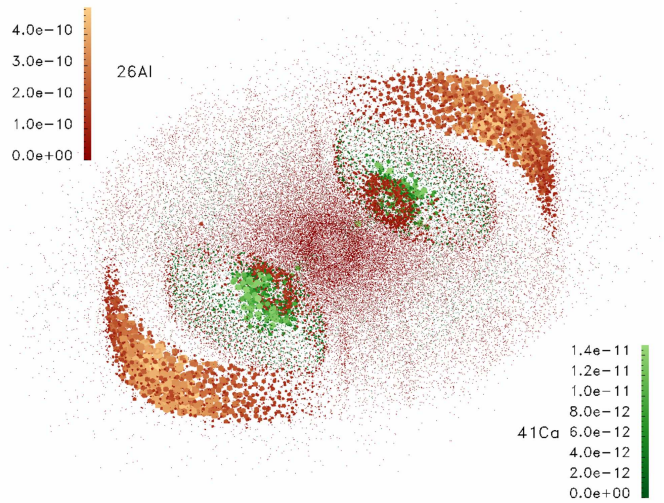

Figure D.16: Same as Figure D.15 but with ^{41}Ca shown in green. The highest ^{41}Ca abundance is adjacent to the Rings, and only partially overlaps with the Ring-regions.

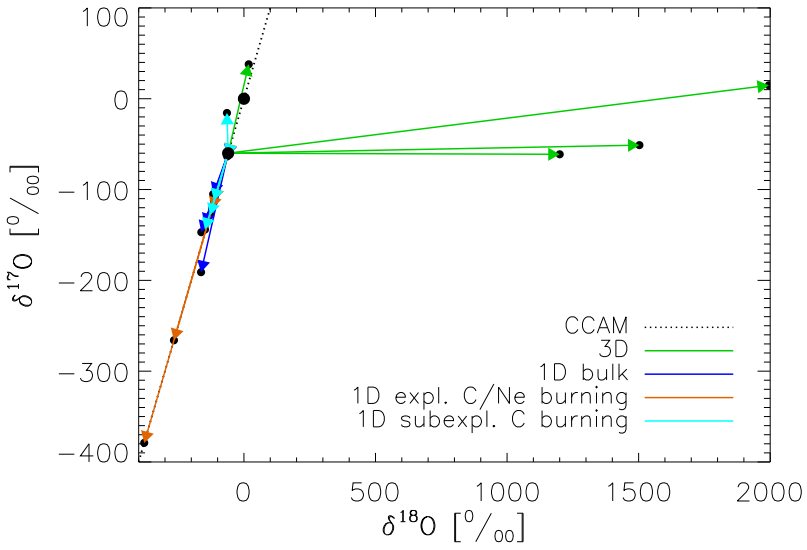

Figure D.17: Three isotope plot showing the shifts in the oxygen isotopes we calculate following injection of supernova material for different scenarios. The shifts from he 3D cases are plotted in green, those from the 1D bulk cases are plotted in blue, the 1D explosive C/Ne burning cases are plotted in orange, and the 1D sub-explosive C burning cases are plotted in cyan. Indicated by the bigger black dots are SMOW at ($0\ ^0/_{00}, 0\ ^0/_{00}$) and our assumed pre-injection composition at ($-60\ ^0/_{00}, -60\ ^0/_{00}$). The very large shift of the 3D bulk scenario was omitted for clarity.

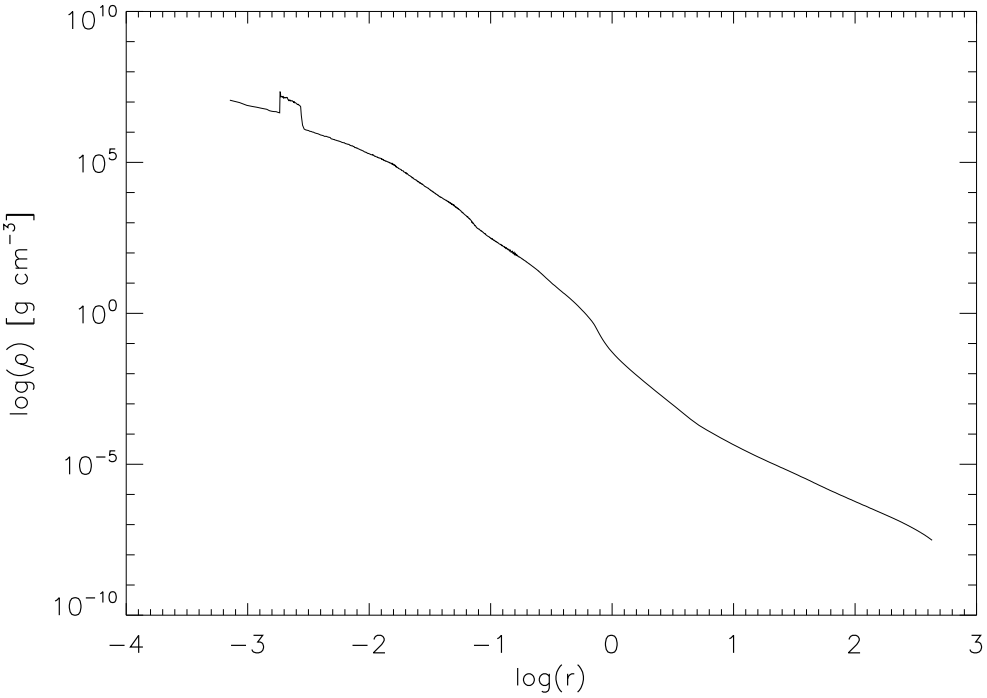

Figure D.18: 1D radial density profile of the progenitor at the point of mapping the explosion into 3D.

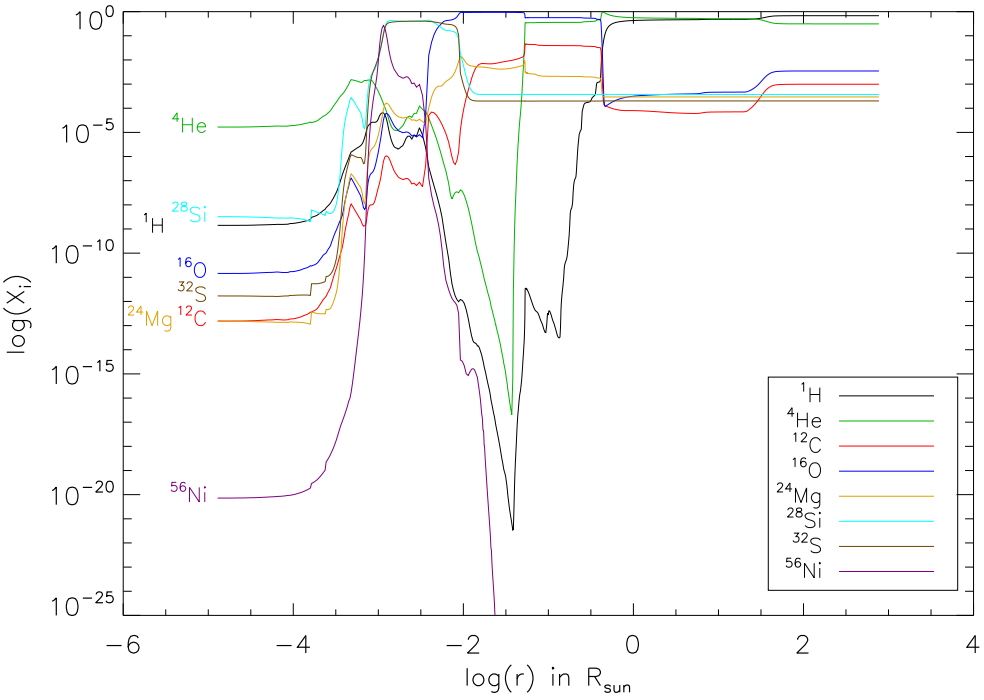

Figure D.19: 1D abundance profile of the progenitor at the point of collapse.

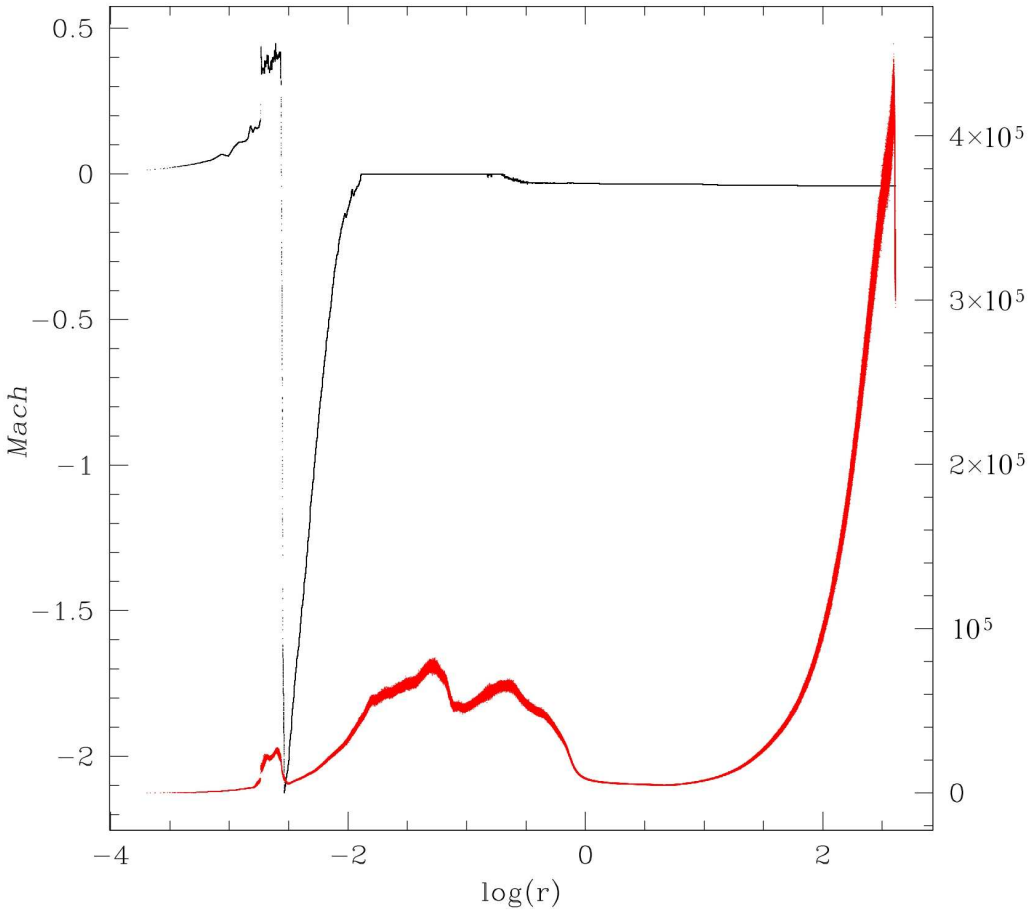

Figure D.20: Mach number (black, left axis) and mass as ρr^3(red, right axis) of the exploded progenitor at the start of the 3D calculations.

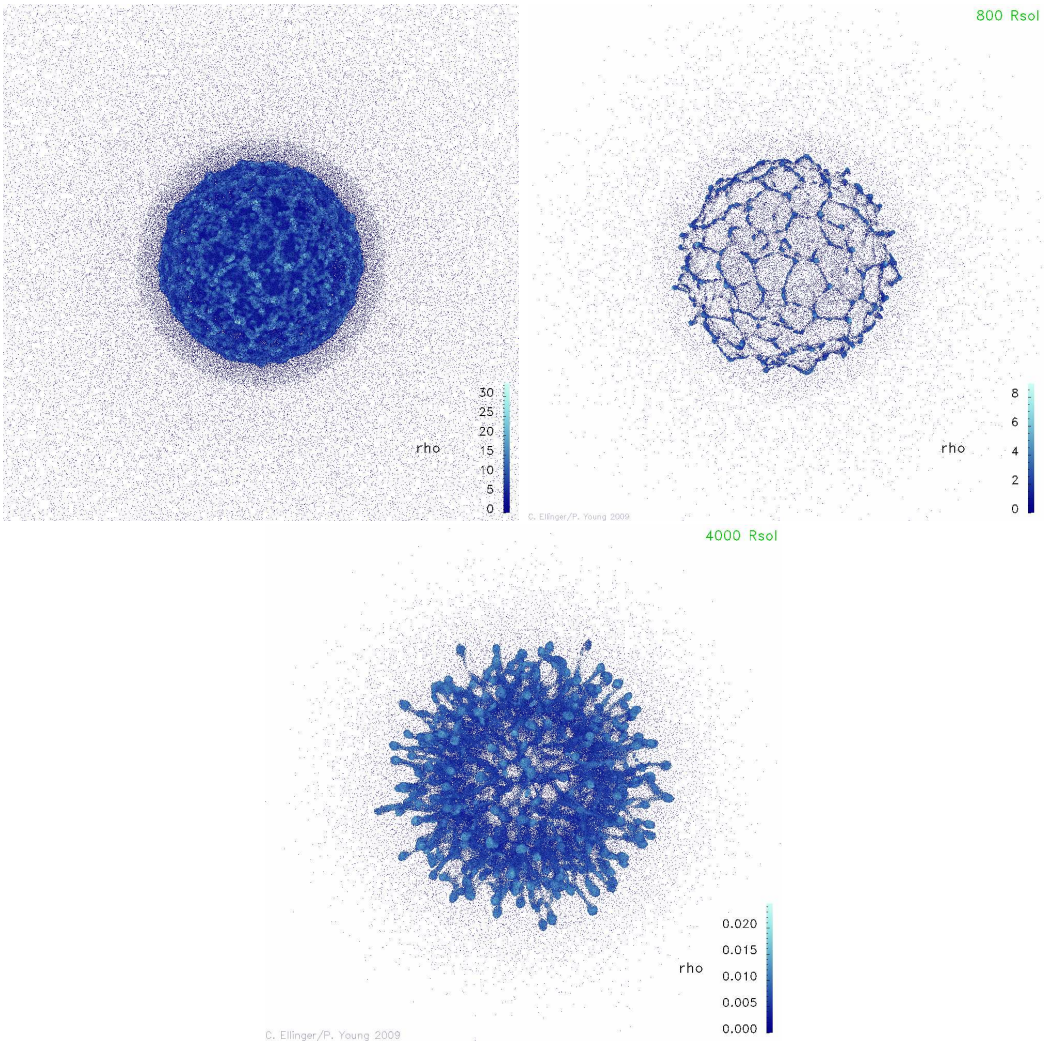

Figure D.21: Shown is a sequence of snapshots from the 1M_no–burn run to show the progression of the RT fingers. The first plot is at $\sim$ 50 min and shows only the central region; the high–mode asymmetry from the forming RT instability is apparent as over–densities arranged in a web like pattern. The second plot is at $\sim$2.6 hrs; the mode/web like pattern is now very apparent. The third plot is at $\sim$26 hrs. The first and third plot show all of the star, the second plot only shows the anterior hemisphere of the star. Both a color gradient and scaled glyph sizes were used to show the different densities.

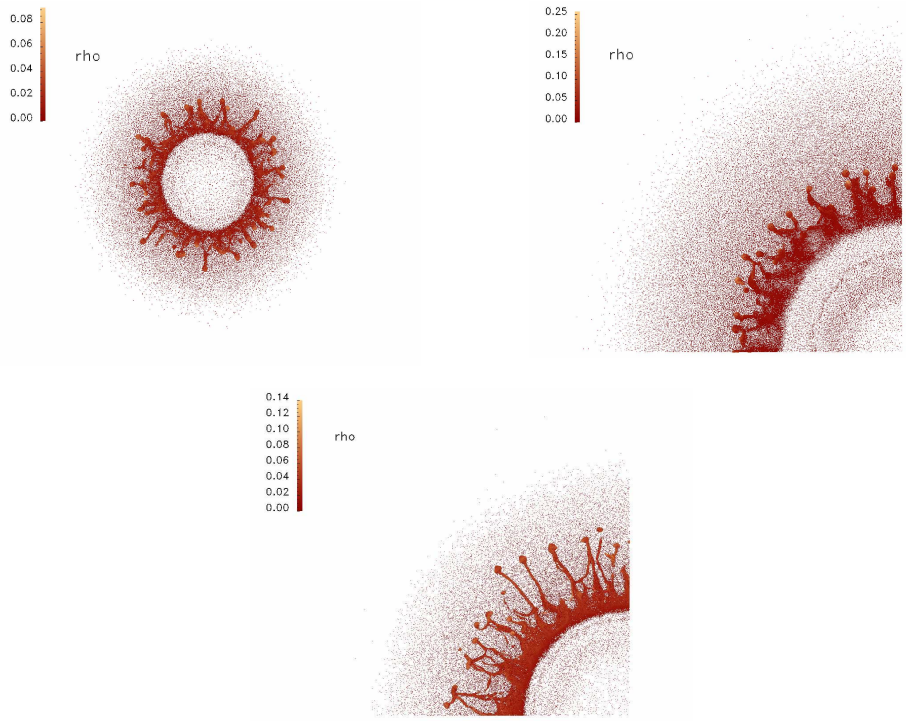

Figure D.22: Shown are density maps for the different resolutions of the canonical run. From top to bottom, the plotted resolutions are for the 1M_burn (at 26.3 hrs, 1304 $R_\odot$), 10M_burn (at 22.6 hrs, 1215 $R_\odot$), and 50M_burn (at 22.0 hrs, 1191 $R_\odot$) runs. All runs are plotted a few hours after shock break out. Each plot spans 1400 $R_\odot$ on a side. Both a color gradient and scaled glyph sizes were used to show the different densities. Lighter shades in the color gradient mark high values, darker shades mark low values. Note that the color gradient spans multiple orders of magnitude. The unit of the density is in code units, where 1 density unit = $1 \times 10^{-6}\ M_\odot / {R_\odot}^3 = 0.6 \times 10^5 \mathrm{g/cm}^3$. The highest density is seen in the clumps, i.e. the mushroom caps of the RT fingers in each run. Although the extend of the fingers is increased in the higher resolution, the size of the clumps remains the same.

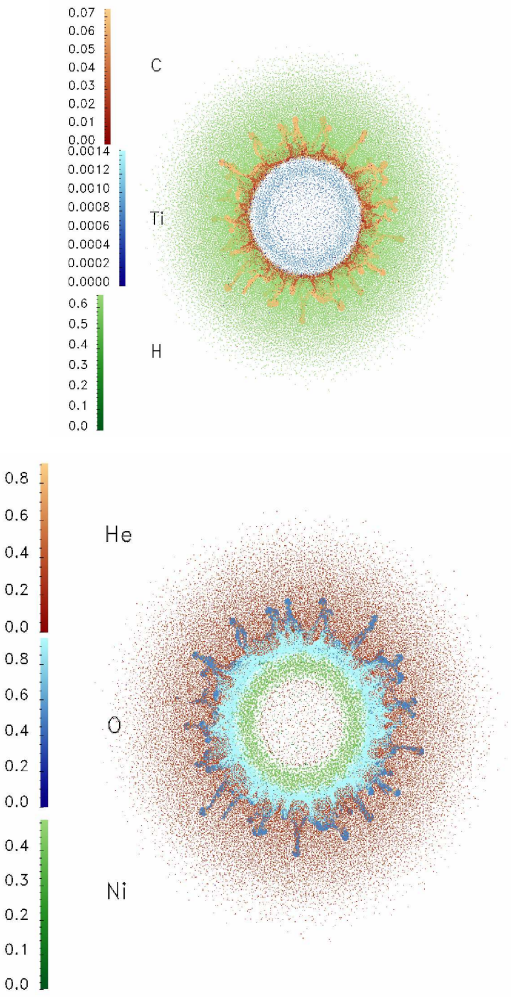

Figure D.23: Abundance maps for run 1M_burn (26.3 hrs after explosion). The radius of the star at this point is 1304 $R_{\odot}$. Plotted abundances are at the same time step as the density in fig. D.22 and are shown in mass fraction per particle. The RT fingers are apparent as high concentrations of C and He, and medium concentration of O. Ni remains inside of/below the RT region.

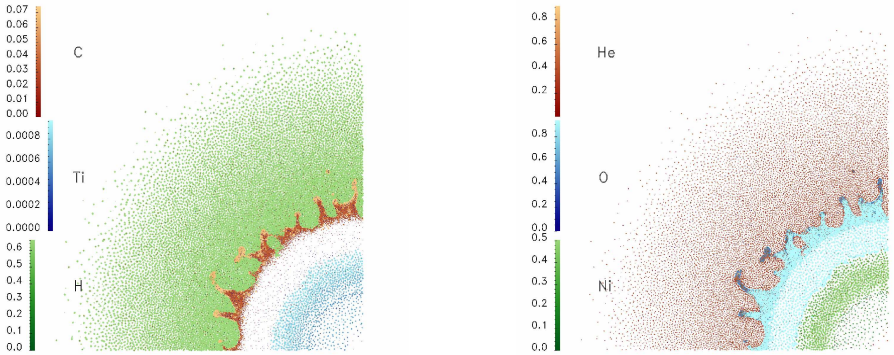

Figure D.24: Same as figure D.23, but for run 10M_burn.

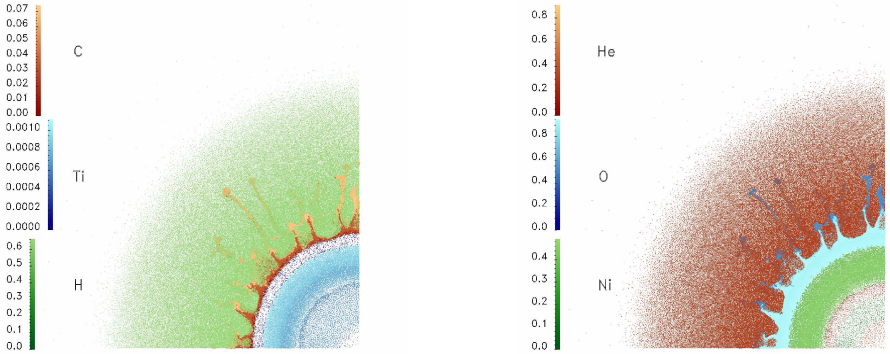

Figure D.25: Same as figure D.23, but for run 10M_burn.

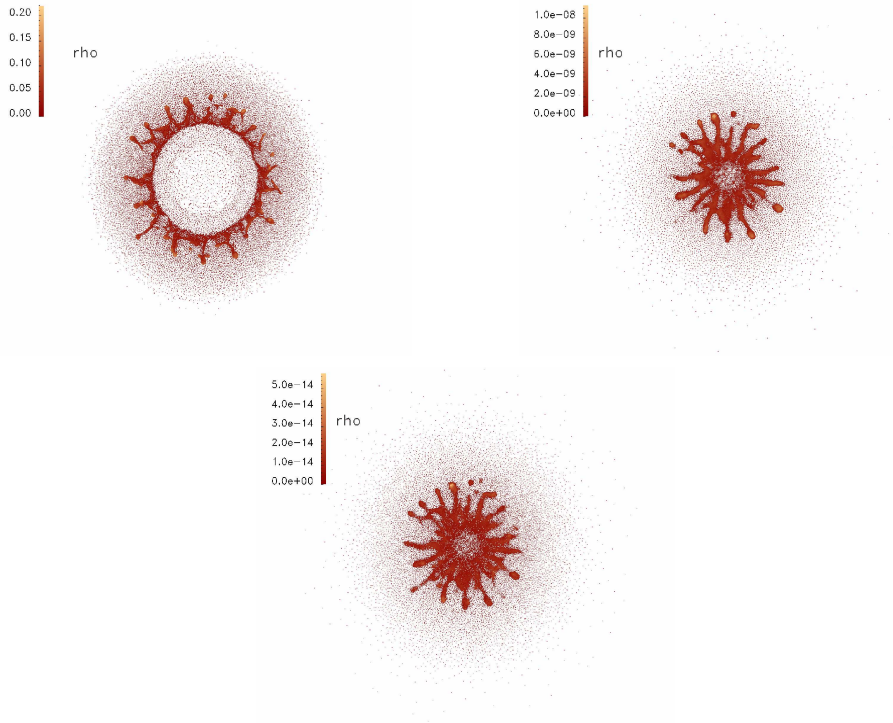

Figure D.26: Density maps for run 1M_no–burn at different time steps in the evolution. The top left is at 19.8*hrs*, 934 $R_\odot$, top right is at 0.517*yrs*, 334477 $R_\odot$, and bottom is at 31.8*yrs*, 2.07×10^7 $R_\odot$. Note the absence of the Ni-bubble in the second and third plots.

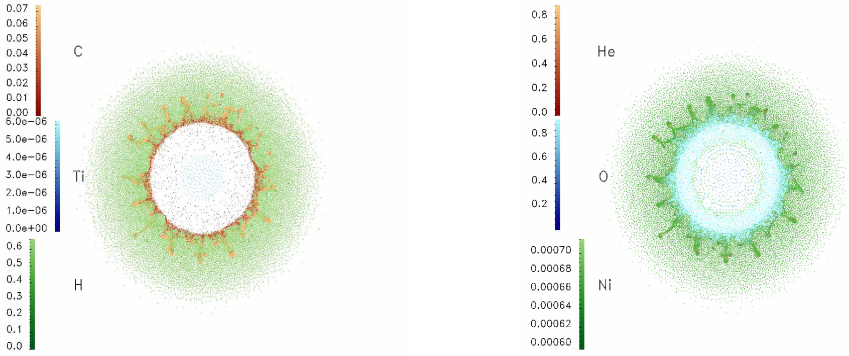

Figure D.27: Abundance maps of selected isotopes for run 1M_no–burn at the first snapshot in figure D.26. Ni seems rather prevalent in the H- envelope, though note that it is at a very low abundance, and actually Fe, not Ni.

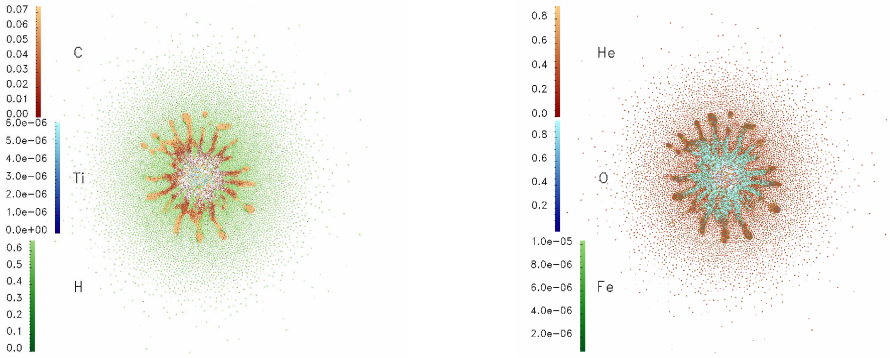

Figure D.28: Abundance maps of selected isotopes for run 1M_no–burn at the second snapshot in figure D.26. Some H has visibly been mixed down below the C-rich region. O has been mixed out as well as in. Note the absence of the Ni-bubble since the decay of Ni was not tracked in this run.

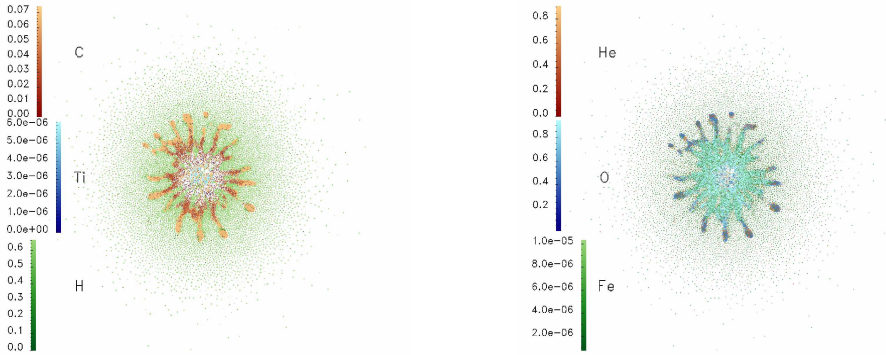

Figure D.29: Same as figure D.28, but for the third snapshot in figure D.26. Differences in the plots are due to different rendering of the glyphs.

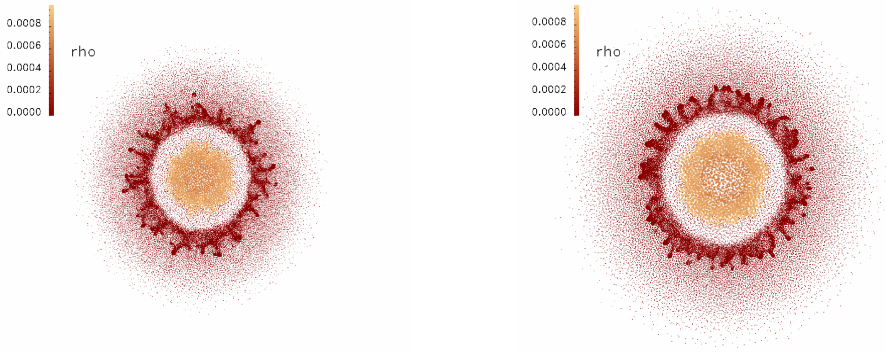

Figure D.30: Comparison between 1M_burn_38nbrs (left) and 1M_burn_70nbrs (right) simulations: Density maps. The 1M_burn_38nbrs run is at 19.4 hrs after explosion, at a size of 975 $R_{\odot}$. The 1M_burn_70nbrs run is at 24.0*hrs* after explosion, at a size of 1240 $R_{\odot}$.

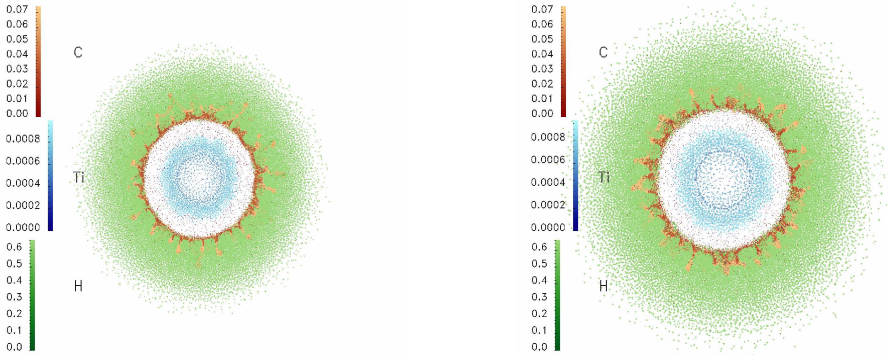

Figure D.31: Comparison between the 1M_burn_38nbrs (left) and 1M_burn_70nbrs (right) simulations: Abundance maps.

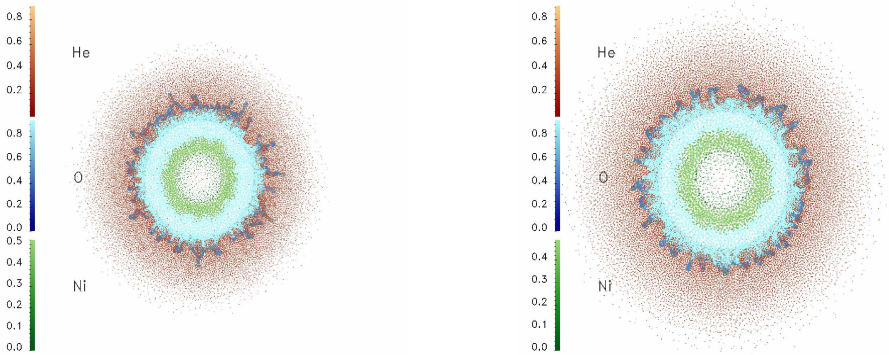

Figure D.32: Comparison between the 1M_burn_38nbrs (left) and 1M_burn_70nbrs (right) simulations: Abundance maps.

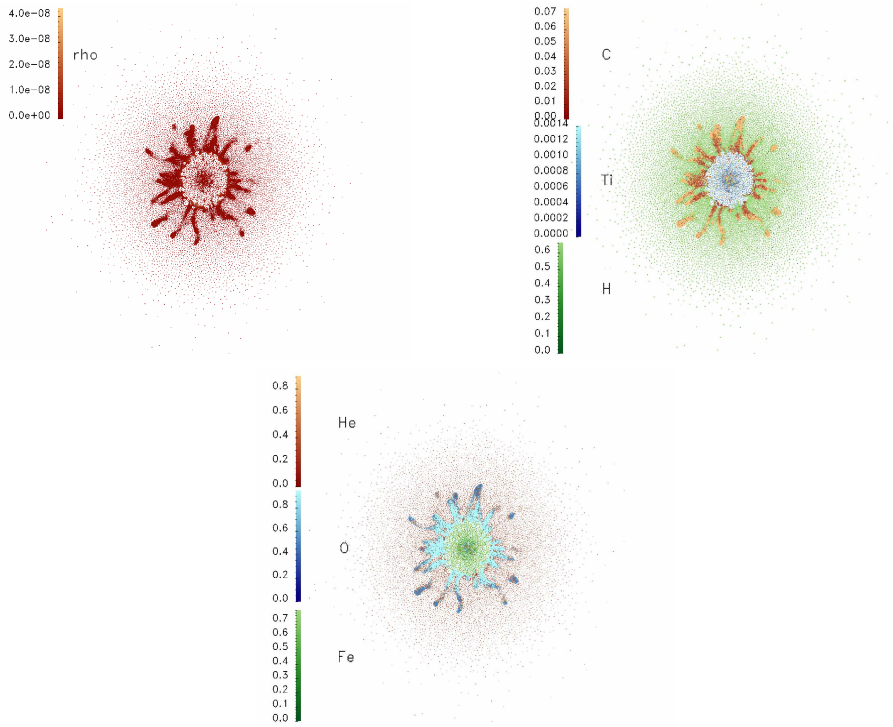

Figure D.33: Density and abundance maps for run 1M_jet2. Plots are at 0.507*yrs* after the explosion, at a size of 326168 $R_{\odot}$.

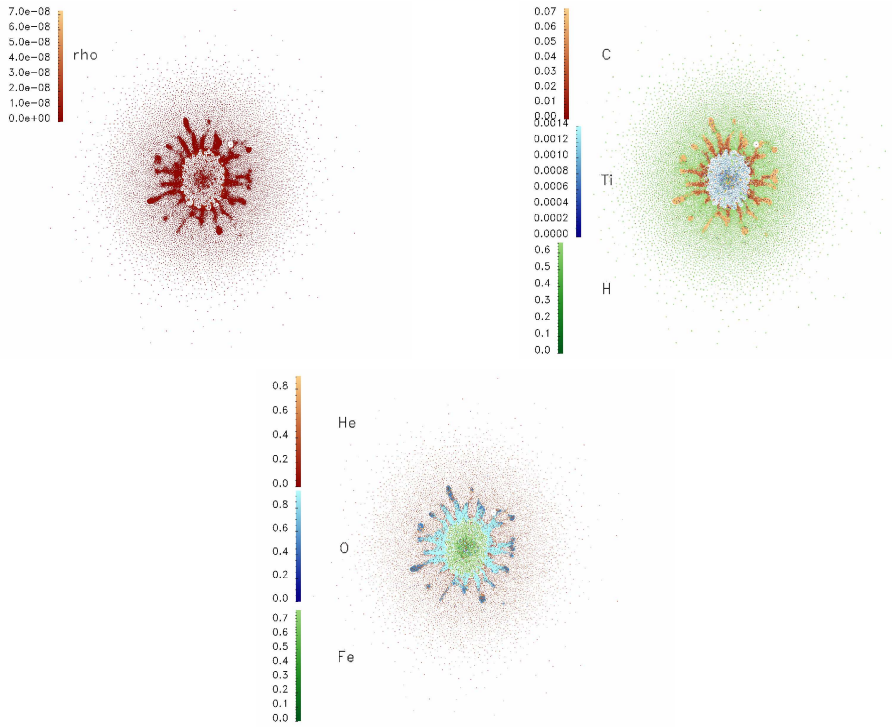

Figure D.34: Density and abundance maps for run 1M_jet4. Plots are at 0.489*yrs* after the explosion, at a size of 314849 $R_{\odot}$.

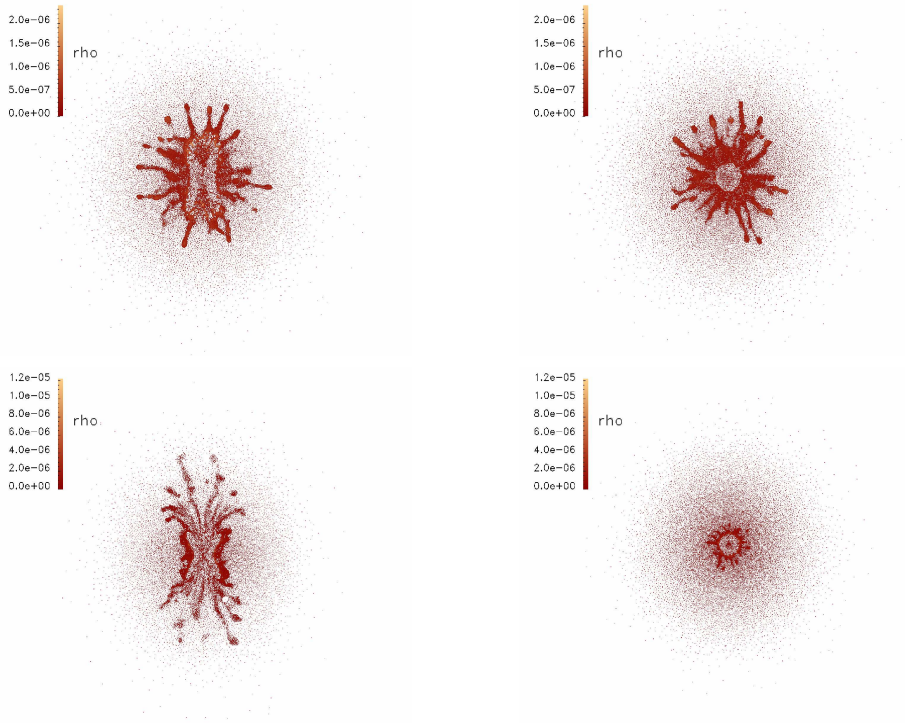

Figure D.35: Shown are the density maps for scenario 1M_jet4L (top panels) and 1M_jet4LL (bottom panels). The asymmetry implemented is the jet4 asymmetry in HFW 03 at different time steps in the explosion.

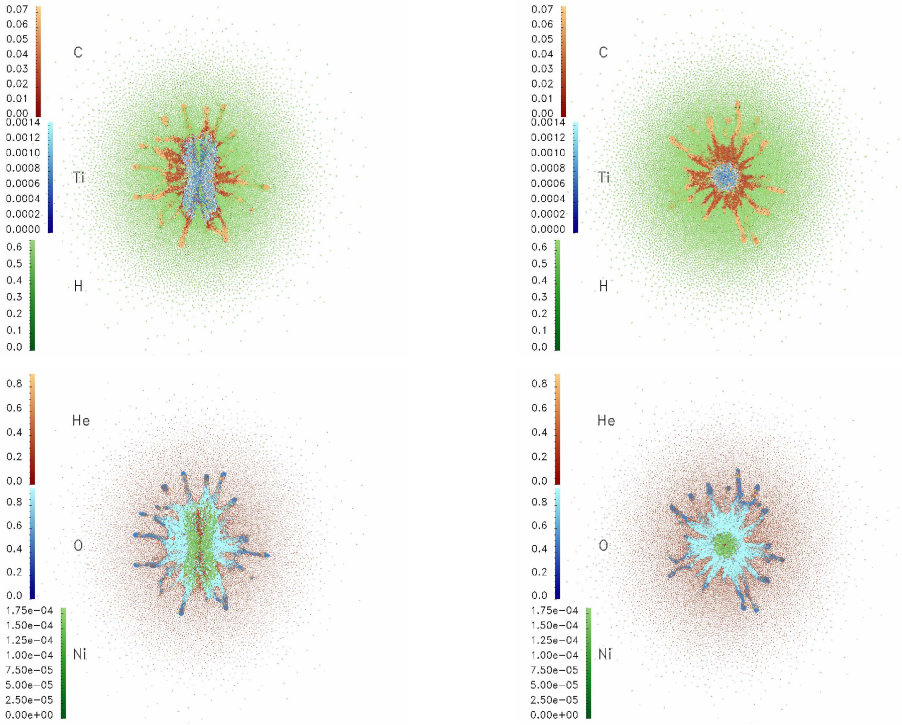

Figure D.36: Abundance maps for the 1M_jet4L scenario; shown are slices parallel and perpendicular to the polar axis. H and He are visibly mixed inwards along the asymmetry axis, while Ni/Fe and Ti are mixed somewhat closer into the RT fingers.

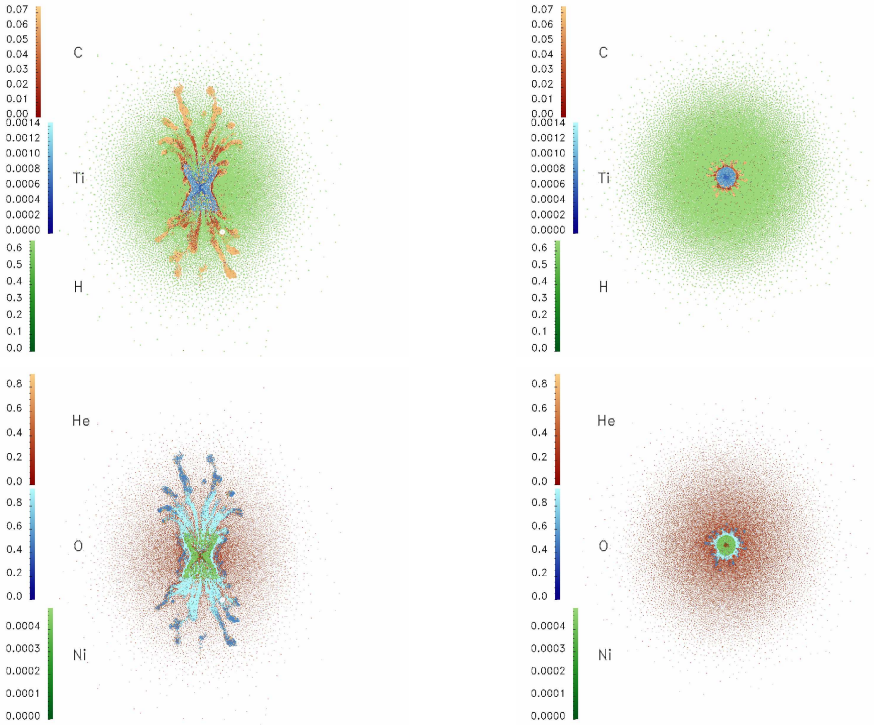

Figure D.37: Abundance maps for the 1M_jet4LL scenario; shown are slices parallel and perpendicular to the polar axis.

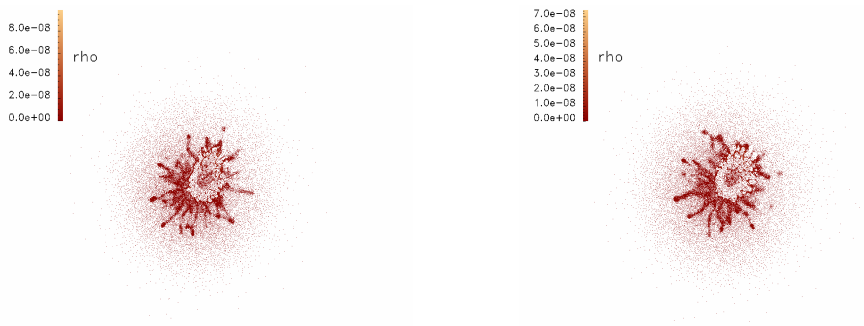

Figure D.38: Shown are density plots for the single-lobe scenarios 1M_single–jet2 and 1M_single–jet4.

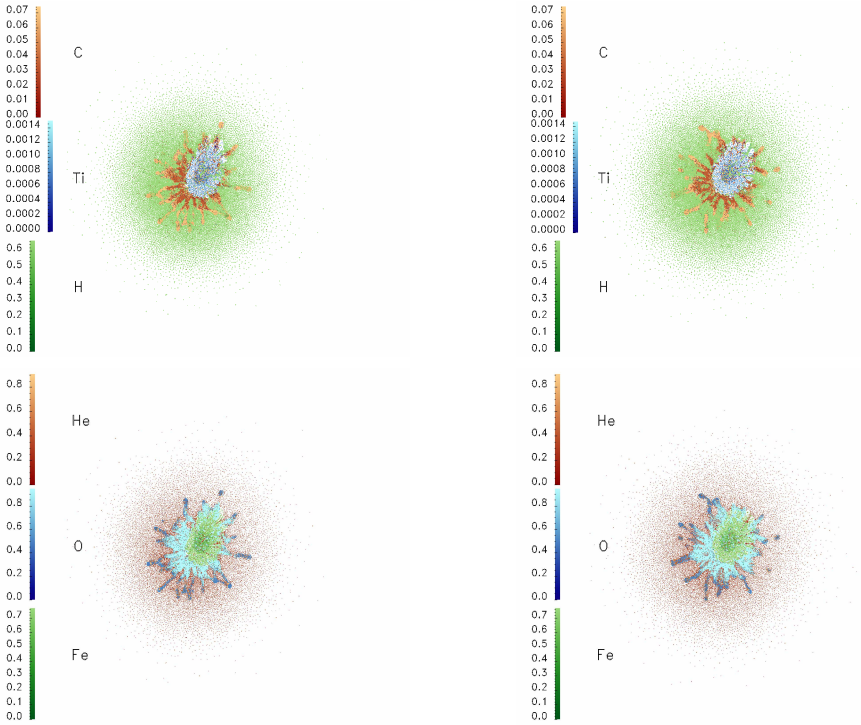

Figure D.39: Shown are abundance maps for the single-lobe scenarios 1M_single–jet2 and 1M_single–jet4.

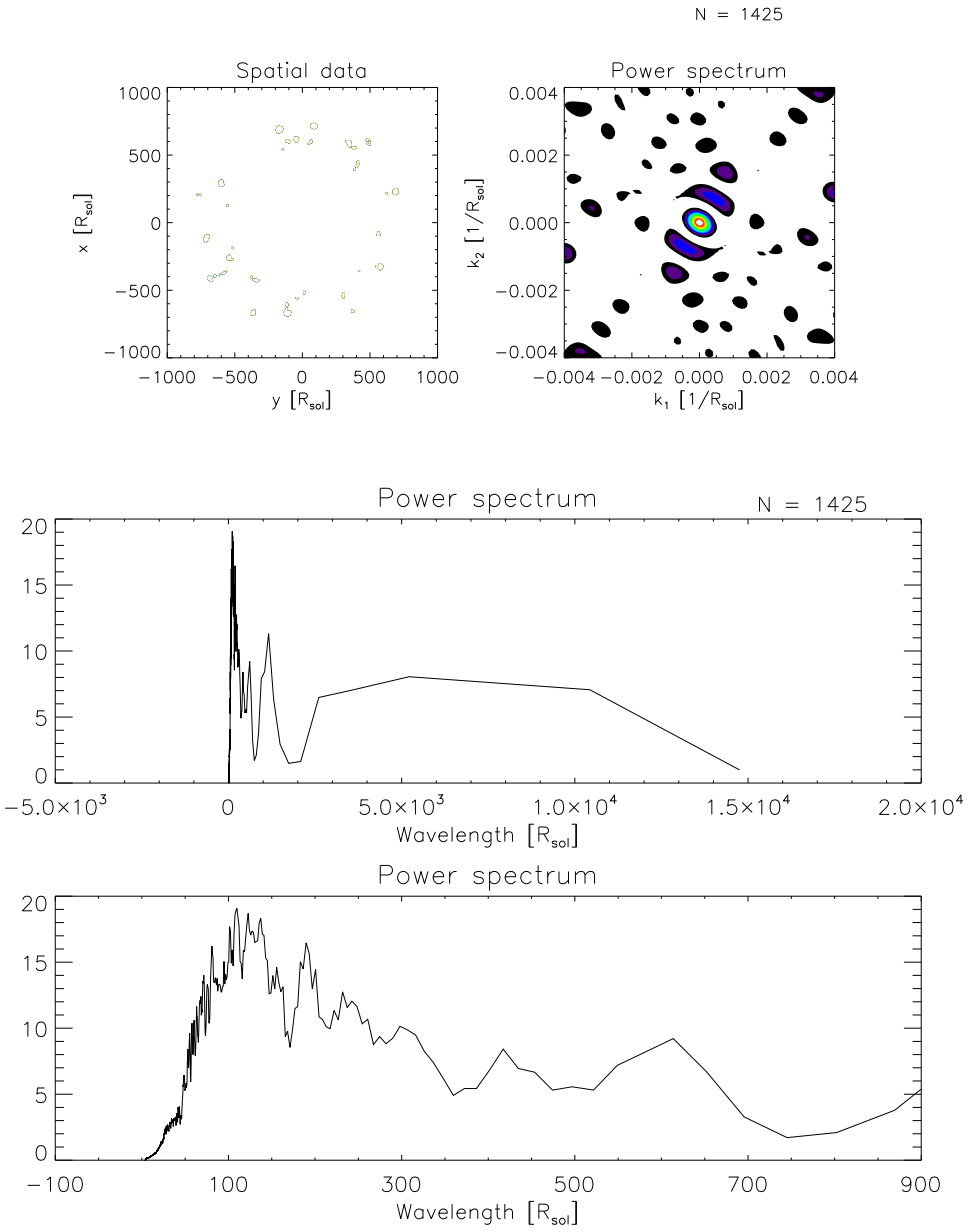

Figure D.40: Plotted are the 'image' (i.e. data slice; top left), the 2D power spectrum (top right), the 1D summed power spectrum for the whole range of wavelengths (middle), and the 1D summed power spectrum expanded for short wavelengths (bottom panel) for the canonical run at 26 hrs, corresponding to the time step plotted in figures D.22 and D.23. The number of SPH particles included in the data image is indicated above the middle panel. Features seen in the power spectrum are discussed in the text. All following plots are organized in a similar fashion

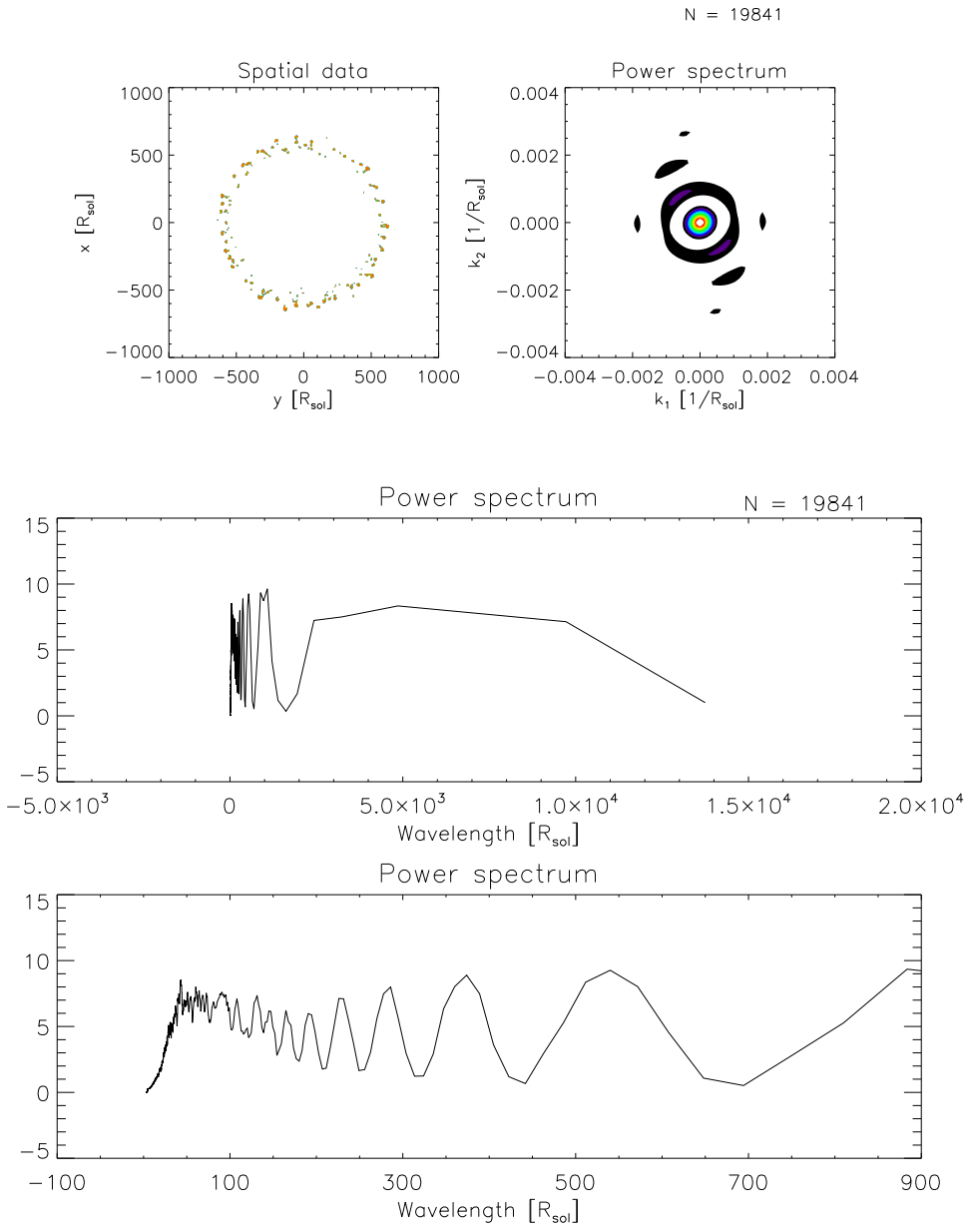

Figure D.41: The 10M_burn run at 22.6 hrs, corresponding to the time step plotted in figures D.22 and D.24.

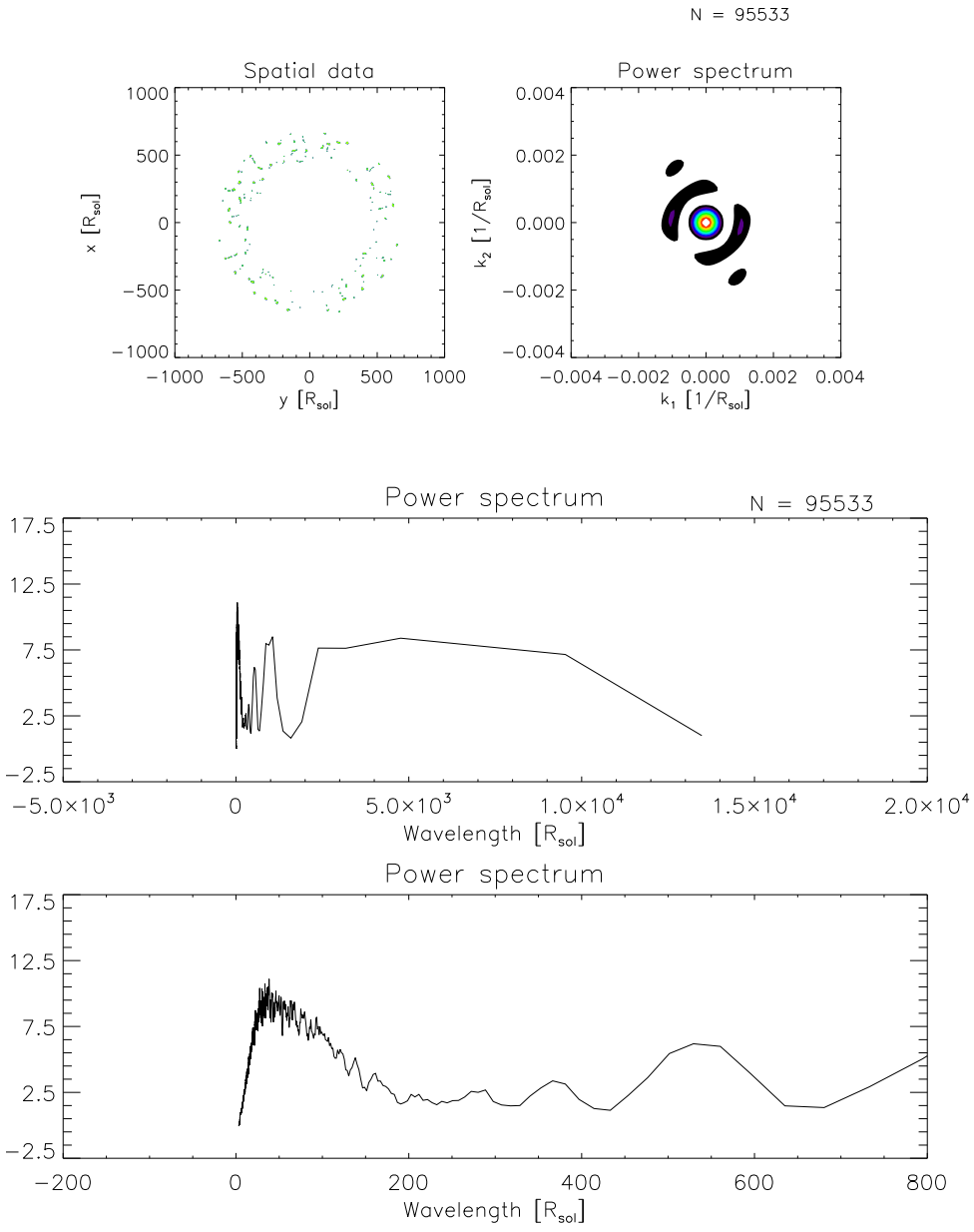

Figure D.42: The 50M_burn run at 22.0 hrs, corresponding to the time step plotted in figures D.22 and D.25.

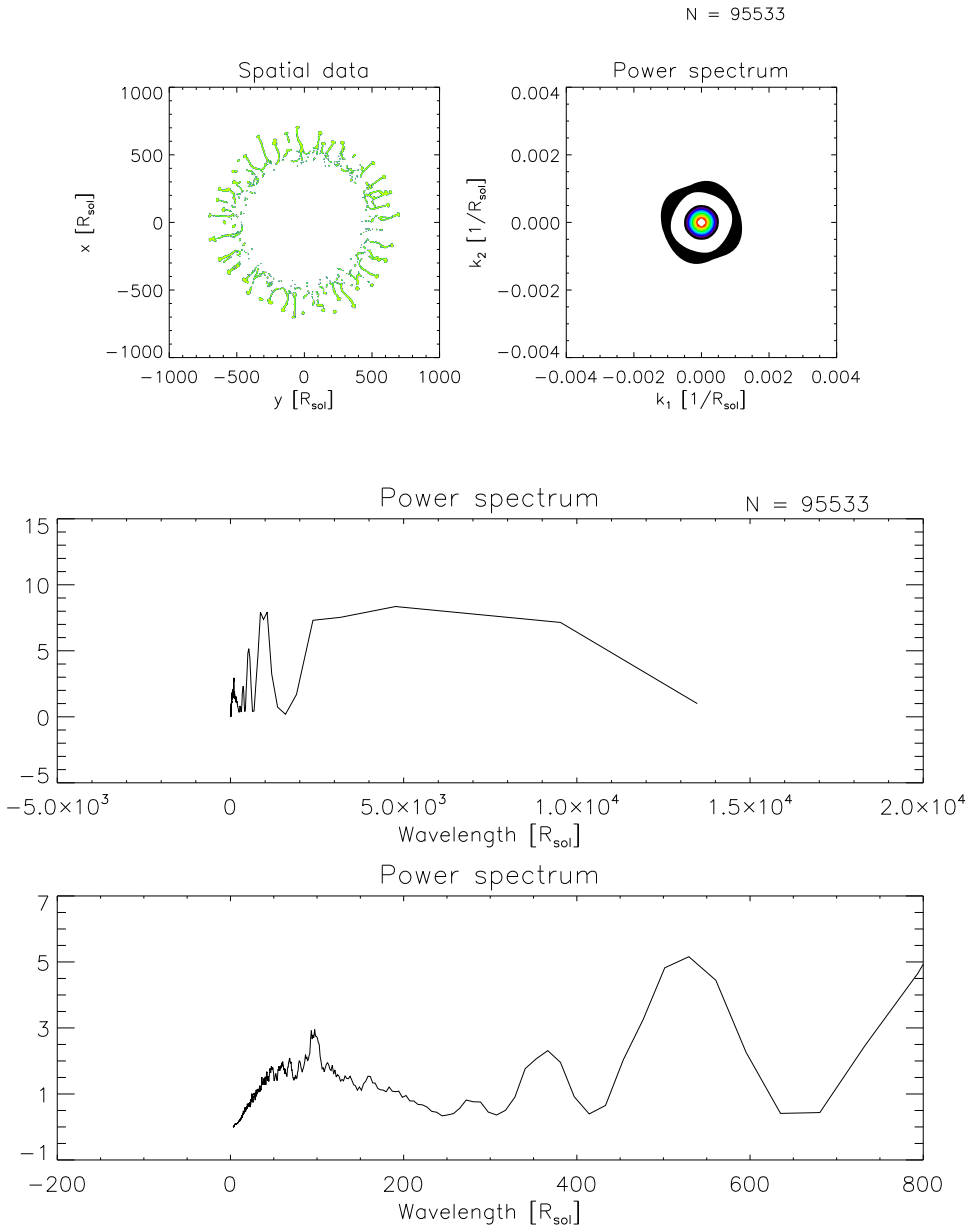

Figure D.43: Same as figure D.42, but with a lower density threshold to examine the filamentary structure. In comparison with that plot it can be noted that there are overdense clumps throughout the entire RT unstable region.

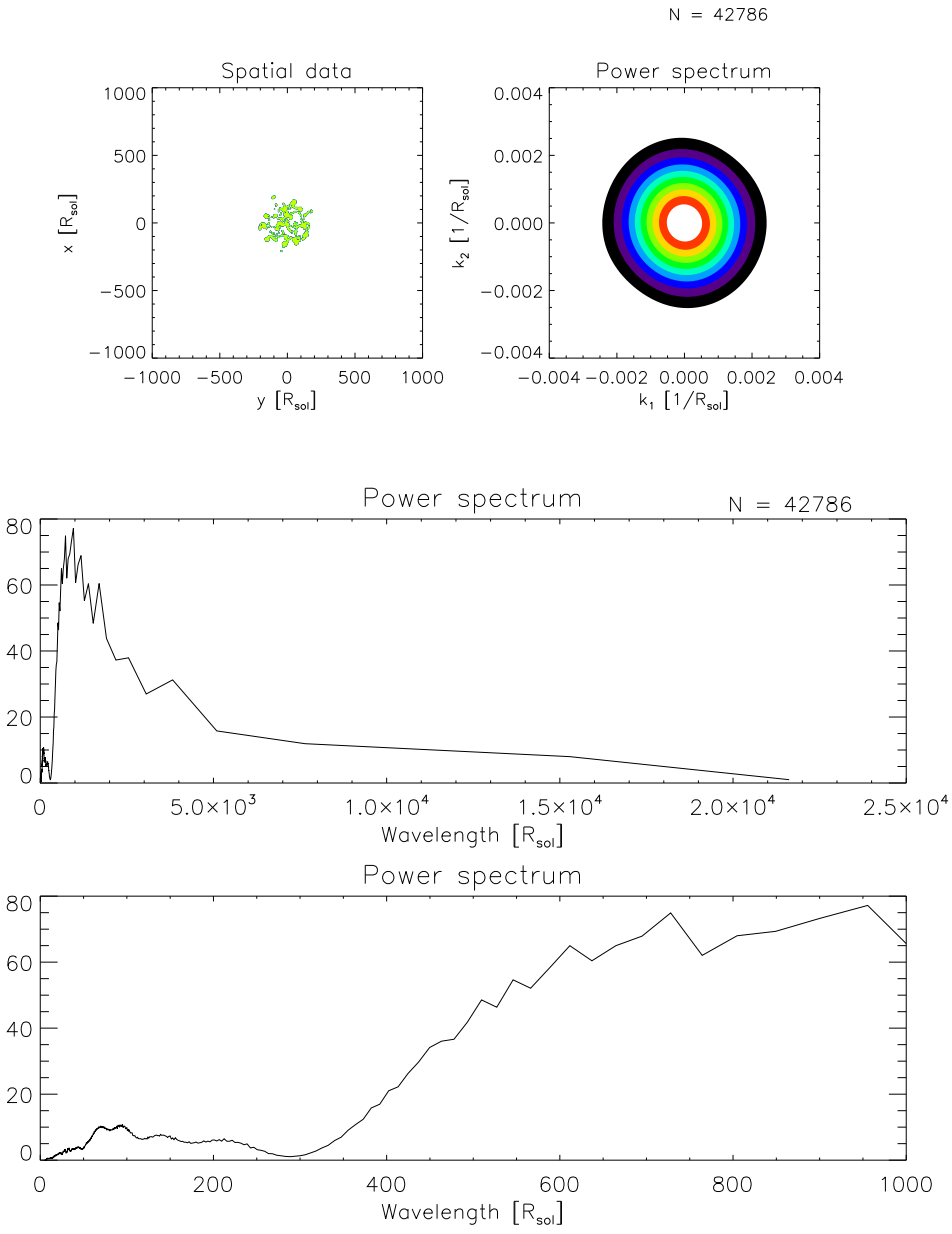

Figure D.44: Same as figure D.42, but for a slice near the edge of the star to show the web structure.

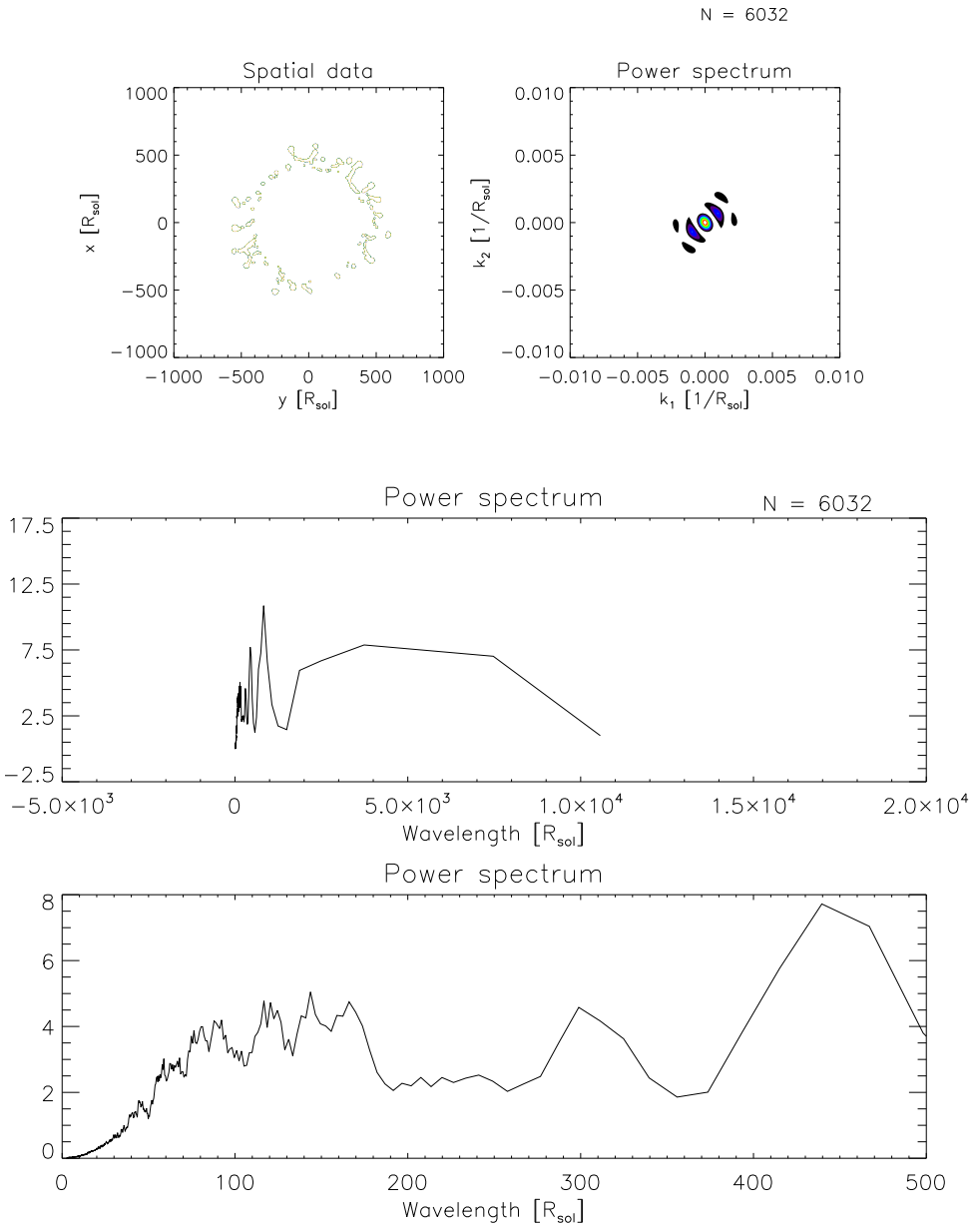

Figure D.45: Run 1M_no–burn at 19.9hrs corresponding to the time step plotted in figures D.26 and D.27.

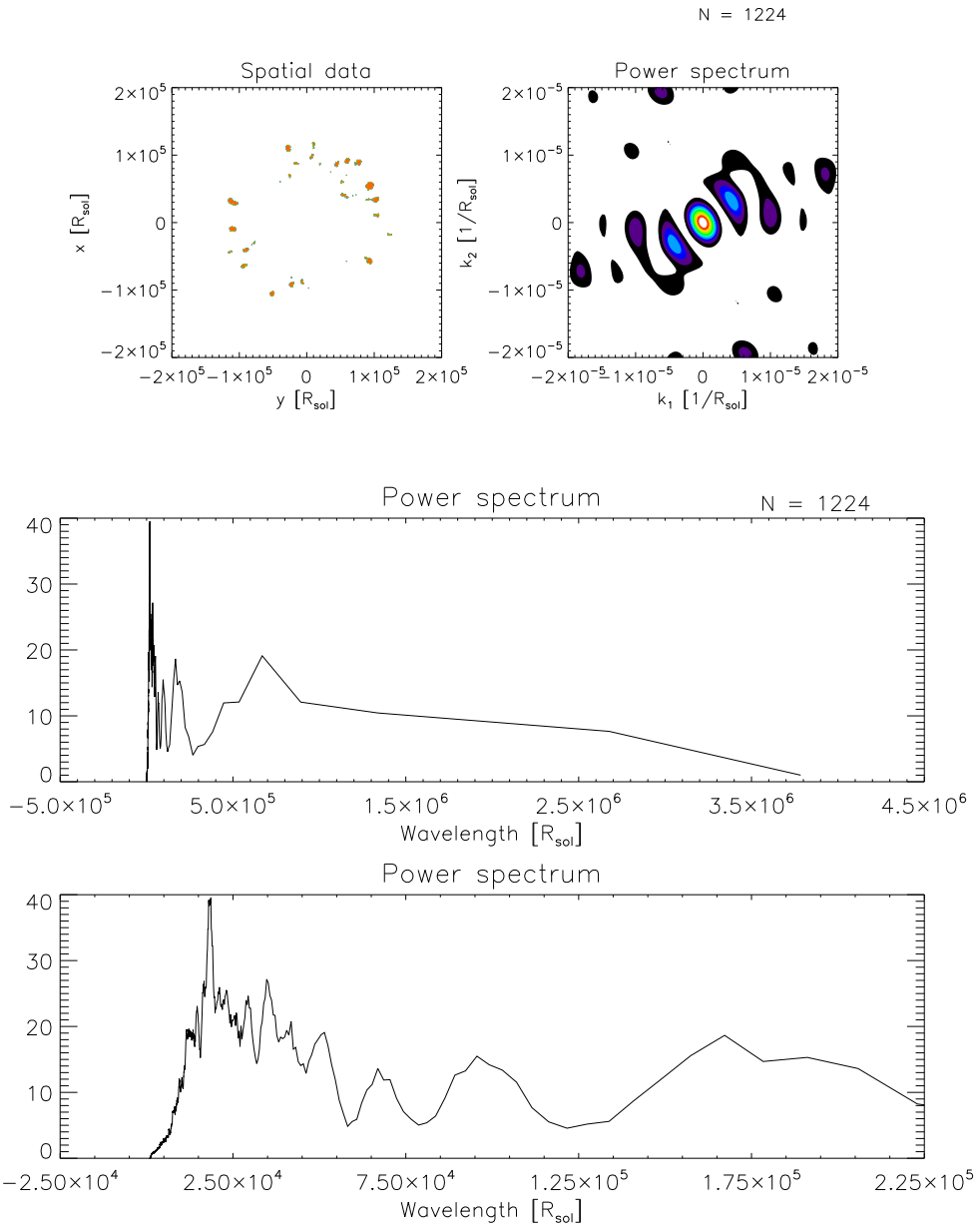

Figure D.46: Run 1M_no–burn at 0.517yrs corresponding to the time step plotted in figures D.26 and D.28.

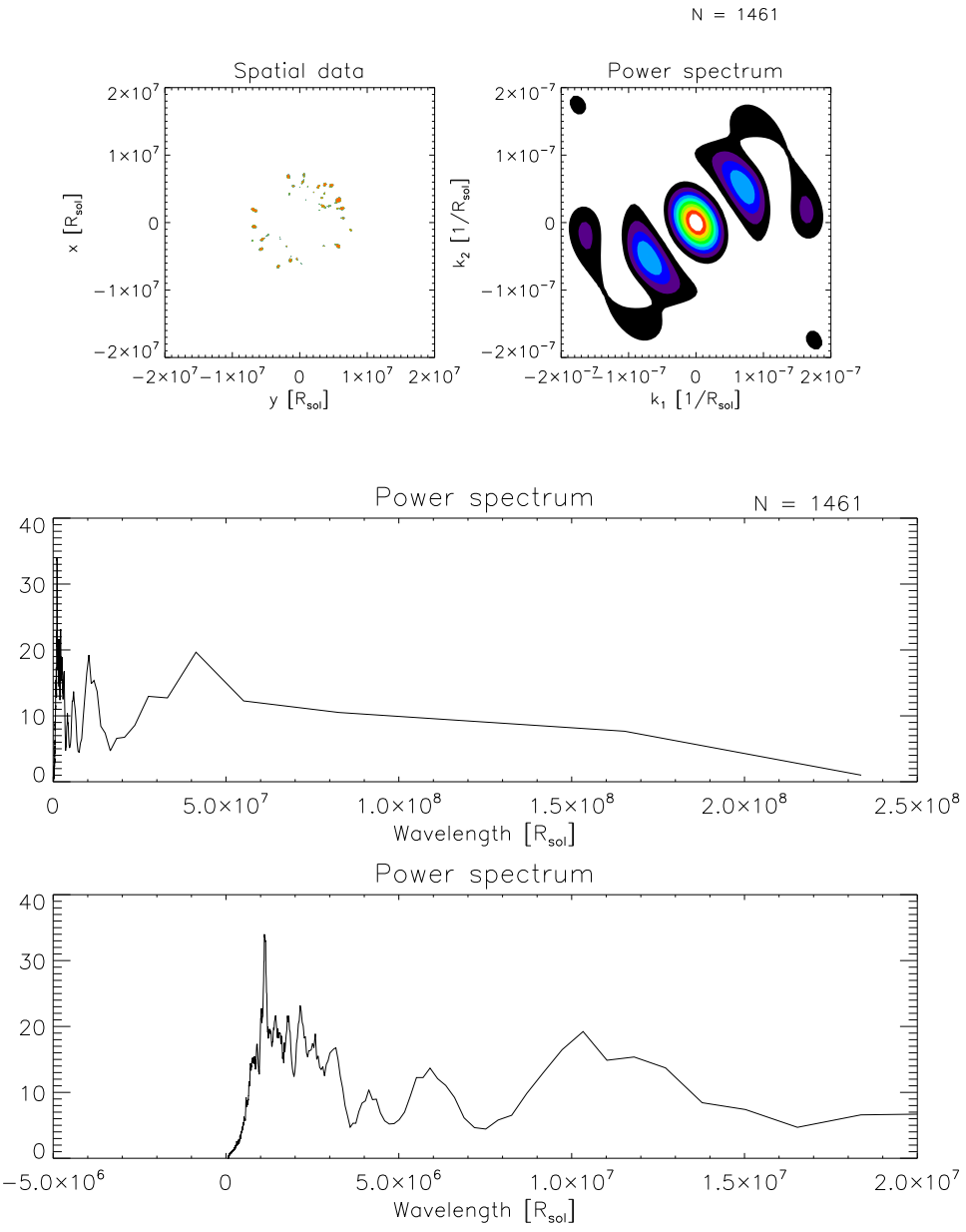

Figure D.47: Run 1M_no–burn at 31.8 yrs corresponding to the time step plotted in figures D.26 and D.29.

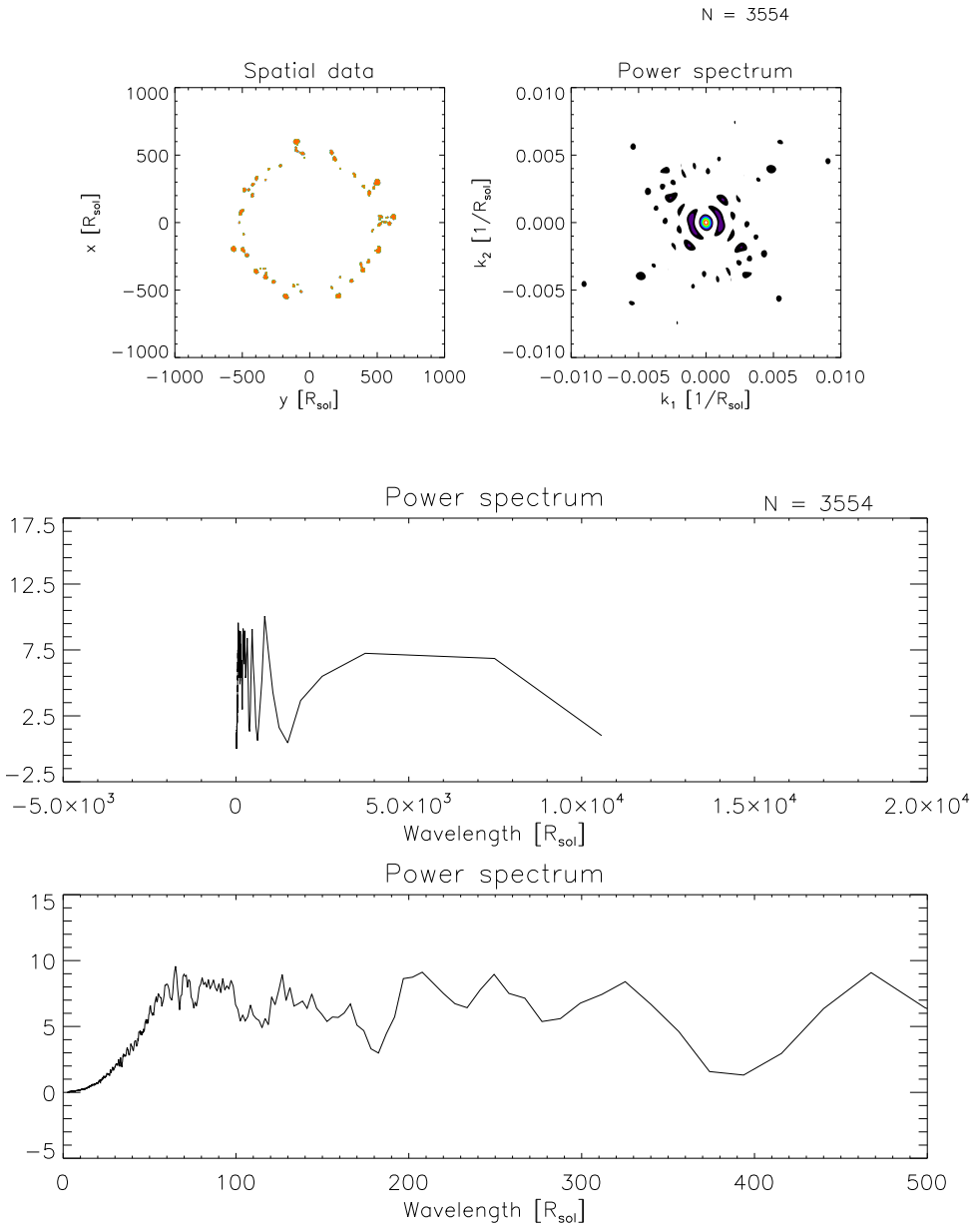

Figure D.48: Run 1M_burn_38nbrs at 19.4 hrs corresponding to the time step plotted in figures D.30, D.31, and D.32.

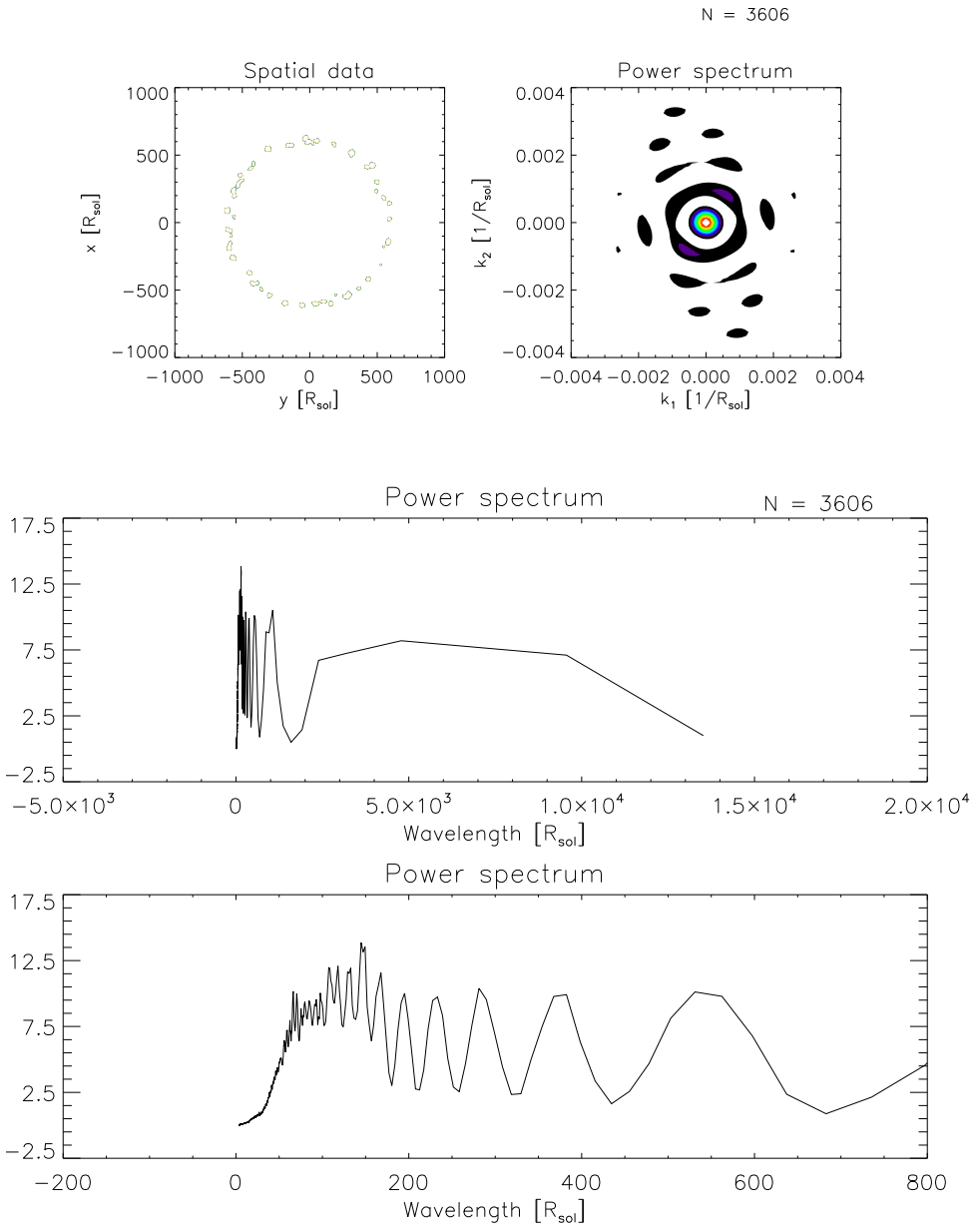

Figure D.49: Run 1M_burn_70nbrs at 24.0 hrs corresponding to the time step plotted in figures D.30, D.31, and D.32.

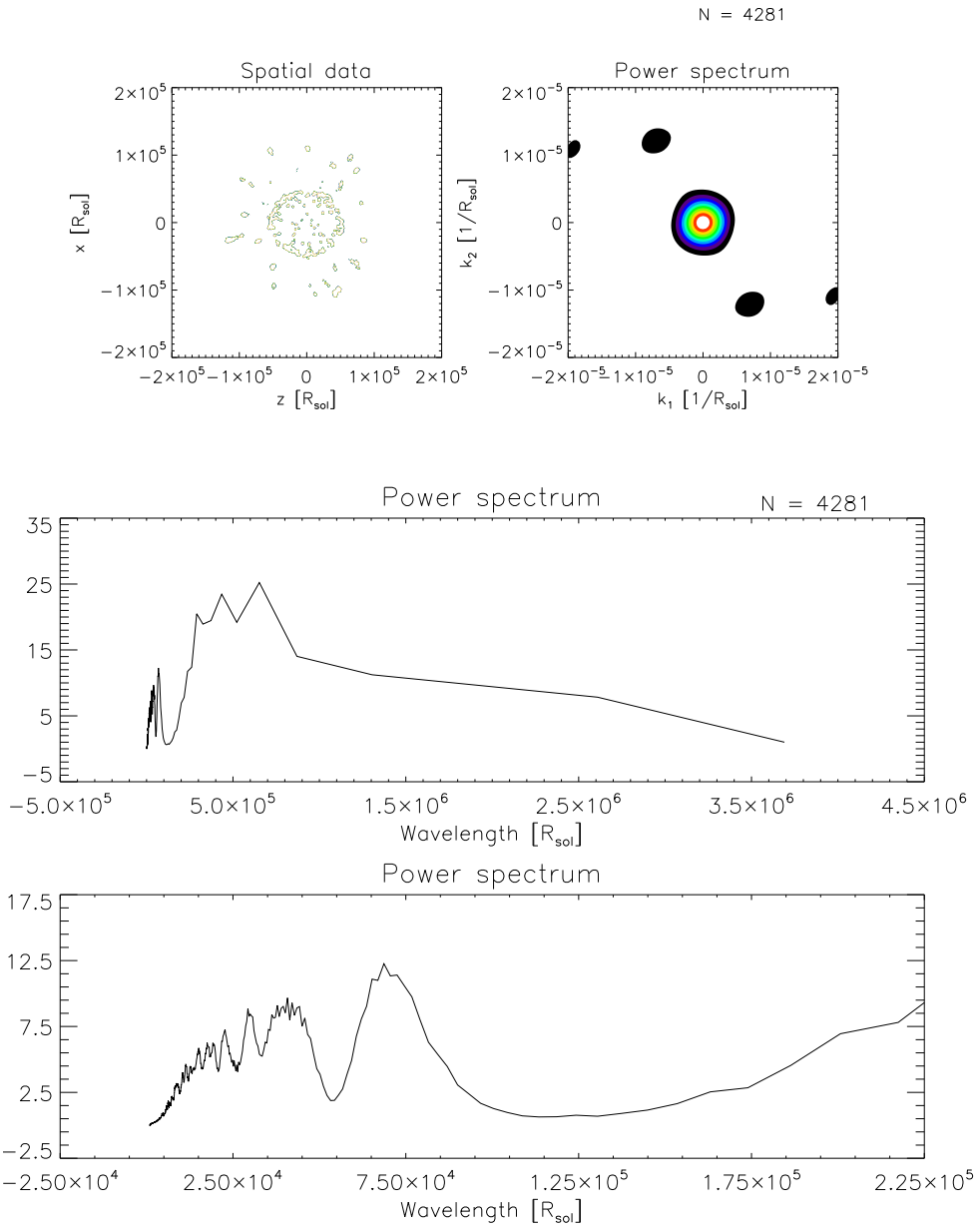

Figure D.50: The jet2 scenario in run 1M_jet2 at 0.507yrs corresponding to the time step plotted in figure D.33. Plotted is a slice parallel to the ”jet”-axis (z-axis).

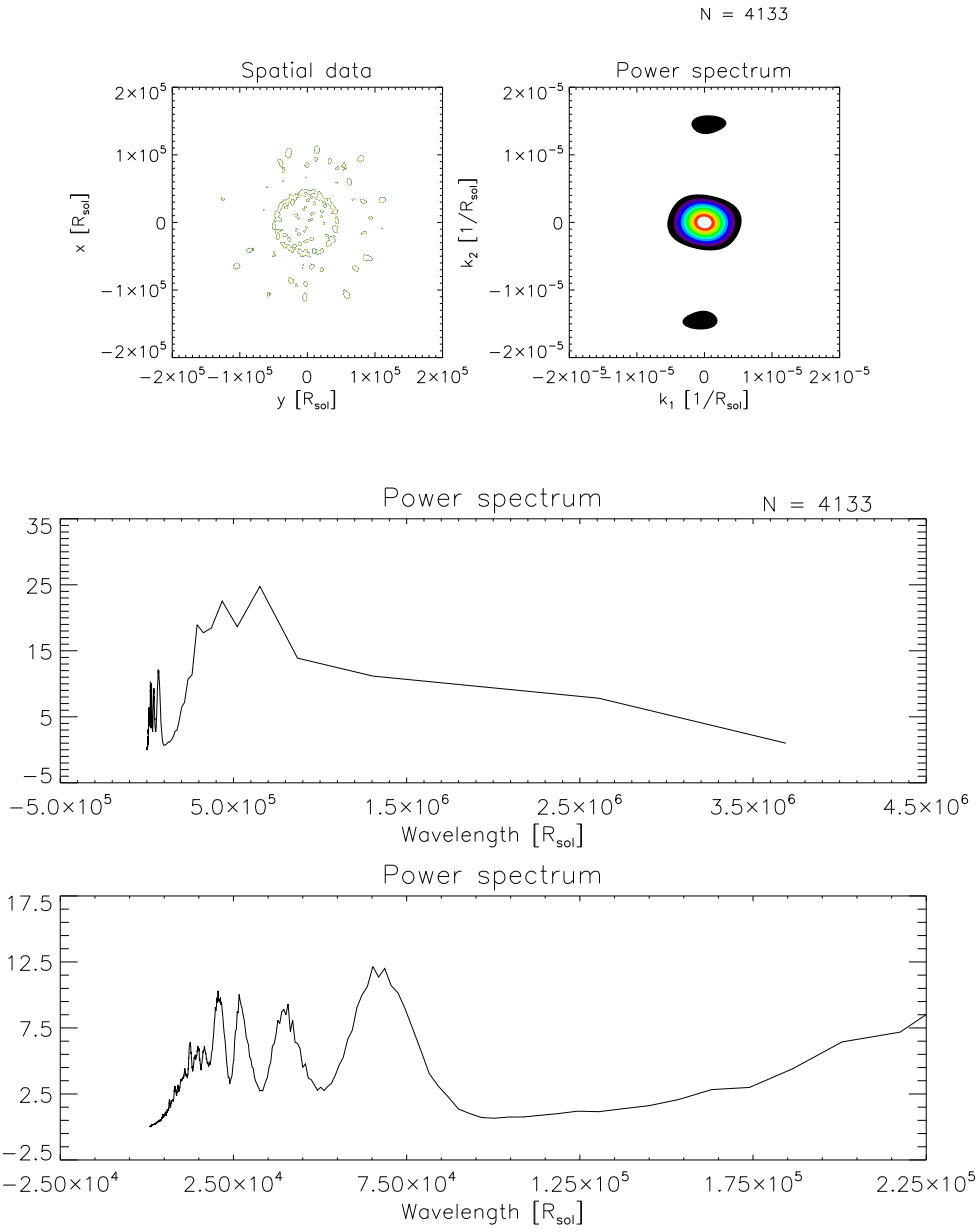

Figure D.51: Same as figure D.50, but for a slice perpendicular to (i.e. looking down) the ”jet”-axis. Note that the gap in RT clumps in the 2nd quadrant is due to the particular slice being plotted.

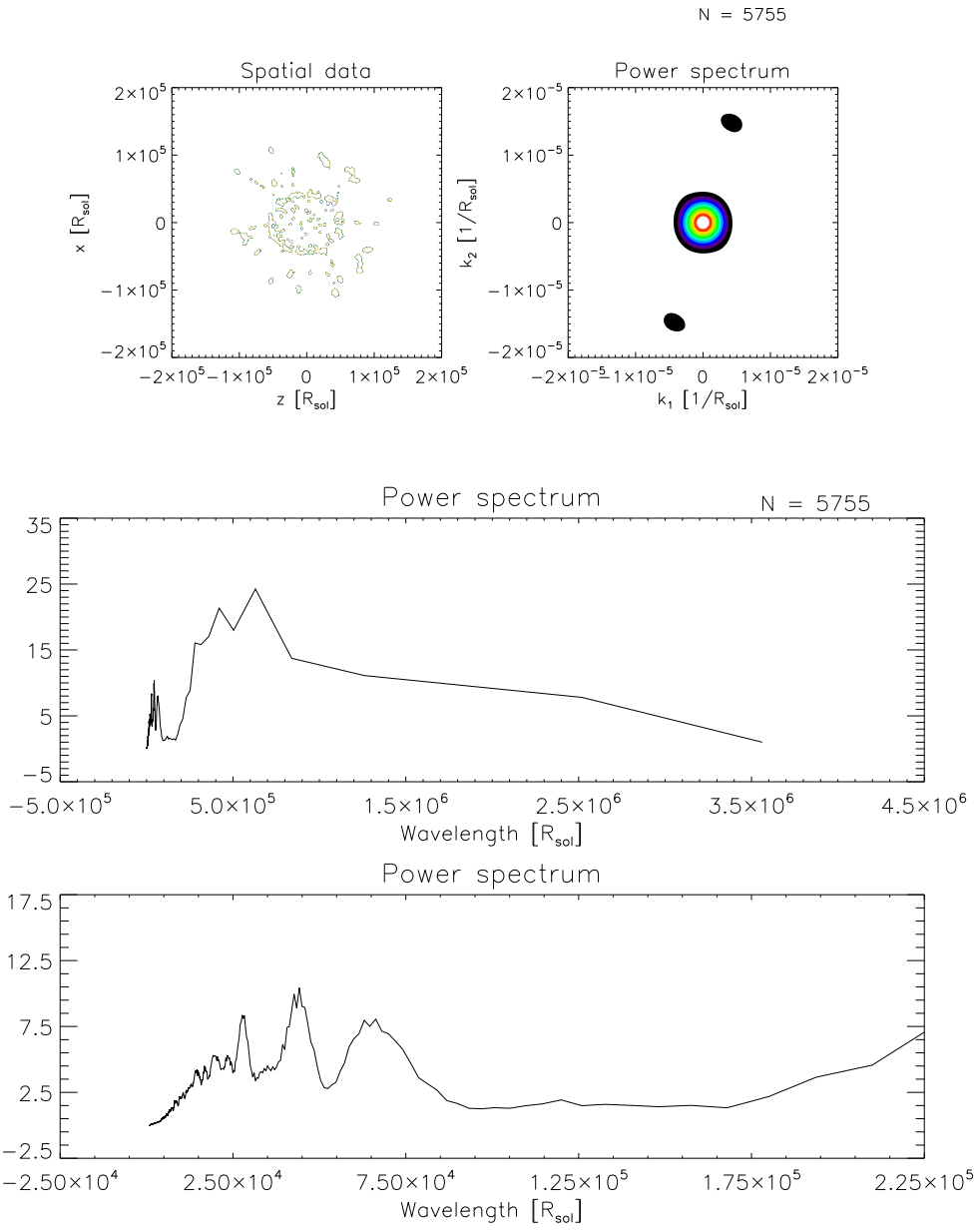

Figure D.52: The jet4 scenario of 1M_jet4 at 0.489yrs corresponding to the time step plotted in figure D.34. Plotted is a slice parallel to the ”jet”-axis (z-axis).

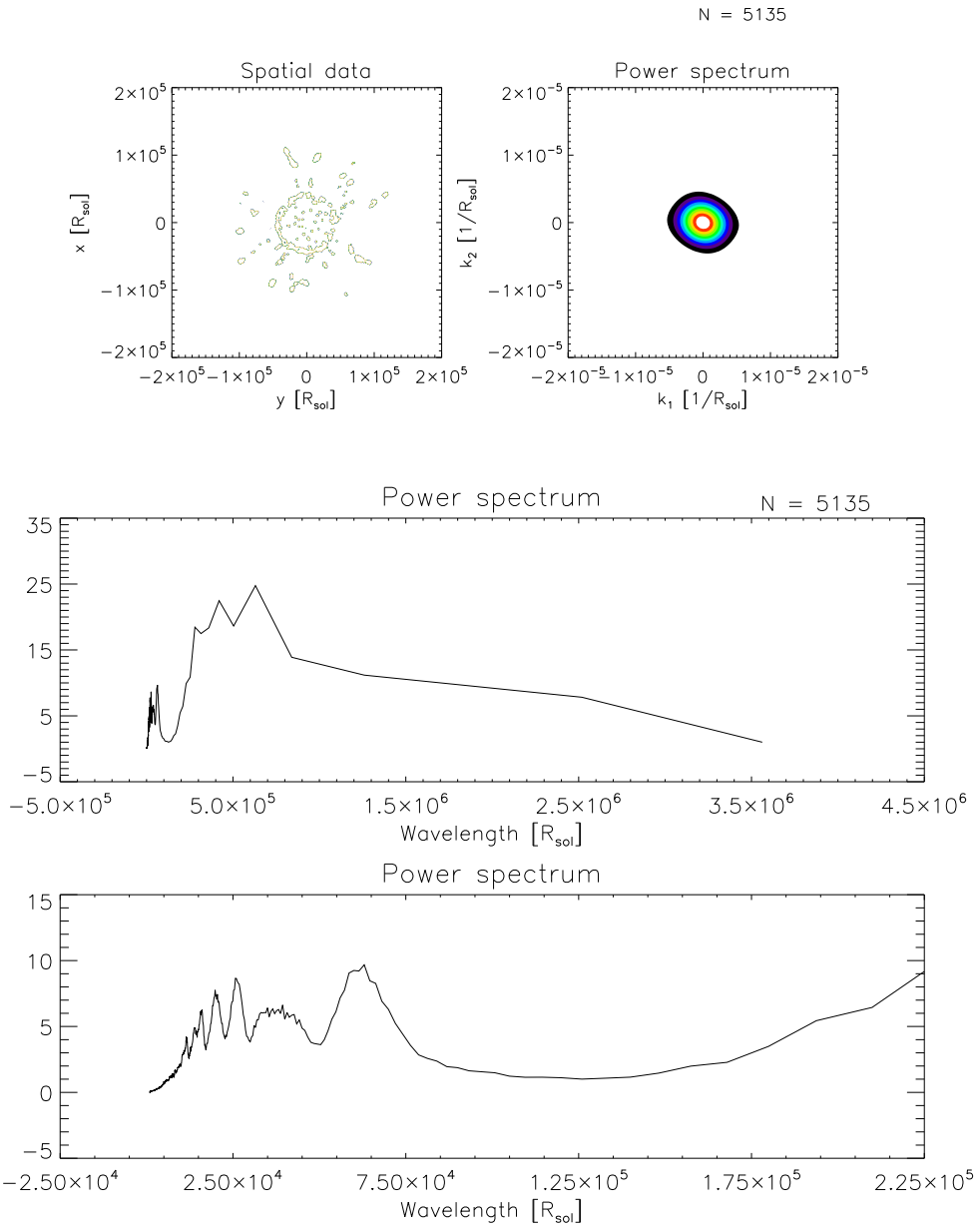

Figure D.53: Same as figure D.52, but for a slice perpendicular to (i.e. looking down) the ”jet”-axis.

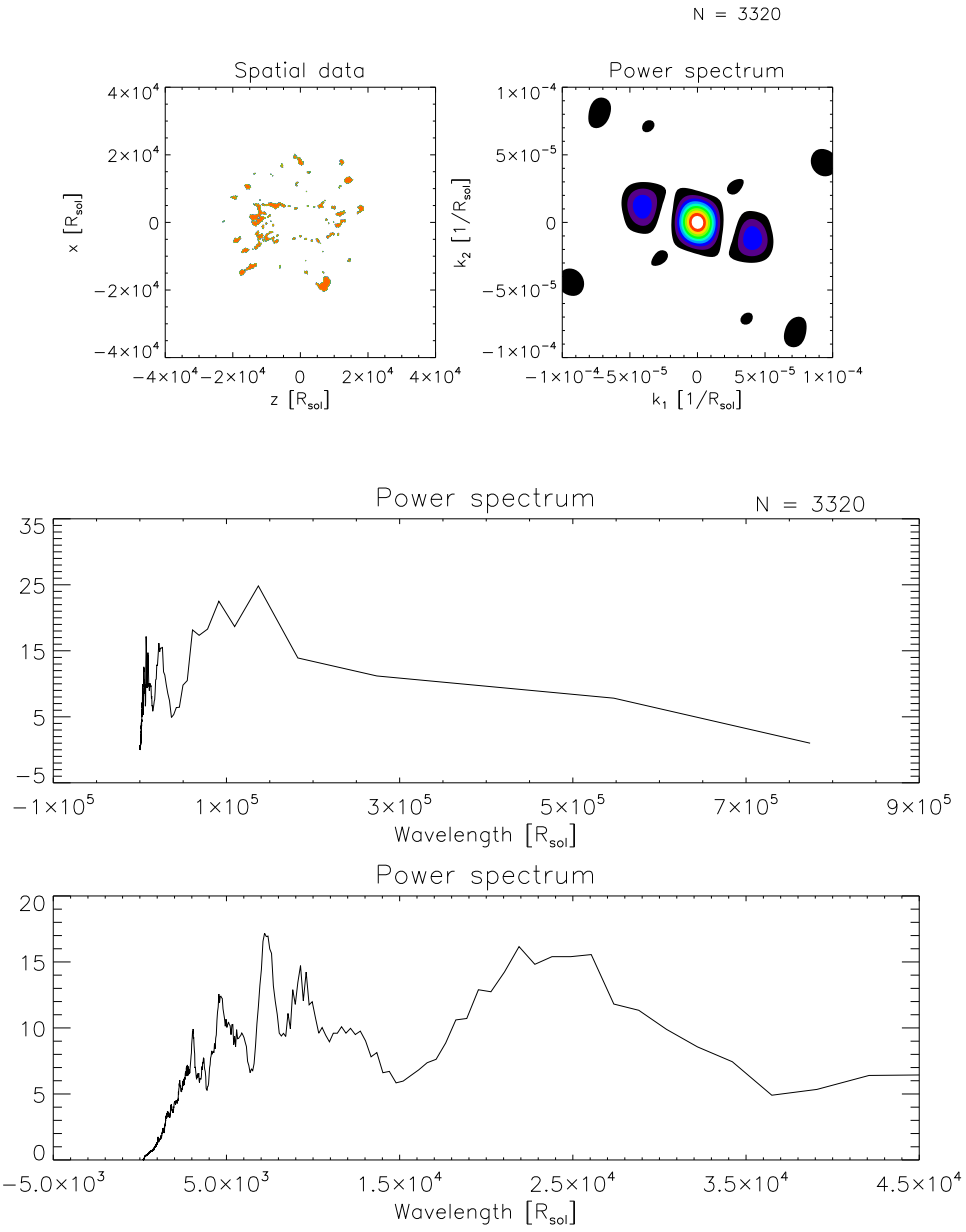

Figure D.54: The jet4 scenario of run 1M_jet4L at 17.6hrs corresponding to the time step plotted in figures D.35 and D.36. Plotted is a slice parallel to the ”jet”-axis (z-axis).

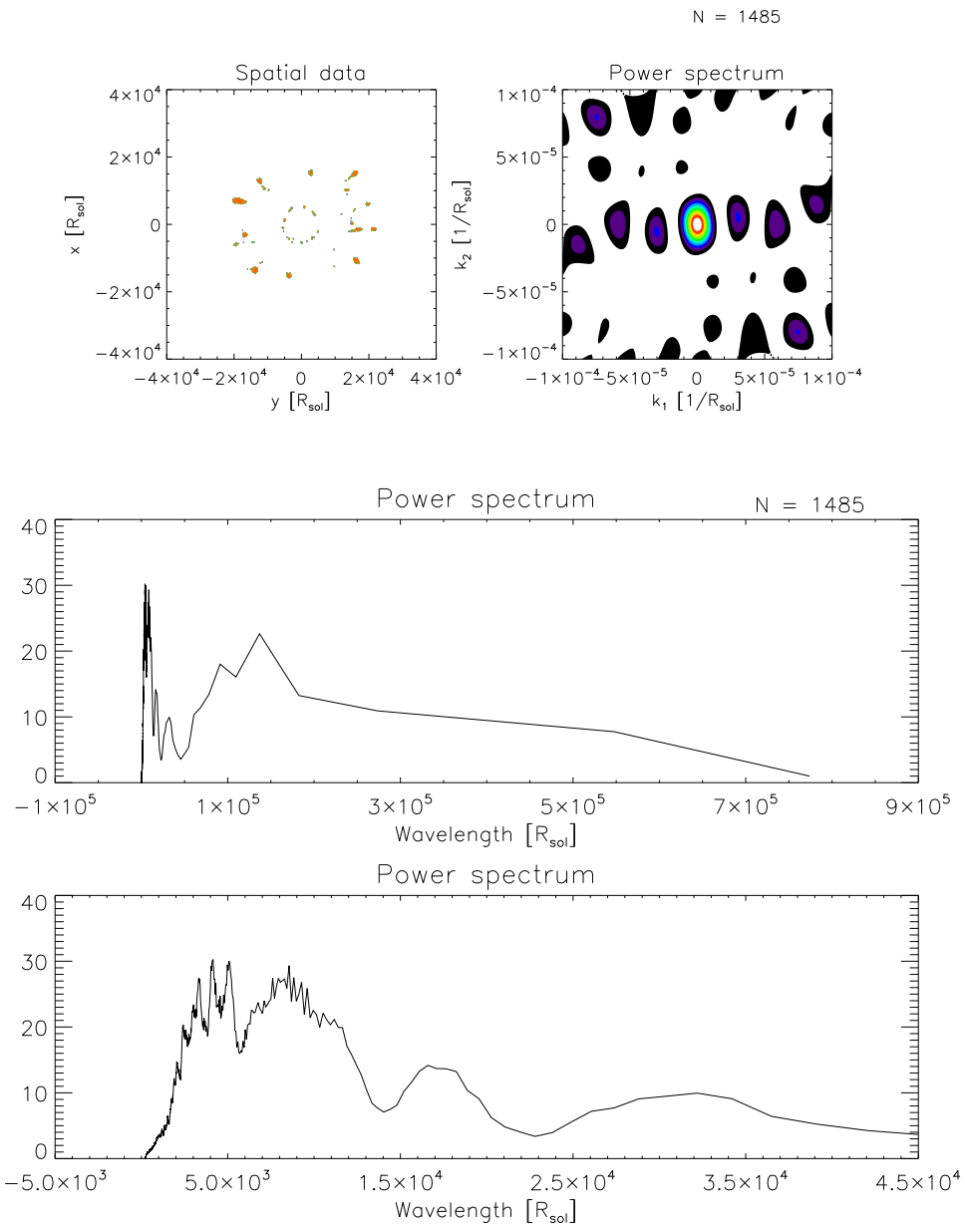

Figure D.55: Same as figure D.54, but for a slice perpendicular to the ”jet”-axis.

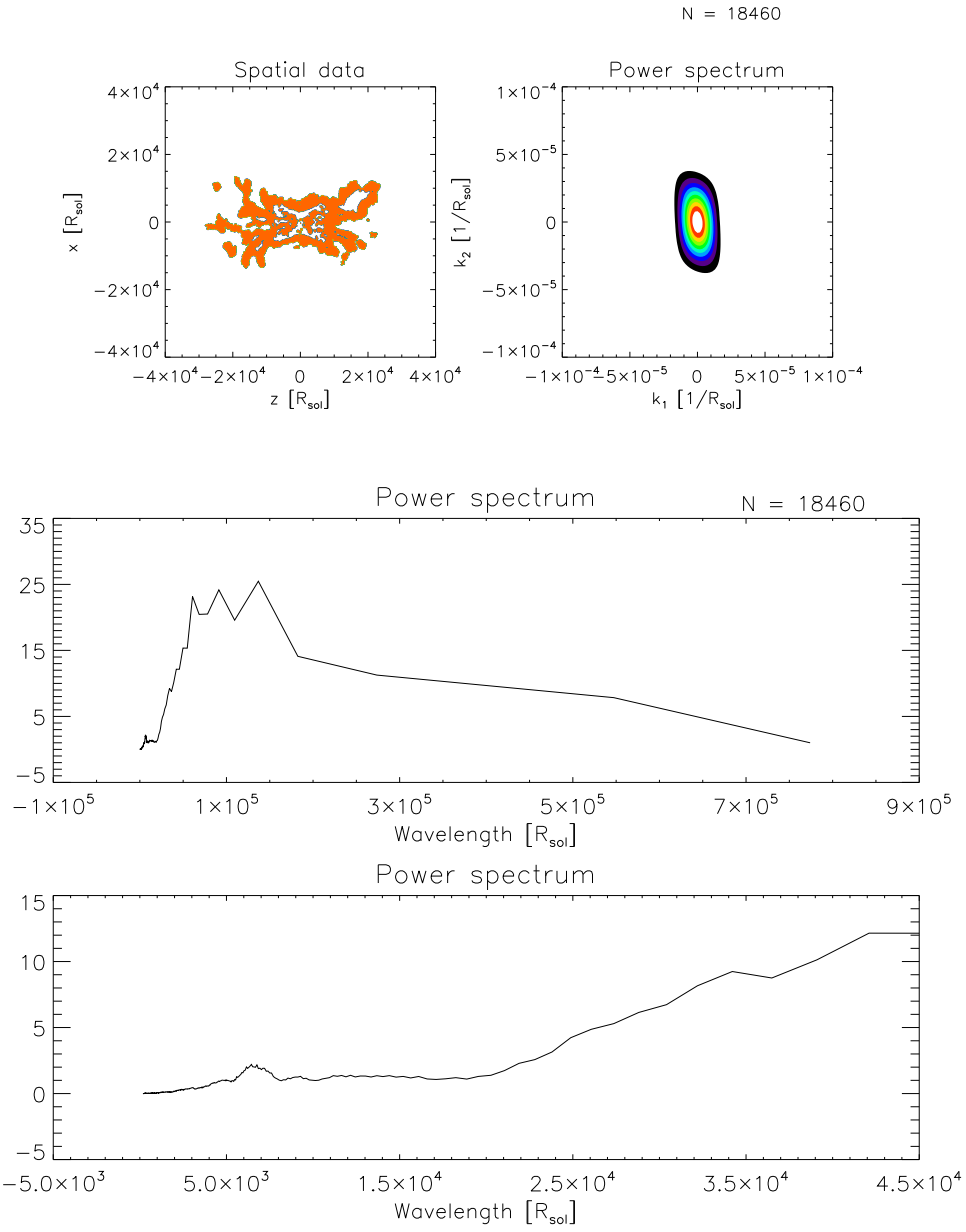

Figure D.56: The jet4 scenario of run 1M_jet4LL at 19.0hrs corresponding to the time step plotted in figures D.35 and D.37. Plotted is a slice parallel to the ”jet”-axis. Note that the ”smeared out” appearance of the RT structures is due to the chosen density threshold to select the region; a higher density threshold was found to only select a fraction of the RT clumps, thus this lower one was used.

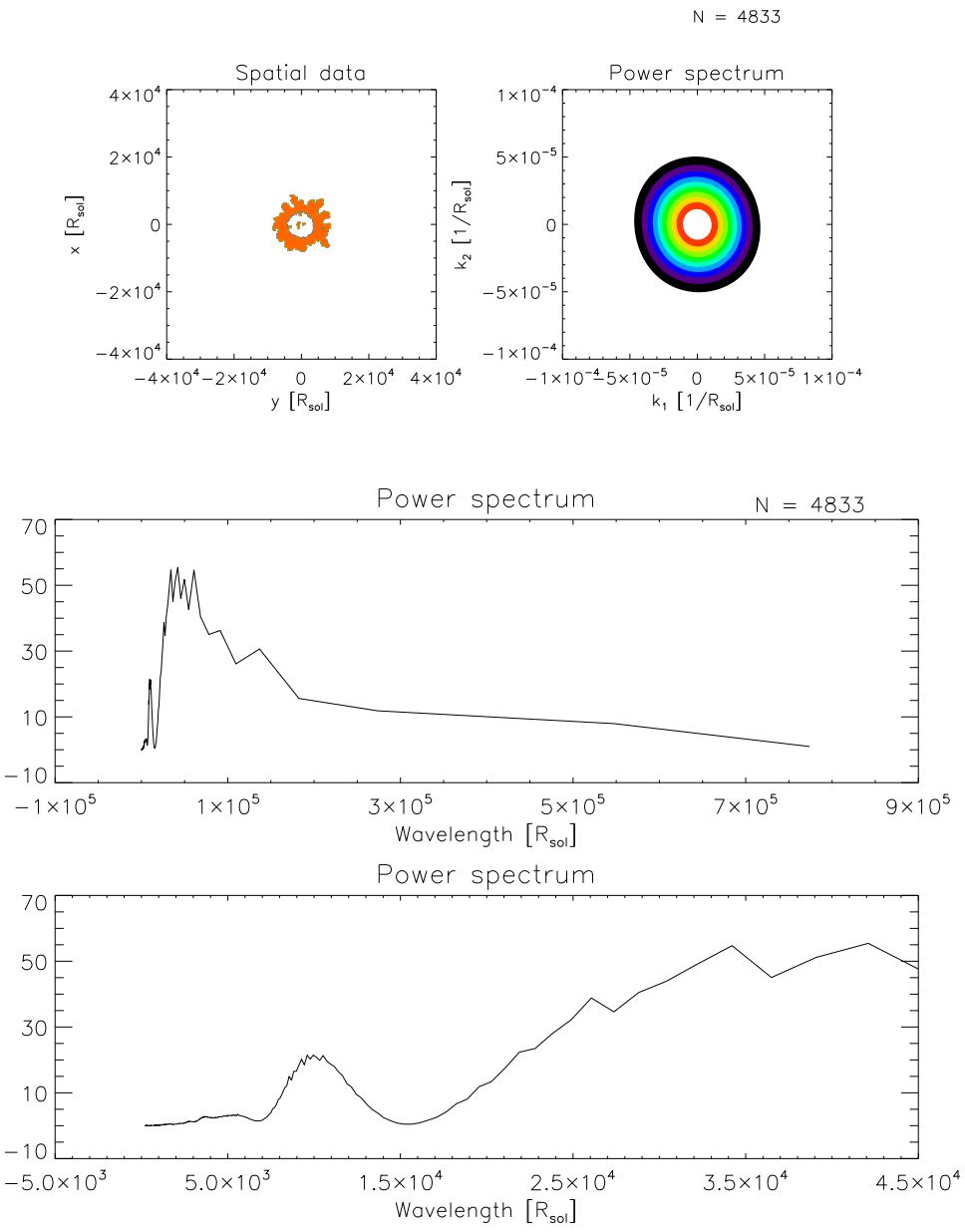

Figure D.57: Same as figure D.56, but for a slice perpendicular to the ”jet”-axis.

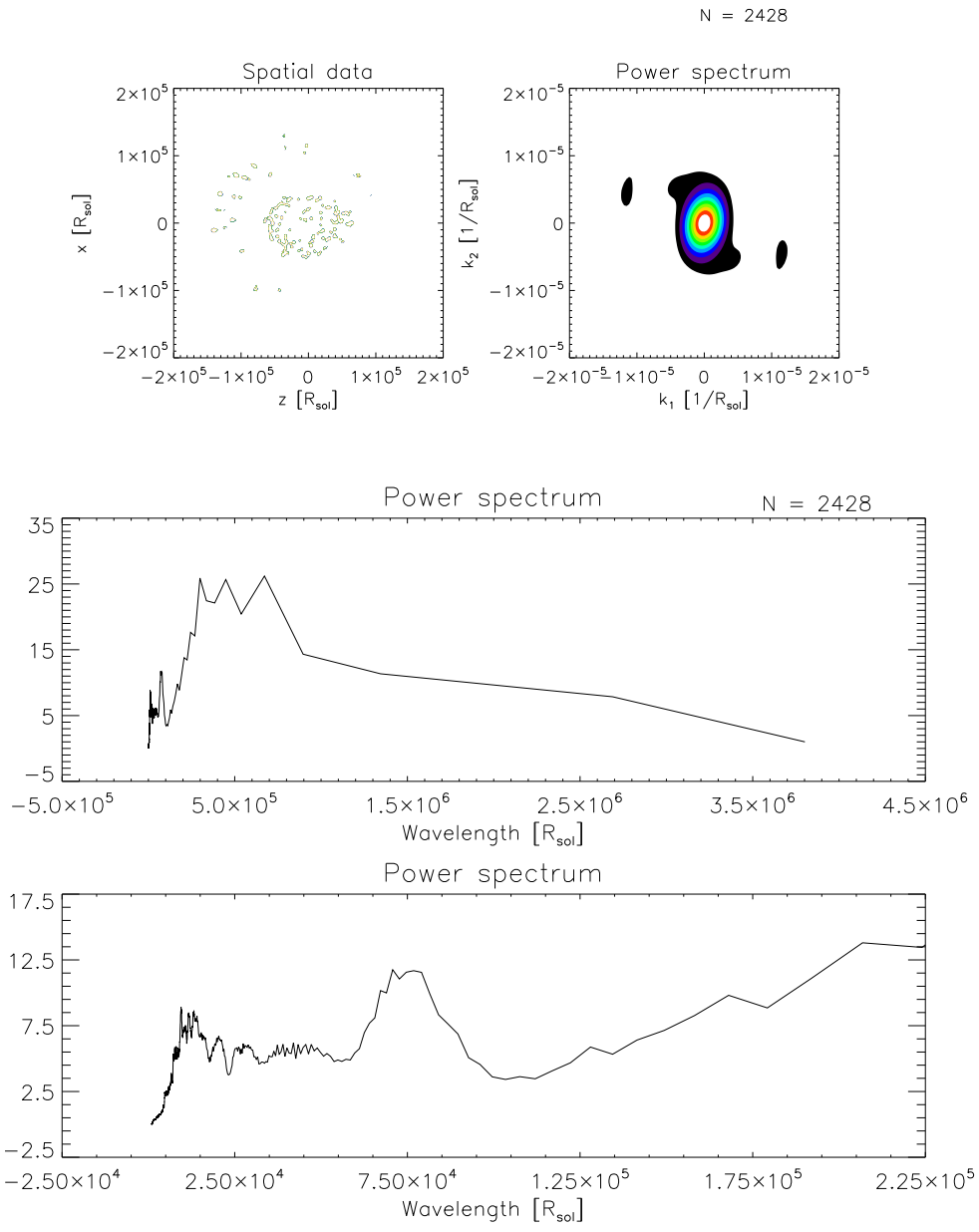

Figure D.58: The single-lobe scenario 1M_single–jet2 at 0.506yrs corresponding to the time step plotted in figures D.38 and D.39. Plotted is a slice in the xz-plane (roughly parallel to the lobe). Note that the absence of clumps in the fourth and first quadrant is an effect of the single ”jet”; the RT fingers and clumps in the direction of the ”jet” showed an increased density, thus the density threshold to select the region cut out the clumps in the opposite direction.

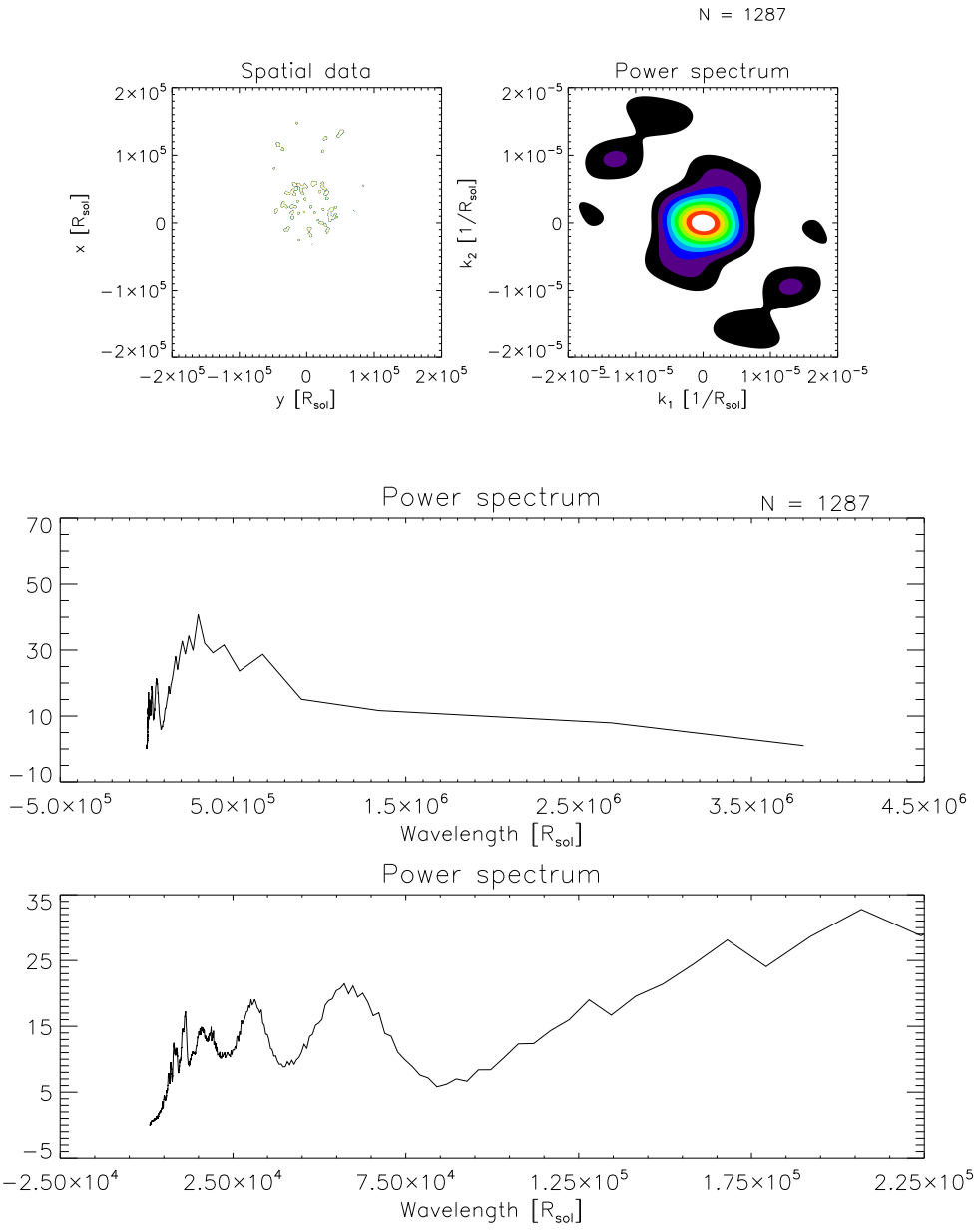

Figure D.59: Same as figure D.59, but for a slice in the xy-plane (approximately perpendicular to the lobe).

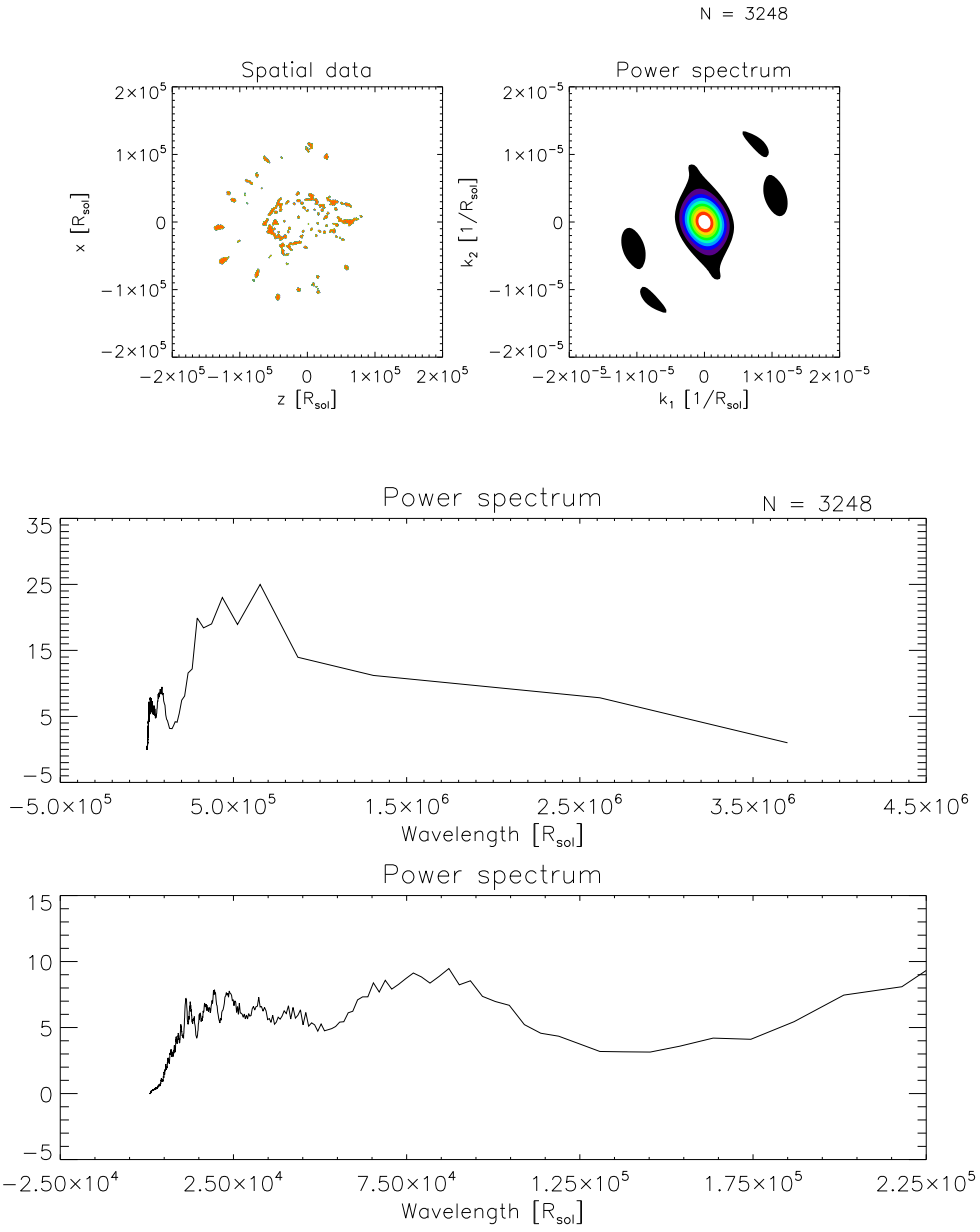

Figure D.60: The single-lobe scenario 1M_single–jet4 at 0.484yrs corresponding to the time step plotted in figures D.38 and D.39. Plotted is a slice in the xz-plane (roughly parallel to the lobe). Slightly less apparent is an absence of clumps in the opposite direction of the single ”jet”, since the high-density clumps created by the Ni- bubble effect somewhat counterbalance this appearance.

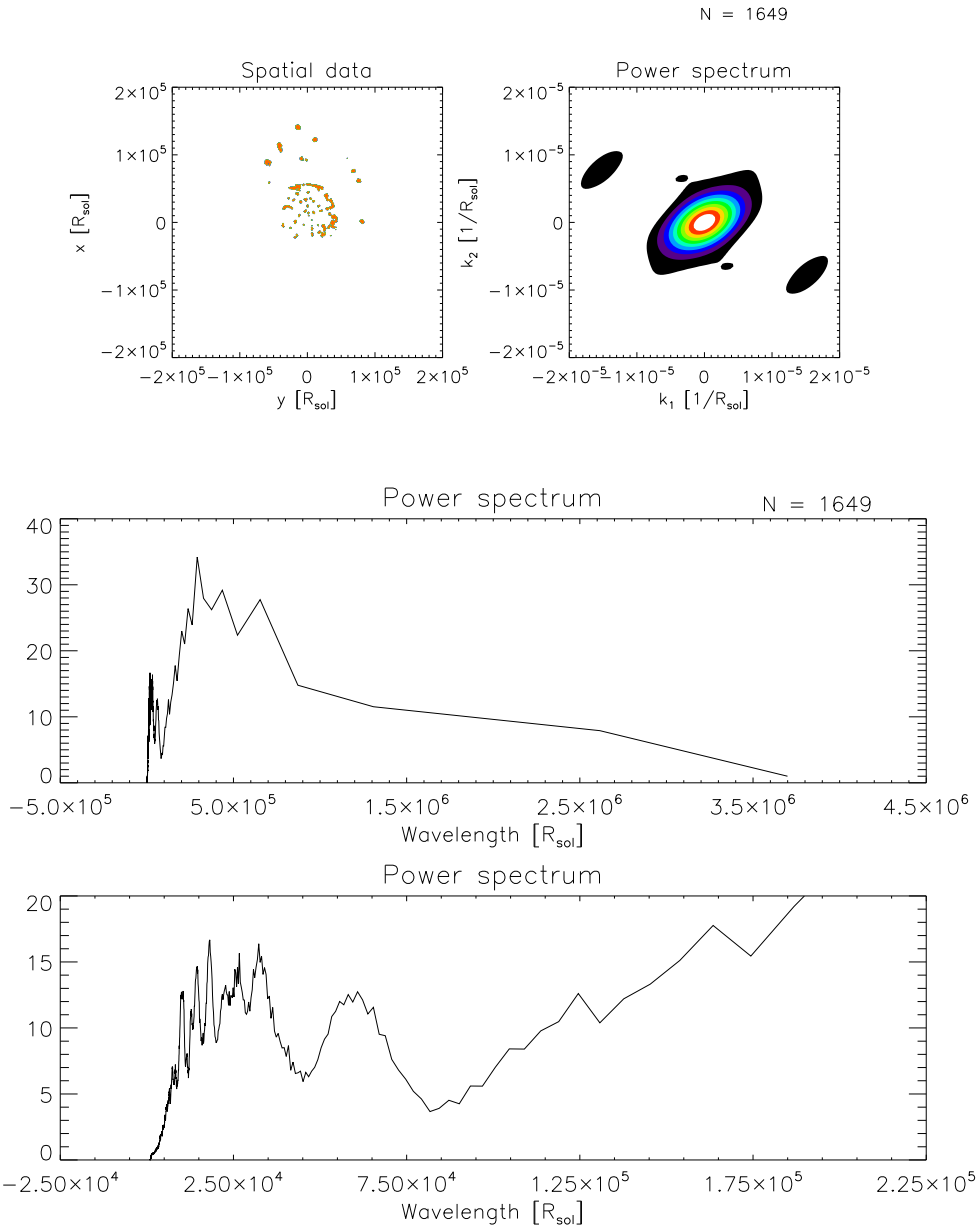

Figure D.61: Same as figure D.60, but for a slice in the xy-plane (approximately perpendicular to the lobe). The density threshold used to select the region exaggerates the absence of clumps opposite of the single lobe.